The Dissertation Committee for Junjing Bao

certifies that this is the approved version of the following dissertation:

Interaction between Plasma and Low-κ Dielectric Materials

COMMITTEE:

Paul S. Ho, Supervisor

Chih-Kang Shih

Zhen Yao

Maxim Tsoi

Jack C. Lee

Interaction between Plasma and Low-κ Dielectric Materials

by

Junjing Bao, B.S.

Dissertation

Presented to the Faculty of the Graduate School of

The University of Texas at Austin

in Partial Fulfillment

of the Requirements

for the Degree of

Doctor of Philosophy

The University of Texas at Austin

May 2008

Dedication

To my parents

Acknowledgements

Life is a journey. I feel lucky and grateful to spend six years on studying and doing research at the University of Texas at Austin.

First, I am deeply indebted to my research adviser Prof. Paul S. Ho for leading me into the semiconductor industry, offering me the chances to get involved into various projects, providing continuous support and guidance throughout my doctoral research. I also would like to thank my committee members Prof. Chih-Kang Shih, Prof. Zhen Yao, Prof. Maxim Tsoi, Prof. Jack C. Lee for their support and advice. I specially thank Dr. Jang-Hi Im for carefully proofreading my dissertation and providing valuable feedback. I would like to thank Michael D. Goodner, Michael L. McSwiney, Moinpour Moinpour, and Grant M. Kloster of Intel for providing the financial support for my thesis research, most of the samples and holding monthly teleconferences to discuss results.

Second, I am grateful to my colleagues and friends at UT-Austin, especially people at J.J. Pickle Research Campus, for their help, advice and discussions about my research. This research can not be completed without many people's help and involvement. Special thanks go to Dr. Junjun Liu for showing me the vacuum work and completing the research of atomic layer deposition together; Hualiang Shi and Huai Huang for completing the research of plasma damage and dielectric recovery together; Hualiang Shi for quantum chemistry calculation; Eunsu Paek and Prof. G.S. Hwang for Monte Carlo simulation of plasma damage; Dr. Bin Li, Dr. Ji-Ping Zhou, Dr. Xiaoxia Gao and Dr. Domingo Ferrer for helping with TEM and EELS; Dr. Yangming Sun for helping with XPS and SEM; Manhong Zhang, Feng Zhu and Brook Chao for dielectric constant measurements; William Fordyce, William Ostler, William James and Gabriel Glenn in MER facilities for helping with miscellaneous mechanical work; Mike Tiner and William M. Lackowski in CNM facilities for using FIB, dicer, etc and our secretary Ms. Jo Ann Smith for always being there to help. I also want to thank many of my Chinese friends at UT-Austin for their friendships and spending time playing balls and hanging out together.

Finally, I would like to thank my family. I am grateful to my parents for their continuous encouragement and patience. It is also a wonderful thing for me to fall in love with Saijuan Zhang, my current fiancée, who is always standing behind me firmly.

Interaction between Plasma and Low-κ Dielectric Materials

Publication No. _______________

Junjing Bao, Ph.D.
The University of Texas at Austin, 2008
Supervisor: Paul S. Ho

With the scaling of devices, integration of porous ultra low-κ dielectric materials into Cu interconnect becomes necessary. Low-κ dielectric materials usually consist of a certain number of methyl groups and pores incorporated into a SiO_2 backbone structure to reduce the dielectric constant. They are frequently exposed to various plasmas, since plasma is widely used in VLSI semiconductor fabrication such as etching, ashing and deposition. This dissertation is aimed at exploring the interaction between plasma and low-κ dielectric surfaces.

First, plasma assisted the atomic layer deposition (ALD) of Ta-based Cu barriers. Atomic layer deposition of Ta barriers is a self-limited surface reaction, determined by the function groups on the low-κ dielectric surface. But it was found $TaCl_5$ precursor could not nucleate on the organosilicate low-κ surface that was terminated with methyl groups. Radical NH_x beam, generated by a microwave plasma source, could activate the surface through exchanging with the methyl groups on the low-κ surface and providing active Si-NH_x nucleation sites for $TaCl_5$ precursors. Results from Monte Carlo simulation of the atomic layer deposition demonstrated that substrate chemistry was critical in controlling the film morphology.

Second, the properties of low-κ dielectric materials tended to degrade under plasma exposure. In this dissertation, plasma damage of low-κ dielectric surface was investigated from a mechanistic point of view. Both carbon depletion and surface densification were observed on the top surface of damaged low-κ materials while the bulk remained largely uninfluenced. Plasma damage was found to be a complicated phenomenon involving both chemical and physical effects, depending on chemical reactivity and the energy and mass of the plasma species. With a downstream plasma source capable of separating ions from the plasma beam and an *in-situ* x-ray photoelectron spectroscopy (XPS) monitoring of the damage process, it was clear that ions played a more important role in the plasma damage process. Increase of dielectric constant after plasma damage was mainly attributed to moisture uptake and was confirmed with quantum chemistry calculation. Annealing was found to be effective in mitigating moisture uptake and thus restoring κ value.

Finally, oxygen plasma damage to blanket and patterned low-κ dielectrics was studied in detail. Energetic ions in oxygen plasma contributed much to the loss of film hydrophobicity and dielectric constant through the formation of C=O and Si-OH. Based on results from residual gas analyses (RGA), three possible reaction paths leading to carbon depletion were proposed. This was followed by analytical solution of the evolution of carbon concentration during O_2 plasma damage. O_2 plasma damage to patterned CDO film was studied by TEM/EELS. And the damage behavior was simulated with Monte Carlo method. It was found that the charging potential distribution induced by plasma was important in determining the carbon loss in patterned low-κ films. The charging potential distribution was mainly related to the geometry of low-κ trench

structures. To recover the dielectric constant, several recovery techniques were tried and briefly discussed.

Table of Contents

List of Tables xi

List of Figures xii

Chapter 1 Introduction 1

- 1.1 Challenges of low k integration 4
- 1.2 Characteristics of low k dielectrics... 21
- 1.3 Interaction between plasma and low k surfaces 14
- 1.4 Organization of the dissertation 29

Chapter 2 Experimental 31

- 2.1 Remote plasma process chamber 31
- 2.2 X-ray techniques 36
  - 5.1.1 X-ray photoelectron spectroscopy (XPS).......................... 36
  - 5.1.2 X-ray reflectivity (XRR) 41
- 2.3 Optical methods 45
  - 5.1.1 Spectroscopic ellipsometer 45
  - 5.1.2 Fourier transform infrared spectroscopy (FTIR)................ 48
- 2.4 Electron microscopy 55
  - 5.1.1 Scanning electron microscopy (SEM)..............................55
  - 5.1.2 Transmission electron microscopy (TEM) 56
- 2.5 Residual gas analysis (RGA) 62
- 2.6 Electrical characterization 64
- 2.7 Summary 66

Chapter 3 Process Enhancements with Plasma Beams 68

- 3.1 Atomic layer deposition 69
- 3.2 Surface effects on atomic layer deposition 76
- 3.3 Effects of plasma beam activation 80
- 3.4 Monte Carlo simulation 87
- 3.5 Summary 95

Chapter 4 Investigation of Plasma Damage of Low-κ Dielectric Surface 97

- 4.1 Experimental study of plasma damage. … ……………………......... 98
  - 4.1.1 Introduction …………………………………………………...98
  - 4.1.2 Damage by Ar, O_2, N_2/H_2, N_2, and H_2 plasma in RIE chamber……………………………………………………100
  - 4.1.3 Damage by NH_3, Ar, He and O_2 plasma in a downstream plasma process…..…...111
- 4.2 Mechanism of plasma damage. …… … ……………………...............121
  - 4.2.1 Impact of water absorption …………………..……………….. 121
  - 4.2.2 Origin of dielectric loss …..123
- 4.3 Summary ……………………………………………………...….129

Chapter 5 Oxygen Plasma Damage Mechanisms and Dielectric Recovery of Low-κ Materials ………..…………………………………………………131

- 5.1 Oxygen plasma damage to blanket and patterned low-κ films………….. 132
  - 5.1.1 Mechanistic study of O_2 plasma damage to blanket low-κ films ……………………………………………………………..132
  - 5.1.2 Mathematical modeling of the damage process……............. 138
  - 5.1.3 Oxygen plasma damage to patterned low-κ material …………. 141
  - 5.1.4 Angle dependence of oxygen plasma damage …………………148
  - 5.1.5 Monte Carlo simulations of charging and ion/neutral flux distribution …………………………………………………. 153
- 5.2 Dielectric recovery … … … … … … … … …………………….......... 157
  - 5.2.1 Recovery of CH_4 beam……………………………….............. 157
  - 5.2.2 Silylation …………………..… … ….….…………………...... 162
- 5.3 Summary …………………………………………………………. 171

Chapter 6 Conclusions and Future Work ...…………………………………………. 173

- 6.1 Conclusions …………………...…... … … … … …..………….. … 173
- 6.2 Suggestions for future work ……... … … …...………………………177

Appendix ...…………………………………………………………….. ……..... 179

Bibliography.……………………………………………………………………….. 183

Vita……...………………………………………………………………………... 196

List of Tables

Table 1.1 Dielectric constant of future low-κ materials ……………………………15
Table 1.2 Example of low-κ dielectric materials and their deposition methods …...18
Table 1.3 Densities, ion and electron temperatures and applications of plasmas ….22
Table 2.1 FTIR peak assignment of the structures in low-κ materials …………….52
Table 2.2 Mass assignment table used in this research ……………………………64
Table 2.3 Overview of various analytical techniques used in this research ……….67
Table 3.1 Relation between film microstructure and its physical property ……….72
Table 3.2 Evaluation of barrier materials ………………………………………….73
Table 3.3 Typical ALD halide process conditions …………………………………76
Table 3.4 Evolution of surface chemical composition of dense OSG after pretreatment of plasma NH_3 and H_2 ……………………………………83
Table 4.1 Carbon composition and dielectric polarization of low-κ films after plasma damage. Samples were treated by H_2, N_2, N_2/H_2, O_2, Ar plasmas at 30 sccm, 30 mtorr for 20 min. in an Oxford RIE chamber ………………..102
Table 4.2 Property of the low-κ film after 100 eV NH_3, Ar and He downstream plasma treatments at 1 mtorr for 15 min ………………………………113
Table 4.3 Characterization of κ=2.5 and κ=2.3 low-κ materials …………………120
Table 4.4 Comparison of hybrid and radical O_2 plasma damage to κ=2.5 and κ=2.3 low-κ materials …………………………………………………...120
Table 4.5 Polarizability of major elements in low-κ materials …………………...124
Table 4.6 Physical properties of major bonds in low-κ materials ………………...125
Table 4.7 Calculated and normalized dipole moments of different bonding configurations ………………………………………………………127
Table 5.1 Density, thickness, and roughness of the low-κ films after hybrid and radical O_2 treatment at 0^0 and 90^0 ………………………………….. 151
Table 5.2 Characterization of the low-κ material after plasma CH_4 treatment on oxygen ashed CDO films ……………………………………………158
Table 5.3 Measurement of the refractive index @ 633 nm and dielectric constant of the pristine, ashed and subsequent CH_4/H_2 repaired low-κ films ……...161
Table 5.4 Measurement of water contact angles after the vapor silylation treatments of TMCS, DMDCS and PTMOS/TMCS ………………………………165
Table 5.5 Area of major FTIR peaks and the measurement of water contact angles ……………………………………………………………………..170

List of Figures

Figure 1.1 Schematic diagram of BEOL interconnect RC circuit model …………… 2

Figure 1.2 Trend of gate, interconnect and sum of the delays with technology generation ……………………………………………………………………………3

Figure 1.3 Cross section of IBM airgap microprocessor ……………………………..4

Figure 1.4 Trench first dual damascene process flow ………………………………..6

Figure 1.5 Via first dual damascene process flow ……………………………………7

Figure 1.6 EM fundamental: EM is induced by the electrons' collision with metal atoms under external electric field ………………………………………..8

Figure 1.7 SEM images of void and hillock induced by EM on the metal line ……...8

Figure 1.8 (a) Via depletion and (b) line depletion of EM failure …………………...9

Figure 1.9 An energy band diagram illustrating electron driven Cu migration process ..……………………………………………………………………..11

Figure 1.10 SEM image of void formation at the via bottom under stress migration ..13

Figure 1.11 Sketch of the dielectric constant as a function of the frequency of electrical field ……………………………………………………………...17

Figure 1.12 Structure of HSQ (R=H) and MSQ (R=CH_3) …………………………...19

Figure 1.13 Structure of OSG ………………………………………………………...19

Figure 1.14 Normalized interline capacitance for lines embedded in SiO_2 and κ =2 porous low-κ film ……………………………………………………..25

Figure 1.15 Increase of dielectric constant of MSQ by different plasma …………….28

Figure 1.16 Electrical performance of photoresist stripping by different plasma on patterned porous MSQ …………………………………………..…28

Figure 1.17 Surface silylation of the damaged OSG surface with TMCS or HMDS ..29

Figure 2.1 Ultra high vacuum cluster tools for *in-situ* XPS and residual gas studies of plasma processing. Some important items are labeled as a). Gate valves; b). Load lock; c). Docking stations; d). Plasma process chamber; e). Evaporator; f). Residual gas analyzer …………………………………...32

Figure 2.2 Illustration of Oxford Scientific mini atom/ion hybrid source …………34

Figure 2.3 I-V curve measured by a Langmuir probe at the anode voltage of 400 V (left) and 1200 V (right) ……………………………………………………35
Figure 2.4 Core level X-ray photoemission process ………………………………..37
Figure 2.5 X-ray photoelectron spectroscopy survey of typical low-κ materials …..38
Figure 2.6 Sample structures and ARXPS strategy to detect (a) trench bottom and (b) trench sidewall ……………………………………………………………..41
Figure 2.7 Reflection and refraction of X-ray on the surface and interface of low-κ /Si bi-layer film stack ………………………………………………………42
Figure 2.8 Typical X-ray reflectivity spectra of low-κ SiCOH (t=188 nm) and high-κ HfO_xN_y (t=2 nm) on Si substrate ………………………………………..44
Figure 2.9 Reflection and refraction of (a) s-polarized and (b) p-polarized light waves at the interfaces of two media with refractive index n_1 and n_2 …………46
Figure 2.10 Schematic view of an FTIR system ……………………………………..50
Figure 2.11 Typical FTIR spectrum of OSG ………………………………………….51
Figure 2.12 FTIR peak deconvolution of anti-symmetrical Si-O-Si into the components of cage, network and suboxide ……………………………53
Figure 2.13 Schematic drawing of the three bond structures of Si-O-Si ……………53
Figure 2.14 Example of using subtractive FTIR technique to characterize the hydrophobic property of low-κ materials ………………………………54
Figure 2.15 (a) SEM and (b) STEM images of the cross section of low k materials after reactive ion etching He/O_2 plasma damage ………………………..58
Figure 2.16 (a) STEM cross section image of a via in the interconnect; (b) EELS spectrum of the barrier property; (b) EDX spectrum of the barrier property. The beams of EELS and EDX focus at the same position as indicated by the red spot in the STEM image …………………………...60
Figure 2.17 FIB micrographs of (a) a sample being milled by focused ions; (b) a frontal view of final TEM sample (~30 nm) ……………………………62
Figure 2.18 (a) Schematic of metal-insulator-semiconductor structure; (b) Typical C-V curve for a p-doped wafer ………………………………………………66
Figure 3.1 Illustration of one cycle of atomic layer deposition ……………………..70
Figure 3.2 Trend of the barrier thickness with the MPU pitch and production year ..70
Figure 3.3 Typical ALD growth curve on $SiLK^{TM}$ surface ………………………..75
Figure 3.4 Ta4p and N1s XPS spectra on (a) MSQ and (b) $SiLK^{TM}$ after 80 identical ALD cycles …………………………………………………………...77
Figure 3.5 Formation of Ta-O on OSG ……………………………………………..78
Figure 3.6 C1s XPS spectra of pristine $SiLK^{TM}$ and $SiLK^{TM}$ after 30 ALD cycles ...79
Figure 3.7 Coordination of Ta 5d orbits with carbon π electrons on the aromatic ring ……………………………………………………………………………80
Figure 3.8 ALD growth on pristine OSG and OSG after pretreatment of plasma NH_3 and H_2 ……………………………………………………………………81

Figure 3.9 Effects of NH_x pretreatment on ALD growth on dense OSG. N1s spectra a) of clean surface; b) after pretreatments; c) after 30 ALD cycles on untreated film; d) after 30 ALD cycles on pretreated film ……………...82

Figure 3.10 Ta4p and N1s peaks after the plasma pretreatment of (a) H, NH_x sequentially and (b) NH_x only ……………………………………...84

Figure 3.11 (a) TEM image of ALD Ta_3N_5 on p-OSG substrate; (b) Fourier transformed micrograph of Ta_3N_5 ……………………………………85

Figure 3.12 SEM images of (a) the pristine trench structure; (b) the identical trench structure after 200 ALD cycles …………………………………………87

Figure 3.13 Three types of growth modes: (a) Volmer-Weber (VW) growth (island formation); (b) Frank-van der Merwe (FM) growth (island formation); (c) Stranski-Krastanov growth (layer and island formation) ……………..…88

Figure 3.14 Formation of contact angles at the interface ……………………………89

Figure 3.15 Flow chart of the Monte Carlo simulation program ……………………92

Figure 3.16 Monte Carlo simulation of the effects of surface function groups and reaction probability on ALD growth ……………………………………93

Figure 3.17 Monte Carlo simulation of initial 20 ALD cycles growth on a) pristine porous OSG surface; b) activated porous OSG with 50% reactive sites ..94

Figure 4.1 FTIR spectra of low-κ film after Ar, O_2, N_2, N_2/H_2, and H_2 plasma treatments at 30 sccm, 30 mtorr and 150 w for 20 min. in an Oxford RIE chamber ……………………………………………………………...104

Figure 4.2 XRR fitted density and thickness results of the plasma damaged region. Samples were treated by Ar, O_2, N_2, N_2/H_2, and H_2 plasmas at 30 sccm, 30 mtorr and 150 W for 20 min. in an Oxford RIE chamber ……………...105

Figure 4.3 Normalized thicknesses of low-κ film after plasma treatments. Samples were treated by different plasmas at the bias power of 50 W and 200 W in an Oxford RIE chamber ……………………………………………..106

Figure 4.4 (a) C/Si and (b) O/Si obtained by XPS surface scan at the exit angle of 30^0 ($\sin 30^0=0.5$) and 90^0 ($\sin 90^0=1$) after 15 sccm He and 15 sccm O_2 plasma ……………………………………………………………………..107

Figure 4.5 C/Si obtained by XPS surface scan at the exit angle of 30^0 ($\sin 30^0=0.5$) and 90^0 ($\sin 90^0=1$) after He plasma, O_2 plasma, their mixture and their sequential treatment …………………………………………………108

Figure 4.6 Surface roughness of (a) pristine MSQ and (b) surface after He plasma damage …………………………………………………………………109

Figure 4.7 Load displacement curve of nanoindentation test on pristine and He/O_2 plasma damaged surface ……………………………………………110

Figure 4.8 Evolution of the surface elemental concentration with plasma dosage. Samples were treated by downstream NH_3 plasma for 15 min., 40 min. and 6 hours respectively …………………………………………………115

Figure 4.9 XPS depth profiling of the low-κ dielectric film damaged by a 400 eV downstream NH_3 plasma at 1 mtorr for 6 hours ………………………116

Figure 4.10 High resolution TEM images of (a) Pristine CDO; (b) CDO damaged by a 400 eV downstream NH_3 plasma at 1 mtorr for 6 hours. Low-κ surfaces were coated with photoresist to prevent samples from being damaged during TEM sample preparation ……………………………………….116
Figure 4.11 (a) FTIR and differential FTIR spectra show the increase of Si-OH and moisture uptake in the low-κ sample after NH_3 plasma. (b) Differential FTIR spectra show changes of Si-O-Si (suboxide, network and cage) and Si-CH_3 after NH_3 plasma treatment. Samples were treated by 400eV NH_3 plasma at 1 mtorr for 15 min. …………………………………………..118
Figure 4.12 Ratios of C/Si within 5 nm at top of the low-κ film after He and NH_3 plasma treatment at 1 mtorr for 40 min.. Hybrid species include both ions and neutrals where the ion energy was 100eV and the radical species consist of neutrals only …………………………………………………...119
Figure 4.13 Recovery of the refractive index after plasma damage by annealing. Samples were treated by downstream hybrid plasmas of 600 eV He, 50 eV NH_3, and 400 eV Ar respectively at 1 mtorr for 40 min and then annealed at 130°C for 1 hour …………………………………………………..122
Figure 4.14 Differential FTIR spectra of low-κ films after annealing at 100°C, 140°C and 250°C for 1 hour respectively. Samples were damaged by N_2/H_2 plasma for 20 min. in an Oxford RIE chamber ………………………...123
Figure 4.15 Two equivalent circuits ………………………………………………...128
Figure 5.1 XPS C1s sprectra after the treatment of (a) 400 eV hybrid O_2; (b) radical O_2 for 15 min. ………………………………………………………….133
Figure 5.2 Differential FTIR spectra after the treatment of 400 eV hybrid O_2 and radical O_2 for 15 min. ……………………………………………………134
Figure 5.3 (a) XPS C1s spectra and (b) FTIR Si-OH sprectra after identical 15 min. treatments by the hybrid O_2 and radical O_2 ……………………………135
Figure 5.4 (a) RGA scan of the reaction byproducts during the damage process by 200 eV hybrid O_2 for 15 min.; (b) Magnified RGA showing the production of CO_2 and H_2O ………………………………………………………..136
Figure 5.5 RGA analysis of CO_2 and H_2O produced by identical hybrid and radical O_2 beam treatment ……………………………………………………..136
Figure 5.6 Schematic drawing of the kinetic damage process by oxygen ions and neutrals ………………………………………………………………...138
Figure 5.7 Relation between normalized field and sidewall damage and K_a/K_d. $Y_iK_in_{is}/K_dn_{Os}$ is assumed to be 10 ……………………………………..140
Figure 5.8 SEM images of patterned low-κ films after the treatment of (a) 50 eV hybrid O_2; (b) 400 eV hybrid O_2; (c) 900 eV hybrid O_2; (d) (e) (f) radical O_2. Significant damaged areas were circled out ………………………143
Figure 5.9 Cross section TEM images of patterned low k films after the treatment with (a) 400 eV hybrid O_2; (b) radical O_2 …………………………...144
Figure 5.10 EELS line scan of the carbon concentration on the sidewall after the treatment with 400 eV hybrid O_2, 900 eV hybrid O_2 and radical O_2 …..145
Figure 5.11 EELS point analysis of the carbon concentration on the sidewall after RIE O_2 plasma treatment …………………………………………………146

Figure 5.12 EELS point analysis of the carbon concentration on the sidewall and the trench bottom after RIE O_2 plasma treatment. The aspect ratio of the trench is 1:1 ……………………………………………………………147
Figure 5.13 EELS point analysis of the carbon concentration on the sidewall and the trench bottom after RIE O_2 plasma treatment. The aspect ratio of the trench is 1:2 ……………………………………………………………147
Figure 5.14 Relation between C-H/Si and the beam incident angles after 400 eV hybrid O_2 and radical O_2 ……………………………………………………148
Figure 5.15 Relation between FTIR peak area ratio of Si-CH_3/Si-O and Si-OH/Si-O and the beam incident angles after (a) 400 eV hybrid O_2; (b) radical O_2 ………………………………………………………………………..149
Figure 5.16 Relation between water contact angles and the beam incident angles after 400 eV hybrid O_2 and radical O_2 ………………………………………150
Figure 5.17 Relation between refractive indices at 633nm and the beam incident angles after 400 eV hybrid O_2 and radical O_2 ……………………………………150
Figure 5.18 Potential contours within a 0.5 μm wide trench with AR=1. Electrons and ions are generated at the V=0 upper boundary ………………………...154
Figure 5.19 Normalized neutral and ion flux at AR=1 trench ……………………...155
Figure 5.20 Normalized incident kinetic energy of ions at AR=1 trench …………..155
Figure 5.21 Evolutions of XPS C1s peak after the treatment of hybrid and radical CH_4 on the surface of (a) pristine low k and (b) O_2 damaged low k ………..159
Figure 5.22 (a) C-V and (b) I-V characteristics of the oxygen ashed sample before and after plasma CH_4 repair ……………………………………………...160
Figure 5.23 Experimental setup of vapor silylation processes in Ho's lab …………163
Figure 5.24 XPS C1s spectra after the vapor silylation treatments of TMCS, DMDCS and PTMOS/TMCS ……………………………………………………165
Figure 5.25 Illustration of the mass transfer and surface reaction in the vapor silylation process ………………………………………………………………………167
Figure 5.26 Schematic diagram of a silylation process setup ………………………169
Figure 5.27 FTIR spectra of the sample after plasma O_2 ashing, scCO_2 TMCS silylation and subsequent annealing ……………………………………170
Figure 5.28 Distribution of water contact angles after various adjustments of silylation process parameters ……………………………………………………..171

Chapter 1 Introduction

Innovation is the soul of the semiconductor industry. New devices, new materials and new structures are always the headlines of the newspaper and pose far-reaching influences on our lives. As predicted by Moore's law in 1965, the number of transistors placed on an integrated circuit increased exponentially, doubling approximately every two years [1]. This trend has continued for more than 40 years and is not expected to stop for another decade at least.

Silicon is the most commonly used semiconductor material today. A wafer, made of extremely pure silicon, typically goes through the manufacturing steps of front-end-of-line (FEOL) and back-end-of-line (BEOL) processes before being tested and packaged for delivery. FEOL processing refers to the formation of transistors directly on the silicon. BEOL processing involves creating metal wires, which are mechanically supported and electrically isolated by dielectrics, to interconnect transistors.

With the aggressive device scaling, device performance is improved through the reduction of gate length, gate dielectric thickness and junction depth. However, in the BEOL, as indicated by a schematic model in Fig. 1.1,

Metal resistance $R=2\rho L/PT$;

Interline capacitance $C=2(C_L+C_V) = 2\kappa\varepsilon_0 (2LT/P+LP/2T)$;

Therefore, $RC = 2\rho\kappa\varepsilon_0 (4L^2/P^2+L^2/T^2)$;

Where $P=W+S$, $W=S$; L and ρ are the length and resistivity of the metal; κ is the dielectric constant of the insulator; ε_0 is the permittivity of vacuum.

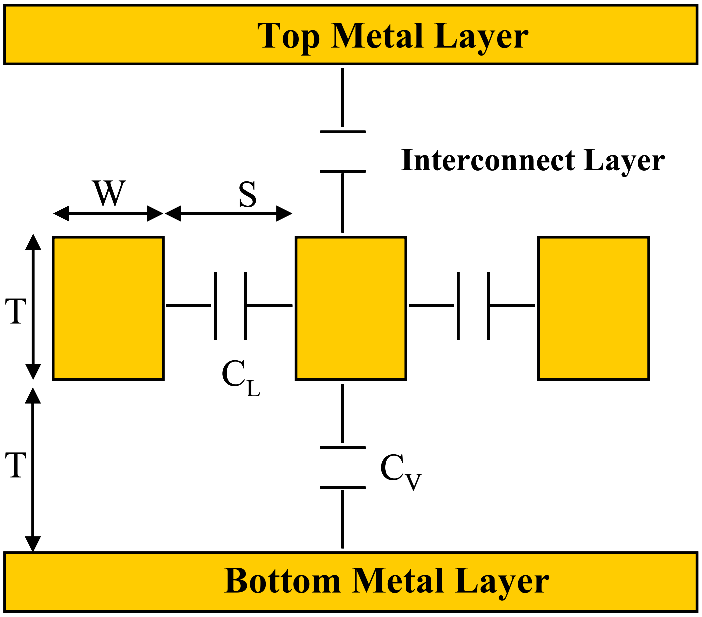

Fig. 1.1 **Schematic diagram of BEOL interconnect RC circuit model. (From [2])**

The resistance (R) and capacitance (C) of the wiring structure increase significantly due to the decrease of conductor cross section area and spacing, thus hindering the signal transmission speed of integrated circuits. Some other interconnect performance issues include cross talk, noise, power dissipation, and power distribution. Design engineers may propose using repeaters and reverse scaling to mitigate RC delay temporarily, but in the long run, a lower resistivity metal and lower permittivity dielectric must be integrated into BEOL interconnects to compensate for the effects of geometry scaling and boost the chip performance further [3].

The three best room temperature conductors on the earth are silver (1.60 μΩ·cm), copper (1.67 μΩ·cm) and gold (2.3 μΩ·cm). Al (2.69 μΩ·cm) ranks the fourth. Aluminum (Al) and silicon dioxide (SiO_2) were used in the traditional metal interconnect stacks. The industry is gradually replacing Al with Cu and SiO_2 (κ =4.5) with low-κ dielectrics. Cu offers an approximate 37% reduction in resistivity and low-κ dielectrics usually offers at least another 33% reduction in dielectric constant. As a result shown in Fig. 1.2, compared with Al/SiO_2, the interconnect delay and sum of delays of Cu/ low-κ are significantly reduced. Compared with the debut of Cu metallization ten years ago, the industry has delayed the introduction of lower dielectric materials due to integration and reliability issues. Vacuum is believed to be the ultimate insulator. In May 2007, IBM announced integrating vacuum holes into copper interconnects with a self-assembly technique. As shown in Fig. 1.3, this airgap structure, actually vacuum, has an ultimate dielectric value of κ=1, leading to 35% higher speed in current flow or 15% lower power consumption [5]. Whether this structure is reliable during mass production is still to be investigated.

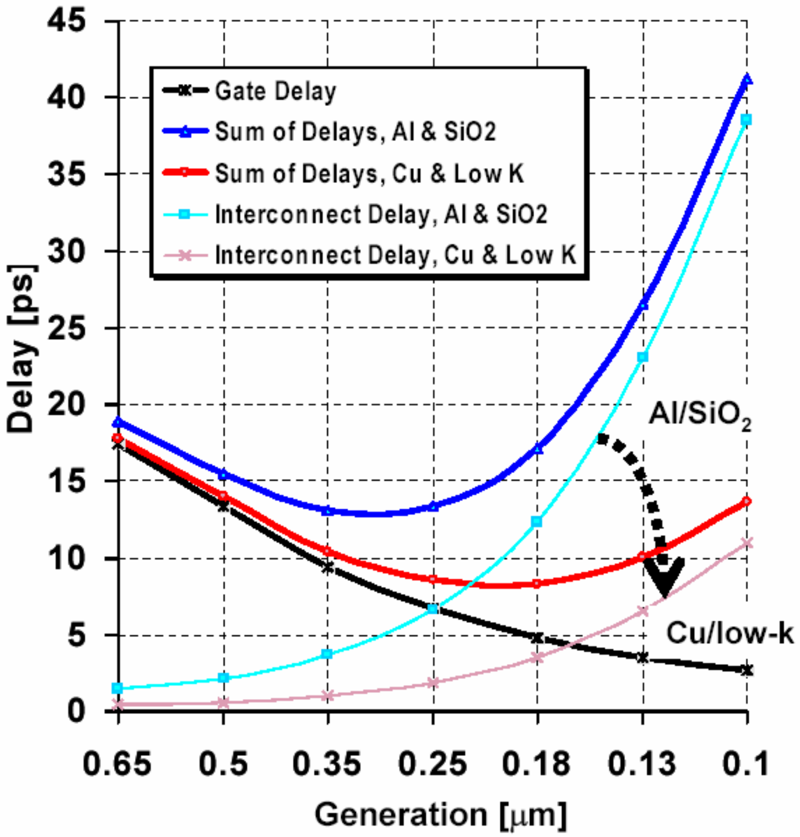

Fig. 1.2 **Trend of gate, interconnect and sum of the delays with technology generation. (From [4])**

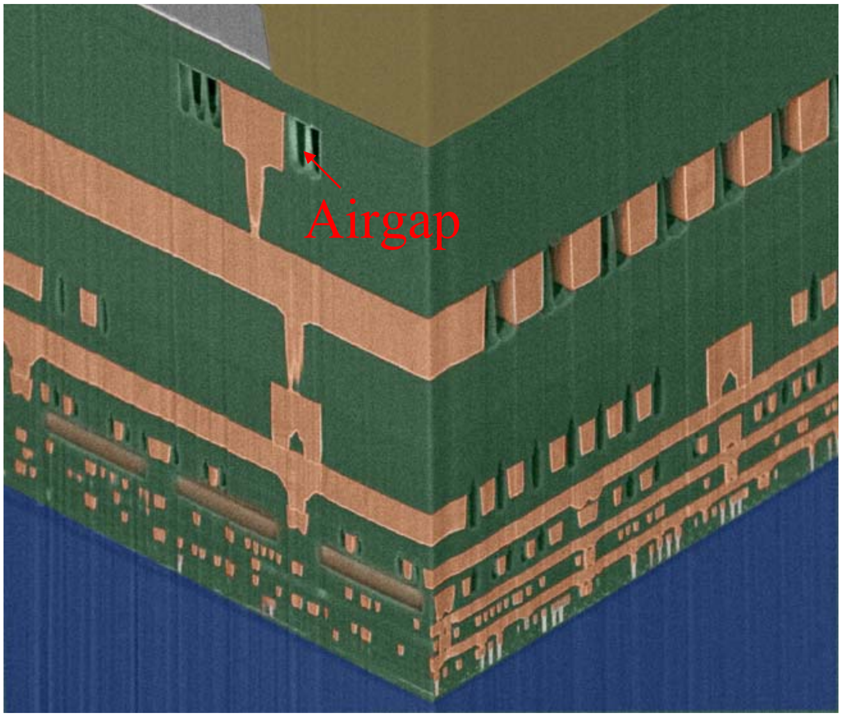

Fig. 1.3 Cross section of IBM airgap microprocessor. (Courtesy of IBM)

1.1 Challenges of low-κ integration

In the past, Al interconnect was formed with a subtractive reactive etching technology. Here, aluminum is deposited as a blanket film, patterned using photoresist, and then unwanted portion of Al is etched away. A dielectric material is then deposited to fill the openings between the exposed isolated wires. For Cu interconnects, subtractive etching technology is not applicable due to the limited number of volatile copper compounds. Instead, the industry employs a damascene technology as follows: The dielectric material is deposited as a blanket film, patterned, and then etched, leaving holes called “trenches” or “vias”. Cu is superfilled into the holes with an electrochemical deposition (ECD) technique on a physical vapor deposition (PVD) Cu seed layer over

Ta/TaN barrier layer. Finally, Excessive Cu is removed and the surface is planarized with chemical mechanical polishing (CMP) for subsequent processes. Compared with the single damascene process where Cu is deposited into dielectric holes to form either filled vias or metal lines separately, the dual damascene process creates trench and via, then fills them with metals in a single step, thus saving manufacturing costs. In addition, via resistance is reduced and reliability is improved due to the reduction of interfaces in the via (e.g. one bottom via interface for DD Cu vs. a top and bottom via interface for SD Cu) and full line/via register at the top of the via. The challenge of dual damascene technology lies in the etching of and deposition into high aspect ratio structures and complicated integration schemes [6].

Quite a few integration schemes were developed, such as trench first, via first, self aligned, and top dual hardmask. But each scheme has its own integration issues and challenges. Via first and trench first processes are the approaches most commonly used in the mainstream semiconductor fabrication.

Fig. 1.4 demonstrates the trench first integration process flow. Photoresist is applied to the wafers and patterned. Trench is created by plasma etching that cuts through the surface hardmask (SiO_2), and ILD until the embedded etch stop (SiN) is reached. Then, the trench photoresist is stripped and the via photoresist is applied and patterned. Later, via is created by plasma etching that cuts through the surface hardmask, ILD, until the SiO_2 barrier at the via bottom. Finally, the photoresist is stripped and the SiO_2 barrier at the via bottom is opened by dry etching. The trench first approach was used in the early damascene (0.35 μm or 0.25 μm node) and is hard to be extended to a smaller technology to define smaller structures, because when photoresist pools in the open trench before via patterning, resolving fine via structures on such thick photoresist is very difficult compared with that on the thin photoresist. It is necessary to implement a thin-imaging-resist layer for small dimension structures. By contrast, the via first approach avoids the photoresist pooling effect by forming vias before trenches as indicated by Fig. 1.5. After the trench photoresist is applied and patterned, some photoresist remain at the bottom of the via. These pooling photoresist, unrelated to geometry patterning, protects the lower via from being over etched during the subsequent trench etch process [7].

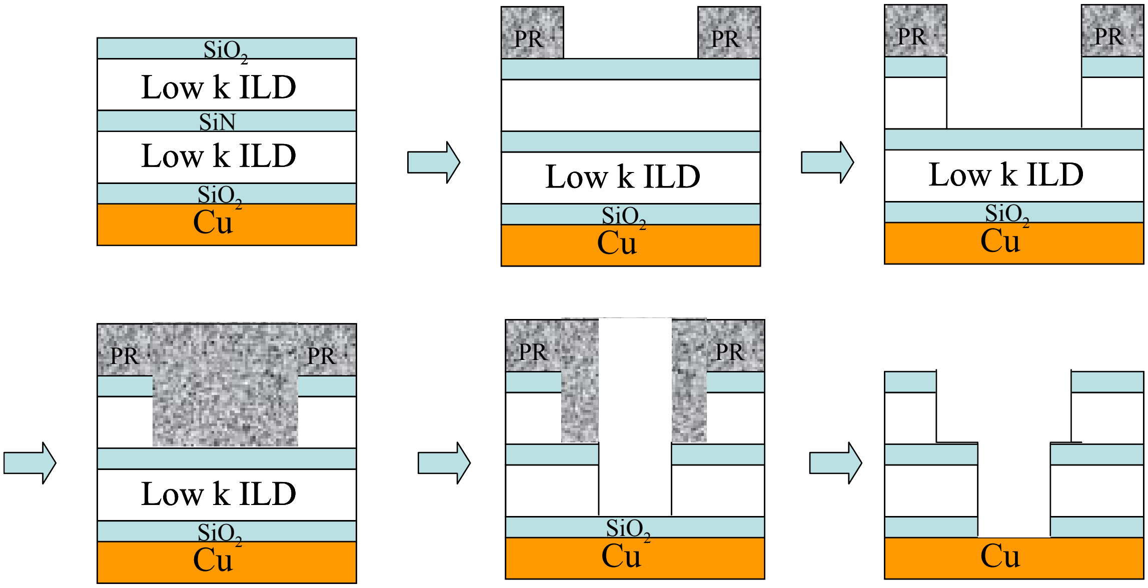

Fig. 1.4 **Trench first dual damascene process flow.**

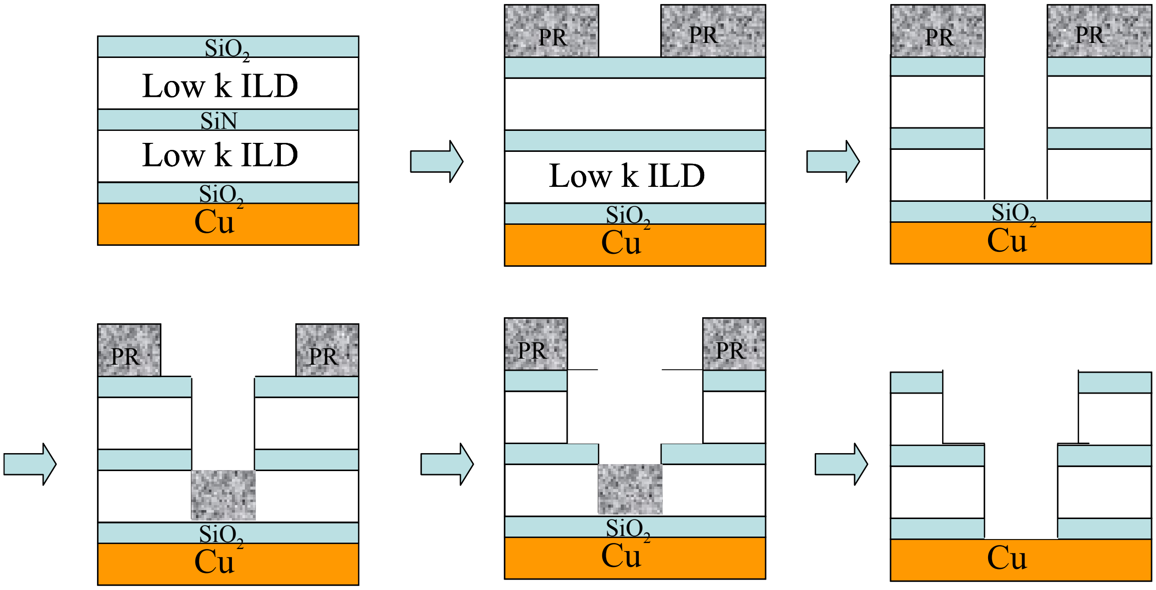

Fig. 1.5 Via first dual damascene process flow.

In order to qualify a technology node or a customer product, BEOL integration engineers usually have to optimize unit processes to pass the reliability tests of electromigration (EM), time dependent dielectric breakdown (TDDB), and stress migration (SM).

EM is an atomic diffusion phenomenon in metals driven by electron wind force from momentum exchange of collision between atoms and electrons. Fig. 1.6 is a schematic view of the EM mechanism. It was first observed in the Al circuit that carried a current density as high as 10^6 A/cm^2. It is the sum of mass transport through the lattice, the grain boundaries, and the interfaces. In the complicated small interconnect structures, such a high current density leads to voids at the cathode and extrusion/hillock at the anode. Then the circuit will fail or short at these flux divergence points [8]. Fig. 1.7 shows an example of a circuit failure due to EM.

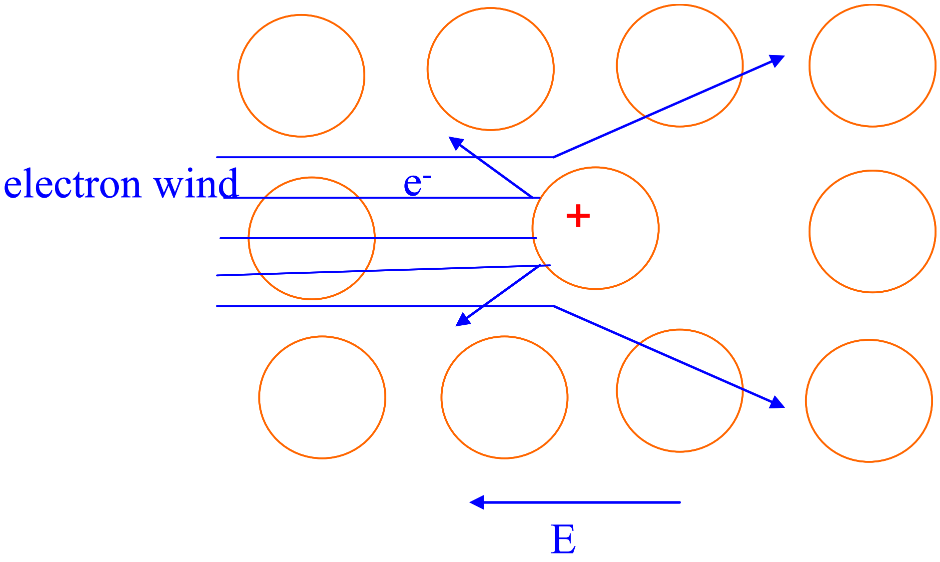

Fig. 1.6 **EM fundamental: EM is induced by the electrons' collision with metal atoms under external electric field.**

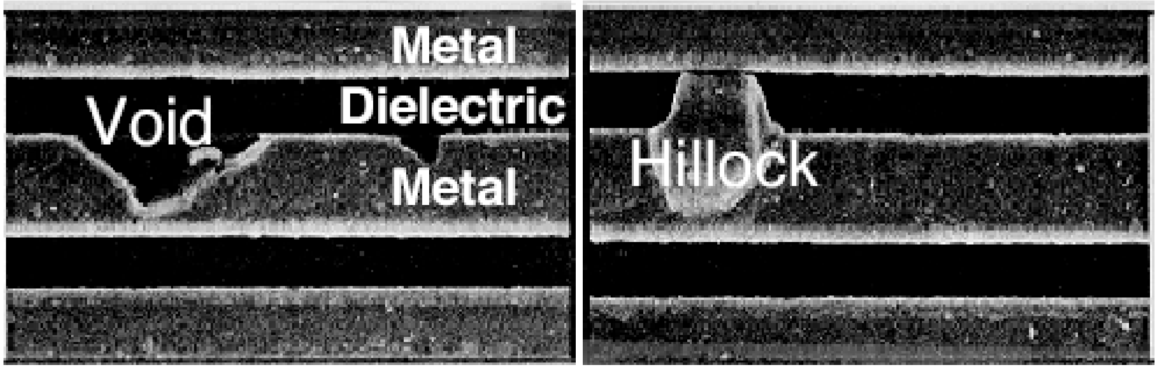

Fig. 1.7 **SEM images of void and hillock induced by EM on the metal line. (From [9])**

Compared with Al, Cu has a heavier atomic weight and higher melting point. Therefore, Cu atomic diffusion should be slower at the same temperature and its EM reliability is better. But it turned out not to be as good as we expected. EM in Al is dominated by grain boundary diffusion, while EM in Cu is dominated by surface diffusion [10] [11]. Compared with natural passivating oxide on the Al surface, Cu does not adhere to oxide surfaces well. Furthermore, CMP generates a significant number of defects on the top surface of Cu lines. With increasing current density and interface area to volume ratio due to line scaling, the interfacial diffusion will increase and EM lifetime will decrease. Depending on the electron flow direction, EM failure can be categorized into two distinct types: via depletion (Fig. 1.8 (a)) and line depletion (Fig. 1.8 (b)). In the via depletion, electrons flow from an underlying Cu via upwards to a dual damascene line. In the line depletion, the electron flow direction is reversed. Statistical studies found that via depletion showed both strong mode and weak mode while line depletion only showed strong mode. Strong mode is usually related to the process defects or bad adhesion at the Cu/cap interface that is the major EM diffusion path in Cu dual damascene interconnects [12] [13]. On the other hand, weak mode usually relates to thin barrier, barrier oxidation, processing defects, etc [14]. Since only a very small amount of material depletion in the via is required to form a void and cause circuit open, weak mode failure generally occurs before strong mode failure and thus can significantly change the standard deviation (σ) and mean time to failure (t_{50}) of EM failure distribution. This is often referred to as early EM failure [15] [16].

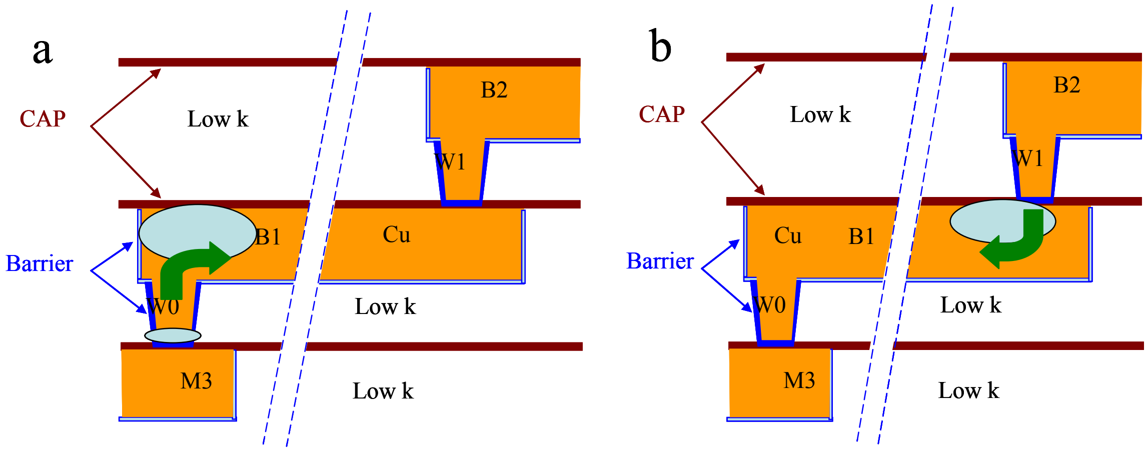

Fig. 1.8 (a) Via depletion and (b) line depletion of EM failure.

Electrical reliability is evaluated by time dependent dielectric breakdown (TDDB) test. The test is usually conducted at 100-175^{0}C on the interdigitated comb-serpentine structure, with combs positively biased and serpentine grounded. There exist both intrinsic and extrinsic breakdown. Intrinsic dielectric breakdown is the low-κ molecular bond breakage due to thermal chemical reaction. Extrinsic breakdown is the short between two metal lines caused by Cu out-diffusion due to weak Cu/cap interface, line edge roughness, line spacing delta, via striation, etc [17].

At the current 65 nm technology node, Cu out-diffusion occurs earlier than the thermal electrical breakdown. From the thermodynamics standpoint, Cu diffusion into low-κ is driven by the enthalpy of formation of Cu oxygen bond. It is hypothesized that accelerated electrons injected from the cathode follow "Schkotty Emission". Some of them could undergo "thermalization" under high field and high temperature conditions, and later part of these energetic electrons would impact the Cu atoms and generate positive Cu ions at the anode. Those Cu ions could inject into the dielectric under the field along a fast diffusion path (eg. Cu/cap interface) to create damage in the dielectric. Migrated Cu ions may recombine with electrons to form Cu atoms. Finally, the Cu atoms form clusters of nano-particles, creating a conducting bridge to short metal lines. Or, the diffused Cu atoms may catalyze breakage of weak low-κ bonds due to their large atomic weight and subsequent mechanical strain and physical collision. Fig. 1.9 is the energy diagram to illustrate the above discussed electron-fluence driven, Cu-catalyzed low-κ breakdown mechanism [18].

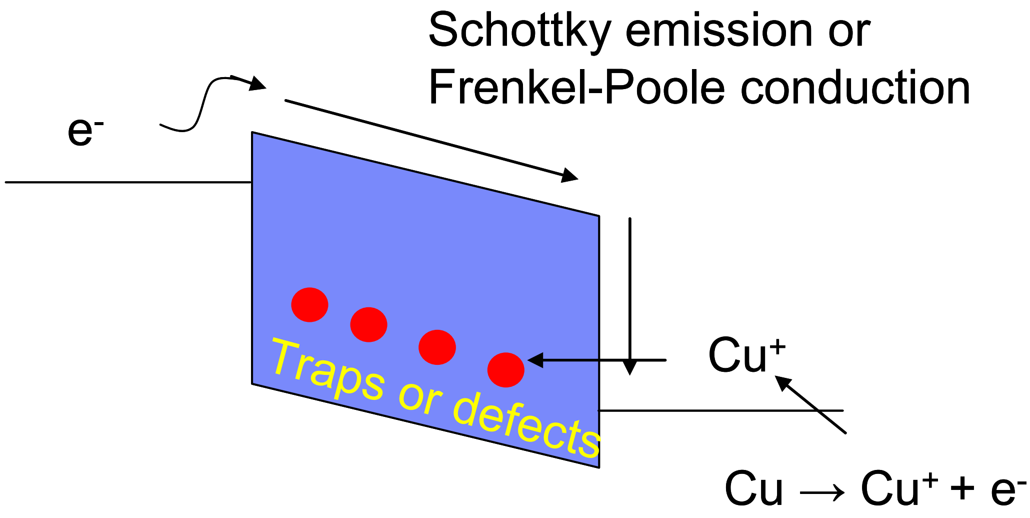

Fig. 1.9 **An energy band diagram illustrating electron driven Cu migration process.**

Stress migration is another test of interconnect reliability. In the traditional Al interconnect, the coefficient of thermal expansion (CTE) of Al (23.1 ppm/^{0}C) is larger than that of surrounding SiO_2 (0.5 ppm/^{0}C). Therefore, the Al interconnect is under tensile stress when it is cooled to lower temperatures. The magnitude of the stress in Al may exceed the yield strength of Al. On the other hand, since the stress close to defects is relatively low, the stress gradient may drive Al atoms from a less tensile location to a more tensile location. It results in void growth and stress relaxation until a stable state. When the temperature increases, Al diffusion increases, voids nucleate and thermal mechanical stress decreases. Until at higher temperatures, the Al interconnect is under compressive stress and void formation is suppressed. This void formation in the metal without electric current is called stress migration. The interplay between the driving force and diffusion pathway causes the highest void nucleation rate at an intermediate temperature [19] [20].

Unlike stress induced voids in Al interconnects at the triple points of the grain boundary, voids in Cu interconnects usually grow at the flux blocking boundary of the via bottom due to the presence of a metal diffusion barrier. Fig. 1.10 is an SEM image of void formation under a via due to stress migration. Compared with PVD deposition of Al at high temperatures with large grain sizes, in the dual damascene processes, Cu is electroplated at a low temperature with smaller grain sizes. Their microstructures will evolve during subsequent high temperature annealing, resulting in supersaturated vacancies. Finite Element Analysis (FEA) reveals that the via bottom is under a low tensile stress state, thus it acts like a reservoir to collect vacancies from Cu grain boundaries and interfaces. This fact is more pronounced in the case of small vias connected with wide Cu lines. Finally, the via resistance increases and the local joule heating melts the metal lines. On the other hand, voids may also form within vias or lines. They are initiated by process defects coming from unoptimized barrier/seed deposition conditions, improper Cu plating or CMP. Under a high tensile stress state, the voids will diffuse and nucleate as discussed above [21].

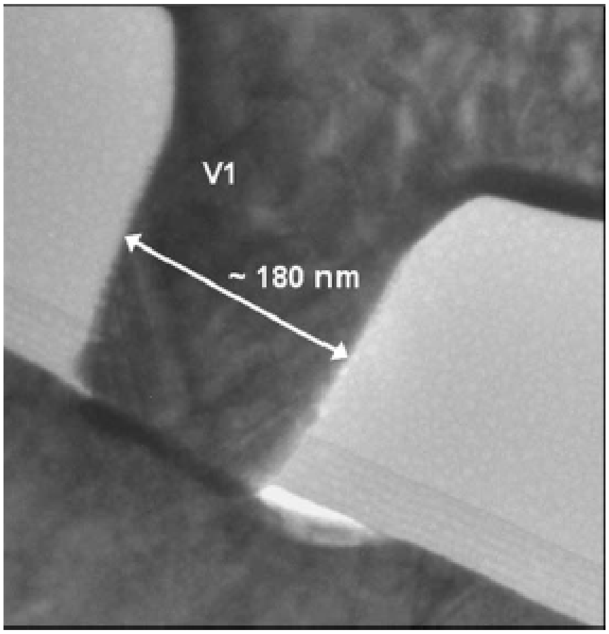

Fig. 1.10 SEM image of void formation at the via bottom under stress migration. (From [19])

Generally speaking, stronger bond and higher material density lead to a larger atomic polarizability, that is to say, higher dielectric constant, and vice versa. Young's modulus of most low-κ materials is at least one order of magnitude lower than that of SiO_2 (~59 GPa). The compliant low-κ materials adhere weakly to other materials and are not effective in confining the mass transport along Cu lines during electromigration. Moreover, the CTE of Cu is 16.5 ppm/^{0}C, while the CTE of many organic low-κ materials is higher than 50 ppm/^{0}C. Large thermal stress induced by the thermal loading in the integration processes can drive delamination or cracks to propagate along the weak low-κ interfaces. In the far back end processes, (e.g. a plastic flip-chip package), the thermal stress generated at the chip/underfill or chip/solder bump interfaces due to CTE mismatch between packaging materials can be coupled into the deformation along weak interfaces in the Cu/low-κ interconnects. In addition, the thermal conductivity of most low-κ materials is between 0.15 and 0.35 W/m K, much smaller than that of SiO_2 (1.26 W/m K), making the joule heating another reliability concern in the interconnect structures [22] [23] [24].

With the scaling of devices, the process complexity worsens unless the processes are carefully monitored and controlled. Good design rules and process optimization will help maximize the chip performance and reliability. For example, formation of stress induced under-via voiding is related to the interconnect geometry that determines the “active diffusion volume”. Therefore, voiding can be mitigated through inserting dummy vias or stress control layers, or incorporating multi-via structures. For the EM of Cu interconnects, since the weak interface between Cu and the cap layer provides the fastest diffusion path, strengthening their interfacial bonding with some adhesion promoters can improve EM lifetime. CoWP was reported to be the best promoter option so far [25]. However, CoWP is still not used in the manufacturing line due to difficulty of selective deposition on Cu surface and the possible metal contamination. From the manufacturing standpoint, how to balance performance, yield, and cost is very important. Future process development will require fine tuning of many process steps instead of a single step to achieve the final target.

1.2 Characteristics of low-κ dielectrics

Excerpted from ITRS 2007, Table 1.1 contains the dielectric constant values of low-κ materials for future technology nodes. Effective dielectric constant is the combined κ value of bulk low-κ dielectrics and other dielectrics (hardmask, etchstop etc.) between the wires. Dielectric constant of the current 65nm technology is around 2.4, but it is going to drop significantly to 1.8 in the 22nm circuit in 10 years. Integration of low-κ dielectrics into Cu interconnects is very challenging because low-κ dielectrics have poor mechanical strength, low electrical breakdown, poor thermal conductivity, physical and chemical sensitivity to plasma, moisture adsorption, and weak adhesion etc. [27]

Table 1.1 Dielectric constant of future low-κ materials. (From [26])

Year of Production	2007	2010	2013	2016	2019
DRAM ½ pitch (nm)	65	45	32	22	16
Bulk k value	≤2.4	≤2.2	≤2.0	≤1.8	≤1.6
Effective k value	2.7-3.0	2.5-2.8	2.1-2.4	1.9-2.2	1.6-1.9

Dielectric constant κ, also called relative permittivity ε_r, is a measure of the extent to which a material concentrates electrostatic lines of flux. It is defined as the ratio of the capacitances of a capacitor with or without the dielectric in place. Physically, the atoms of a material consist of positive point charges at the center surrounded by negative charge cloud. In response to an external electric field, the negative cloud tends to distort and resist the outside electric field by inducing a dipole moment [28]. The relation between the polarization $\vec{P}$ and the electric field $\vec{E}$ can be derived as $\vec{P} = \chi_e \varepsilon_0 \vec{E}$. χ_e is the electrical susceptibility and is defined as $\chi_e = \varepsilon_r - 1$. The local electrical field $\vec{E}_{local}$ inside the dielectric medium can be expressed as $\vec{E}_{local} = \vec{E} + \vec{P} / 3\varepsilon_0$. The induced dipole moment is proportional to the local electrical field $\vec{E}_{local}$: $\vec{P} = N\vec{p} = \alpha N \vec{E}_{local}$. α is the polarization constant and N is the density. Finally, the macroscopic property of a dielectric material, dielectric constant κ can be connected with the microscopic property of the material, the polarizability α through the Debye equation: $\frac{k-1}{k+2}=\frac{1}{3\varepsilon_0}\sum_i N_i\alpha_i$. The total polarizability α can be separated into three parts: electronic polarization, ionic polarization and dipolar polarization. Therefore, the Debye equation can also be written as $\frac{k-1}{k+2}=\frac{N}{3\varepsilon_0}(\alpha_e+\alpha_i+\frac{p^2}{3kT})$. Electronic polarization, α_e, relates to the distortion of the electron clouds surrounding the nucleus under an electric field. Ionic polarization, α_i, results from the motion of nuclei by the electric field. It stems from the partial charges on the atom of the molecule due to the different electronegativity of atoms. $\frac{p^2}{3kT}$ is the thermal average of permanent electric dipole moments that are typical for liquids but not for solids. N is the density, the number of molecules per m^3 [29]. A sketch of the total dielectric constant as a function of the frequency of the electrical field is given in Fig. 1.11. In the visible and ultra-violet frequency region (10^{14}~10^{15} Hz), only electrons can respond to the time varying fields. In the microwave and infrared region (10^{12}~10^{13} Hz), both ionic and electronic polarizations contribute to the total dielectric constant. In the radio frequency region (10^9 Hz), all three polarizations are taken into account. Therefore, studying the dielectric constant at different frequency regions can determine which components are more important for the total dielectric constant [30].

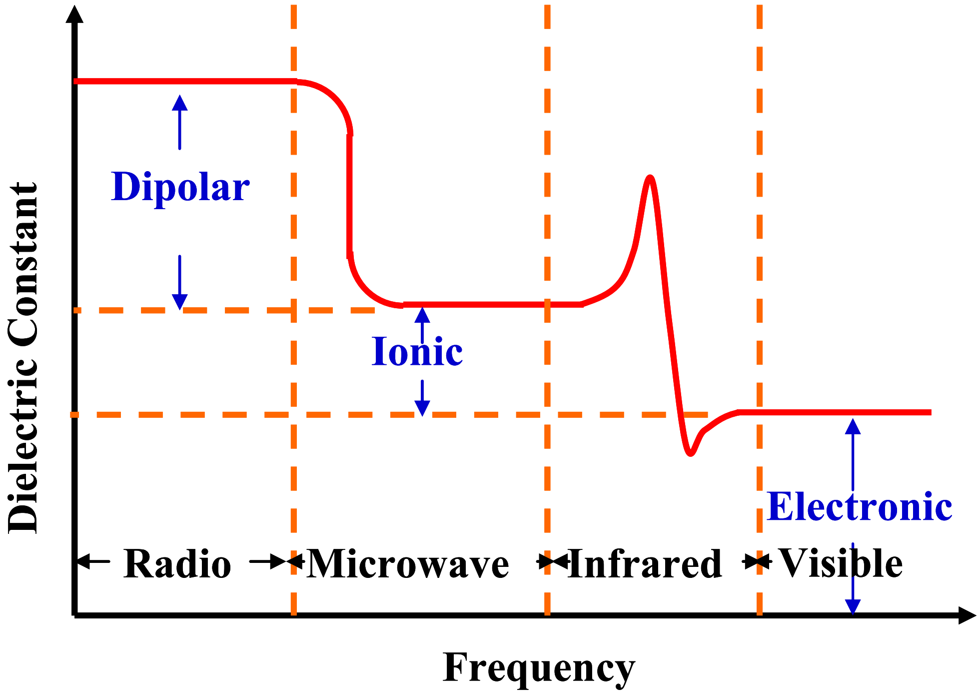

Fig. 1.11 Sketch of the dielectric constant as a function of the frequency of electrical field. (From [30])

Hydrogen, carbon, oxygen, silicon and fluorine are among the most commonly used elements in low-κ materials. The rank of their electronic polarizability is Si (5.38) >C (1.76) >O (0.802)>H (0.667)>F (0.557) [31]. According to Pauling's rule, the ionic characteristic of a certain molecule is determined by the difference of electronegativity of its atoms. The rank of electronegativity is F (4.0)>O (3.5)>C (2.5)>H (2.1)>Si (1.8) [32].

Clearly, there are two possible ways to synthesize low dielectric constant materials: One is to introduce low polarizability components: replacing Si-O with Si-H or Si-CH_3; the other is to reduce the volume density: adding voids/pores into the molecule.

Table 1.2 lists some example low-κ dielectric materials and their deposition methods.

Table 1.2 Example of low-κ dielectric materials and their deposition methods.

Material	Dielectric constant	Deposition method
Fluorinated silicate glass (FSG or SiOF)	3.2-3.6	CVD, doping SiO_2 with fluorine
Carbon doped silicon dioxide (CDO, BD, Aurora, Coral)	~3.0	CVD, doping SiO_2 with carbon
Hydrogen silsesquioxane (HSQ)	2.8-3.0	Spin-on, silicon based polymeric dielectric materials
Methyl silsesquioxane (MSQ)	~2.7	Spin-on, silicon based polymeric dielectric materials
Organic polymeric dielectrics (SiLK)	2.2-2.6	Spin-on

According to how the pores are introduced, low-κ materials can be classified as a constitutive porous material or a subtractive porous material. The final structure of constitutive porosity depends on the original and as-deposited structural arrangement. But the subtractive porosity is created by removing certain parts of the original structure. Constitutive porous materials include silsesquioxane (SSQ) based, silica based, organic polymers and amorphous carbon [33].

This thesis studies silsesquioxane based and silica based materials. MSQ and HSQ are representatives of SSQ based constitutive porous materials. They contain both cage and network substructures. Si-O-Si bond angle of cage substructures is $\sim 150^0$ and that of network substructures is $\sim 144^0$. The concentration of each substructure can be modified under processing certain conditions like heating. Fig. 1.12 shows an elementary unit of SSQ dielectric material. The cage substructure, with larger Si-O-Si bond angles, contributes to void formation and thus lower volume density. Usually, the more cage substructures; the higher the porosity; the lower the dielectric constant.

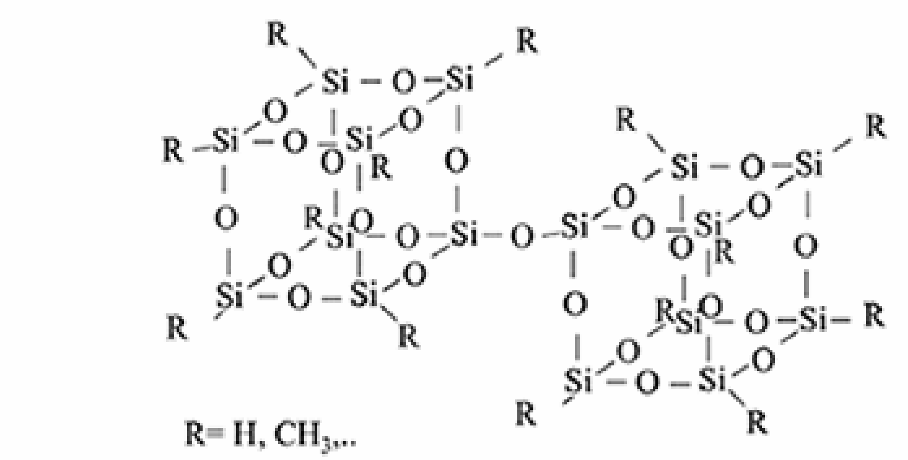

Fig. 1.12 Structure of HSQ (R=H) and MSQ (R=CH_3). (From [33])

Silica based materials have the basic tetrahedral structure unit, in which silicon sits at the center of a regular tetrahedron of oxygen atoms. Besides cage and network substructures, it also contains suboxide substructure that has a Si-O-Si bond angle of less than 140^0. Introduction of fluorine or carbon increases the interatomic distance or “free volume” of silica and thus decreases dielectric constant. Organosilicate glass is a typical silica based material. Its molecular structure is shown in Fig. 1.13.

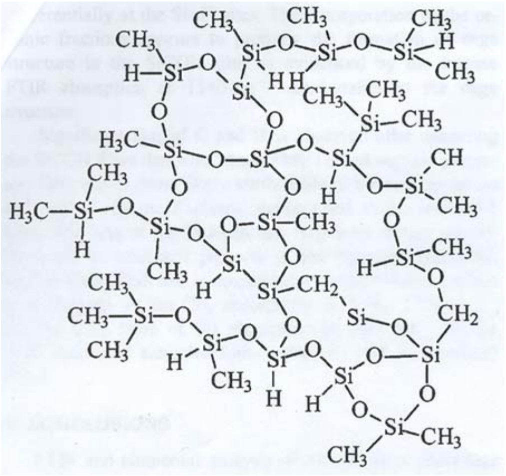

Fig. 1.13 Structure of OSG. (From [34])

It is very difficult and challenging to develop low-κ materials with good thermal and mechanical properties. Due to the porosity introduced to reduce dielectric constant, low-κ materials in general consist of weaker bonds and have lower mechanical strength in comparison with SiO_2. The degree of porosity is related to the dielectric constant while the structures and distribution of pores determine the material properties. Even different sample deposition techniques can result in different thermal and mechanical properties of low-κ films. Compared with CVD deposited low-κ materials, spin-on deposited low-κ films have a lower degree of cross-linking and thus weaker mechanical strength and lower thermal stability [35].

This thesis focuses on understanding possible process interactions with low-κ dielectrics in the damascene processing integration. They include thin film deposition on porous dielectrics and plasma damage of low-κ materials. For example, to block copper diffusion into low-κ dielectrics, a thin layer of Ta/TaN barrier metal is required. Since the Ta/TaN barrier is required to be thin and uniform, it is expected to be deposited with atomic layer deposition technique, which is a self-limited surface chemical reaction [36]. Low-κ surfaces are terminated with methyl groups, which are not good nucleation sites for Ta/TaN barrier metal deposition with atomic layer deposition technique. To get around this problem, the surface must be activated by replacing the methyl groups with phenol, sinanol or amine groups [37]. Considering the manufacturability and tool productivity, this surface activation process can be achieved through plasma treatment. On one hand, plasma may activate the low-κ surface and facilitate high quality barrier film growth; on the other hand, plasma may damage the low-κ materials. The reason comes from two aspects: metastable, energetic ions and radicals in plasma can cause both chemical reaction with and physical bombardment to low-κ materials; Low-κ materials contain weak bonds like Si-H or $Si\text{-}CH_3$ that are chemically unstable and pores that facilitate penetration of plasma species [38]. Therefore, the plasma processes must be optimized. These two topics are discussed in detail in this thesis.

International Technology Roadmap for semiconductors had set the goal of implementing low-κ materials (2.0~2.5) in 2001. But it was revised to an effective value of 2.7~3.5 for 180 nm technology node. At this moment, low-κ dielectrics with k between 2.5 and 3.0 were successfully integrated into 65 nm or 45 nm circuits by several companies. The industry is working hard towards 2.3 or 2.0 ultra low-κ porous materials or even approaching the ultimate limit of 1.0 with airgap or vacuum.

1.3 Interaction between plasma and low-κ surfaces

Plasma, a fourth state of matter, is a collection of free charged particles moving in random directions that is, on the average, electrically neutral. Electrons and ions, coexisting in the plasma, interact with each other through electromagnetic fields. The plasma state is usually characterized with charge particle density (m^{-3}) and the equilibrium ion temperature T_i and electron temperature T_e (eV). Bellan classified them into three types: non-fusion terrestrial plasma, fusion-grade terrestrial plasma and space plasma [39]. Table 1.3 lists their densities, ion and electron temperatures and applications.

Table 1.3 Densities, ion and electron temperatures and applications of plasmas.

Plasma category	Density (m^{-3})	Temperature	Application
Non-fusion terrestrial plasma	10^{14}~10^{22}	Weakly ionized, $T_i<T_e$, close to R.T.	Neon signs, fluorescence lamps, processing plasma
Fusion-grade terrestrial plasma	10^{19}~10^{21}	Fully ionized, 10~10,000 eV,	Certain magnetic devices in inertial fusion
Space plasma	10^{6}~10^{20}	Fully ionized, 1~100 eV	Interstellar space, solar atmosphere

Of particular importance is the plasma interaction with the wall surfaces surrounding the plasma. The electron thermal velocity $(eT_e/m)^{1/2}$ is at least 100 times the ion thermal velocity $(eT_i/M)^{1/2}$ because M/m ~ 1836 and $T_e \geq T_i$. Some electrons near the wall are lost leading to a sheath region $n_i >> n_e$. The net positive charges within the several Debye long sheath lead to a potential profile positive in the plasma and falling to zero near the wall surfaces. This reflects electrons moving towards the surface back into the plasma and accelerates the ions entering the sheath into the wall.

Ionization of atoms or molecules in the plasma excitation can be obtained by collision~~s~~ of energetic particles, strong electric fields acting on bond electrons or ionizing radiation. According to the energy coupling mode, the plasma source can be divided into capacitively coupled plasma, inductively coupled plasma, wave-heated plasma, and electrodeless plasma. Capacitvely coupled plasma (CCP), one of the most common plasma sources, consists of two metal electrodes placed in a reactor. One electrode is connected with a single radio-frequency (13.56 MHz) power supply and the other is grounded. Electrons respond to the high voltage and acquire high energy. At a high enough electrical field, electron avalanche occurs when high energy electrons ionize gases through collision and produce abundant secondary electrons. In the inductively coupled plasma (ICP), energy is supplied by electrical currents produced by electromagnetic induction. According to Maxwell's theorem, a time varying current through a coil will produce a time varying magnetic field around the coil, which leads to azimuthal electric currents to ionize gas molecules. The ICP plasma temperature ranges from 6,000 K to 10,000 K and its density is as high as 10^{15} m^{-3}. Wave-heated plasma has different modes like electron cyclotron resonance (ECR), helicon discharge, surface wave sustained mode, etc. Among them, ECR is widely used. It is based on the fact that plasma can be efficiently created by a static magnetic field and a high-frequency electromagnetic field at the electron cyclotron resonance frequency. It has the advantage of confining the ions for long enough time for multiple collisions, so the plasma density can be very high [40].

Plasma is used in almost one third of the semiconductor fabrication: plasma deposition, etching, implantation, etc. For deposition, the plasma induced fragmentation, free radical generation, and ion bombardment results in the process occurring at a much low temperature than the nonplasma system. For etching, plasma has advantages over wet chemistry because it can be highly directional and very selective by choosing proper plasma species and energy. For implantation, a specific dose or number of dopant ions follow a random trajectory, scatter off the lattice silicon atoms, lose energy, and come to rest at a certain location inside Si [41].

A big issue of low-κ integration is the plasma damage or undercut to low-κ dielectrics during the resist removal process. O_2 plasma is generally used in plasma etching of low-κ or ashing of photoresist residue. CO, CO_2, NH_3, He, and H_2 plasma etc.

are alternatives. But O_2 plasma tends to degrade low-κ materials through removing CH_3 groups. The existence of pores in ultra low-κ material enhances penetration of plasma species and causes more damage. If the plasma energy is high, Si-O-Si backbone may even be broken due to physical bombardment. As a result, methyl groups are depleted, pores collapse, the film densifies, and the dielectric constant increases. More seriously, the low-κ surface is transformed from hydrophobic to hydrophilic. Moisture uptake into the low-κ material further increases dielectric constant, and the polar group Si-OH degrades interconnect reliability such as current leakage [42] [43]. The damage is restricted to the film surface and can be removed by diluted hydrogen fluorine (DHF). But the etch front of low-κ after DHF was reported to be so rough that issues of barrier deposition and low-κ adhesion emerged [44].

When the technology approaches 45 nm or lower, low-κ materials have more methyl groups and pores. They are more sensitive to plasma chemistry and the depth of the damage region can be significant comparable to the line width. Fig. 1.14 shows the normalized interline capacitance for lines embedded in SiO_2 and porous low-κ film ($\kappa = 2$). $S^'$ is the thickness of the damage region. The normalized capacitances for the regions with different damage thickness are comparable to one another when the interline spacing is over 100nm. When the interline spacing decreases from 100nm to 50 nm, the normalized capacitance is expected to double for $S^'=0$, triple for $S^'=20$ nm and fourfold for $S^'=30$ nm.

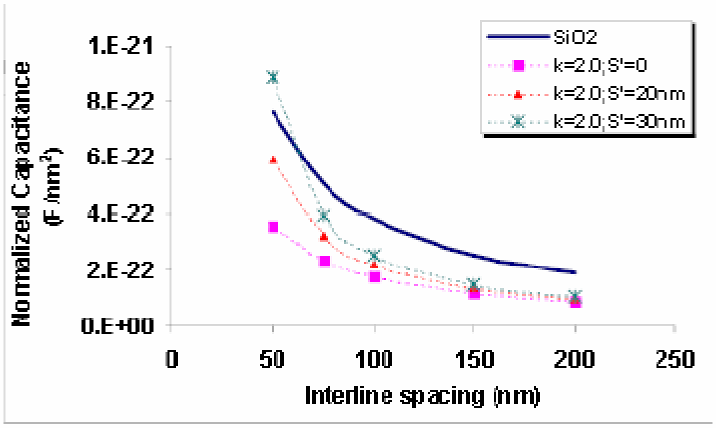

Fig. 1.14 **Normalized interline capacitance for lines embedded in SiO_2 and κ =2 porous low-κ film. (From [45])**

Proposed by Cui et al [46], plasma treatment of low-κ material can be regarded as a mutually limiting densification and removal process as follows: Upon initial exposure to plasma, a dense surface layer is immediately formed, which impedes further penetration of plasma ions and reduces further film densification. The dense surface layer can be thinned down through physical bombardment. As a result, plasma can penetrate the thin layer and causes film densification again. The film densification and removal will reach dynamic equilibrium finally.

Modification of structures and properties of low-κ materials depended on plasma chemistry, treatment temperature and the history of film preparation. Therefore, observations for a certain low-κ material at a specific condition cannot be extended to another low-κ at the identical process condition [47]. In particular, plasma damage of a blanket film cannot be extrapolated to that of a patterned film. The patterned film profile will influence the transport of reactive gases, plasma sheath, and the transport of ions and electrons, inducing the impingement of scattered ions on large sidewall area. The fundamental understanding of the plasma damage of patterned films is still unclear [48]

[49] [50]. This thesis work will focus on employing computational simulation to obtain the electron potential distribution on patterned low-κ after plasma treatment. Ions and electrons in the plasma carry charges. They will impinge on the low-κ surfaces after multiple collision or scattering. Meanwhile, the charged surface will affect the subsequent plasma ions and electrons. After a certain time and enough plasma particles, the number of charges on the low-κ surface will reach equilibrium and the electron potential distribution will become stable. The electron potential distribution will affect the trajectory of ions that are major causes of low-κ carbon depletion. The electron potential distribution is determined by both the plasma parameters and the geometry of patterned low-κ material [51].

Plasma damage to low- κ dielectrics is limited to the few nanometers on the top surface. For the blanket films, most analytical techniques can be applied to study the physical properties (density, thickness, etc) and chemical signatures (elemental composition, bonding, etc). The precision of plasma damage measurement is determined by the limitation of instruments [52]. For the patterned films, Low-κ damage on the sidewall can be evaluated through electrical tests such as capacitance and RC measurements, and profile distortion after PR tripping, especially after dipping the stripped samples into diluted 1% HF solution, Besides the electrical or microscopy analysis, angle resolved X-ray photoelectron spectroscopy (XPS) and electron energy loss spectroscopy (EELS) can be employed to investigate changes in the elemental composition on the sidewall. By rotating the sample to certain angles, XPS can detect the electrons emitted from the sidewall only. Therefore, the elemental composition on the sidewall can be extracted. XPS is a non-destructive technique while EELS is a destructive technique. The original sample is destroyed and only a small and thin piece is taken to do analysis under transmission electron microscopy. The thickness of the damage region and elemental concentration can be extracted with this method. Iacopi et al suggested a quick and efficient way to evaluate the plasma damage in the patterned low-κ materials. They regarded the damaged part of the dielectric as uniform regions parallel to the sidewall, characterized by a certain thickness and dielectric constant. It is possible to extract the thickness of the damage layer from plotting 1/C versus interline spacing [53].

The plasma damage problem is being addressed in two aspects: One is to select alternative plasma etch/ash species and optimize their processes; the other is to recover the dielectric loss. Extensive research has been dedicated to compare various plasma damages to low-κ films in order to select the best stripping species (e.g. fluorocarbon [54], H_2/He [55], NH_3 [42] [56], H_2 [57], N_2/H_2 [46], CO_2 [58]) Fig. 1.15 shows the increase of κ values on MSQ blanket films after various plasmas. O_2 plasma generated the most severe low-κ damage. Dielectric constant change by H_2 plasma was also very large with respect to O_2 plasma for the identical process conditions. N_2 containing plasmas showed much smaller low-κ damage, while NH_3 chemistry gave the best performance. Fig. 1.16 presents the electrical performance of various photoresist stripping on patterned porous MSQ, which is indirectly correlated with the low-κ damage on the sidewall. O_2 plasma resulted in the highest line capacitance and RC constant, while NH_3 plasma had some of the best values for these parameters and thus was a better candidate species for PR stripping than H_2 or O_2 containing plasma [42].

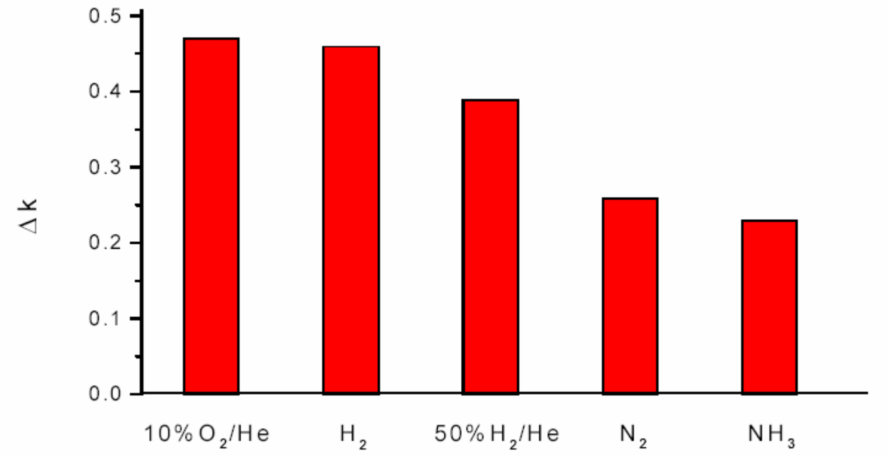

Fig. 1.15 **Increase of dielectric constant of MSQ by different plasma. (From [42])**

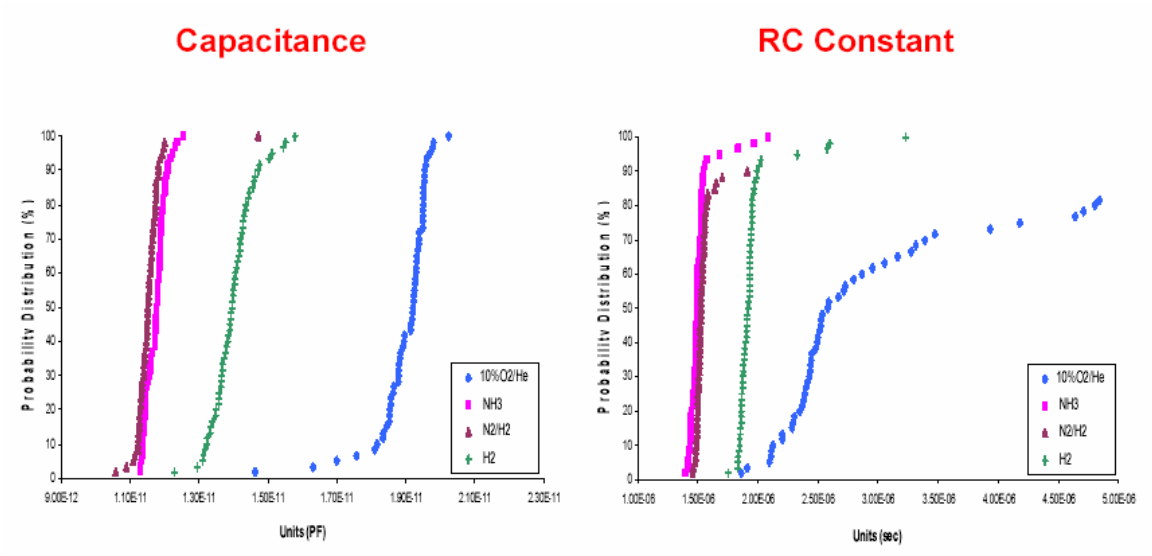

Fig. 1.16 **Electrical performance of photoresist stripping by different plasma on patterned porous MSQ. (From [42])**

The dielectric recovery is being explored in many ways and can be generally grouped into the following two categories: using plasma species like CH_4 [59] [60], He [61], As [62] to compensate the oxygen damage effects such as removing OH or adding CH_3 on the surface with plasma CH_4; using silylation agents like HMDS [63], TMCS [64], $scCO_2$ [65] [66] to react with OH and replenish the surface with hydrophobic CH_3

groups as illustrated in Fig. 1.17. It is still under investigation on which kind of dielectric recovery chemistry or technique is the best [67] [68] [69] [70]. A complete solution to prevent dielectric loss by plasma damage probably requires both plasma process optimization and silylation recovery.

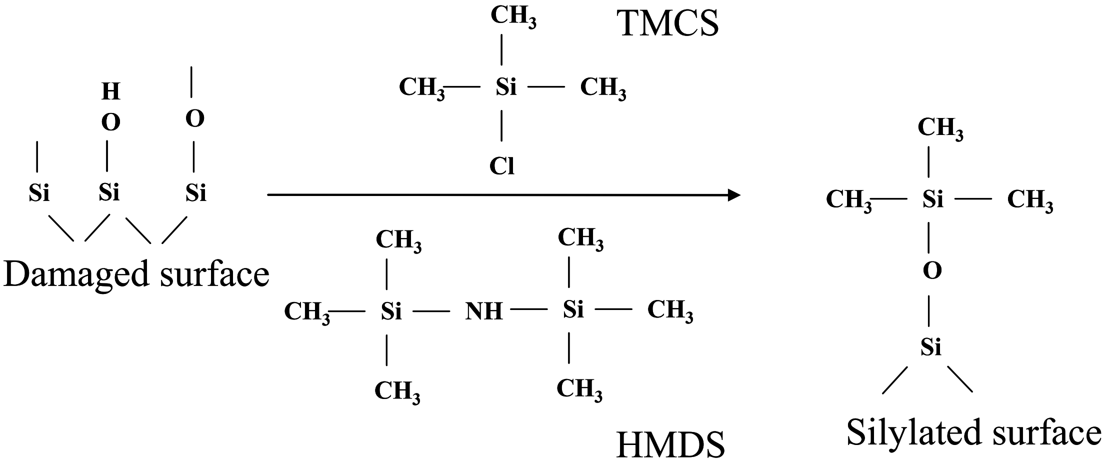

Fig. 1.17 Surface silylation of the damaged OSG surface with TMCS or HMDS.

1.4 Organization of the dissertation

This dissertation focuses on understanding the interaction between plasma and low-κ surfaces in BEOL fabrication. It contains six chapters:

Chapter 1 introduces the semiconductor fabrication, esp. back end of line fabrication. Cu and low-κ dielectrics are imminent industry trends to keep pace with Moore’s law. The process integration due to the material properties of Cu and low-κ dielectrics are discussed. Fundamental plasma concepts are also introduced in details.

Chapter 2 presents the experimental details: the plasma chamber setup scheme and its special connection with an in-situ XPS analysis chamber. Multiple analytical techniques, including Fourier Transform Infrared (FTIR) Spectrometer, Spectroscopy ellipsometer, X-ray reflectivity (XRR), Transmission electron microscopy (TEM), electron energy loss spectra (EELS), and Metal-insulator-semiconductor (MIS) dielectric constant measurement are employed to analyze the films and reviewed here.

Chapter 3 studies the plasma modification of low-κ surfaces. Chemistry of low-κ, e.g., functional groups, is observed to affect the Ta/TaN barrier quality deposited by the atomic layer deposition technique that is surface self-limited. With plasma activation to replace unfavorable function groups in the low-k film, the Ta barrier quality is much improved.

Chapter 4 explores the plasma damage of low-κ dielectric surfaces. Damage by different plasma species is compared. The mechanism of plasma damage is investigated in a downstream plasma chamber that is coupled with in-situ XPS analysis. The reasons of dielectric constant increase after plasma damage is experimentally observed and discussed.

Chapter 5 investigates the oxygen plasma damage to low-κ dielectrics. Damage of both blanket and patterned low-κ is compared. Then, the damage is mathematically analyzed and computationally simulated. To recover the dielectric loss, three ways of plasma CH_4 beam, super critical CO_2 silylation, and vapor silylation are explored. Their dielectric recovery effect and challenges are discussed.

Chapter 6 summarizes this research and proposes the future work.

Chapter 2 Experimental

To understand the interaction between plasma and low-κ dielectric surfaces, an ultra high vacuum (UHV) cluster tool has been constructed, which includes a remote plasma chamber with the capability of in-situ XPS analysis and residual gas analysis. Together with other auxiliary instruments and analytical techniques, various properties of the low-κ film can be measured. Therefore, the principle of the interaction between plasma and low-κ dielectric surfaces can be extracted.

Here, the main analytical techniques are grouped into the following categories: X-ray techniques (XPS, X-ray reflectivity etc), optical methods (FTIR, spectroscopy ellipsometer, etc), electron microscopy (SEM, TEM, EELS, etc) and electrical characterization (C-V, leakage current etc). This chapter will review the basic principles of these techniques, the information they can provide, and their advantages and disadvantages in the low-κ materials study.

2.1 Remote plasma process chamber

The remote, also called downstream, plasma studies were performed in a UHV system designed in the laboratory consisting of a plasma process chamber connected to an XPS analysis chamber via a loadlock as shown in Fig. 2.1. It contained three docking stations and two orthogonal transfer arms for sample transfer among the three chambers without breaking the vacuum. The plasma process chamber (typical pressure ~10^{-7} torr) and load lock (typical pressure ~10^{-8} torr) were pumped out with mechanical and turbo pumps. The pressure inside the XPS analysis chamber could reach as low as 10^{-9} torr through additional ion pump and titanium sublimation pump.

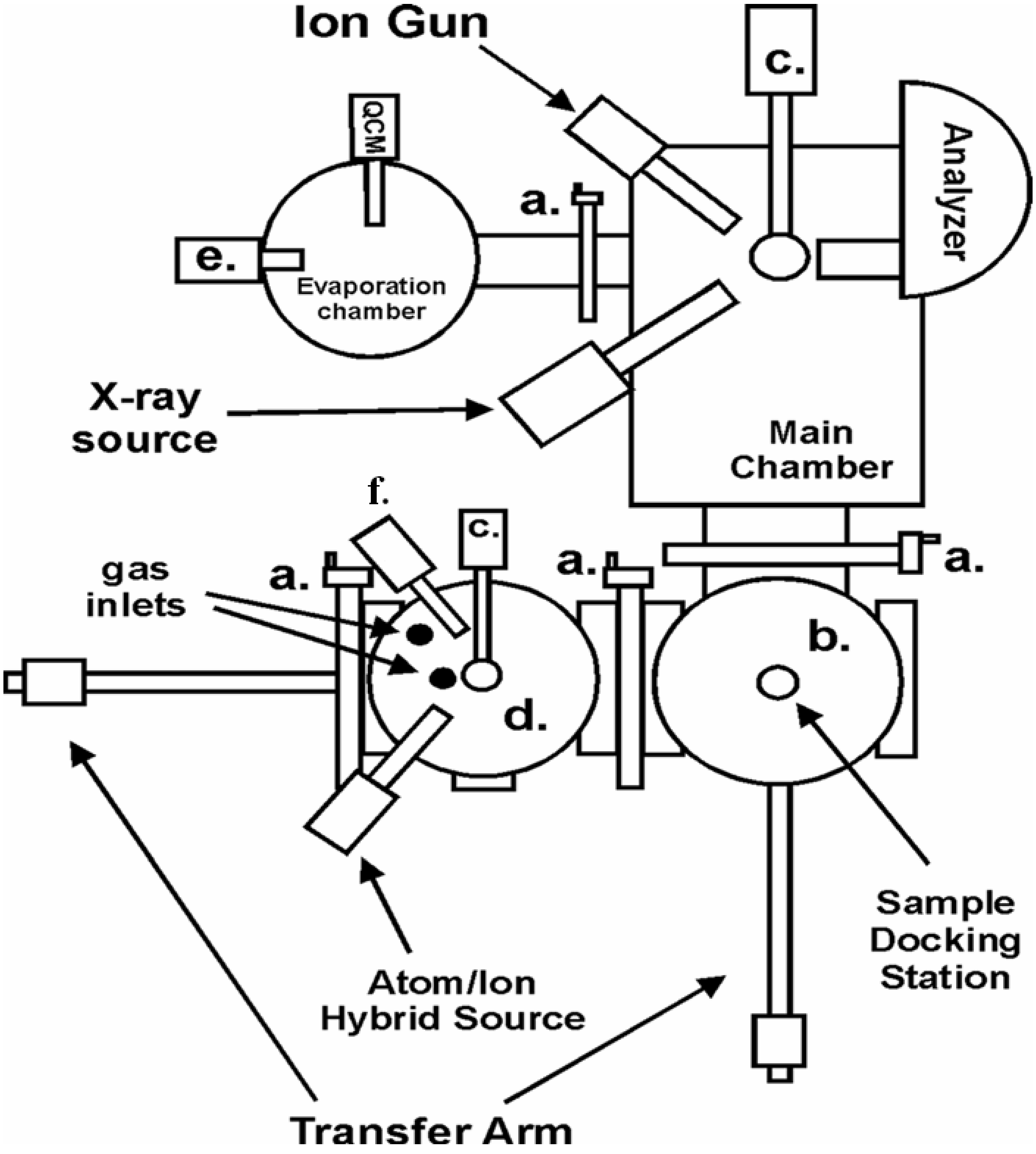

Fig. 2.1 **Ultra high vacuum cluster tools for *in-situ* XPS and residual gas studies of plasma processing. Some important items are labeled as a). Gate valves; b). Load lock; c). Docking stations; d). Plasma process chamber; e). Evaporator; f). Residual gas analyzer.**

Remote plasma such as NH_3 was generated by cracking NH_3 gas molecules with 2.45 GHz electron cyclotron resonance (ECR) inside an Oxford Scientific mini atom/ion hybrid source. The source was mounted on the plasma process chamber and aimed at the sample surface at an angle of about 40 degrees from a distance of about 10 cm. Gas molecules were transported into the hybrid plasma source to produce certain plasma species. A mini pneumatic gate valve, controlled by a LabView software program, was inserted in between the hybrid plasma source and process chamber to control the plasma processing time.

Fig. 2.2 is a schematic diagram of the ECR hybrid plasma source. Under an 86mT magnetic field, electrons gyrate around the magnetic field due to the Lorentz force. If the frequency of the injected microwave matches the gyration frequency, the electrons can be resonantly accelerated or decelerated. A high mirror ratio of the magnetic field leads to long confinement time for the plasma electrons. Thus, they are able to enter the resonant region for multiple times, gain higher energy, and crack gas molecules into ions and neutrals more efficiently. The filamentless design feature permits the operation with most gases including reactive ones such as oxygen, hydrogen, and chlorine [1] [2].

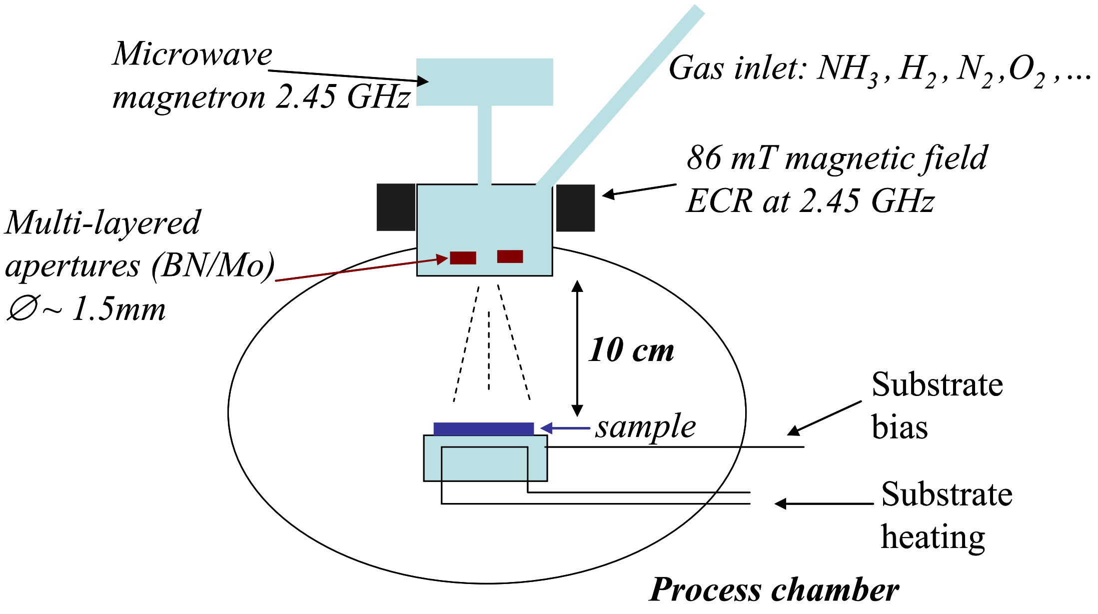

Fig. 2.2 **Illustration of Oxford Scientific mini atom/ion hybrid source.**

The hybrid source can be switched between the atom mode and the hybrid mode through a layered shutter made of boron nitride (BN) aperture and molybdenum (Mo) grids. At the atom mode, the dielectric BN/Mo aperture can be rapidly charged with ions to filter out ions in the beam. In this way, ions in the beam can be differentially pumped away by the mechanical pump in the load lock, and thus only neutral species can reach the center of the plasma chamber through the aperture. At the hybrid mode, a high positive voltage, anode voltage, is applied to the Mo grid to accelerate ions and neutralize charge accumulation on the aperture. A negative voltage, extractor voltage, is also provided to enhance the ion current at low anode voltage with little effects on ion energy [3]. Ions up to 2.2 keV energy can be added to the neutral species in the process chamber. In this thesis, the term hybrid or plasma beam refers to a mixture of ions and neutral species, while the term radical or atomic beam refers to only the neutral species.

Plasma parameters, like density and flux, are affected by the dissociation efficiency of the gas molecules, gas flow rate, chamber pressure, radical recombination rates, etc. Therefore, it is very difficult to measure them accurately. In the present case, the hybrid beam contained both ions and neutrals, and they needed to be characterized separately. In general, plasma can be characterized by a single Langmuir probe inserted into the chamber. The electrode is applied with a constant or time-varying electrical potential. The measured currents and potentials determine the physical properties of the plasma. Fig. 2.3 shows the measured I-V curve in plasma Ar when the anode voltage was 400 V and 1200 V. At the anode voltage of 400 V, the current signal was comparable to the background. This implies that the ion density was close to or lower than the setup sensitivity of 10^{13} m^{-3}. When the anode voltage rose to 1200 V, the plasma density increased and the ion saturation current was observed to be 0.0006 A. The following is the mathematics to estimate the ion density:

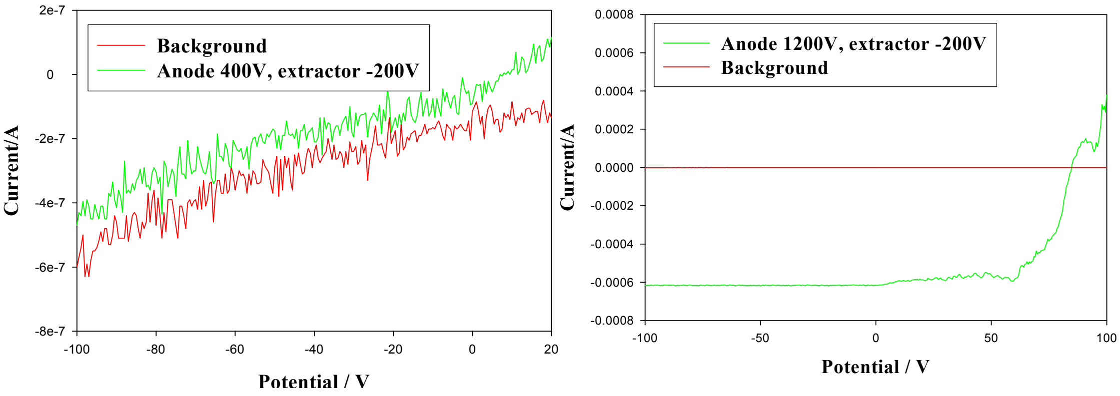

Fig. 2.3 **I-V curve measured by a Langmuir probe at the anode voltage of 400 V (left) and 1200 V (right). (Courtesy of H. Huang & H. Shi)**

Ions were accelerated under the anode voltage: $eV_A = \frac{m_i v_i^2}{2}$ (2.1)

Ion current density $j_i = n_i e v_i$ (2.2)

Ion current collected at the electrode of the Langmuir probe. $I_i = j_i A$ (2.3)

The Langmuir probe electrode area A=10^{-4} m^2. Then, ion density can be derived as

$$n_i = \frac{I_i}{A}\sqrt{\frac{m_i}{2e^3 V_A}} = \frac{0.0006}{10^{-4}}\sqrt{\frac{40\times1.67\times10^{-27}}{2\times(1.6\times10^{-19})^3\times1200}} = 4.9\times10^{14}\ /\mathrm{m}^3 \qquad (2.4)$$

Parameters of the atom flux can be determined indirectly. Here is an example. A piece of germanium with clean surface was oxidized in the loadlock with dry air. The oxide thickness was deduced to be 4.5Å from a 30% decay of the elemental Ge3d signal in the GeO_x overlayer, as measured by in-situ XPS. Then the oxide was observed to be totally removed with atomic hydrogen beam after 40 minutes treatment.

The surface density of oxide was estimated to be

$$\frac{\rho\cdot N_A}{M}\cdot4.5\times10^{-8}\times2 = \frac{4.5\times6.02\times10^{23}\times4.5\times10^{-8}\times2}{104.59} = 2.3\times10^{15}\ /cm^2 \qquad (2.5)$$

Since each oxygen atom consumes two hydrogen atoms to form water vapor, the surface density of hydrogen was around 4.6×10^{15} /cm^2. Considering the treatment time was 40 min., the atom beam flux can be estimated to be in the order of 10^{12} atoms/ (cm^2·s). Details of this experiment were described in J. Liu's dissertation [4].

2.2 X-ray techniques

2.2.1 X-ray photoelectron spectroscopy (XPS)

X-ray photoelectron spectroscopy is a surface analytical technique to detect elements heavier than He. When low energy X-ray (e.g. K-α line of Al, 1.487 keV) is incident on the sample surface, the photoemission processes as illustrated in Fig. 2.4 occur: the photon energy is absorbed and interacts with the core level electrons, resulting in photoemission of an electron. According to the law of energy conservation:

$$\Phi + E_{kin} - (-E_B) = \hbar\omega \tag{2.6}$$

Where Φ is the work function between the sample and the spectrometer, E_{kin} is the kinetic energy of the emitted electron, E_B is the binding energy of the inner shell electron, and $\hbar\omega$ is the photon energy [5].

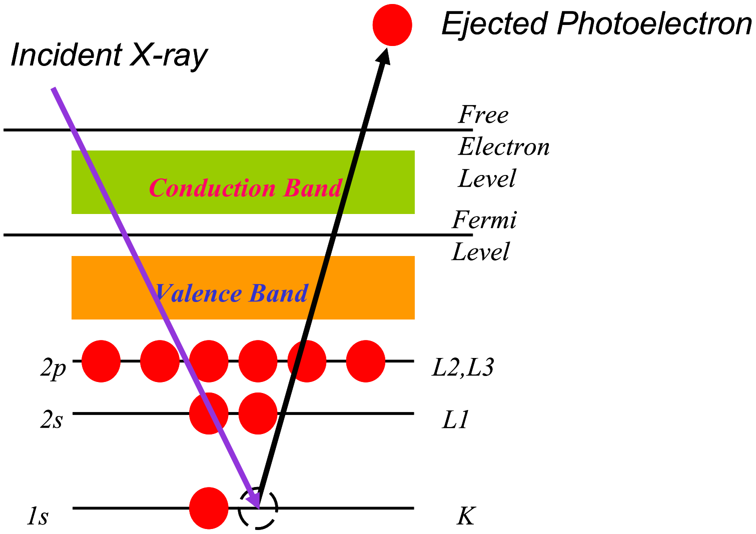

Fig. 2.4 **Core level X-ray photoemission process**

Fig. 2.5 shows the typical XPS survey of OSG materials. The horizontal axis, B.E., is the binding energy, which is required to release an electron from its atomic or molecular orbital. It is a characteristic value of atoms or molecules. Peaks exist at the characteristic binding energy level of species. Therefore, it can be used to identify elements inside a material. Some typical binding energy values used in this thesis work are: F1s (-686 eV), O1s (-532 eV), N1s (-402 eV), C1s (-285 eV), Si2s (-153 eV), Si2p (-103 eV) and Ta4f (-25 eV).

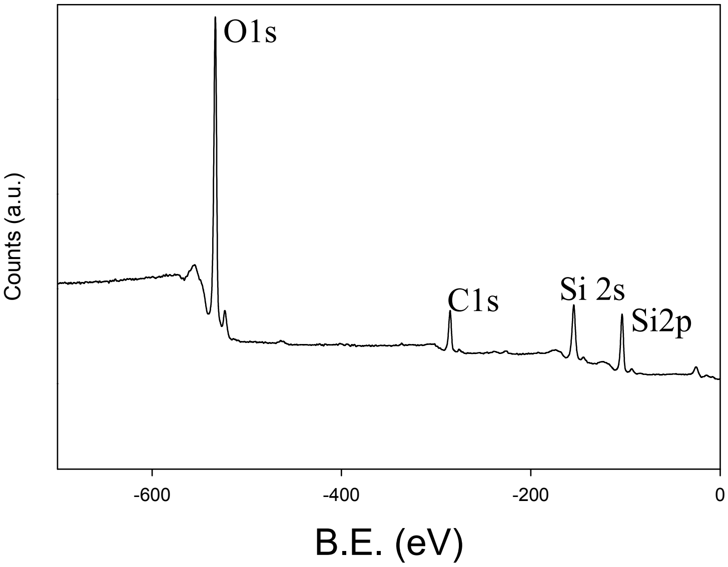

Fig. 2.5 X-ray photoelectron spectroscopy survey of typical low-κ materials.

The detected binding energy of an electron in a given element is related to the chemical environment of the element. The charge potential on a specific electron is summarized as $E_i = E_i^0 + kq_i + \sum_{i \neq j} \frac{q_i}{r_{ij}}$. The term $\sum_{i \neq j} \frac{q_i}{r_{ij}}$ represents the potential at position i due to the surrounding electrons. If the valence electron charges are withdrawn, they will have less screening effects on core electrons and thus cause an increase in binding energy. If the valence electron charges are added up, they will have more screening effects on core electrons and thus cause a decrease in binding energy. This small chemical shift can be used to identify the chemical states of atoms [6]. For example, the binding energy of Si 2p electrons in SiO_2 was observed to shift by 4.25 eV to higher binding energy from what is in elemental Si [7].

For the present study, a nonmonochromatized Al kα (1486.6 eV) x-ray source was used to generate photoelectrons which were analyzed using a Leybold hemisphere analyzer operating at 38.45eV pass energy. The nominal energy resolution was estimated to be around 1.0 eV. Surface charging was an inherent issue for XPS analysis because electrical insulators could not dissipate charges generated by photoemission processes. Technically, the charges could also be compensated with a low energy electron flood gun. During the data analysis, the charging effect was corrected by using peaks with known positions as a reference (e.g. 103.3 eV Si 2p in OSG sample).

XPS spectroscopy plots the number of detected electrons at different binding energies. CasaXPS Gaussian-Lorentzian product with a weight factor around 50-60%, was employed to de-convolute the spectra. For the purpose of background corrections, Shirley background subtraction, which assumes that background photoelectron intensity at any energy is due to the secondary electron emission and is linearly proportional to all the electrons with higher kinetic energies, was mostly applied. Otherwise, linear background subtraction was used instead. After the background subtraction, the atomic concentration was obtained by dividing the integrated area of each spectrum with the corresponding atomic sensitivity. According to the literature and fine adjustments by experiments, the atomic sensitivities in this dissertation were chosen to be Ta4f (2.4), N1s (0.42), C1s (0.25), O1s (0.90), Si2p (0.27) and Si2s (0.26).

Angle-resolved XPS is capable of detecting photoelectrons escaping from different depth regions of the sample. The sampling depth is estimated to be $3\lambda\sin\theta$, where θ is the electron exit angle and λ is the attenuation length 2~4 nm. Two major exit angles used in the study were 30° and 90°. The sampling depth at 30° exit angle was

3λ/2~ 5 nm, while the sampling depth at 90° exit angle doubled to 3λ~ 10 nm. Therefore, XPS scan at 30° exit angle mostly provided surface information and the scan at 90° exit angle provided the mixture information of bulk and surface. For example, after helium plasma treatment, it was observed that C/Si in the low-κ material almost doubled at the 90^0 scan than at 30^0 scan. The reason was that plasma treatment depleted the carbon on the low-κ material surface while its bulk remained unaltered. Therefore, the carbon concentration at the top surface was much less than that at the bulk.

With the option of sputtering Ar ion beam on the sample surface and collecting the emitted photoelectrons simultaneously, XPS depth profiling reveals the element composition at different depth regions from the top surface to the bulk. It was performed in a PHI 5700 XPS system equipped with dual Mg X-ray and Al X-ray source at the CNM of the University of Texas at Austin. The photoelectrons emitting from the sample surface were detected at an exit angle of 45^0. The sputtering rate varied from material to material and could be calibrated accordingly.

Angle resolved XPS can be applied to study not only blanket films but also patterned films. An example is given in Fig. 2.6. They consist of some especially designed parallel structures with an aspect ratio of 1:1. The XPS detector remains at a fixed angle of 45^0 with respect to the normal to the sample surface. When the structures are positioned parallel to the detector orientation like Fig. 2.5 (a), the XPS detector will collect the electrons exiting from the trench bottom. When the structures are positioned perpendicular to the detector orientation like Fig. 2.5 (b), the XPS detector will only see the electrons exiting from the trench sidewall. The electrons from the trench bottom are shadowed by the trench sidewall since the aspect ratio is 1:1. A fixed angle of 45^0 or bigger is chosen to ensure the only electrons reaching the detector originate from the trench sidewall [8].

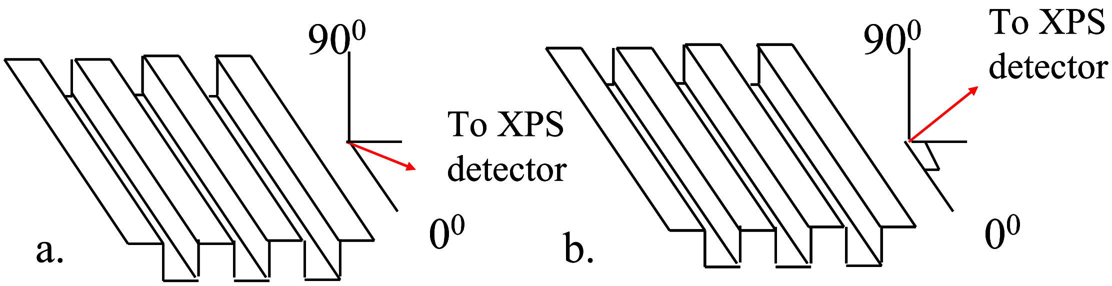

Fig. 2.6 Sample structures and ARXPS strategy to detect (a) trench bottom and (b) trench sidewall

2.2.2 X-ray reflectivity (XRR)

X-ray reflectivity is a powerful non-destructive analytical tool to determine the physical properties (thickness, density, roughness) of thin films. A highly collimated and monochromated X-ray beam is incident on a sample surface at low incident angles (0^0~5^0) and the reflectance beam intensity is recorded. Here, the incident angle is defined as the angle between the X-ray and the sample surface. As illustrated in Fig. 2.7, when X-rays are incident on multi-layer thin films, they will both reflect back into the atmosphere and penetrate into the solids at the gas-solid boundary in observance of the Snell's law. Since solids have a refractive index lower than the atmosphere (n=1), total reflectance can occur below the critical angle θ_c that is usually less than 1^0. Beyond that, beam intensity gradually drops due to partial penetration of X-ray into the solid [9].

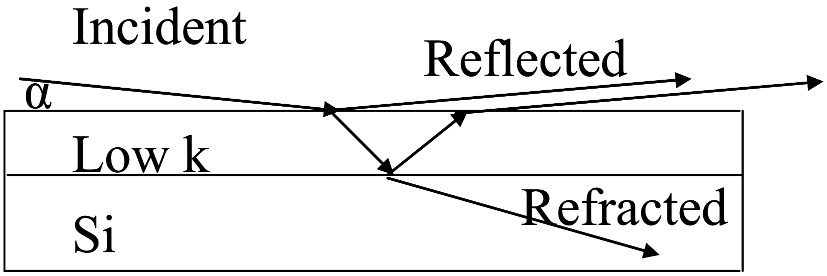

Fig. 2.7 **Reflection and refraction of X-ray on the surface and interface of low-κ /Si bi-layer film stack.**

The complex refractive index of a homogeneous material at X-ray energy range can be written as:

$$n = 1 - \delta - i\beta = 1 - \frac{\lambda^2 r_e N_\alpha}{2\pi} \frac{[(Z + f') - if'']}{A} \qquad (2.7)$$

where δ and β are the dispersion and absorption terms, respectively.

The dispersion term δ acts as a bridge linking the critical angle α_c with the mass density ρ by

$$\delta = \frac{\alpha_c^2}{2} = 2.701 \times 10^{-6} \left(\frac{Z + f'}{A} \right) \rho \lambda^2 \qquad (2.8)$$

where α_c can be experimentally determined from the XRR spectroscopy where the intensity drops to half the maximum intensity value [10]. Specifically, α_c of silicon is 0.223^0. For bi-layer film stack (film and substrate), the number of critical angles in XRR spectroscopy can tell which layer is denser. If there are two critical angles, the bigger angle corresponds to the substrate with higher density and the smaller angle corresponds to the film with lower density. However, if there is only one critical angle, it implies that the film density is higher than the substrate density.

Interference fringes in the XRR spectroscopy are caused by the interference of x-rays reflected at the interfaces between the layers with different refractive index, which implies a different composition or density. Film thickness can be inferred from the periodicity of the interference fringes. According to Bragg's law,

$$m\lambda = 2d\sin\theta \qquad (2.9)$$

Since $\theta<5^0$ in the XRR measurement, $\sin\theta \approx \theta$. Therefore, $d \approx \frac{\lambda}{2\Delta\theta}$ (Assume m=1). The uncertainty of film thickness calculation was reported to be 0.2nm or even lower [11].

Real surfaces/interfaces are not infinitely sharp but have certain roughness. The roughness was observed to affect the electron density and thus XRR spectroscopy. By introducing "Debye-Waller-like" decay term, the amplitude of reflectivity can be expressed as $R = R_F e^{-(\sigma Q)^2}$ [12]. Here, the roughness σ originates from averaging (over the coherence length of the X-ray (~1-10 μm)) the root-mean-square of both the microscopic surface roughness and the intrinsic interfacial width. It caused the reduction of reflectivity intensity at high incident angles. The bigger the decrease of reflectivity intensity, the larger the roughness. For a bi-layer film stack (film and substrate), the evolution of XRR curve amplitude reveals which interface is rougher. If the amplitude remains constant, then $\sigma_f = \sigma_s$; If the amplitude decreases, the smaller density layer is rougher; If the amplitude increases first and decreases next, the bigger density layer is rougher [13].

X-ray reflectivity measurement in this dissertation was performed in a Philips X'Pert MRD system. X-ray wavelength was 1.5405 Å of Cu Kα. Its resolution was around 5 arcsec in θ and 2θ-θ scans. Actual samples usually contained more than one thin layer on the substrate; therefore, it was difficult to read the density, thickness or roughness directly from the curve. Fitting with X'Pert software was frequently used in the data analysis. Curve fitting was time consuming and depended on the selected models. Each layer contained at least three parameters (t, ρ and σ). It was useful to minimize these parameters during model fitting, or fit t, ρ and σ step by step instead of fitting them altogether [14].

Fig. 2.8 shows the typical XRR of low-κ and high-κ materials with different thickness. Since thickness t is inversely proportional to Δθ, the thicker low-κ sample has smaller Δθ than the thinner high-κ sample. Thus, it is very hard to identify the interference fringes in the XRR spectra of thick film and difficult for curve fitting too. In other words, sample~~s~~ thickness is required to be thin enough to perform precise XRR measurement. Here, XRR was performed on ~100 nm thin films. The fitting range was from 0.3^0 to 1.5^0. The final fit value was less than 100 in order to obtain satisfactory results.

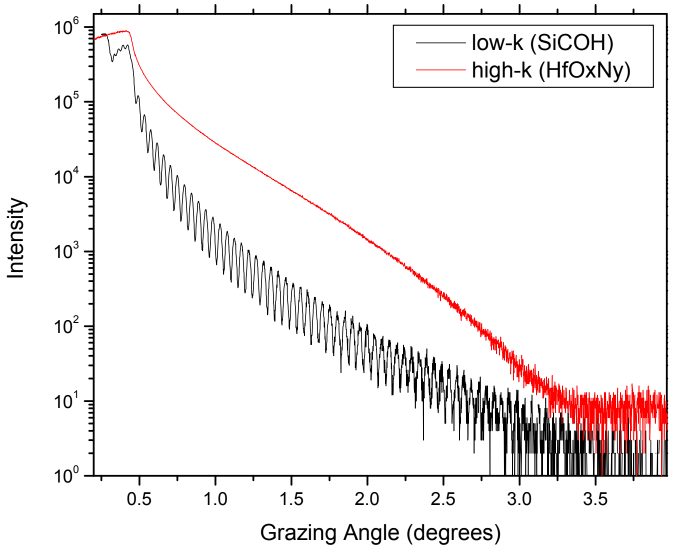

Fig. 2.8 **Typical X-ray reflectivity spectra of low-κ SiCOH (t=188 nm) and high-κ HfO_xN_y (t=2 nm) on Si substrate.**

2.3 Optical methods

2.3.1 Spectroscopic ellipsometer

Ellipsometry is a nondestructive, contactless optical technique to investigate the dielectric properties (complex refractive index, thickness) of thin films. The accuracy of thickness given by spectroscopy ellipsometer can be a few angstroms. Drude developed the principle of this method [15]. It measures the change of polarization of monochromatic light reflected from the sample. The polarization states of the incident beams can be decomposed into a component **s** that is oscillating perpendicular to the plane of incidence and parallel to the sample surface, and a component **p** that is oscillating parallel to the plane of incidence. R_s and R_p denotes the amplitudes of s and p components of the reflection beam normalized to those of the incident beam. Ellipsometry measures the ratio of R_p over R_s:

$$\rho = \frac{R_p}{R_s} = \tan\Psi e^{i\Delta} \qquad (2.10)$$

Here, $\tan\Psi$ is the relative amplitude ratio and Δ is the phase shift.

The theoretical derivation of R_p and R_s is given by Fresnel [16]. According to electromagnetic wave theory, a light wave consists of an electrical field vector $\vec{E}$ and magnetic vector $\vec{B}$, which are oscillating perpendicular to each other. The relation between their magnitudes is given by Maxwell's equation: $|B| = n\ |E|$. If light wave is incident at an angle θ_i on the boundary surface of an isotropic medium with a refractive index n, one part of the wave will be reflected at an angle $\theta_r = \theta_i$ and the other part will refract at an angle θ_t. In Fig. 2.9 (a), for an s-polarized light wave, vector $\vec{E}$ is assumed to pointing outward from the paper and vector $\vec{B}$ is assumed to pointing parallel to the paper. According to the Maxwell's theorem, tangential E and H, and normal B and D are continuous across the boundary. Therefore,

$$E_{0s}+E_{rs}=E_{ts}; \qquad (2.11)$$

$$n_1(E_{0s}\cos\theta_i - E_{rs}\cos\theta_i) = n_2E_{ts}\cos\theta_t \qquad (2.12)$$

Based on these equations, the reflection coefficient:

$$R_s=(\frac{E_{rs}}{E_{0s}})^2=(\frac{n_1\cos\theta_i-n_2\cos\theta_t}{n_1\cos\theta_i+n_2\cos\theta_t})^2 \qquad (2.13)$$

Meanwhile, in Fig. 2.9 (b), for a p-polarized light wave,

$$n_1E_{0p}+n_1E_{rp}=n_2E_{tp}; \qquad (2.14)$$

$$E_{0p}\cos\theta_i - E_{rp}\cos\theta_i = E_{tp}\cos\theta_t \qquad (2.15)$$

Then, the reflection coefficient:

$$R_p=(\frac{E_{rp}}{E_{0p}})^2=(\frac{n_1\cos\theta_t-n_2\cos\theta_i}{n_1\cos\theta_t+n_2\cos\theta_i})^2 \qquad (2.16)$$

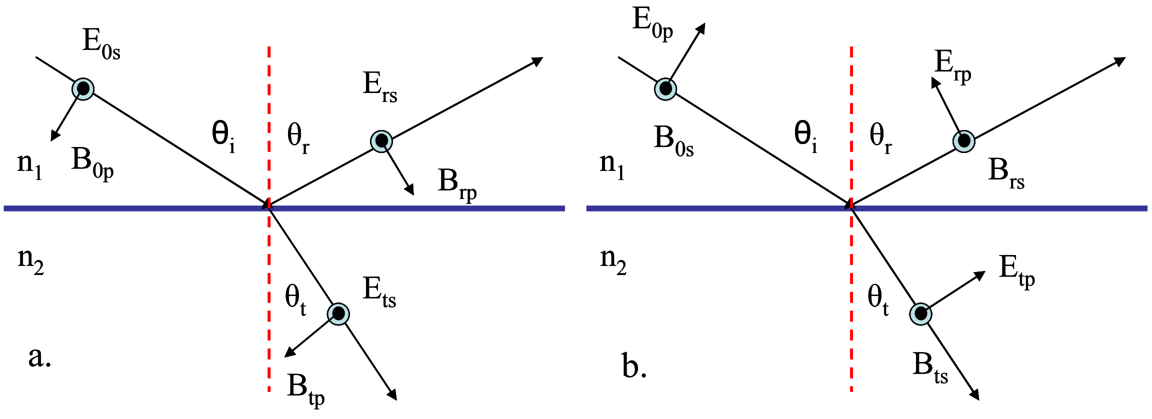

Fig. 2.9 **Reflection and refraction of (a) s-polarized and (b) p-polarized light waves at the interfaces of two media with refractive index n_1 and n_2.**

Obviously, $\tan\Psi$ and Δ measured in ellipsometer are related to the dielectric properties of materials. For multi-layer thin film, reflected waves at each interface have a different phase~~s~~ and amplitude. They will exhibit an interference pattern in the detector.

Spectroscopic ellipsometer extends the range of ellipsometer by employing more than one wavelength and incident angle to optimize the measurement of the physical parameters. J.A. Woollam VASE at J.J. Pickle Research Center of UT-Austin is a highly precise ellipsometer with the capability of variable wavelength (193 nm to 2500 nm) and angle~~s~~ (0^0 to 90^0). Desired physical properties of materials are extracted through a model-based analysis using the equations to describe interaction of light and matters. The most commonly used model is the Cauchy's dispersion equation $n(\lambda) = A + \frac{B}{\lambda^2} + \frac{C}{\lambda^4} + \cdots$. Cauchy's equation is an empirical relationship between dielectric constant of materials, and the wavelength. A, B, C etc are coefficients. It is valid for the normal dispersion in the visible wavelength region. During the modeling, a layered structure is proposed with the thickness, order and dielectric constants of each layer specified. The computer programs adjust the parameters until reaching a low mean squared error (MSE), which is a statistical value to quantify the difference between experimental and calculated model data [17]. An empirical value of MSE for a good fit is 30.

Ellipsometer is widely used in the semiconductor industry since it is integrated into the manufacturing lines as a process monitor for the thin film deposition, etching, etc. Its scatterometry feature can also measure the line width of patterned films [18] [19]. With ellipsometry porosimetry, the porosity of low-κ materials can be deduced by measuring the change of the optical properties and thickness upon absorbing and desorbing volatile species at certain pressures. Compared with other porosity measurement techniques like PALS [20] and X-ray porosimetry[21], ellipsometry porosimetry has the advantages of carrying out all the measurements in a film, small surfaces (including patterned wafers), and at room temperature [22].

2.3.2 Fourier transform infrared spectroscopy (FTIR)

FTIR is an analytical technique to identify the molecular structures of a material such as functional groups and chemical bonds. Atoms in a molecule assume different types of vibrational modes: symmetrical and anti-symmetrical stretching, scissoring, rocking, wagging, twisting, etc. Each vibration mode has its own wavenumber, i.e. an energy level. Atoms in vibration absorb energy in the infrared range if there is a change of the dipole moment. That is to say, only the vibration modes that induce dipole moments are infrared active.

Infrared spectroscopy has two modes: transmission mode (FTIR) and reflectance mode (FTIR-ATR). At the transmission mode, the infrared beam penetrates the whole sample and the detector behind the sample records the transmittance, and the ratio of the transmitted to incident light intensities. At the reflectance mode, an optically dense and high index crystal (typically 2.38 to 4.01, e.g. ZnSe) is held in good contact with the sample surface. The infrared beam, directed on the crystal, goes into total internal reflectance. This creates an evanescent wave that can extend beyond the surface of the crystal into the sample with a penetration depth of only a micron (0.5 ~ 1 μm). The detector records the relative change of beam intensities. Clearly, FTIR measures the bulk properties of the sample while FTIR-ATR measures the surface properties. Compared with the large database of FTIR, ATR is not preferred due to the difficulty of interpreting the data [23].

According to the Beer's law,

The absorbance of the sample $A = \alpha tc$ (2.17)

The transmittance $T = \frac{I_1}{I_0} = 10^{-A} = 10^{-\alpha tc}$ (2.18)

where, $\alpha = \frac{4\pi k}{\lambda}$ is the absorption coefficient of the absorber; t is the travel distance of light; c is the concentration of the absorbing species in the sample.

Fig. 2.10 is a schematic view of an FTIR system. Its optical part is similar to the Michelson Interferometer. The mechanical convolution of the transmitted intensity of an IR source can be Fourier transformed back to a frequency dependent intensity profile. The beam splitter (a half-silvered mirror) splits the incident laser beam onto a fixed mirror and a moving mirror. After reflectance upon the two mirrors, the split beam recombines at the beam splitter, directs to the sample and the transmittance is recorded at the detector. Once the beam distance from the beam splitter to the fixed mirror is not equal to the distance to the moving mirror, the two reflected beams do not have the same phases. This phase difference leads to wave interference. The computer collects the interferogram and performs Fourier transformation to obtain a spectrum of intensity vs. wavenumber [24]. The resolution of the wavenumber is determined by the maximum translation of the moving mirror: $\Delta \overline{v} = \frac{1}{2L}$.

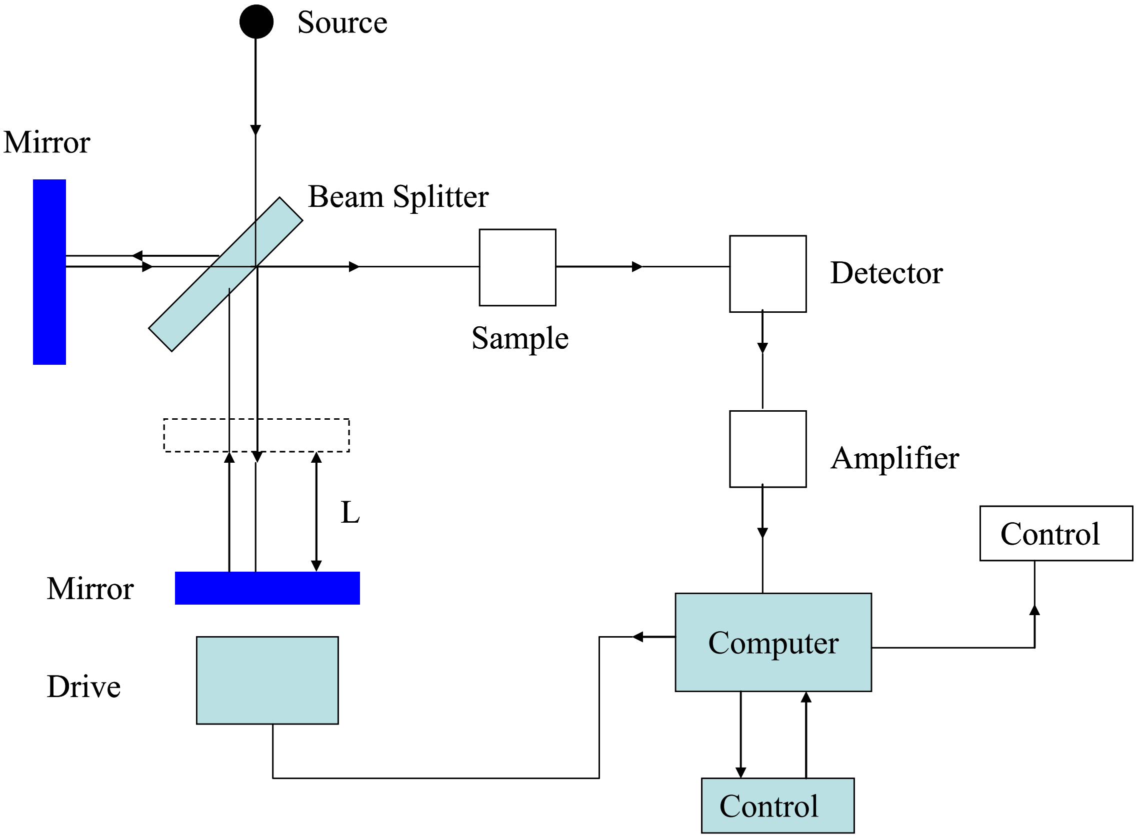

Fig. 2.10 **Schematic view of an FTIR system**

The instrument used in this research was a Nicolet Magna-IR 560 spectrometer with the wavenumber resolution of 4cm^{-1}. The spectrometer was purged with nitrogen to maintain a dry and clean environment during experiments. 256 scans of spectra ranging from 400 to 4000 cm^{-1} are usually collected. The final spectrum is the average of the 256 scans. Since the low-κ films were usually deposited on Si substrate, FTIR spectrum of the background, i.e. Si substrate, was obtained first by removing the deposited film with a razor blade~~s~~ or buffered HF. The sample spectrum was obtained by subtracting the background spectrum. Omnic software is frequently used to process the FTIR spectra.

Depending the materials that are characterized, peaks at certain positions should be zero. Baseline correction is a first and important step before fitting the FTIR data. In order to compare the FTIR spectra, the baseline must be consistent for all spectra. In this thesis work, the selected baseline zero points for the low-κ spectra were 3999.703 cm^{-1}, 2818.594 cm^{-1}, 1801.203 cm^{-1}, 1330.514 cm^{-1}, 658.101 cm^{-1}, and 523.618 cm^{-1}.

Fig. 2.11 is a typical FTIR spectrum of organosilicate glass (OSG) material. The wavenumbers at the peak are a characteristic value of the molecular structure in OSG. The integrated area of the peak represents the relative concentration of the structure. Specifically, the peak at 2970 cm^{-1} is assigned to anti-symmetrical stretch of CH_x and the peak at 2180 cm^{-1} is assigned to Si-H. The symmetrical bending of $Si-CH_3$ is located at 1273 cm^{-1}. The broad peak between 900 and 1250 cm-1 belongs to the anti-symmetrical stretch of Si-O-Si [25]. A more complete list of the interesting molecular structures in low-κ materials is given in Table 2.1.

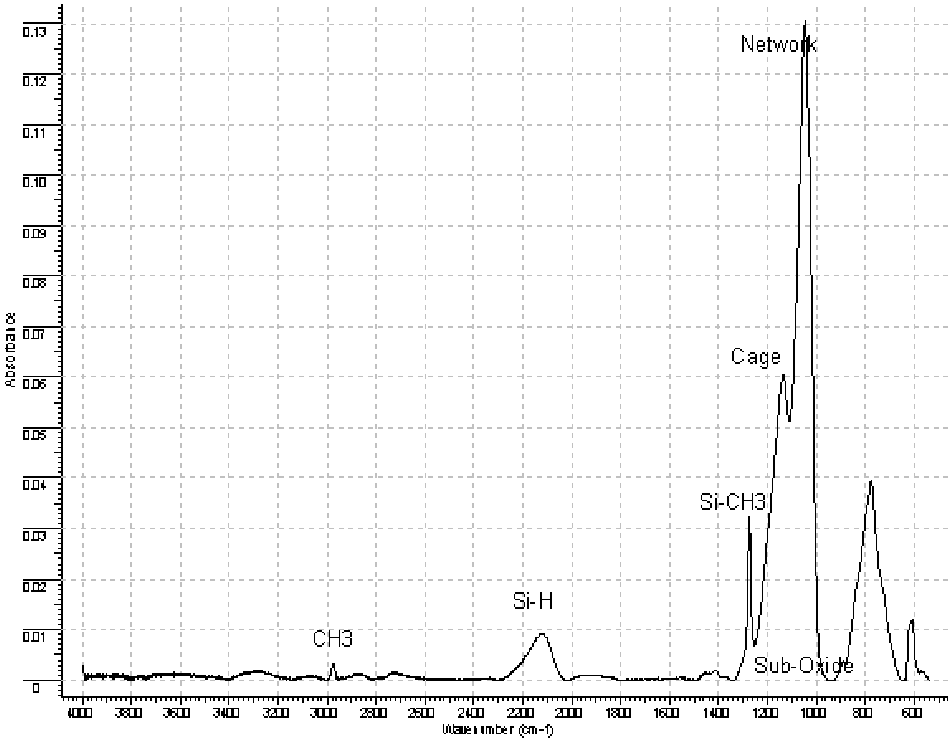

Fig. 2.11 Typical FTIR spectrum of OSG

Table 2.1 FTIR peak assignment of the structures in low-κ materials

Band Position (cm^{-1})	Identification	Vibration Modes
3650	H bonded Si-OH	
3400-3300	Absorbed H_2O	
3100-2800	$C\text{-}H_x$	Anti-symmetric stretching
2400-2000	Si-H	Symmetric stretching
1550-1425	CH_2 (Si free)	Bending
1300-1250	$Si\text{-}CH_3$	Symmetric bending
1250-950	Si-O-Si	Anti-symmetric stretching
890	H-Si-O	Bending
848	H-Si-O, $Si\text{-}Me_3$	Bending
802	$SiMe_2$	Anti-symmetric rocking
778	$SiMe_1$, $SiMe_3$	Rocking

The broad anti-symmetrical stretch of Si-O-Si between 900 and 1250 cm-1 can be deconvoluted into three individual peaks (see Fig. 2.12) at 1135 cm^{-1}, 1063 cm^{-1}, and 1023 cm^{-1}. The Si-O-Si bonding angle in a fully relaxed stoichiometric thermal silicon dioxide is ~140^0 and thus an FTIR peak is around 1080 cm^{-1}. Due to the deposition conditions of the low-κ materials and the neighboring of Si with other non-oxygen atoms, the Si-O-Si bonding angle varies. The vibration frequency $\omega \propto \cos\theta$. For the cage structure Si-O-Si~150^0, and the corresponding wavenumber is 1135cm^{-1}; for the suboxide structure Si-O-Si<140^0, and the corresponding wavenumber is 1023cm^{-1}. Three bond structures of Si-O-Si are shown in Fig. 2.13. The cage structure enlarges the volume of SiO_2 and reduces the dielectric constant. In the suboxide structure, compared with O, the less electronegative atom X such as C, Si, H, distorts the tetrahedral and reduces the Si-O-Si bond angle due to weak attraction of the bonding electrons on the Si-X bond [26].

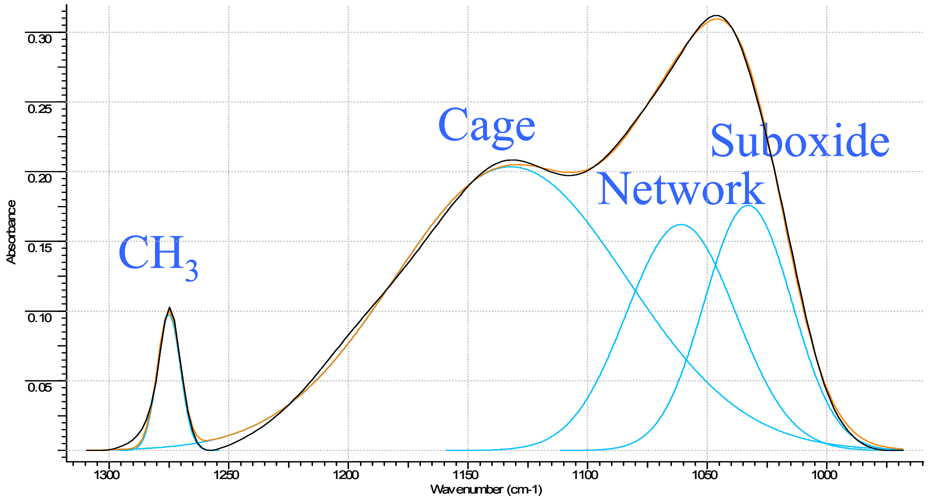

Fig. 2.12 **FTIR peak deconvolution of anti-symmetrical Si-O-Si into the components of cage, network and suboxide**

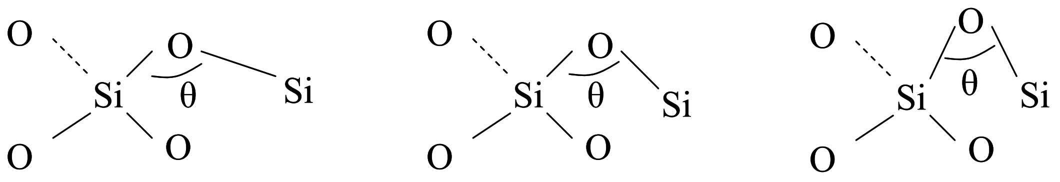

Cage: Si-O-Si~150^0 Network: Si-O-Si~140^0 Suboxide: Si-O-Si<140^0

ν=1135 cm^{-1} ν=1063 cm^{-1} ν=1023 cm^{-1}

Fig. 2.13 **Schematic drawing of the three bond structures of Si-O-Si**

Through comparing the structural modification of low-κ materials before and after certain processes, the mechanism of the process can be well understood. But at certain conditions, for example, plasma ashing process, the structure modification is so small that it is difficult to identify the changes of the molecular structures. Subtractive FTIR is often employed here to make the changes more clear. It is simply obtained by subtracting the first FITR curve from the second FTIR curve: Subtractive FTIR = FTIR A - (Thickness A/Thickness B) × FTIR B. Considering that the FTIR peak is influenced by the film thickness, the film thickness adjustment factor should be used. Fig. 2.14 is an example of using subtractive FTIR technique to characterize whether the low-κ material is hydrophilic or hydrophobic. The low-κ sample was boiled in water at 100^{0}C for one hour and the FTIR spectrum of the low-κ sample before and after boiling was collected. Subtractive FTIR spectrum was obtained by subtracting the postboil FTIR spectrum from the preboil FTIR spectrum. It was found that the subtractive FTIR was almost flat at zero intensity in the whole IR region, indicating the low-κ sample remained unaltered after water boiling and thus was very hydrophobic.

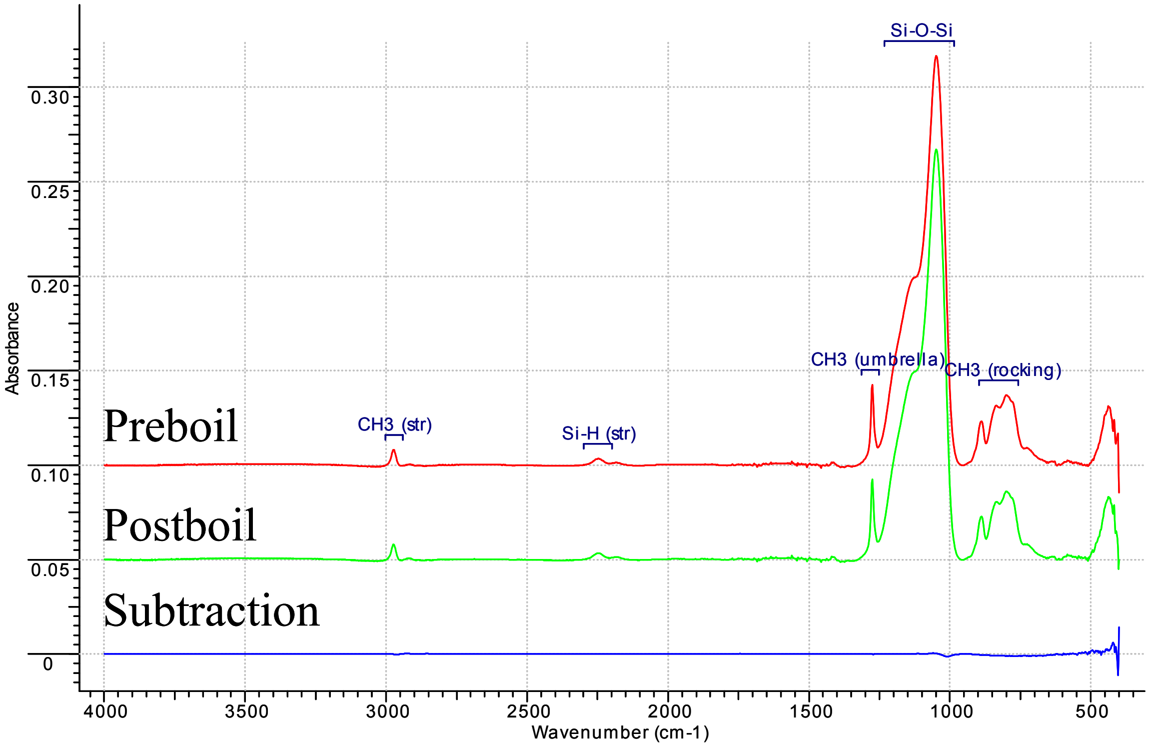

Fig. 2.14 **Example of using subtractive FTIR technique to characterize the hydrophobic property of low-κ materials**

2.4 Electron microscopy

2.4.1 Scanning electron microscopy (SEM)

Scanning electron microscopy, developed by a German scientist Manfred von Ardenne in 1937 [27], is an imaging technique that detects the signals from the interaction between the incident electrons and the sample. It is probably the most widely used instrument in semiconductor fabrication for measurement and inspection. When the electrons are incident on the sample, they will extend around 5 microns into the sample and lose energy through scattering and absorption within an interaction volume. As a result, the electron emission and electromagnetic radiation from the sample occur to produce an image. The detected signals include secondary electrons, characteristic x-rays, back scattered electrons, Auger electrons, visible light, and absorbed currents. Secondary electron imaging is its primary imaging mode. Backscattered electrons mode collect electrons from a much larger interaction volume and thus yield additional information like grain boundaries, textures, etc. The measured intensity is displayed as a gray-level on a CRT. Variations in the specimen result in the variations of the produced signal intensity. The image contrast results from the spatial variations in the number of signal carriers that are produced and actually detected.

In general, the SEM image intensity is sensitive to the surface topography and local composition of the specimen and the electrical properties of the specimen surface. Specialized SEM images may be used to deduce information about the voltage variations across the specimen, the magnetic domain structures at the surface of the specimen, the crystallographic perfection of the specimen, etc.

The insulator material is usually coated with a layer of metal Pt in case the surface charging on the dielectric surface affects the image quality. Sometimes, low electron accelerating voltage is employed to eliminate image distortion. SEM can be used to inspect both flat surfaces and patterned surfaces. The sample surface can be rotated to inspect the sample from different view angles. Patterned samples can be cleaved with a diamond saw and placed vertically under SEM to inspect the cross-section images. The LEO 1530 SEM at CNM of UT-Austin has been used widely in this research to inspect the cross-section of patterned low-κ films. It is equipped with a GEMINI field emission column and a thermal field emitter. The operating voltage ranges from 200 V to 30 kV. The image resolution can be as good as 3 nm at 1 kV.

2.4.2 Transmission electron microscopy (TEM)

TEM employs a beam of high energy electrons to transmit through a very thin sample. The beam interacts with the sample and the electrons passing through the sample are magnified, focused, and recorded by a detector, monitor or CCD camera. Considering the Rayleigh criterion and spherical aberration, the TEM resolution is:

$$r(\beta) = \sqrt{r_{th}^2 + r_{sph}^2} = \sqrt{(0.61\frac{\lambda}{\beta})^2 + (C_s\beta^3)^2} \qquad (2.19)$$

where β is the aperture collection semi-angle, C_s is the spherical aberration, λ is the wavelength of the incident beam.

When $\beta_{opt} = 0.77(\frac{\lambda}{C_s})^{\frac{1}{4}}$, the minimum resolution is $r_{\min} = 0.91(C_s\lambda^3)^{\frac{1}{4}}$

Typically, r_{min} is around 0.25 - 0.3 nm. The lower the C_s and λ are, the better the resolution is. The wavelength, λ can be reduced by accelerating the electrons with higher voltages. Spherical aberration is caused by the lens field acting inhomogeneouly on the off-axis beams. The further off-axis electrons are bent more strongly towards the axis. As a result, a point object is imaged as a disk. This can be reduced through special adjustments of the lens field. For thick films, the chromatic aberration may affect the TEM resolution because of the electron energy loss in the specimen. For example, an energy loss of 15-25 eV can induce r_{chr} to be ~2 nm at 100 keV. In order to achieve good TEM images at 100 keV, the film thickness is required to be at least 30 nm [28].

At the conventional TEM mode, the beams reaching the sample are usually parallel. At the scanning TEM mode, the beam is focused as a spot on the sample. The specimen is scanned in a raster. The image is serially recorded. The scanning tunneling electron microscopy (STEM) technique generates atomic resolution images whose contrast is directly related to the atomic number Z. The primary advantage of STEM is the wide range of signals that may be detected. They include secondary electrons, backscattered electrons, transmitted forward scattered electrons, and transmitted diffracted electrons. The effective resolution of the STEM image is limited by the largest phenomena of the following three factors: probe size, beam spread in specimen, and interaction volume for the signal of interest [29]. Fig. 2.15 compares the image quality of SEM and STEM taken at the same location. The blanket sample was treated by He/O_2 plasma in an RIE chamber. The damaged region that was depleted with carbon was hard to be distinguished under SEM. However, STEM was more sensitive to the atomic number Z, and the damaged region sandwiched between photoresist and bulk low-κ showed clear color contrast and its thickness was estimated to be around 70 nm.

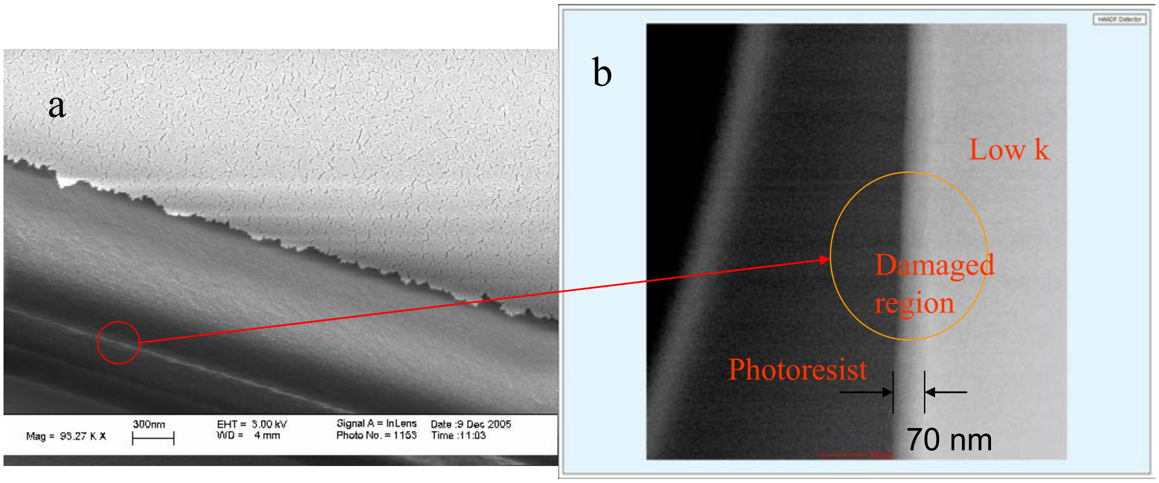

Fig. 2.15 **(a) SEM and (b) STEM images of the cross section of low k materials after reactive ion etching He/O_2 plasma damage.**

The energy of the TEM electron beam incident on the sample is lost through inelastic scattering, which includes phonon excitation (~0.02 eV), inter- and intra-band transitions (5-25 eV), plasmon excitations (~5-25 eV), and inner-shell ionizations (~10-1000 eV). The amount of energy loss is recorded in an electron spectrometer. This technique is called electron energy loss spectroscopy (EELS). A typical EELS spectrum consists of three parts: zero loss peak at 0 eV, low loss region (<100 eV) and high loss region (>100 eV). The zero loss peak intensity is the highest because it represents the electrons that interact with the sample elastically or not at all. Their electron energy loss is almost zero. The spectrum at the low loss region is contributed by the beam interactions with loosely bound conduction electrons (plasmon oscillations) and valence-band electrons (inter- and intra-band transitions). Plasmons are longitudinal wave-like oscillations of weakly bonded electrons. Plasmon loss occurs both on the sample bulk and surface and dominates in materials with free electron structures such as Li and Na. Inter- and intra-band transitions are induced by the energy transfer from an incident electron to a core electron to change its orbital state. It is possible to compare the obtained low loss spectrum with that in the library for element phase identification. The high loss spectrum, a small ionization edge riding on a strong plural-scattered background, originates from the inner shell electron excitation and is the most useful. The energy onset of the ionization edge is characteristic of an element. Differences in the fine structure of the edge reflect the chemical bonding effects and structural effects. Therefore, EELS is a powerful technique for the element identification. Compared with energy dispersive x-ray spectroscopy (EDX), EELS is more capable of identifying light elements and the chemical status of elements. The energy resolution of EELS is ~1 eV or less, while the energy resolution of EDX is a few times larger, ~10 eV. Also, EELS beam detection area is more local than EDX. In short, EELS is a good complement for X-ray spectroscopy [30]. Fig. 2.16 presents a STEM image of a via in the interconnect system. EELS and EDX spectroscopy were performed at the same position to analyze the element composition at the metal barrier. From the peak locations, EELS could identify Ti, N, and O easily. In EDX, Ti peak was well above the background noise, but the O and N peaks were comparable to the background noise. In addition, the energy levels for both O and N in EDX were close to zero because they are light elements. Therefore, the O and N peaks in EDX were jumbled mixed. Comparison of the EDX and EELS spectra indicated that EELS was more sensitive to light elements than EDX.

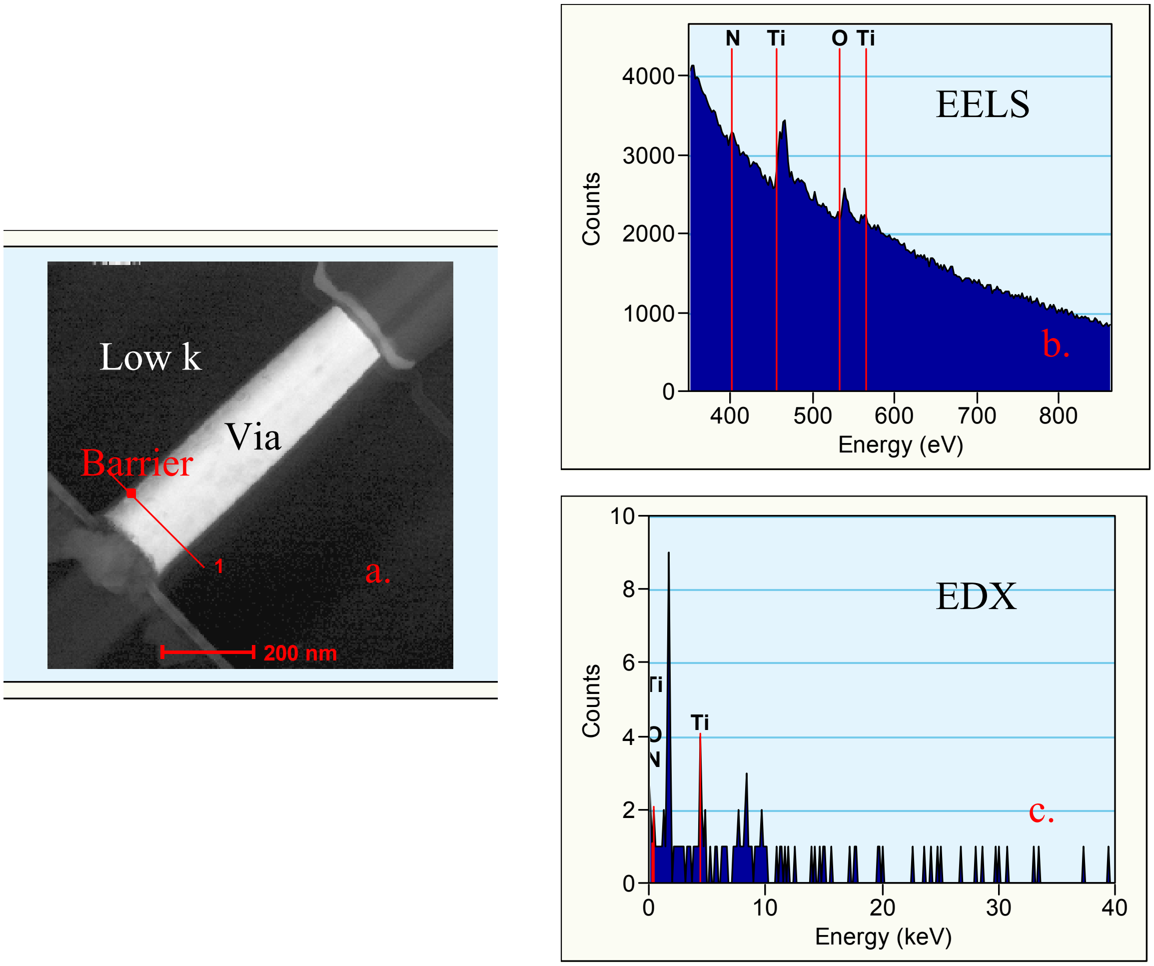

Fig. 2.16 **(a) STEM cross section image of a via in the interconnect; (b) EELS spectrum of the barrier property; (b) EDX spectrum of the barrier property. The beams of EELS and EDX focus at the same position as indicated by the red spot in the STEM image.**

Energy filtering TEM (EFTEM) incorporates an energy selecting slit, placed in front of the camera, to permit only electrons within a certain range of energy being recorded. This technique removes the possible effects of chromatic aberration on the image quality. By selecting electrons within the different energy regions, the energy loss spectrum representing different elements in the sample can be obtained. Combining STEM, an elemental distribution map can be obtained.

TEM sample preparation is a time-consuming process. In this thesis work, TEM samples were prepared by focused ion beam (FIB). Similar to the use of electrons in SEM, FIB uses gallium ions that are accelerated to 5-50 keV and focused on the sample by an electrostatic lens. The samples were normally prepared for cross-sectional view. Prior to FIB, the sample surface was first spun with to about 1 μm thickness, and then annealed in an oven at 120^0C for one hour to solidify the photoresist. In the study of carbon depletion on the sample surface or the sidewall of a patterned low-κ material, in order to minimize the influence of carbon in photoresist on EELS carbon measurement, a layer of 30~50 nm Cr was inserted between the sample and the photoresist to act as a barrier of avoiding the mixture of low-κ material and photoresist. On the surface of photoresist, a layer of platinum was deposited to facilitate image focus under FIB. The sample was first narrowed down to ~80 μm by a dicer. Then the diced chip was glued on a half-cut copper ring TEM sample holder. During FIB cut, a current level of 20,000 pA was first used from both sides to approach the target area at the center. The beam current was gradually reduced until 100 pA, corresponding to the sample thickness of ~1 μm. The current used for the final cut was as small as 50 pA. In this way, the artifacts or damage by the gallium ions could be minimized. Fig. 2.17 shows two micrographs during the TEM sample preparation by FIB milling. The final sample thickness is usually about 50 nm for high resolution TEM, and the thickness is required to be 30 nm or thinner for EELS.

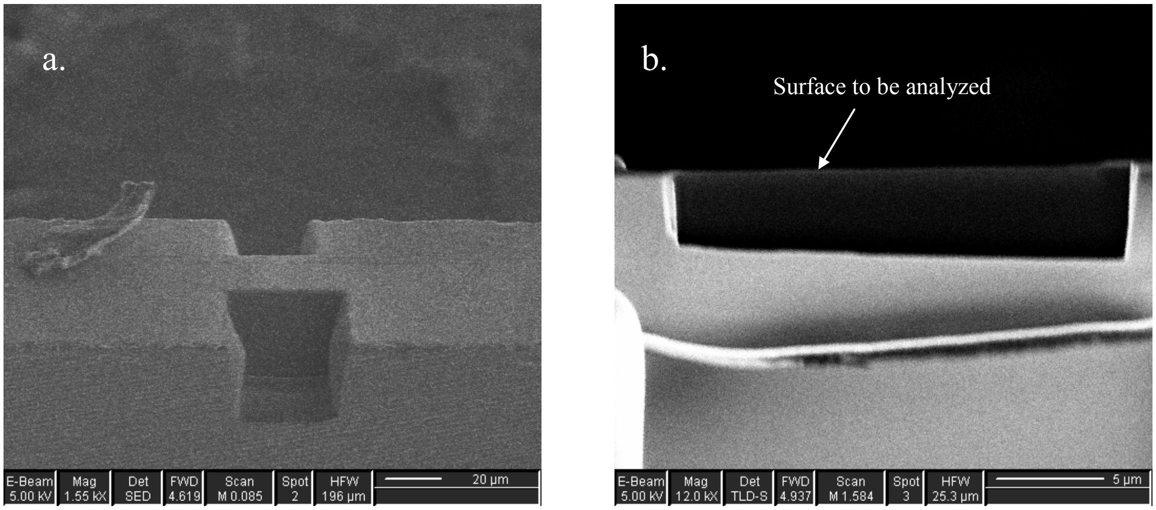

Fig. 2.17 FIB micrographs of (a) a sample being milled by focused ions; (b) a frontal view of final TEM sample (~30 nm).

2.5 Residual gas analysis (RGA)

RGA is an analytical technique to detect and identify the gases inside a chamber. The RGA used was an e-Vision type product purchased from MKS. It was operated through MKS Easyview software or using the ASCII protocol.

The e-Vision comprised of a quadrupole analyzer, an e-Vision control unit, a low voltage power supply, and other necessary parts. It was connected with a HP computer through an Ethernet port.

By virtue of their functions, an RGA is composed of four parts: an ionizer, a quadrupole filter, an ion detector, and a flanged housing. In the ionizer, an electron beam, generated by a hot emission tungsten filament, strikes the gas atoms or molecules and ionize them. The ionized atoms or molecules are identified by a mass analyzer. The RF quadrupole, consisting of four cylindrical rods, provides a combination of DC and AC voltage with different frequency. At an applied frequency, only ions with a specific mass to charge (m/e) ratio can reach the detector. The detector converts the filtered ion beam into an electrical current that can be sent to be electronics for amplification or display. Usually, at low sensitivity, a Faraday cup is used as the detector. An electron multiplier will be required if the ion beam current is very low. The flanged housing, comprising of a standard 2.75” conflate flange with an electrical feedthrough, carries various supplies and signals to and from the quadrupole analyzer [31].

MKS e-Vision has a 2’’ single mass filter, a Faraday detector with a maximum operating pressure 5×10^{-4} Torr and a detection range from 1 to 100 a.m.u.. The RGA spectrum shows the partial pressure of various species with different mass to charge ratio (m/e). It can be exhibited at both analog and digital mode. It may be confusing because a single mass to charge ratio value can correspond to a few different species. Knowledge of dissociation of molecules helps to understand the spectrum more precisely. For example, when the MSQ low-κ materials are treated by plasma oxygen, it is believed that oxygen will deplete methyl groups and produce carbon dioxide and water. Therefore, it is expected that a significant increase of methyl (m/e=15), carbon dioxide (m/e=44) and water (m/e=18) should be observed when the RGA spectra collected before and after plasma damage are compared. Table 2.2 summarizes the mass assignment used in the plasma damage study.

Table 2.2 Mass assignment table used in this research. (Adapted from [32])

m/e (amu)	Ion	Parent substance	Sources
1	H^+	Hydrogen	Hydrogen, water, hydrocarbons, boranes, etc.
2	H_2^+	Hydrogen	Hydrogen, water, hydrocarbons, boranes, etc.
6	C^{++}	Carbon	Carbon containing compounds
7	N^{++}	Nitrogen	Air, amonia, nitrogen compounds
8	O^{++}	Oxygen	Air, water, oxides, etc.
13	CH^+	Carbon hydrogen	Carbon containing compounds, hydrocarbons
14	N^+, CH_2^+, CO^{++}	Nitrogen, carbon hydrogen, carbon monoxide	Air, amonia, amines etc. Hydrocarbons, reaction of oxygen with carbon, carbonyl compounds
15	CH_3^+	Methyl	Hydrocarbons
16	O^+	Oxygen	Air, water, oxide
18	H_2O^+	Water	Water
22	CO_2^{++}	Carbon dioxide	Reaction of carbon and oxygen
28	CO^+	Carbon monoxide	Carbon oxides, carbonyl compounds
32	O_2^+	Oxygen	Air, oxygen
44	CO_2^+	Carbon dioxide	Carbon dioxide, reaction of oxygen with carbon compounds

2.6 Electrical characterization

The major electrical characterization in this thesis was the measurement of dielectric constant with a metal-insulator-semiconductor structure by a HP 4194A Impedance Phase Analyzer. Fig. 2.18 (a) illustrates the metal-insulator-semiconductor structure. About 1 μm thick aluminum dots were deposited by a sputtering process and patterned by a shadow mask. The directional physical sputtering made the dots not perfectly round. In order to minimize the percentage of the fringe capacitance in the total measured capacitance, the dot was fabricated large enough, with a diameter of ~ 1.6 mm. To improve electrical contact, the backside of the sample was also coated with ~0.3 μm thick aluminum. A 1 MHz high frequency capacitance-voltage (CV) sweep was carried out to measure dielectric constant. The gate bias voltage applied on the aluminum dot varied from -100 V to 100 V. Fig. 2.18 (b) shows the typical C-V curve for a p-doped wafer. It consisted of a maximum capacitance at the strong accumulation region and a minimum capacitance at the strong inversion region. In the accumulation region (V_G< -10 V for low-κ), all charges applied on the metal dot were balanced by the majority carriers in the silicon substrate. The low-κ dielectric constant can be deduced as follows:

$$\kappa = \frac{C \times d}{\varepsilon_0 \times A} \qquad (2.20)$$

where C is the capacitance at the strong accumulation, d is the thickness of the low-κ material, A is the area of the aluminum dot, ε_0 is the permittivity of vacuum: 8.854 pF/m.

The above description is the measurement of out-of-plane dielectric constant. Industry also measures in-plane dielectric constant with an intra capacitor consisting of double-combed interdigitated pattern. The two measured κ values can be different because the low-κ material may be anisotropic [33]. In this thesis, in-plane dielectric constant was not characterized due to the unavailability of the comb structures from customers.

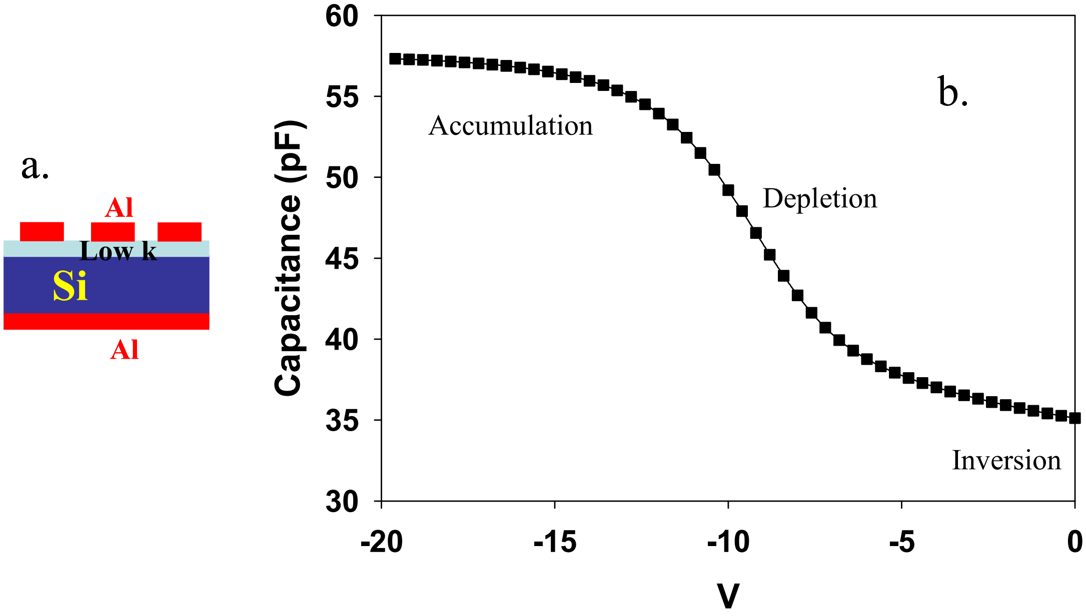

Fig. 2.18 (a) Schematic of metal-insulator-semiconductor structure; (b) Typical C-V curve for a p-doped wafer.

2.7 Summary

The main chamber and the analytical techniques used in this research work have been discussed in this chapter. The experimental setup provided an in-situ XPS analysis capability after the various processes or treatments. Coupled with RGA to in-situ monitor the reaction byproducts, it was very suitable for mechanistic study of the processes of plasma low-κ interactions or film depositions. The elemental composition and chemical bonding environment could be identified with XPS, EDX or EELS. The molecular structures of polymers could be characterized by FTIR. Refractive index was obtained by spectroscopy ellipsometry. Film density was measured by X-ray reflectivity. Dielectric constant was measured by a MIS structure. SEM or TEM could provide images of the sample. Besides the above techniques, some other auxiliary analytical techniques which could possibly be used in the following chapter include AFM (surface roughness), Raman spectroscopy (bonding configuration), contact angle goniometer (density of surface polarity), etc. Due to the length limitation of this dissertation, they were not discussed in detail in this chapter. Instead, their principles will be briefly mentioned during the data presentation in Chapter 4. Table 2.3 presents a good review of the instruments used in this research. Good sources of the overview of the various analytical techniques in semiconductor fabrication are given in the references [34] [35] [36].

Table 2.3 Overview of various analytical techniques used in this research

Analytical technique	Purpose	Instrument
ARXPS	Chemical composition	Axis Ultra DLD
FTIR/ATR	Bond configuration	Nicolet Magna 560 with Harrick ATR
Raman	Bond configuration	RENISHAW Raman Spectroscopy
SE	Refractive index, thickness	J. A. Woollam M-2000 Spectroscopic Ellipsometer
XRR	Density, thickness	PANanalytic's X-ray Reflectivity
Contact Angle	Polar term density	CA100 Ramé-Hart Goniometer
MIS	Dielectric constant, C-V, I-V	HP 4194A Impedance Phase Analyzer
AFM	Surface roughness	Digital instrument
XPS depth profile	Atomic concentration	PHI 5700 x-ray photoelectron spectroscopy
EELS/TEM	High resolution image, elemental identification	JEOL 2010F, FEI TECNAI G2 F20 X-TWIN
SEM	Image	LEO, FEI Strata™ DB235 SEM/FIB
RGA	Reaction byproducts	MKS e-Vision+
TGA	Weight loss	Perkin Elmer Thermogravimetric Analyzer

Chapter 3 Process Enhancements with Plasma Beams

Copper can easily diffuse to mix with dielectric bulk and produce defects harmful for the performance of chips. Therefore, a thin and stable barrier is required to prevent the interdiffusion and reactions between copper and dielectrics in interconnect technology. Atomic layer deposition (ALD), a variant of chemical vapor deposition, is expected to be used in the deposition of Ta/TaN barrier in the technology node of 32 nm and beyond. The quality of ALD film is determined by the surface interaction between ALD precursors and low-κ materials. In this chapter, *In-situ* x-ray photoelectron spectroscopy was employed to study atomic layer deposition of TaN barriers on the low dielectric constant (low-κ), organosilicate (OSG) dielectric surfaces. The evolution of the low-κ substrate chemistry revealed an initial transient region mainly controlled by the substrate surface chemistry. Initial nucleation process on pristine OSG dielectrics was found to be slow due to inadequate silanol sites for chemisorption. Hydrogen and amine radical beams, especially amine radical beams, were observed to enhance significantly the chemisorption of $TaCl_5$ precursor on the OSG surface. The enhancement was attributed to the dissociation of bonded methyl groups from the low-κ surface followed by nitridation with the amine radicals. The role of atomic hydrogen was also examined. Finally, Monte Carlo simulations were performed to illustrate the importance of the substrate chemisorptive sites in controlling the film growth morphology.

3.1 Atomic layer deposition

Atomic layer deposition (ALD), developed in Finland more than 20 years ago, is a self-limiting, gas phase, sequential surface chemistry process [1]. As illustrated in Fig. 3.1, in this thin film deposition process, pulsing of precursor gases and vapors are introduced to the substrate alternately. Purging of the reactor with inert gas between the precursor pulses induces the formation of a saturated chemisorbed monolayer of the precursor. Reaction occurs to the saturated surface, allowing the film to grow to a full or partial layer in each cycle [2]. Theoretically, film thickness can be easily controlled by the deposition cycle. ALD is suitable for film growth on large area substrates with complex shapes, using solid precursors with relatively low vapor pressure~~s~~. It has been used to deposit a dozen of materials such as II-VI and III-V compound semiconductors, elemental silicon, silicon dioxide, and metal oxides, and nitrides [3] [4]. Compared with those deposited by physical vapor deposition (PVD) or chemical vapor deposition (CVD), conformal films prepared by ALD exhibited better electrical reliability and higher film quality. Although the ALD deposition rate is slow (e.g. only about 0.6 angstrom per cycle for TiN under an optimum condition [5]), it becomes less and less of an issue, with reduced device dimensions and increased aspect ratios in integrated circuits. One major ALD application in BEOL fabrication is the deposition of barrier. Studies showed that 10 Å ALD TaN possessed better diffusion barrier property than 50 Å PVD TaN [6]. As published by ITRS (Fig. 3.2), the barrier thickness will be less than 5 nm after 2008, and smaller in the subsequent years. For deposition in such a small size, ALD will almost be the only choice by the industry [7].

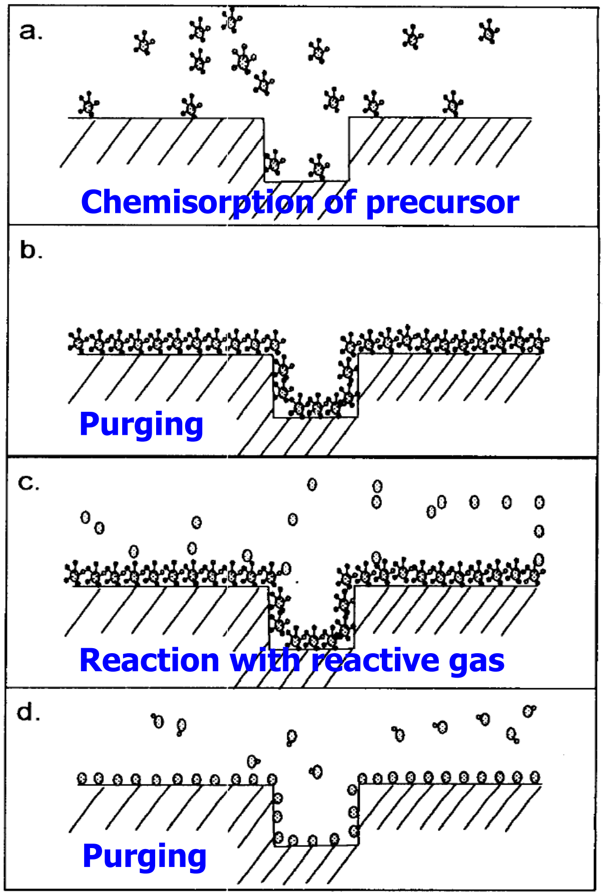

Fig. 3.1 Illustration of one cycle of atomic layer deposition. (From [2])

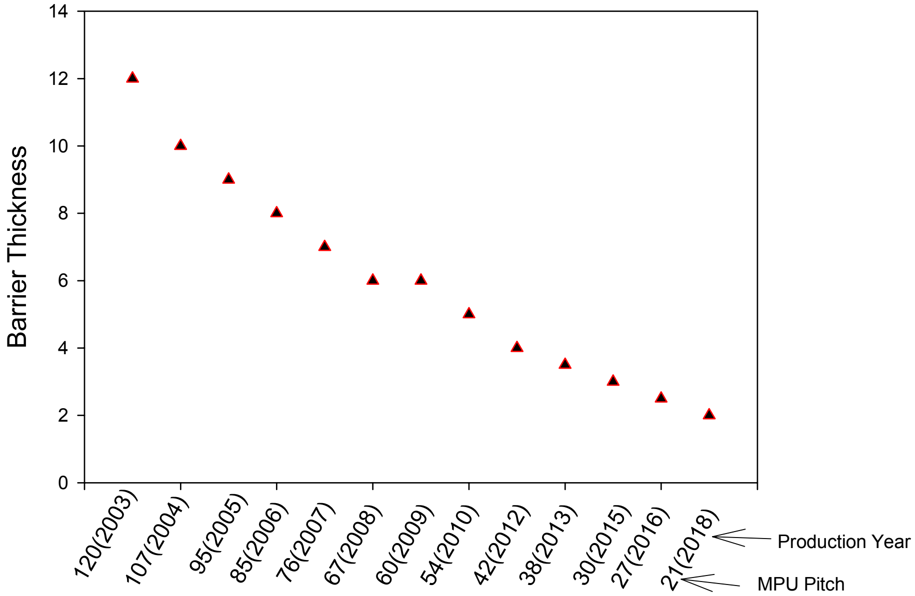

Fig. 3.2 Trend of the barrier thickness with the MPU pitch and production year. (From ITRS 2007)

The barrier films should be pure, dense, conductive, conformal, thin, and show good adhesion properties and low processing temperature (<400^{0}C). The conformality requirement is especially demanding since the aspect ratios of both trenches and vias have increased. Although PVD is still being used in the mainstream technology, it is hard for it to achieve good conformality and full step coverage when the aspect ratios increase and films become ultra thin.

Transition metal carbides and nitrides such as TiN, TaN, TaC and WCN are regarded as best candidates for barrier. They have properties characteristic of both covalent compounds such as high melting points, thermodynamic stability, extreme hardness, etc., and of metals such as good thermal and electrical conductivity. The microstructure of the film must be optimized in the film deposition because it will affect the quality of the final film. The relation between the microstructure and its physical property is summarized in Table 3.1. It is clear that an ideal barrier film is expected to be amorphous with α phase and hexagonal close packed (hcp) structure. Compared with 150-220 μΩ•cm for β-phase Ta, the resistivity of α-phase Ta is only 15-30 μΩ•cm; Compared with the typical bcc-TaN, hcp-TaN has the advantage of closer packing and lower resistivity for similar adhesion to silicon dioxide. An earlier report of resistivity versus temperature showed no barrier failure in Cu/hcp-TaN (250 Å)/Si stack to the test limit of 800^{0}C [8].

Table 3.1 Relation between film microstructure and its physical property.

α -phase	Low resistivity
β -phase	High resistivity
Amorphous	Random orientation, good prevention of diffusion
Polycrystalline	Orientation, easy to diffuse
Hcp	Dense structure, outstanding barrier performance
Bcc	Sparse structure, poor barrier performance

D. Edelstein et al. evaluated the properties of many candidate materials (Table 3.2) deposited with PVD technique [8]. Generally speaking, bilayer barrier is more desirable. Many candidates are eliminated due to poor adhesion to Cu or ILD and copper poisoning and corrosion. For example, TiN/Ta deposition requires two separate chambers and may cause Cu corrosion in some CMP processes. Compared with Ta based PVD, Ti based PVD shows additional disadvantages of worse step coverage and increased pinch-off. Step coverage and resistivity are related to the deposition method, which can be improved by ALD. TaN/Ta is the only material left to meet the entire requirements after strict screening.

Table 3.2 Evaluation of barrier materials. (From [8])

†=CVD available, *=Ionized-PVD available, ?=not investigated

Attributes	Cr	TiN	TiN/Ti	Ti/TiN	TiN/Ta	TaN	β-Ta	TaN/Ta	TaSiN	WN_x
Cu barrier	X	√	√	√	√	√	√	√	√	√
Adhesion on ILD	√	√	√	√	√	√	X	√	√	√
Cu on liner adhesion	√	X	√	X	√	X	√	√	X	?/X
Liner on Cu adhesion	√	?	?	√	?	√	√	√	√	?
Low in-plane R	√	X	√	√	?	X	X	√	X	X
Cu poisoning	√	√	X	√	√	√	√	√	?	√
CMP	?	X	X	X	X/√	√	√	√	√	?
Single chamber	√	√	√	√	X	√	√	√	√	√
Via, contact R	√	√	X	?	√	√	√	√	√	?/√
Contact R	√	√	√	√	√	√	√	√	√	?
Cu corrosion	?	X	X	X	X/√	√	√	√	√	?
Thermal stability	?	√	X	X	√	√	√	√	?	√
Stress cracking	X	√	√	√	√	√	√	√	√	√
Step coverage	?	√†*	√†*	√†*	√*	√*	√*	√*	√	√†
Final	X	X	X	X	X	X	X	√	X	X

Metal halides reduced by ammonia, or metal organic precursors (metal alkyl amides) reduced by ammonia or hydrogen radical is often chosen to be the chemistry for the deposition of Ta_3N_5. In the conventional CVD process, gas phase $TaCl_5$ and NH_3 are transported to the sample surface together, and they react to produce a solid phase Ta_3N_5. The additional HCl gas is pumped away. The reaction can be expressed as: $TaCl_5$ (g) + NH_3 (g) → Ta_3N_5 (s) + HCl (g). The growth of Ta_3N_5 purely depends on the amount of $TaCl_5$ and NH_3 and it is unrelated to the sample surface. However, in atomic layer deposition, the growth rate varies initially with the pulse time per cycle for precursor exposure or reactive gas exposure, and then saturates after sufficient exposure time per cycle. Therefore, the film growth can be divided into a nucleation region and a linear growth region. In the nucleation region, the incoming precursor molecules react with the functional groups on the sample surface. Only after the sample surface is fully covered with a layer of reaction products, linear growth will occur. Fig. 3.3 shows a typical ALD growth curve on SiLK^{TM}. The ALD growth rate in the nucleation region was lower than that in the saturation region. The ALD growth becomes linear after saturation of surface adsorptive sites with "monolayer" coverage.

The growth of Ta_3N_5 in atomic layer deposition can possibly be expressed as:

Nucleation: $Si\text{-}NH_2 + TaCl_5\ (g) \rightarrow SiNH\text{-}TaCl_4\ (s) + HCl\ (g)$.

Layer by layer growth: $SiNH\text{-}TaCl_4 + NH_3 \rightarrow SiNH\text{-}Ta(NH_2)_4 + HCl$

$SiNH\text{-}Ta(NH_2)_4 + TaCl_5 \rightarrow SiNH\text{-}Ta(N(TaCl_4)_2)_4 + HCl$

Here, $Si\text{-}NH_2$ provides chemisorptive nucleation sites for precursor $TaCl_5$. If the sample surface lacks adequate chemisorptive sites, the ALD process will take a long incubation time before a linear growth rate can be reached and the film becomes continuous [9].

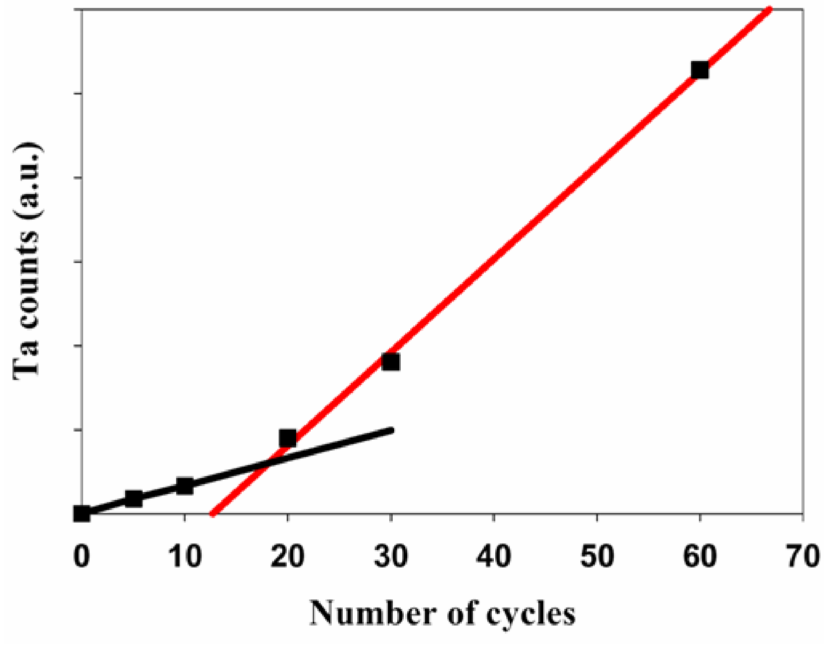

Fig. 3.3 Typical ALD growth curve on SiLK^{TM} surface.

Table 3.3 summarizes typical ALD halide process conditions in the current experiments. Samples were resistively heated to 300-390ºC for $TaCl_5$ processes by a Molybdenum heating wire underneath the holding plate. The solid precursor in a $TaCl_5$ ampoule was heated to 80^{0}C to raise the precursor vapor pressure and carried to the process chamber by Ar carrier gas. The tubing and the valves were kept at 120°C, the highest temperature that the seal in the valves could survive. The chamber wall was heated up to 200°C to prevent any condensation inside the chamber, the downstream throttle valve, and the turbopump. The flow rates for all gases were set to 100 sccm, and the chamber pressures during the process were set to 20 mtorr. By probing Ta/Si with XPS, the pulse time of precursor $TaCl_5$ was found to be at least 14 seconds in order to achieve maximum chemisorption~~s~~. Excessive ammonia was used to ensure complete chemical reaction with chemisorbed precursor molecules. In one ALD cycle, typical process conditions were 14 seconds of precursor, 4 seconds of purging, 4 seconds of ammonia, and finally 3 seconds of purging.

Table 3.3 Typical ALD halide process conditions.

Reaction temperature	300-390 °C
Ampoule temperature	80°C
Tubing & valve temperature	120°C
Flow rates	100 sccm
Process pressure	20 mtorr
Pulse time (precursor, purge, ammonia, purge)	14s,4s,4s,3s

3.2 Surface effects on atomic layer deposition

ALD growth was performed on three different low-κ films: MSQ, OSG, and SiLK^{TM}. Samples were cleaned by acetone, deionised water, and nitrogen sequentially, and then by outgassing at 300^{0}C for at least 2 hours at 10^{-7} torr. After 80 identical ALD cycles, no Ta_3N_5 was observed on MSQ; only a small amount of Ta_3N_5 was formed on OSG; and the formation of Ta_3N_5 on SiLK^{TM} was very appreciable. Fig. 3.4 presents the Ta4p and N1s XPS spectra on MSQ and SiLK^{TM} after 80 identical ALD cycles. The N/Ta ratio was about 1.6, close to the ratio of the dielectric phase of tantalum nitride, Ta_3N_5. The Ta4p and N1s XPS spectra developed on SiLK^{TM} appeared very prominent, compared with those negligible Ta4p and N1s XPS spectra on MSQ. Results on OSG were not presented because nitrogen in pristine OSG might mix up with nitrogen in the final Ta_3N_5 films.

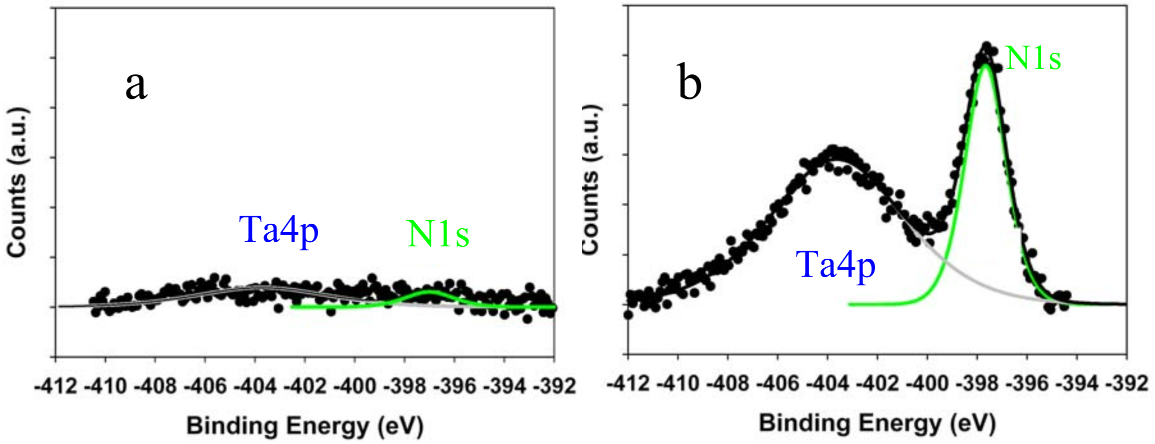

Fig. 3.4 Ta4p and N1s XPS spectra on (a) MSQ and (b) SiLK^{TM} after 80 identical ALD cycles.

After 80 ALD cycles on the dense OSG substrate, there were almost no appreciable changes in Si2p and C1s spectra. In Fig. 3.5, the deconvolution of O1s peak after 80 cycles was compared with O1s peak of the clean sample. It showed that a small metal oxide was developing at -530.6eV, suggesting a possible bonding of the incoming Ta with O. The slow ALD nucleation on OSG might be due to inadequate silanol (Si-OH) bonds on the surface. Also, during outgassing, condensation of Si-OH bonds to siloxane might further reduce the nucleation sites.

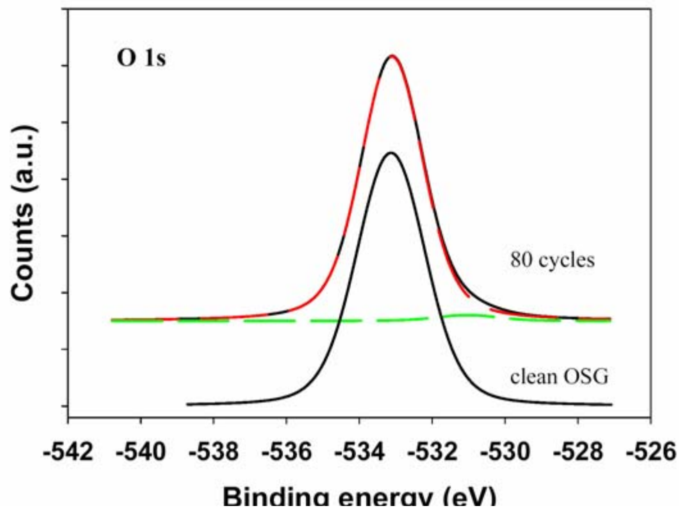

Fig. 3.5 Formation of Ta-O on OSG.

SiLK^{TM} is a type of highly cross-linked polyphenylene thermoset commercialized by the Dow Chemical Company [10]. Its carbon peak can be deconvoluted into a sharp primary peak at about -284.8eV, an ether carbon (C-O-C) peak at -286.3eV and π-π^* shake-ups between -290eV and -292eV characteristic of aromatic ring structures [11] [12]. Since the amount of oxygen in SiLK^{TM} was almost negligible, the interaction between carbon and Ta played an important role in the nucleation of $TaCl_5$ on SiLK^{TM}. Fig. 3.6 presents the evolution of C1s spectra during ALD Ta(N) on SiLK^{TM}. SiC was not observed because no obvious carbide peak was formed at -282.9eV. Instead, the π-π* shakeups decreased with deposition. It suggested a mild coordination of the precursor molecule on the benzene rings.

Previous studies of e-beam Ta formation on SiLK^{TM} suggested similar results [13] [14]. They were attributed to the formation of charge transfer complexes, which were energetically preferred over the more dramatic breakup of the benzene rings and subsequent formation of the metal carbide bonding due to the strong covalent C-H bonding (~ 400 kJ/mol or 4.3 eV/bond). The ground level of Ta electrons was $4f^{14}5d^{3}6s^{2}$.

The d orbits provided 5 free spaces for occupation of 10 electrons with reversed spin directions for a pair of electrons. The ground level of C electrons was $2s^2 2p^2$. To minimize energy, the pair of electrons in a 2s orbit could be excited to an empty position in 2p space to form sp^3 hybrid bonds. The benzene ring consisted of an σ bond formed by sp^2 electrons and a π bond formed by p electrons. While the σ electrons were restricted to a local region, π electrons could move freely inside the benzene ring. Charge transfer complexes or electron-donor-electron-acceptor complexes provided intermolecular binding through partial electronic charge transfer from π electrons of the donor moieties (e.g. benzene ring) to unoccupied d orbitals (e.g. Ta) of the acceptor moieties [15]. The coordination of a Ta atom on a benzene ring is illustrated in Figure 3.7.

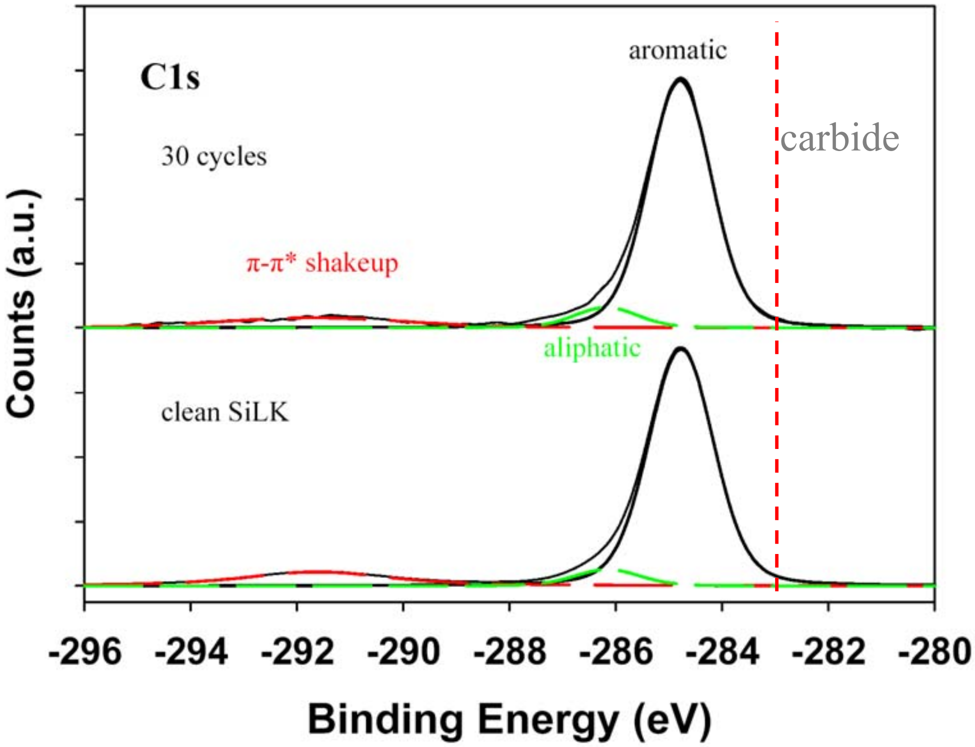

Fig. 3.6 **C1s XPS spectra of pristine SiLK^{TM} and SiLK^{TM} after 30 ALD cycles.**

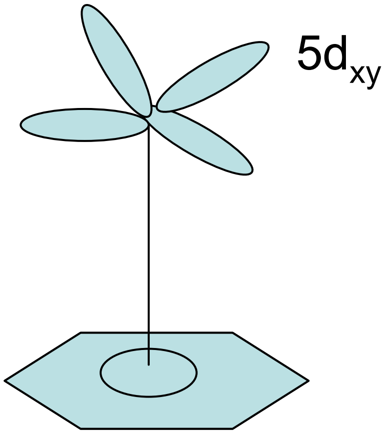

Fig. 3.7 **Coordination of Ta 5d orbits with carbon π electrons on the aromatic ring.**

3.3 Effects of plasma beam activation

Pretreatment of low-κ dielectric surfaces with radical beams was applied to study the surface activation effect on ALD growth. Radical beams, produced in a hybrid plasma source, were intentionally chosen to apply chemical effects to the surfaces and to avoid the physical damage normally caused by energetic ions in the plasma process.

Fig. 3.8 compares the ALD growth on a pristine low-κ OSG and that after plasma pretreatment. For the pristine low-κ OSG, Ta counts were very low even after 30 ALD cycles. However, after the pretreatment of radical H_2 and NH_3, Ta counts were much improved; indicating that plasma pretreatment transformed the inactive OSG surface into an active OSG surface. A transient region followed by a linear growth region was very typical in atomic layer deposition. Part of the substrate was adsorbed with nitride reaction products until it achieved complete "monolayer" coverage. The subsequent growth occurred on the same nitride surface and thus had the same growth rate. Assuming 3.5

nm to be the effective attenuation length for Si2p photoelectrons in a tantalum nitride overlayer, the decay of XPS Si2p signal led to the estimation of ALD growth rate on the pretreated OSG substrate to be 0.19 Å/cycle, close to the ALD growth rate of 0.32 Å/cycle on SiO_2 substrate from the current experimental setup. The difference was attributed to the low density of low-κ materials and non-optimized pre-treatment conditions that might have limited the extent of surface activation.

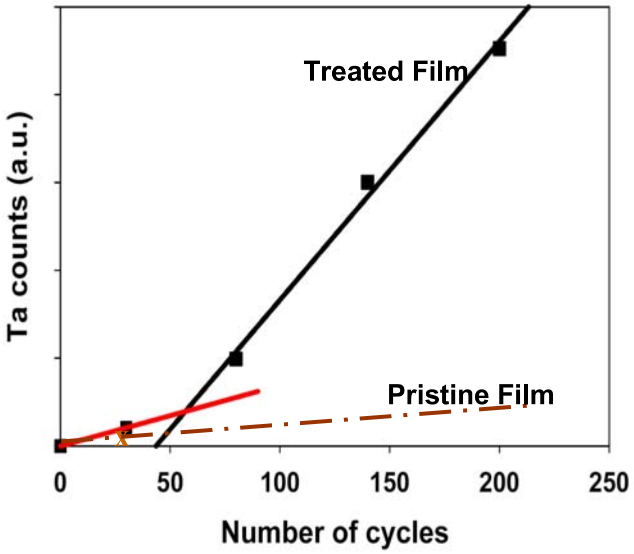

Fig. 3.8 ALD growth on pristine OSG and OSG after pretreatment of plasma NH_3 and H_2.

In XPS spectra, Ta4p was located around -403.0 eV and N1s around -398.0 eV. Fig. 3.9 presents the evolution of XPS peak intensities of Ta4p and N1s on pristine OSG and OSG after plasma pretreatments. A pristine film under pre-existing nitrogen is represented by curve (a), where the binding energy around -399.0eV was attributed to nitrogen in O-Si-N bonding environment. After 30 ALD cycles as shown in curve (c), the Ta4p peak around -403.5eV was still very small and the increase of the nitride peak around -398.0 eV was negligible. After the low-κ film was pre-treated with atomic hydrogen and amine radical beams, its surface was observed to have incorporated a larger concentration of nitrogen as indicated by the higher nitride peak in curve (b). Curve (d) showed the final XPS peak intensities of Ta4p and N1s after the plasma pretreated film was exposed to 30 identical ALD cycles. As a result, the tantalum signal was almost tripled and the nitrogen signal was almost doubled when curves (c) and (d) were compared. For example, the ratio of Ta/Si increased from 0.11 in (c) to 0.25 in (d), indicating that a significant amount of tantalum nitride was already formed in (d).

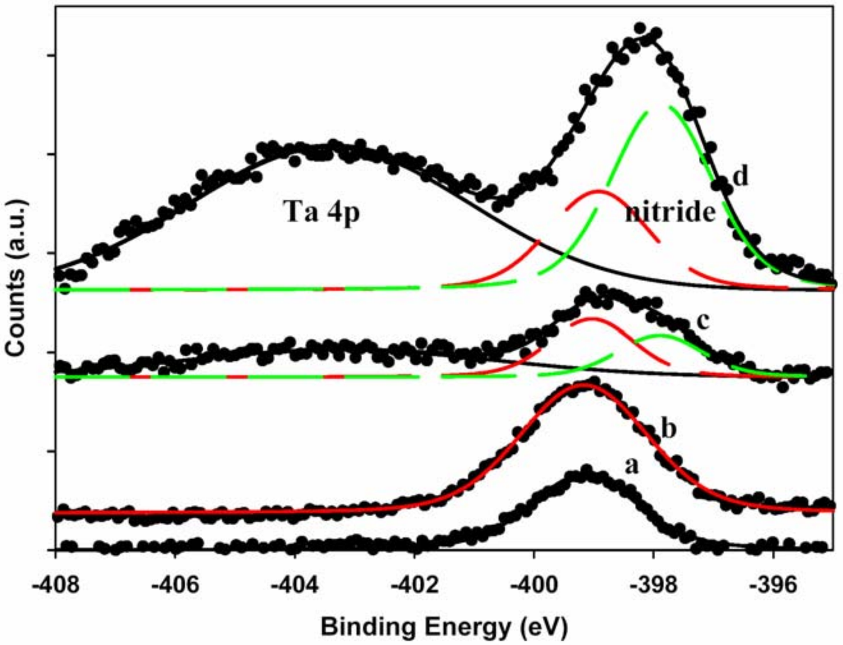

Fig. 3.9 **Effects of NH_x pretreatment on ALD growth on dense OSG. N1s spectra a) of clean surface; b) after pretreatments; c) after 30 ALD cycles on untreated film; d) after 30 ALD cycles on pretreated film.**

Table 3.4 showed the quantification of the surface chemical composition of low-κ films before and after plasma treatment. The escape depth of detected electrons was related to the exit angle through the equation $3\lambda\sin\theta/2$. Therefore the depth in the setup was about 5 nm for the exit angle of 30^0 and 10 nm for 90^0. The slightly different concentrations of C and O at the surface scan with 30° exit angle and the bulk scan with 90° exit angle were attributed to a thin overlayer of carbonaceous contaminants on the low-κ surface after the regular cleaning procedure in the loadlock. After atomic hydrogen pre-treatment to the dense OSG low-κ surface, a little bit of surface carbon was removed and surface homogeneity was improved. Pure atomic hydrogen did not seem to modify the film composition too much except certain surface cleaning. After additional amine radical and atomic hydrogen were both applied by cracking NH_3, the surface carbon concentration was further reduced from 21.2% to 16.0% and the surface nitrogen concentration was enriched from 4.0% to 7.0%, while the surface concentrations of O and Si remained around 44% and 31%, respectively. It suggested that amine radical and atomic hydrogen pre-treatment enabled carbon on the low-κ surface to be depleted and nitrogen to be enriched, i.e. methyl groups were replaced by amino groups at the surface region. The bonding energies for Si-O, Si-N, Si-H and $Si\text{-}CH_3$ were ~800 kJ/mol, ~470 kJ/mol, ~300kJ/mol and ~320kJ/mol, respectively [16] [17]. Formation of stable Si-N is more thermodynamically favored over Si-H and $Si\text{-}CH_3$, especially when the energetics of plasma facilitates the change of Gibbs free energy more negative.

Table 3.4 Evolution of surface chemical composition of dense OSG after pretreatment of plasma NH_3 and H_2.

	Pristine Film		After H		After H and NH_x (30^0)
	30^0	90^0	30^0	90^0	
O	42.7%	40.7%	44.1%	43.7%	44.1%
C	23.6%	25.0%	21.2%	21.0%	16.0%
Si	30.2%	30.7%	30.6%	31.1%	31.6%
N	3.4%	3.6%	4.0%	4.1%	7.0%

In order to distinguish the effects of atomic H and atomic NH_x, one OSG sample was treated by atomic NH_x only and the other was treated by atomic H and NH_x sequentially. ALD growth on these two samples was examined. XPS spectra of Ta4p and N1s are presented in Fig. 3.10. The Ta4p peak on the OSG without atomic H preclean was not noticeable while it was appreciable on the OSG with atomic H preclean. It was suspected that the enhancement effect by NH_x pretreatment was not fully appreciated because the contamination layer, rich in C and O, blocked the interaction between the incident NH_x radicals and surface methyl groups. As indicated by Table 3.4, the contamination layer consisted of carbon and oxygen and could be removed by atomic H. As a result, the fresh OSG surface would have been exposed after atomic H preclean.

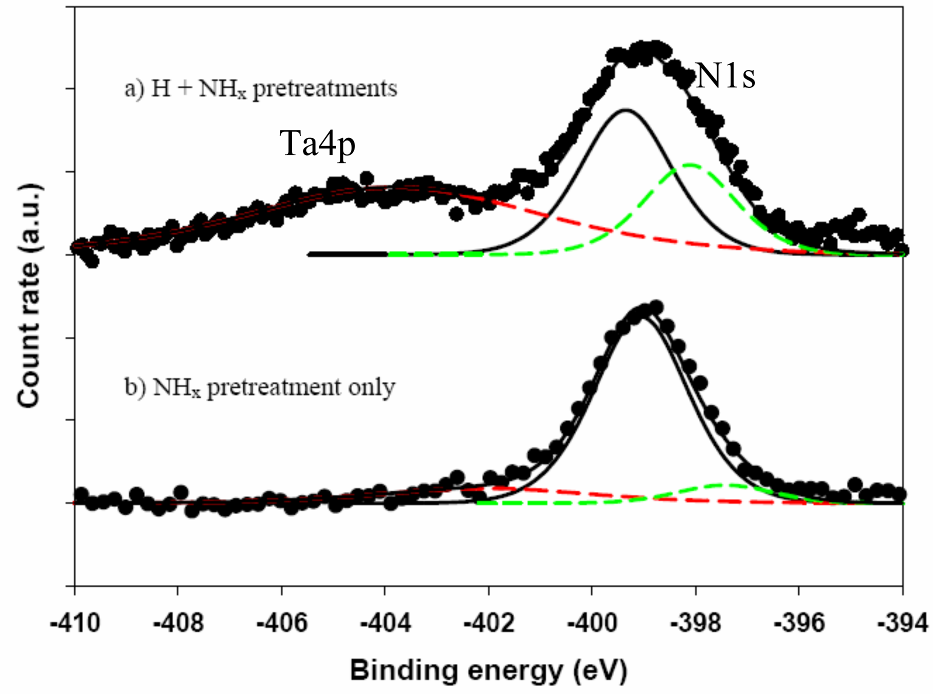

Fig. 3.10 **Ta4p and N1s peaks after the plasma pretreatment of (a) H, NH_x sequentially and (b) NH_x only.**

Fig. 3.11 (a) shows a TEM image of ALD Ta_3N_5 on a mesoporous OSG substrate pretreated with H and NH_x radical beams. Fig. 3.11 (b) shows the Fourier transformed micrograph of Ta_3N_5. The deposited Ta_3N_5 was confirmed to be amorphous as no bright spots in this reciprocal space, i.e. no lattice structures or crystalline structures in the real space, could be deduced from the Fourier transformed micrograph. Since Ta_3N_5 is amorphous and contains heavy atoms, metal Cr was deposited on the top surface to distinguish the layer of Ta_3N_5. Cr also protected the thin Ta_3N_5 from being damaged by the dicer cut or the FIB ion milling. The thickness of Ta_3N_5 was estimated to be around 10 nm. Although there was an intermixing region at the barrier/ low-κ interface due to precursor penetration, the film deposited appeared very dense, implying a good barrier property.

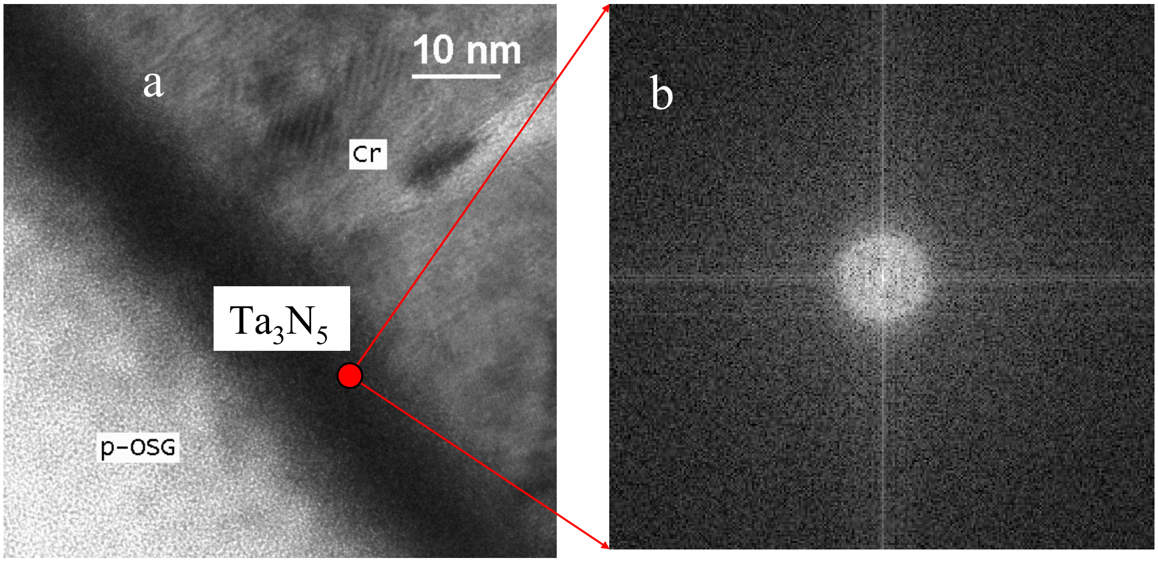

Fig. 3.11 **(a) TEM image of ALD Ta_3N_5 on p-OSG substrate; (b) Fourier transformed micrograph of Ta_3N_5.**

Theoretically speaking, atomic layer deposition (ALD) is a superconformal deposition technique which can provide uniform film coverage regardless of the physical contour of the substrate surface. This is because the chemisorption process in ALD is primarily controlled by the surface chemistry and the choice of precursor. Physical features or surface morphologies are not expected to play a role in controlling uniformity of the deposition. However, several practical factors can affect the conformality of ALD film coverage. First, a flow type reactor can not maintain a hydrostatic pressure inside the chamber; consequently, there is always certain directionality in precursor delivery. The directionality can be aggravated for high aspect ratio (AR) structures. Second, the dispersion of the precursor and the reagent may be different during the ALD cycle. Thus different areas in a high AR structure can be exposed to different amounts of precursor and reagent during deposition. In general, the bottom of a narrow and deep trench will have less exposure to precursor and reagent than the open field area. And third, when the precursor and regent molecules impinge onto the substrate surface, their sticking coefficient may depend on the inclination angle of the surface relative to the gas flow direction.

ALD deposition of Ta barrier onto OSG trenched structures with a line spacing of 0.250μm and an AR of 1:1 for 200 ALD cycles was examined by SEM. Conformal barrier coverage on the sidewall and bottom of the trench was observed, as indicated by the cross section SEM images in Fig. 3.12. A clear difference in the edge contrast was found. Without barrier deposition, the contour of the trench features was very dim. With the barrier deposition, the trench contour became very uniformly bright, probably due to the atomic number (Z) contrast effect and indicating good coverage of Ta_3N_5 barrier.

Interestingly, without the atomic hydrogen cleaning, only a very small amount of Ta_3N_5 barrier deposition was observed on the OSG surface. In general, the plasma treatment used for trench patterning can activate the OSG surface, which is similar to other surface activation treatments, such as the amine radical beam treatment. However, the plasma treatment will leave behind polymeric residues which have to be cleaned, for example, by using hydrogen as in this study, before full exposure of active surface groups for ALD nucleation [18].

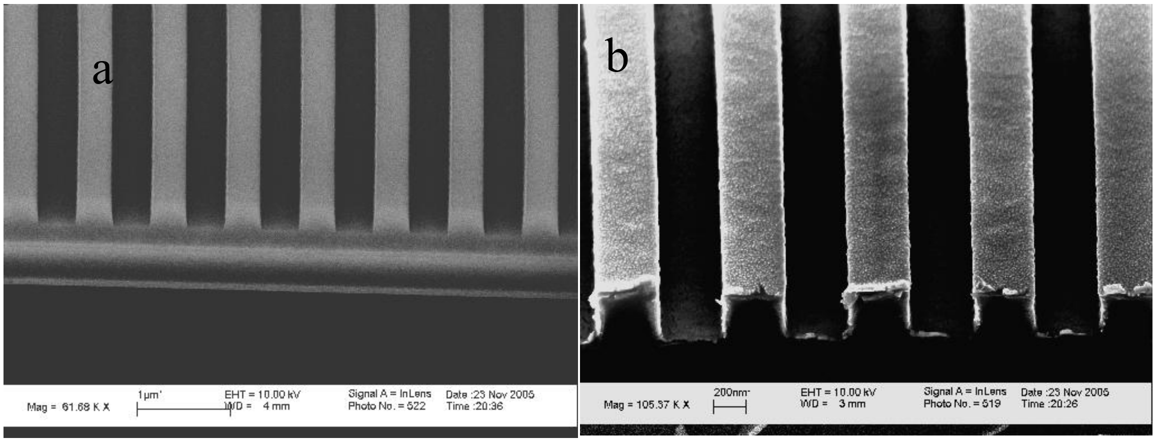

Fig. 3.12 SEM images of (a) the pristine trench structure; (b) the identical trench structure after 200 ALD cycles

3.4 Monte Carlo Simulation

As determined by the interaction strength between adatoms and the surface, i.e. the chemical potential, the growth of epitaxial thin films on a single surface can be divided into three types: Volmer-Weber (VW) growth, Frank-van der Merwe (FM) growth and Stranski-Krastanov growth. They are illustrated in Fig. 3.13. In the Volmer-Weber (VW) growth, the interactions between adatoms are stronger than those between the adatoms and the surface. It leads to the formation of 3D adatom clusters or islands. In Frank-van der Merwe (FM) growth, adatoms attach preferentially to surface sites in a chemical (such as ALD) or physical way (such as MBE), resulting in atomically smooth, fully formed layers. This two dimensional layer-by-layer growth indicates the formation of complete films prior to the growth of subsequent layers. In the Stranski-Krastanov growth, the layer-by-layer growth transits to the island growth at a critical layer thickness, which is dependent on the chemical and physical properties, such as surface energies and lattice parameters, of the substrate and the film. It is an intermediary process characterized by both 2D layer and 3D island growth [19].

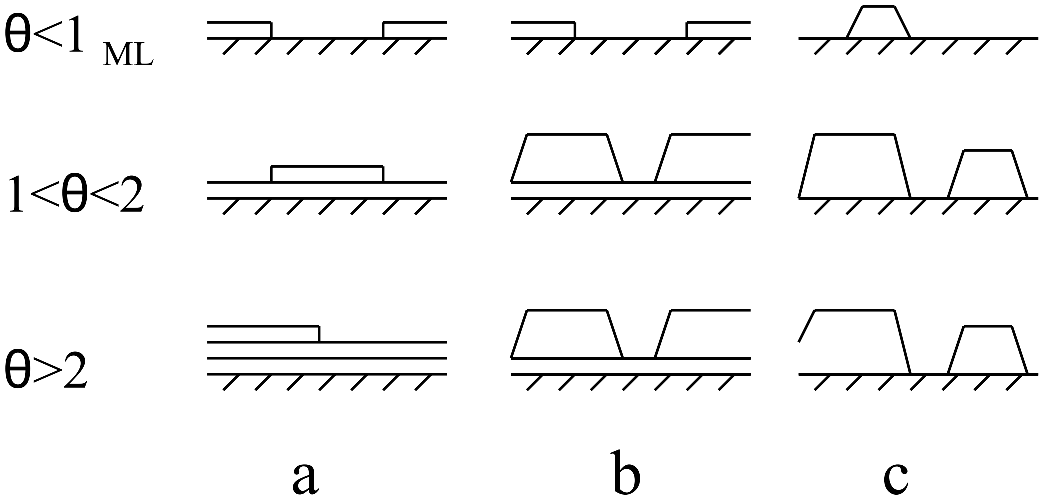

Fig. 3.13 Three types of growth modes: (a) Volmer-Weber (VW) growth (island formation); (b) Frank-van der Merwe (FM) growth (island formation); (c) Stranski-Krastanov growth (layer and island formation).

Fig. 3.14 shows the formation of contact angles when two surfaces meet. γ_S is the solid air surface tension; γ_F is the liquid air surface tension and γ_{SF} is the solid liquid surface tension. θ is the contact angle. Since the forces on the horizontal direction must be balanced, $\gamma_S = \gamma_{SF} + \gamma_F\cos\theta$. For the island growth, $0^0<\theta<90^0$, $\gamma_S < \gamma_{SF} + \gamma_F$, adatom cohesive force is stronger than surface adhesive force. For the layer by layer growth, $\theta \rightarrow 0^0$, $\gamma_S \gg \gamma_{SF} + \gamma_F$, surface adhesive force is stronger than adatom cohesive force [20].

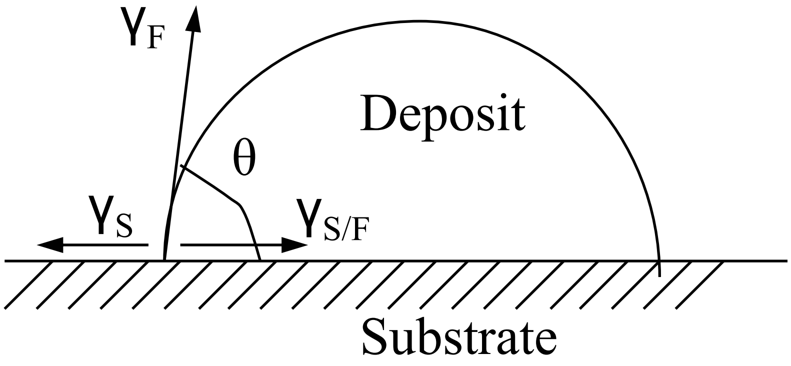

Fig. 3.14 Formation of contact angles at the interface.

Simulation of atomic layer deposition is complicated because it involves many simultaneous process steps. Generally speaking, at the atomic scale, atoms are deposited with a flux of F. They diffuse on the surface with a constant rate D. They may meet to form a dimmer or cluster, attach to existing islands, detach from island edges or diffuse along island edges. The incident atoms may be deposited on top of islands or re-evaporate. Finally, these nucleation and growth processes reach dynamic equilibrium [21].

Physically, the vapour deposition arrival rate $R = \frac{p}{\sqrt{2\pi mkT}}$, where p is the vapour pressure. Re-evaporation characterization time $\tau_a = \gamma^{-1}\exp(E_a / kT_s)$, where E_a is the activation energy of re-evaporation and T_s is the temperature of substrate. Surface diffusivity $D_s = \lambda^2 \gamma_{diff} = \lambda^2 \gamma_s \exp(-E_d / kT_s)$, where E_d is the activation energy of surface diffusion [22].

Therefore, there are four major parameters (λ, b, $P_{up/down}$ and P_{hop}) in kinetic Monte Carlo simulations. The adatom migration length λ is related to the coefficient of diffusion D and the flux intensity F through the equation λ^4=D/F; The parameter of lateral interaction b=exp (-E/kT); The parameter of interlayer diffusion P_{up} represents the probability of atom hops to the upper layer and P_{down} represents the probability of atom hops to the lower layer; Diffusion of hop probability to cross the step is represented by the factor P_{hop}=exp(-E_{st}/kT) [23] [24].

The major challenge and difficulty of Monte Carlo simulations lies in identifying which and how many microscopic processes need to be included into the simulation. A typical kinetic Monte Carlo simulation usually contains an updated list of all possible events that can occur and the rates for each event. Six steps are executed in one cycle of computation [25]:

1) Assume each event j has rate R_j;

2) Calculate total event rate $R_J = \Sigma R_j$;

3) Select event j to occur with probability $P_j = R_j/RT$;

4) Perform event j;

5) Update time t = t – ln(r)/RT where 0<r<1 is a uniform random number;

6) Go to 1) and repeat.

Here, a simple Monte Carlo simulation of the initial growth was carried out to illustrate the effect of surface activation on ALD growth. Since atomic layer deposition is a chemically dominant process, the surface diffusion was not considered in the simulation to simplify the problem. Fig. 3.15 is the flow chart of the Monte Carlo simulation program. It is a one dimension program written and debugged in Matlab software. Initially, a periodical 1D 100 (Columns) × 1 (Line) coordinate matrix was generated with 100 atom sites. For pristine OSG, only 10 out of the 100 sites, i.e. 10%, were randomly picked to be chemisorptive. The percentage of active sites was assumed to increase to 50% after plasma pre-treatment. Since a typical growth rate was 0.24 Å/cycle at higher temperature and 2.5Å was assumed to be the covalent radius of ALD Ta_3N_5, the reaction probability between $TaCl_5$ and NH_3 was estimated to be $0.24/2.5 \approx 10\%$. One $TaCl_5$ molecule consisted of a Ta atom at the centre surrounded by five chlorine atoms and one NH_3 molecule consisted of an N atom at the centre surrounded by three hydrogen atoms. In each cycle, $TaCl_5$ first adhered to the active sites through the combination of H and Cl and the by-product HCl was pumped away. Subsequently, NH_3 was adsorbed to $TaCl_5$ with a reaction probability of 10%. This iteration repeated until several cycles were completed. After several cycles, the matrix became 2 dimensional because of the incident atoms in $TaCl_5$ or NH_3. The matrix data were output into TXT files and then drawn by using one black dot to represent one atom.

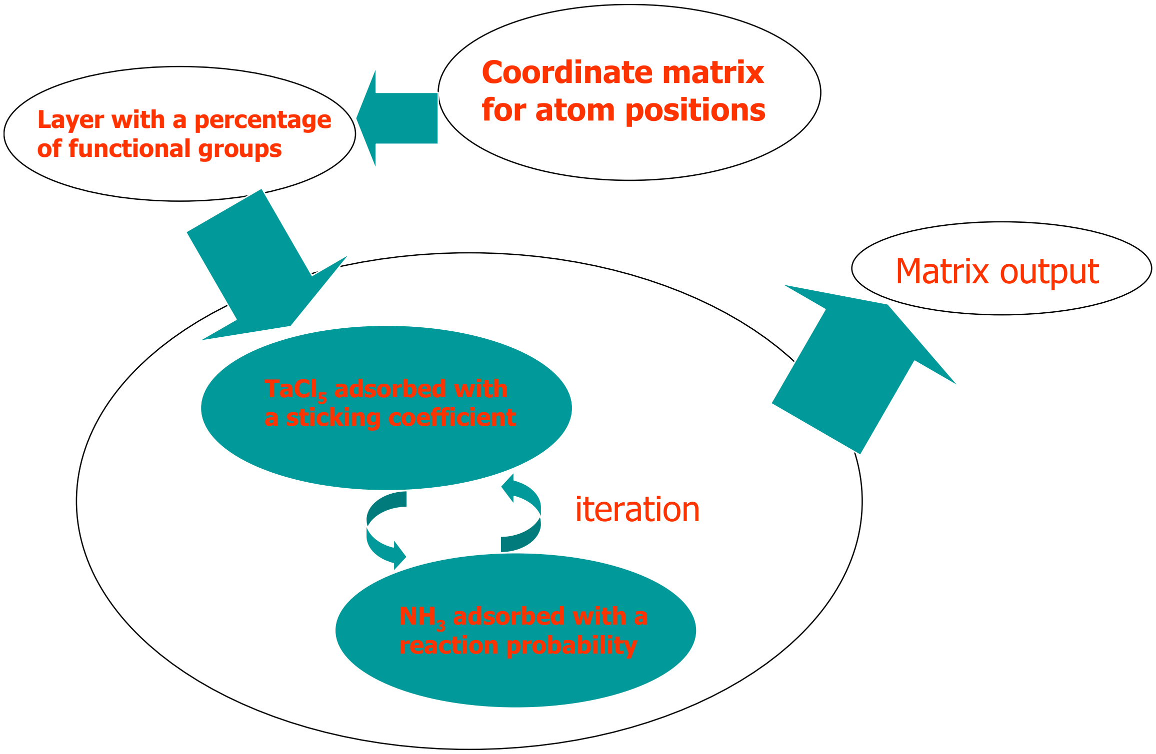

Fig. 3.15 Flow chart of the Monte Carlo simulation program.

Fig. 3.16 shows the formation of clusters on low-κ surfaces after 10 ALD cycles. If the coverage of initial surface functional groups was 10% as shown in (a) and (c), the island formation, i.e. Volmer-Weber (VW) growth of deposited films was clear, no matter what the reaction probability was. However, with the increase of the coverage of initial surface function groups from 10% to 50%, a more uniform and continuous film coverage resulted as shown in (b) and (d). In other words, substrate surface chemistry was very important for layer by layer Frank-van der Merwe (FM) growth. Surface activation was necessary if the pristine sample could not provide enough active sites. In addition, with enough surface activation and sufficient nucleation (50%), the film growth rate became faster when the reaction probability increased from 10% to 50%. The film growth rate strongly depended on the reaction probability, instead of the substrate chemistry.

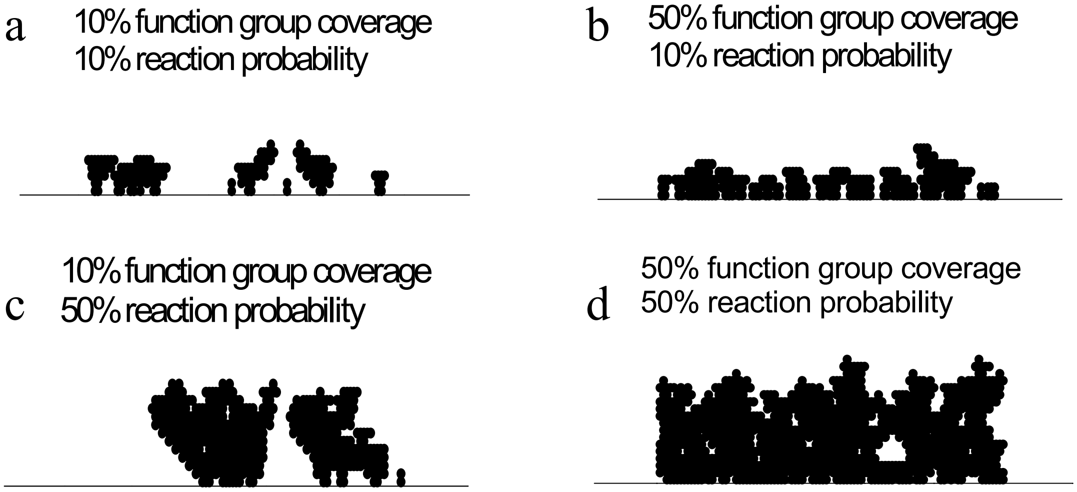

Fig. 3.16 Monte Carlo simulation of the effects of surface function groups and reaction probability on ALD growth.

The Monte Carlo simulations were later extended to a 2D case to compare the initial growth of ALD films on porous inactive surface with that on the activated surface. 2D 200 (Columns) × 100 (Lines) matrix was generated. A green dot, i.e. a molecule, occupied two points on the matrix network grid. The pores were assumed to be empty squares without any dots filled inside. They were randomly distributed on the low-κ material surface. The diameter of pore openings was assumed to be 2.5 times the molecule size, i.e. 5 points. Fig. 3.17 (a) shows 20 cycles of ALD growth on the pristine porous OSG, which was assumed to contain 10% active sites only. The pore openings in a sense could be treated as additional inactive areas. Under this condition, the low-κ material surface exposed to plasma was expanded and ALD nucleation on the sparsely distributed chemisorptive sites deeper into the pores became difficult. As a result, the large island growth mode and discontinuous initial coverage, i.e. Volmer-Weber (VW) growth mode, was observed. In order to seal the porous surface, it takes deposited molecules a long time to form clusters to eventually bridge the inactive areas. At the same time, although the pore openings are sealed, the rough surface due to the growth of islands on inadequately activated surface will influence the subsequent processes of PVD Cu seed and ECP Cu plating. Compared with Fig. 3.17 (a), Fig. 3.17 (b) shows identical 20 ALD cycles on activated OSG porous surface. To mimic the true situations in plasma pretreatment, only the sites at the surface down to 2 molecule sites were assumed to be activated while the rest of the positions inside the pores were still inactive regions. It was assumed that there were 50% reactive sites in the activated region while there were only 10% reactive sites in the inactivated region. After the identical 20 ALD cycles, the molecules adhered to the activated region faster. Therefore, in very few initial cycles, they bridged and sealed the pore openings. The subsequent deposition would be similar to the ALD deposition on dense OSG surface with enough reactive sites. Continuous and uniform films were grown on the surface.

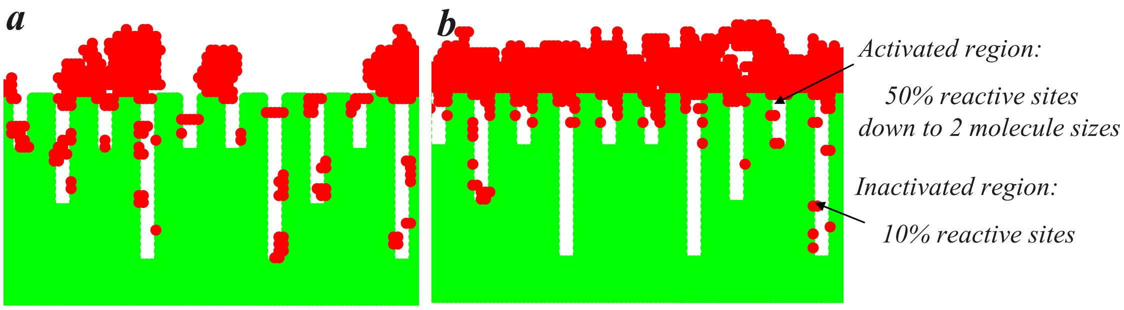

Fig. 3.17 Monte Carlo simulation of initial 20 ALD cycles growth on a) pristine porous OSG surface; b) activated porous OSG with 50% reactive sites.

IMEC performed similar Monte Carlo simulations to study the PVD TaN growth on porous HSQ and SiOCH. In their case, kinetic parameters were introduced since PVD was a surface diffusion dominant process. The activation energies of surface diffusion of HSQ and SiOCH were different. Lower diffusion material SiOCH promoted the formation of a thin smooth TaN for sealing the pores earlier than higher diffusion HSQ. The latter material resulted in the formation of a rough, deep penetration TaN barrier film. As a result, the minimal TaN thickness needed for complete sealing of the porous film and penetration depth increased with the surface diffusion of TaN on the porous film. It was further concluded that the minimal thickness for pore sealing linearly varied with the pore size and strongly depended on porosity if the pore sizes were relatively small. As pore sizes increased, the minimal thickness varied proportionally to the square of the pore size and had no strong relationship with porosity [26].

3.5 Summary

Atomic layer deposition is a self-limiting surface chemical process. The evolution of surface chemistry during ALD of Ta_3N_5 on low-κ materials was examined by *in-situ* XPS analysis. The ALD growth strongly depended on the surface chemistry of different low-κ materials. Ta_3N_5 grew on OSG through the formation of Ta-O bonds and on SiLK^{TM} though the mild coordination between Ta and the benzene ring. Methyl groups on typical low-κ materials are harmful for Ta halide precursor nucleation. Radical amine beam was capable of breaking methyl groups on the surface and replacing them with active NH_x sites to enhance ALD nucleation. Atomic hydrogen was found to clean the contamination of low-κ films and facilitate the surface activation. Monte Carlo simulation results showed that ALD film morphology was considerably affected by the surface functional group coverage. With sufficient surface activation, the film growth rate strongly depended on the reaction between $TaCl_5$ and NH_3. For porous low-κ materials, surface activation promoted the formation of a continuous and uniform thin film to seal the pores.

Chapter 4 Investigation of Plasma Damage of Low-κ Dielectric Surface

Plasma damage to low-κ dielectric materials was investigated from a mechanistic point of view. Low-κ dielectric films were treated by Ar, O_2, N_2, N_2/H_2, and H_2 plasmas in a standard reactive ion etching (RIE) chamber and the damage was characterized by angle resolved x-ray photoelectron spectroscopy (ARXPS), x-ray reflectivity (XRR), Fourier transform infrared spectroscopy (FTIR), and contact angle measurements. Both carbon depletion and surface densification were observed on the top surface of damaged low-κ materials while the bulk remained largely unaffected. Plasma damage was found to be a complicated phenomenon involving both chemical and physical effects, depending on chemical reactivity and the energy and mass of the plasma species. A downstream hybrid plasma source with separate ions and atomic radicals was employed to study their respective roles in the plasma damage process. Ions were found to play a more important role in the plasma damage process than neutrals. The dielectric constant of low-κ materials could increase up to 20% due to plasma damage and this was attributed to the removal of the methyl group, making the low-κ surface hydrophilic. Annealing was generally effective in driving off moisture uptake to restore the κ value but the recovery was less complete for higher energy plasmas. Quantum chemistry calculation confirmed that physisorbed water in low-κ materials induced the largest increase of dipole moments in comparison with changes of surface bonding configurations, and was primarily responsible for the increase of dielectric constant.

4.1 Experimental study of plasma damage

4.1.1 Introduction

As silicon technology advances beyond the 45nm node, ultra low-κ (ULK) dielectrics with porosity will be required for Cu interconnects [1] [2]. The mechanical and electrical properties of low-κ dielectrics tend to degrade when they are exposed to plasma processes during fabrication. The degradation will affect not only the chip performance but also the circuit reliability, and will be worsened with the incorporation of porosity in the ULK dielectrics [3]. Since plasma processing is commonly used for etching, stripping, and cleaning, this problem raises serious challenges to low-κ integration and has stimulated extensive interests recently in the study of plasma damage of ULK dielectrics [4].

Several recent papers have reported results from plasma damage studies on blanket and patterned low-κ dielectric materials [5] [6] [7] [8]. These studies have largely focused on two aspects of plasma damage to low-κ dielectric materials. The first is to search for effective plasmas to minimize the damage, such as the use of He or NH_3 plasma in the stripping process [9] [10], and the other is to recover the loss of dielectric constant with CH_4 plasma or silylation agents [11] [12] [13] [14].

Current organosilicate low-κ materials are based on methylsilsesquioxane (MSQ) formed with Si-O-Si backbone bonds and incorporating methyl groups and porosity to reduce the dielectric constant. The plasma damage of such materials will in general be a complex phenomenon depending on the process history and involving both chemical and physical interactions between the plasma species and the material constituents. Cui et al. proposed that film densification and material removal were two mutually limiting processes causing the thickness reduction of the SiCOH low-κ films during plasma treatment [10]. A few of other publications have discussed the mechanisms of how plasma interacts with low-κ dielectric surfaces leading to damage. This study investigates the mechanism of plasma damage to porous carbon-doped oxide (CDO) low-κ films. First the nature of damage by different plasma treatments including H_2, Ar and O_2 in a standard RIE chamber was analyzed using multiple analytical techniques including x-ray photoemission spectroscopy (XPS), Fourier transform IR spectroscopy (FTIR), and x-ray reflectivity (XRR). The results quantified the plasma effects on surface chemistry, composition, density, and dielectric constant of the low-κ film, and provided information to understand the chemical and physical effects from the plasma interaction with the low-κ materials. The damage mechanism was further examined using a downstream hybrid plasma source with a unique capability of separating ions from atomic radicals to investigate their respective roles in the damage process.

The dielectric constant of low-κ materials after plasma would generally increase depending on the specific plasma used. Reasons for dielectric constant increase are discussed and the effects for different plasmas are compared in this dissertation. Based on the observation of possible molecular interactions with plasma, quantum chemistry calculations were performed to examine their dipole contributions leading to the increase in the dielectric constant.

4.1.2 Damage by Ar, O_2, N_2/H_2, N_2, and H_2 plasma in RIE chamber

With standard PECVD equipment used in the semiconductor industry, the pristine CDO films were deposited with about 25% porosity to yield a dielectric constant of 2.5, film density of 1.25 g/cm^3, and refractive index at 633 nm of 1.33. Standard plasma processing was performed in an Oxford Plasmalab 80 Plus Reactive Ion Etching (RIE) chamber in the clean room. All the samples were processed at room temperature.

The film thickness and the refractive index at 633 nm were measured with a J. A. Woollam VASE Spectroscopic Ellipsometer 2000. The water contact angle was measured using a CA100 Ramé-Hart goniometer. Chemical bond structures were investigated with Magna 560 FTIR Spectrometer with an attenuated total reflectance (ATR) attachment. FTIR in the transmission mode was used to study the bond structures in the bulk of the film while FTIR in the ATR mode was used to determine the bond structure of the sample surface in contact with the ATR crystal. The surface roughness after plasma treatment was extracted from a 1×1 μm Atomic Force Microscopy image. The film density was determined by measuring x-ray reflectivity using an X'Pert MRD system. The dielectric constant at 1 MHz was obtained by measuring a metal-insulator-semiconductor structure using a HP 4194A Impedance Phase Analyzer.

Pristine CDO films were treated by different plasmas in the Oxford RIE chamber under an identical condition of 30 sccm, 30 mtorr, and 150 w for 20 min. The plasma excitation frequency was 13.56 MHz. The bias voltage was maintained between 360 V and 370 V for Ar, O_2, N_2, and N_2/H_2 plasmas except that the bias voltage to maintain H_2 plasma was around 300 V. The plasma damage was measured by XPS at a take-off angle of 30^0 to examine the changes in the elemental compositions of the low-κ surface. The relation between photoelectron sampling depth and the take-off angle can be expressed as $d \sim 3\lambda \sin\theta$ ($\lambda \sim 2$-4 nm) [15]. At a take-off angle of 30^0, the photoelectrons escaped from a sampling depth of about 5 nm beneath the damaged surface. The XPS results revealed that the surface carbon concentration was reduced due to the loss of the methyl group as a result of plasma interaction with the low-κ dielectric surface. As summarized in Table 4.1, the loss of the surface carbon concentration was the highest by the H_2 plasma, reducing it from the pristine surface of 12.6% to 1.25%. Thus the H_2 plasma was the most effective in removing carbon, i.e. methyl groups on the low-κ surface since it is the lightest and most chemically reactive. For the other plasmas, N_2, O_2, and Ar, the methyl loss was somewhat less, yielding a surface carbon concentration ranging from 1.93% to 2.41%. Accompanying the surface carbon loss, a shift in the binding energy of the C1s peak from the pristine 285.1eV was observed, which can be attributed to the incorporation of electronegative elements into low-κ dielectrics. Since, the more electronegative the element, the larger the shift, the biggest chemical shift of 0.9eV was found to be caused by the O_2 plasma, as expected. Interestingly, a change of the bonding configuration due to physical bombardment of heavy atoms/molecules could also contribute to the chemical shift, such as the increase of 0.5 eV of C1s observed after Ar plasma treatment. In a previous study, when physical bombardment induced amorphous or unbonded carbon atoms in the film, a shift of ~1 eV of the C1s peak was observed [16].

Table 4.1 Carbon composition and dielectric polarization of low-κ films after plasma damage. Samples were treated by H_2, N_2, N_2/H_2, O_2, Ar plasmas at 30 sccm, 30 mtorr for 20 min. in an Oxford RIE chamber.

	Carbon Peak Position (eV)	Surface carbon concentration	Water Contact Angle (^{0})
Pristine	285.1	12.6%	93
H_2	285.2	1.25%	85
N_2	285.8	1.93%	58
N_2/H_2	285.9	2.08%	60
O_2	286.0	2.41%	50
Ar	285.7	2.22%	62

The plasma damage was examined by FTIR and by measuring the water contact angle. The FTIR spectra of the low-κ surface after various plasma treatments are shown in Fig. 4.1. All the low-κ surfaces showed a reduction in the Si-CH_3 peak intensity at 1274 cm^{-1} due to the loss of the methyl group. This was accompanied by an increase of the Si-OH and H_2O peaks between 3200 and 3600 cm^{-1}, changing the surface to be hydrophilic. This result was consistent with the water contact angle measured, which exhibited a decrease after all plasma treatments. The amount of Si-OH after Ar plasma was the second smallest while the surface after O_2 plasma was the most hydrophilic, reducing its water contact angle to as low as 50^0. In contrast, the H_2 plasma tended to transform Si-CH_3 into Si-H, making the surface the least hydrophilic. In general, the low-κ surface after plasma treatment took up more moisture to cause an increase in dielectric constant. This effect will be discussed in a later section.

Interestingly, after H_2 plasma, the Si-O-Si peak intensity between 950 and 1250 cm^{-1} almost did not change at all, but the same peak was significantly modified by Ar plasma. Since this peak was associated with the Si-O-Si backbone structure of the low-κ materials, the result indicated a change of the structural bonding due to the physical bombardment of the plasma and the effect was higher for Ar than H_2. Nitrogen- or oxygen-containing plasmas also caused modifications of Si-O-Si backbone structures. In addition, it was worth noting that nitrogen-containing plasmas promoted the appearance of a wide peak between 1590 and 1625 cm^{-1} which was associated with the Si-NH_x and C=C bonds [17]. This can be attributed to the replacement of methyl groups by amine groups or the interaction of N or NH_x in the plasma with H in the methyl groups, providing unsaturated bonds to form C double bonds.

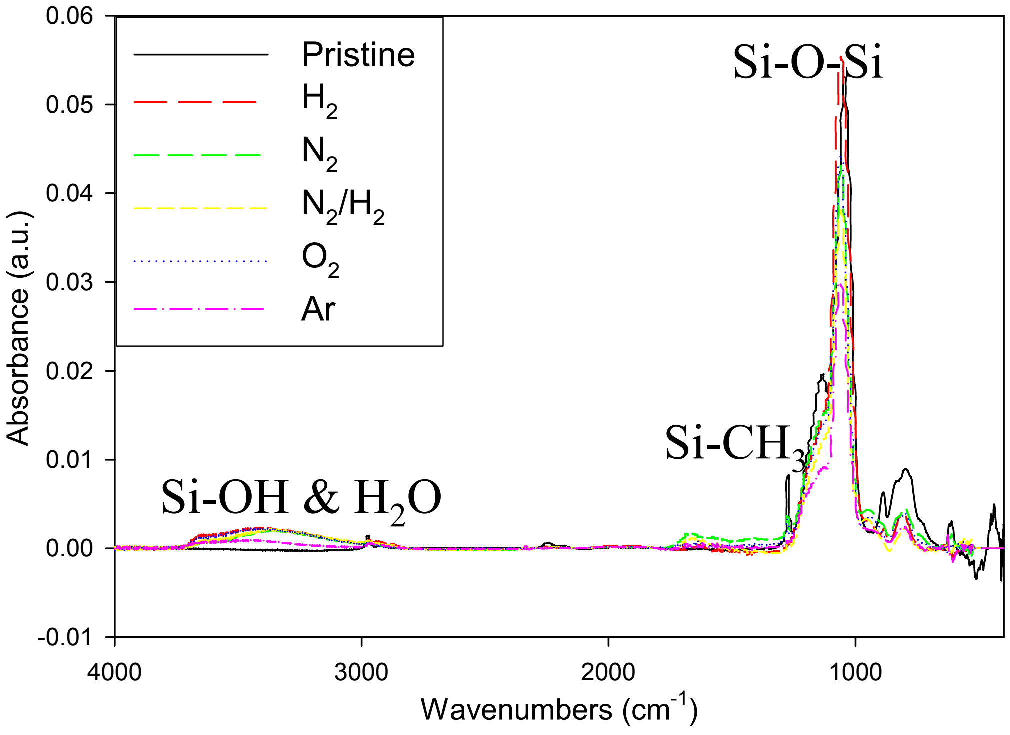

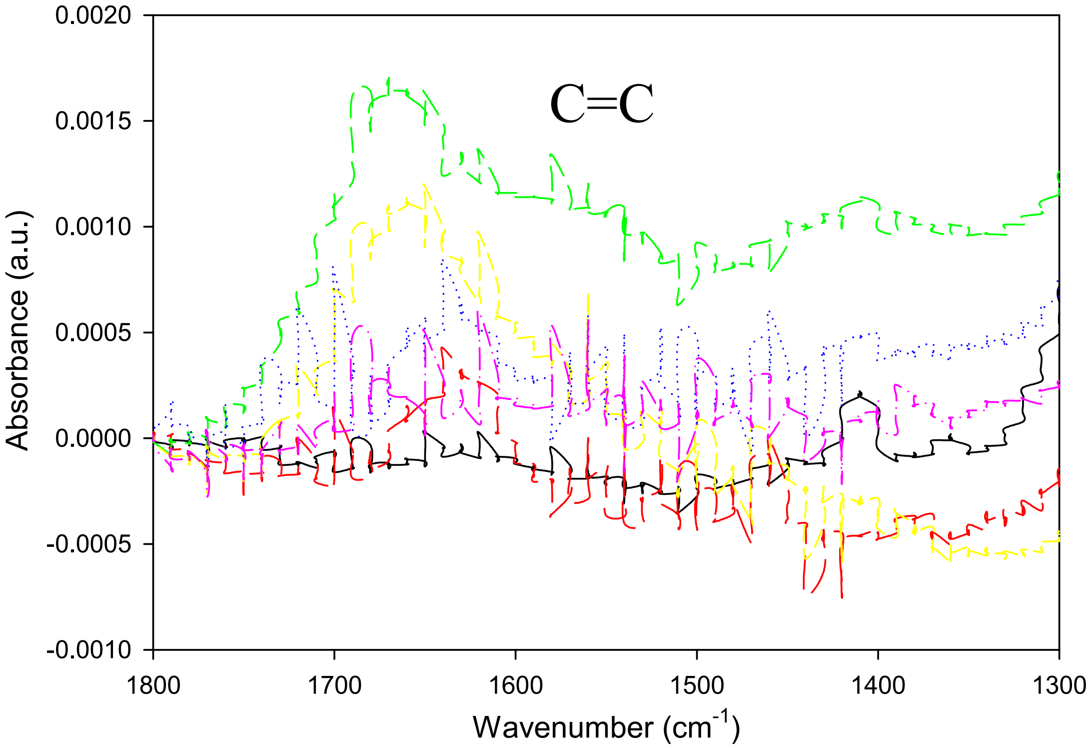

Fig. 4.1 **FTIR spectra of low-κ film after Ar, O_2, N_2, N_2/H_2, and H_2 plasma treatments at 30 sccm, 30 mtorr and 150 w for 20 min. in an Oxford RIE chamber.**

To delineate the chemical and physical nature of the plasma damage, x-ray reflectivity (XRR) measurements were made to investigate the density and thickness of the damaged surface after plasma treatments. A highly collimated and monochromatic x-ray beam was used in the XRR to probe the sample surface at a low angle (0^0-5^0) and the reflected beam intensity was analyzed. In a typical XRR curve, the critical angle provides a measure of the film density; the period of fringes measures the film thickness; and the slope measures the roughness [18]. In the current studies, the XRR curves were fit with X'Pert software to deduce the film density and thickness after various levels of plasma treatments in the Oxford RIE chamber. Fig. 4.2 shows the averaged density and thickness of the damaged layer by different plasma species. It revealed the formation of a thin but dense layer of 20~30 nm on the damaged CDO film surface while the bulk remained unaltered. This layer had a gradient in the density distribution with the highest density on the top. Overall, both the thickness and the density of the damaged layer depended on the mass of the plasma radicals. The density decreased from 2.16 g/cm^3 for Ar plasma to 1.79 g/cm^3 for H_2 plasma, while the thickness increased from 19.8 nm for Ar plasma to 33.8 nm for H_2 plasma. Note here that the bulk density unaffected by plasma was 1.25 g/cm^3. The density trend was consistent with a physical effect due to bombardment by atoms/molecules and was the most effective for the heaviest Ar plasma for densification of the low-κ film surface. The thickness trend was consistent with combined chemical and physical effects due to deeper penetration of the lightest H_2 plasma for modification of the material.

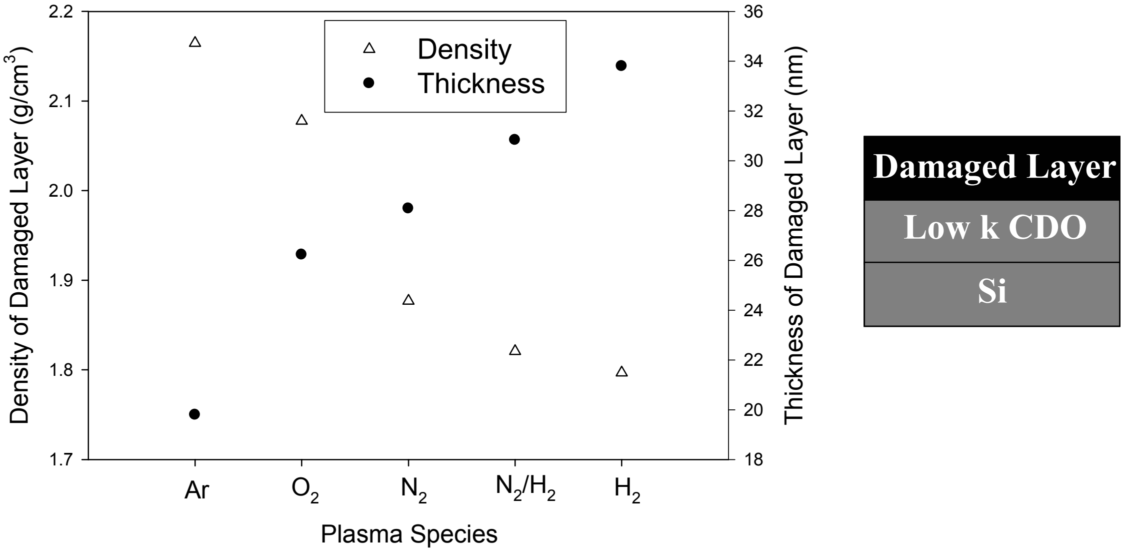

Fig. 4.2 **XRR fitted density and thickness results of the plasma damaged region. Samples were treated by Ar, O_2, N_2, N_2/H_2, and H_2 plasmas at 30 sccm, 30 mtorr and 150 W for 20 min. in an Oxford RIE chamber.**

Experiments were also performed for different plasma treatments at the bias power of 50 W and 200 W while keeping all the other process parameters the same. The normalized thickness changes (Ratio of the thickness between the damaged material and the pristine material) are plotted in Fig. 4.3. At a low bias power of 50 W, the plasma process was dominated by chemical reactions and the low-κ film was etched fastest by H_2 plasma with a thickness reduction of ~14%. In contrast, at 200 W, the low-κ film was etched fastest by Ar plasma with a thickness reduction of ~56% primarily by physical bombardment. This result together with the XRR data on surface densification showed that physical effects were dominated by plasmas with heavy molecular weights at high energy and dose, e.g. Ar and O_2, while chemical effects were dominated by plasmas with light molecular weights at low energy and dose, e.g. H_2 and N_2.

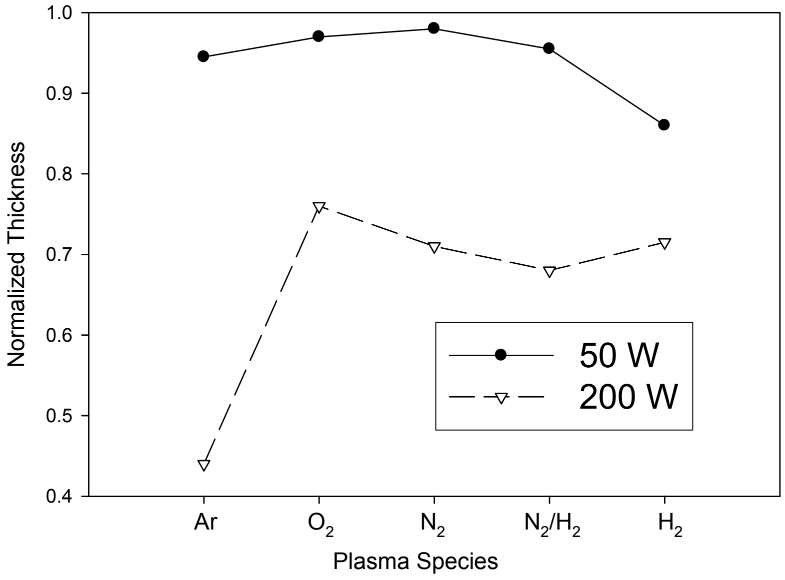

Fig. 4.3 **Normalized thicknesses of low-κ film after plasma treatments. Samples were treated by different plasmas at the bias power of 50 W and 200 W in an Oxford RIE chamber.**

Oxygen plasma damage to blanket low-κ materials can be mitigated by a mixture of certain gases [19] [20]. Helium was particularly interesting because it was light, inert, and had strong bond strength. Fig. 4.4 showed the measurement of C/Si and O/Si after identical He and O_2 RIE plasma treatment by XPS at the exit angle of 30^0 and 90^0. The experiments were performed on a type of JSR MSQ film. The difference of C/Si or O/Si between the exit angle of 30^0 and 90^0 was attributed to the gradient distribution of damage region and different scan depth at different exit angles. Compared with the pristine low-κ material, C/Si was almost halved after 15 sccm He plasma and was only one tenth after 15 sccm O_2 plasma. The oxygen incorporation on the low-κ surface after He plasma was also smaller than that after O_2 plasma. Therefore, it was expected that dilution with He plasma would be helpful to reduce plasma O_2 damage to low-κ materials.

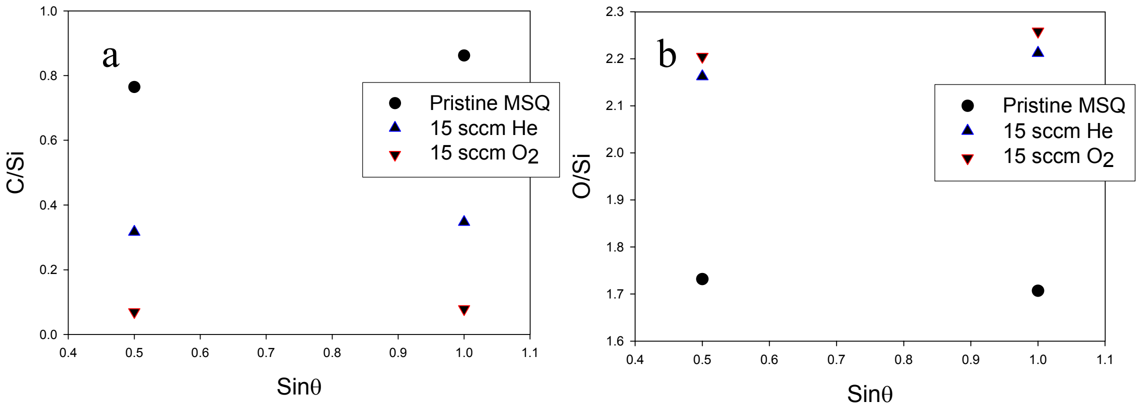

Fig. 4.4 **(a) C/Si and (b) O/Si obtained by XPS surface scan at the exit angle of 30^0 ($\sin30^0=0.5$) and 90^0 ($\sin90^0=1$) after 15 sccm He and 15 sccm O_2 plasma.**

The mixture effect of He into O_2 plasma was further examined by performing more experiments. They included treating the sample with a mixture of He and O_2 plasma and sequential treatment of the sample with He and O_2 plasma. Fig. 4.5 showed C/Si on the low-κ surface obtained by XPS. The addition of He into O_2 plasma lessened the O_2 plasma damage to low-κ materials as indicated by higher C/Si on low-κ surface, regardless of whether it was sequential treatment or mixture treatment. Interestingly, damage due to sequential plasma treatment was less than that due to mixture plasma treatment. It was especially true that, when the surface was pretreated with high power He, the subsequent oxygen plasma damage was much reduced as indicated by the very high C/Si in the diagram. It was suspected that the high power He pretreatment, i.e. a larger amount of He with possible higher energy, induced a certain extent of surface densification that blocked the penetration of oxygen plasma species [21].

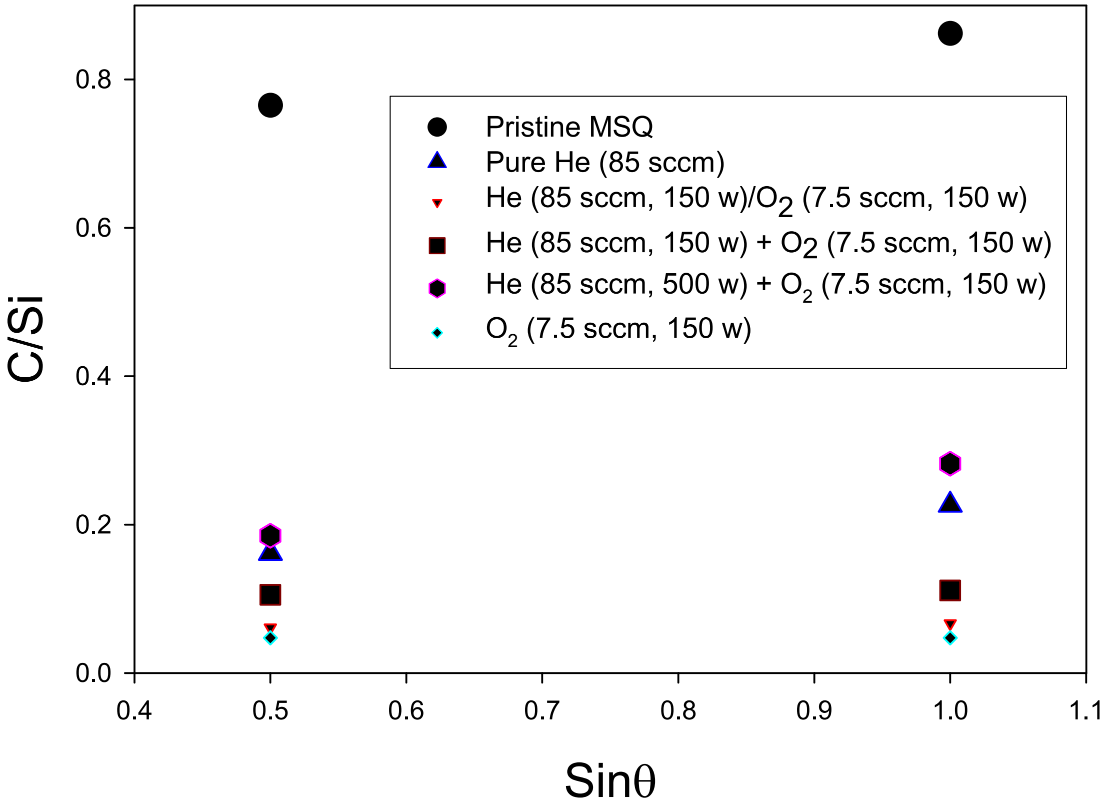

Fig. 4.5 **C/Si obtained by XPS surface scan at the exit angle of 30^0 ($\sin 30^0=0.5$) and 90^0 ($\sin 90^0=1$) after He plasma, O_2 plasma, their mixture and their sequential treatment.**

Surface roughness and the mechanical properties of MSQ also changed after the modification by He plasma and O_2 plasma. Surface roughness was measured by AFM that depicted the surface topography through the precise movement of a piezoelectric probe [22]. As indicated by Fig. 4.6, the surface roughness of the pristine MSQ was 0.97 nm. Due to the energetic bombardment, the surface roughness was reduced to 0.48 nm after He plasma treatment, and to 0.68 nm after oxygen plasma treatment. Oscillation of about ±0.01 nm was observed across the sample surface probably due to the nonuniformity of plasma damage or the limitations of AFM.

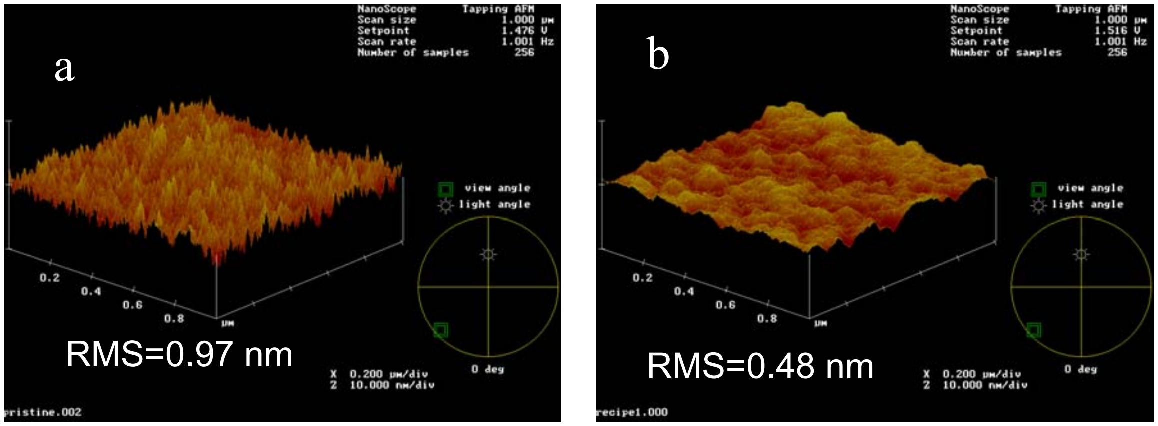

Fig. 4.6 **Surface roughness of (a) pristine MSQ and (b) surface after He plasma damage. (Courtesy of H. Shi)**

Mechanical properties of low-κ materials were characterized by nanoindentation. A hard Berkovich tip with three-sided pyramid geometry and known mechanical properties (e.g. Si or diamond) was pressed into the sample. With the increase of load placed on the indenter tip, a load-displacement curve was obtained to extract mechanical properties. The slope of the unloading curve dP/dh, a combinative contribution from the tested material and indenter, is related to stiffness of the contact, which can be used to calculate the Young's modulus [23]. Fig. 4.7 showed the load-displacement curve of pristine MSQ and MSQ damaged by the mixture of plasma He and O_2. Based on this curve, the Young's modulus of pristine MSQ was extracted to be 2.0 GPa but it increased to 2.6 GPa after plasma damage. The increase of Young's modulus of low-κ materials after plasma damage corresponded well with the increased network structure previously observed by FTIR and the increased surface density by XRR. The mechanical improvement is attributed to chemical bonds, not to van der Waals force. The weak H-Si-O or CH_3-Si-O bonds were transformed to strong O-Si-O or C-Si-O bonds in the plasma damage process. [24]

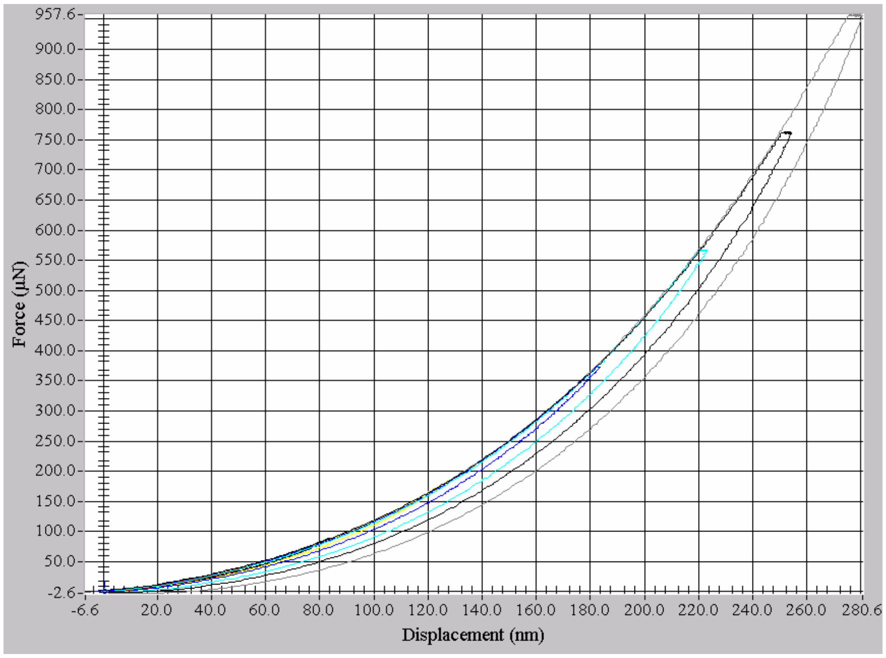

Fig. 4.7 **Load displacement curve of nanoindentation test on pristine and He/O_2 plasma damaged surface. (Courtesy of B. Li, et al)**

4.1.3 Damage by NH_3, Ar, He and O_2 plasma in a downstream plasma process

The downstream/remote plasma studies were performed in an UHV system consisting of a plasma process chamber connected to an XPS analysis chamber via a loadlock as shown in Fig. 2.1. Downstream plasma such as NH_3 was generated by cracking NH_3 gas molecules with 2.45 GHz electron cyclotron resonance (ECR) inside an Oxford Scientific mini atom/ion hybrid source. The source was mounted on the plasma process chamber and directed to the sample surface at an angle of about 40 degrees from a distance of about 10 cm. The substrate was not biased during the plasma processing. The schematic diagram of the plasma source was given in Fig. 2.2. The beam density at the sample surface was estimated to be of the order of 10^{12} atoms/ $(cm^2 \cdot s)$. The plasma chamber pressure was typically maintained at 1.2 mtorr during processing. At any point during processing, the sample could be directly transferred from the plasma chamber to the analysis chamber for *in-situ* XPS analysis without exposing to air and contaminants. Samples were stored in a Labconco vacuum desiccator after analysis.

The XPS experiment has been described in detail in Chapter 2. The base pressure of the XPS UHV chamber typically reached 2×10^{-9} torr. A nonmonochromatized Al kα x-ray source was used to generate photoelectrons, which were analyzed using a Leybold hemisphere analyzer operating at 38.45eV pass energy. A linear background subtraction was used for the C1s spectra and the Shirley background subtraction was applied to other peaks. XPS depth profiling was performed after plasma treatment in a PHI 5700 XPS system equipped with dual Mg X-ray and Al X-ray source. The photoelectrons emitting from the sample surface were detected at an exit angle of 45^0. The Ar ion sputtering rate was calibrated to be 20 nm/min. for the CDO film.

Plasma damage of the low-κ surface was studied using the downstream hybrid source. Experiments were performed at both hybrid and radical/atom mode in order to evaluate the respective roles of ions and atoms in the plasma damage process. In the following, the term hybrid or plasma beam refers to a mixture of ions and neutral species, while the term radical beam refers to only the neutral species. The process parameters such as plasma energy, plasma species, processing pressure, and substrate temperature could be individually controlled. Three types of plasmas, NH_3, Ar, and He, were chosen to study the chemical and physical effects of plasma damage on low-κ dielectrics. The extent of plasma damage was also correlated with the process parameters. In general, the damage was observed to be increased with the increase of ion energy, process time, and substrate temperature. In the investigation of these parameters, the parameter was varied one at a time, while keeping the other parameters constant so that their effects could be clearly separated out.

Summarized in Table 4.2 are the surface roughness, FTIR/ATR bond intensity ratios, water contact angles, and dielectric constants of CDO films after downstream NH_3, Ar, and He plasmas treatment. At 100eV, the low energy plasma treatment had negligible effects on surface roughness and bulk $Si\text{-}CH_3$ concentrations as seen from the FTIR $Si\text{-}CH_3/Si\text{-}O\text{-}Si$ ratios. As analyzed by ATR, the $Si\text{-}CH_3$ bonds on the low-κ surface were all reduced by downstream plasmas, leading to a reduction in the water contact angle. The water contact angle and thus the moisture uptake were the most affected by NH_3 plasma. The reason for this result will be discussed in the next paragraph. Interestingly, the Si-

CH_3 bonds on the low-κ surface were most severely broken by Ar plasma as reflected by its ATR ratio to the Si-O-Si bonds, which was reduced from 0.0155 to 0.0127. However, the water contact angle and the Si-OH concentration after Ar plasma were smaller than that after He plasma treatment. This suggests that some surface densification due to Ar bombardment retarded moisture penetration. This densification can be related to the modification of pore density and pore interconnection in the top surface. It was reported that the low-κ material after Ar plasma showed a 4.4% reduction in open porosity and a 2.2% reduction in the total porosity compared with that after O_2 plasma. This could result in the delayed absorption or diffusion of moisture in the low-κ film [25]. Compared with the dielectric constant of 2.5 of the pristine material, the dielectric constant after plasma damage increased to 2.9-3.0, indicating considerable damage and moisture penetration in the low-κ film.

Table 4.2 Property of the low-κ film after 100 eV NH_3, Ar and He downstream plasma treatments at 1 mtorr for 15 min.

Sample condition	Pristine sample	100 eV hybrid He	100 eV hybrid NH_3	100 eV hybrid Ar
Roughness (nm)	0.327±0.021	0.506±0.081	0.320±0.021	0.296±0.044
ATR Si-CH_3/Si-O-Si	0.0155	0.0154	0.0135	0.0127
FTIR Si-CH_3/Si-O-Si	0.018	0.020	0.016	0.016
FTIR Si-OH/Si-O-Si	0.022	0.055	0.077	0.037
Contact Angle (^{0})	93	86	46	63
Dielectric Constant	2.50±0.03	2.91±0.01	2.91±0.08	3.00±0.07

Compared with Ar and O_2 plasmas, the NH_3 plasma seemed to cause less damage to low-κ materials, especially when used in the downstream mode. This suggests a possibility that downstream NH_3 plasma might be used in the photoresist stripping process [26]. The variation in the surface composition during NH_3 plasma treatment is shown in Figure 4.8 where the carbon concentration was found to decrease due to the removal of methyl groups which were replaced by the NH_x groups during plasma treatment. As expected, the binding energy of the carbon increased due to the incorporation of the electronegative nitrogen. The polar groups of NH_x made the surface hydrophilic leading to moisture uptake and a decrease in the water contact angle, as observed. Although the downstream plasma reaching the substrate was very weak, a gradient in the carbon depletion and a nitrogen penetration layer were found by XPS depth profiling as shown in Fig. 4.9. Based on the Ar sputtering rate of 20 nm/min., the range of carbon depletion and nitrogen penetration was estimated to be about 20 nm. Beyond this range, the carbon concentration became level with no nitrogen in presence, indicating that the damage caused by downstream NH_3 plasma treatment was restricted to near the sample surface with little effect on the bulk chemistry. TEM images in Fig. 4.10 confirmed this conclusion. Here, low-κ surfaces were coated with around 1 micron photoresist to prevent samples from being damaged by FIB or dicer cut during TEM sample preparation. The interface between photoresist and pristine low-κ surface was clear initially, but after damage, it appeared blurred due to the occurrence of plasma damage. This damaged region was estimated to be around 16 nm, close to 20 nm obtained from XPS depth profiling.

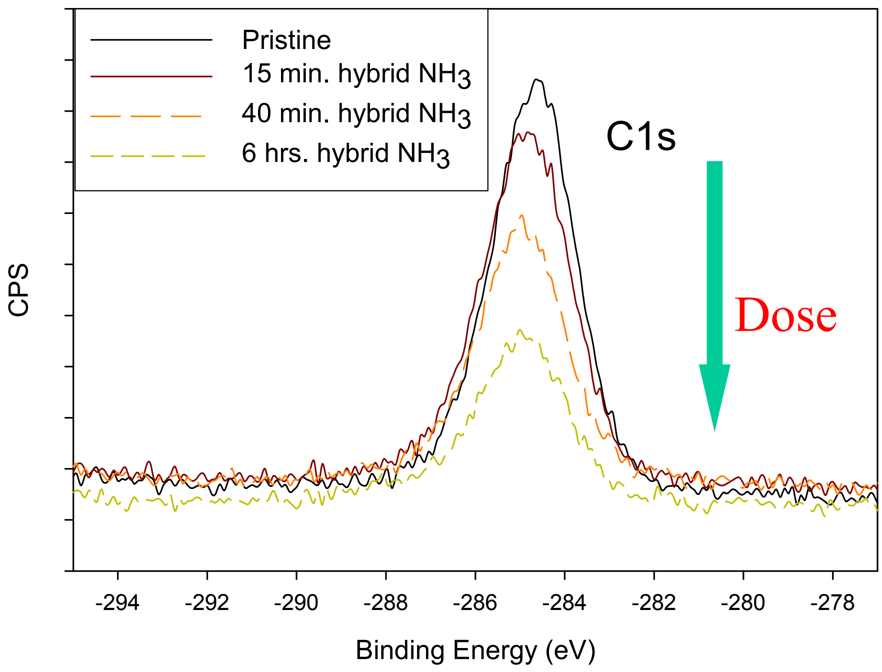

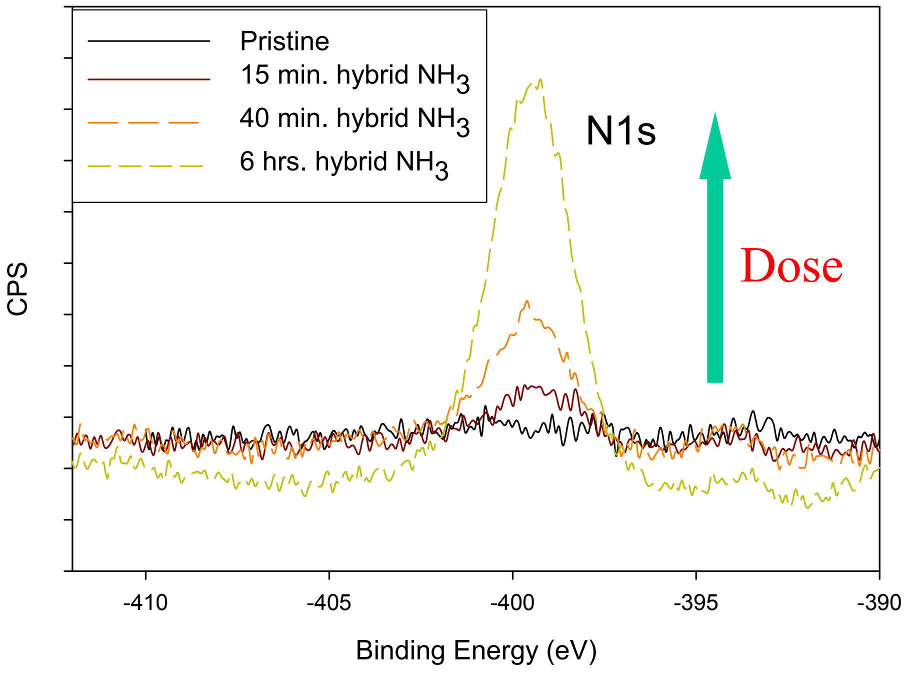

Fig. 4.8 **Evolution of the surface elemental concentration with plasma dosage. Samples were treated by downstream NH_3 plasma for 15 min., 40 min. and 6 hours respectively.**

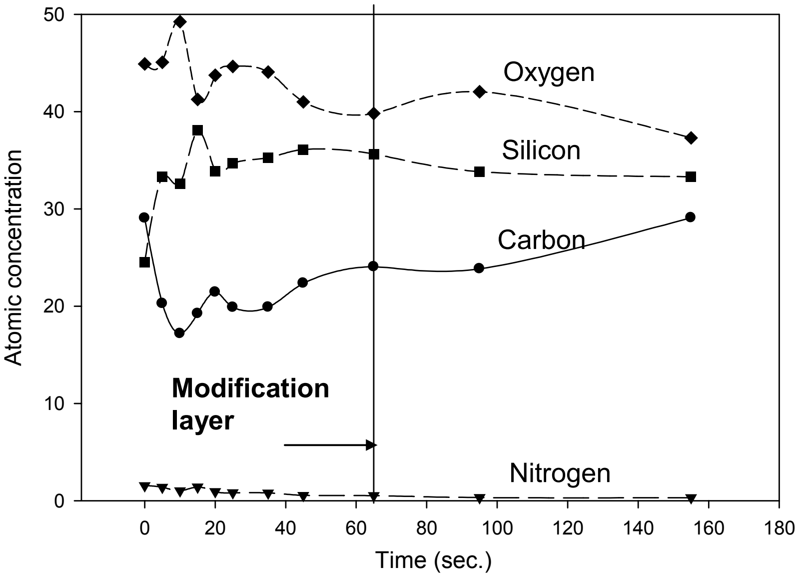

Fig. 4.9 XPS depth profiling of the low-κ dielectric film damaged by a 400 eV downstream NH_3 plasma at 1 mtorr for 6 hours.

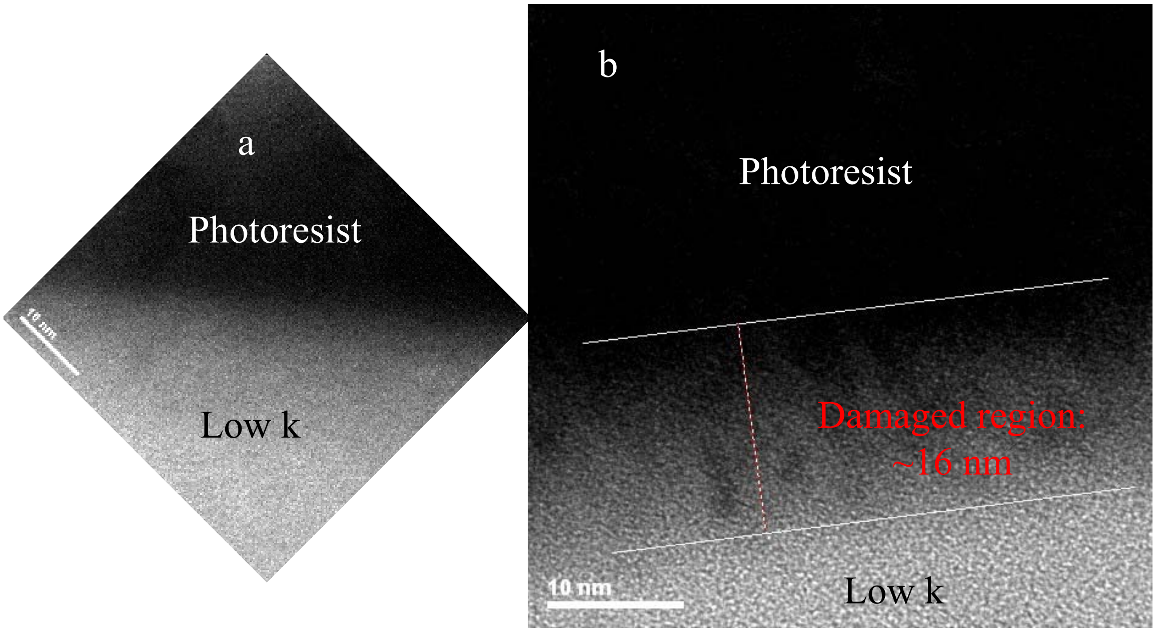

Fig. 4.10 High resolution TEM images of (a) Pristine CDO; (b) CDO damaged by a 400 eV downstream NH_3 plasma at 1 mtorr for 6 hours. Low-κ surfaces were coated with photoresist to prevent samples from being damaged during TEM sample preparation (Courtesy of H. Shi).

Differential FTIR was used to probe the change of bonding characteristics by downstream NH_3 plasma. As shown in Figure 4.11 (a), the differential spectra obtained by subtracting FTIR spectra of the pristine sample showed an increase in Si-OH concentration between 3200 and 3600 cm^{-1}. This indicated that NH_3 plasma transformed the hydrophobic pristine film to become hydrophilic. In Fig. 4.11 (b), the differential spectra revealed a decrease of Si-CH_3 at 1274 cm^{-1} with corresponding changes in the Si-O-Si bonds. In general, the Si-O-Si bonding configurations in MSQ low-κ dielectrics can be deconvoluted into three types: the network structure with a bonding angle of 140^0 at around 1063 cm^{-1}, the suboxide structure of less than 140^0 at around 1023 cm^{-1} and the cage structure of 150^0 at around 1135 cm^{-1} [27]. The differential FTIR spectra in Fig. 4.11 (b) showed an increase of the suboxide bonds with corresponding decreases in the cage and network structures. This indicated that plasma damage not only affected the surface bonding but also induceed structural disorder into the Si-O-Si backbone bonds.

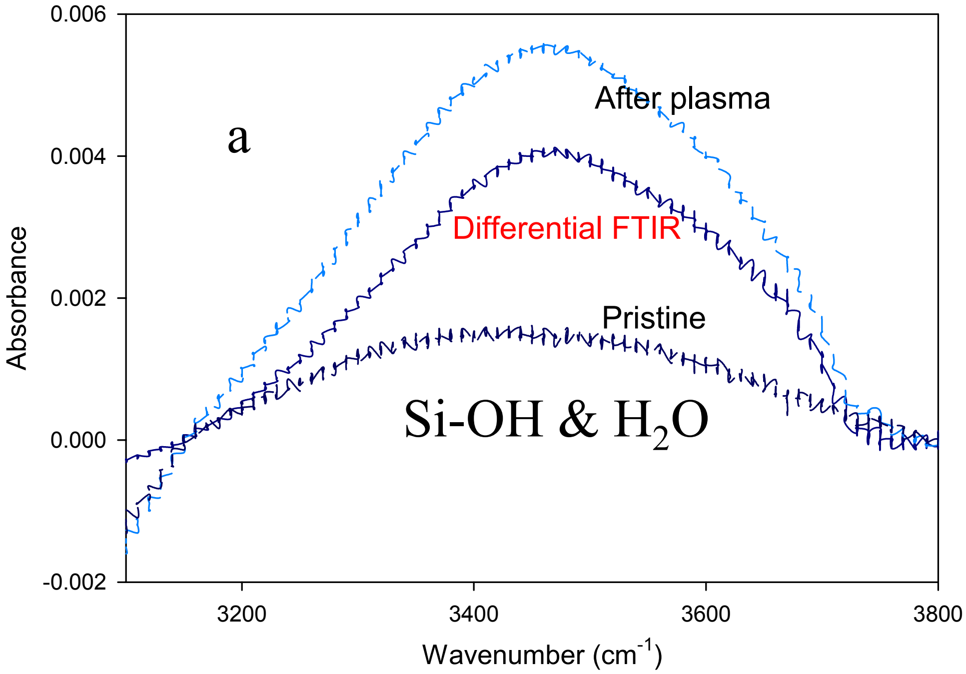

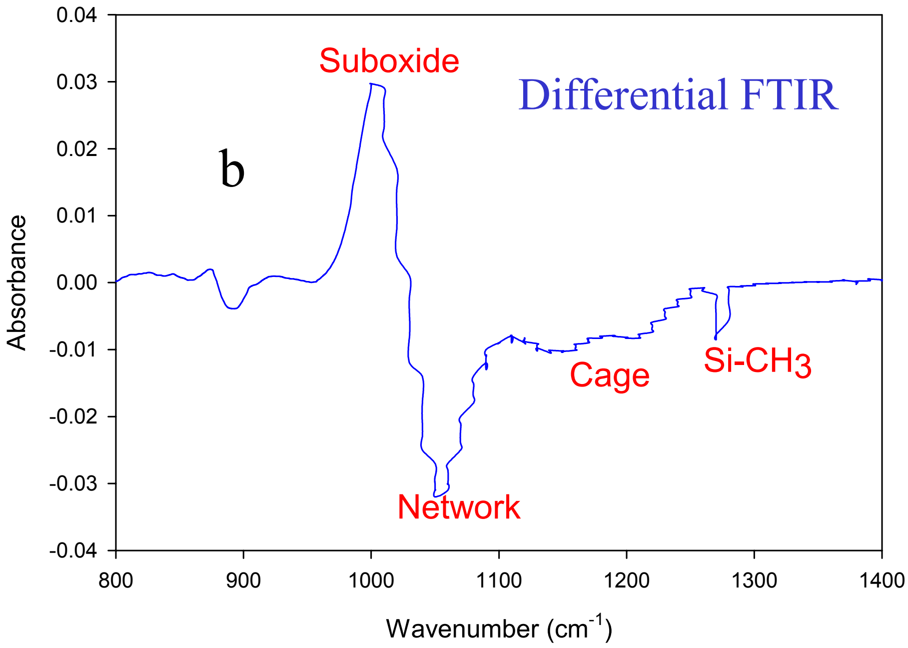

Fig. 4.11 **(a) FTIR and differential FTIR spectra show the increase of Si-OH and moisture uptake in the low-κ sample after NH_3 plasma. (b) Differential FTIR spectra show changes of Si-O-Si (suboxide, network and cage) and $Si\text{-}CH_3$ after NH_3 plasma treatment. Samples were treated by 400eV NH_3 plasma at 1 mtorr for 15 min..**

The results in Fig. 4.12 showed that with the same plasma dosage, the reactive NH_3 beam induced more carbon loss than the inert He. In addition, hybrid beams caused significantly more carbon loss than radical beams, due to the presence of ions in hybrid beams. The ions at metastable states accelerated the loss of the methyl groups because the energetics of the reaction helped to overcome the reaction barrier, increase the reaction probability of the neutral atoms/radicals, and facilitate the generation of reaction byproducts. The synergistic effects of ions and radicals on the etching of materials are well documented in the literature [28] [29]. It is therefore understandable that the ions and radicals played key, yet different, roles in modifying the composition of materials too [30].

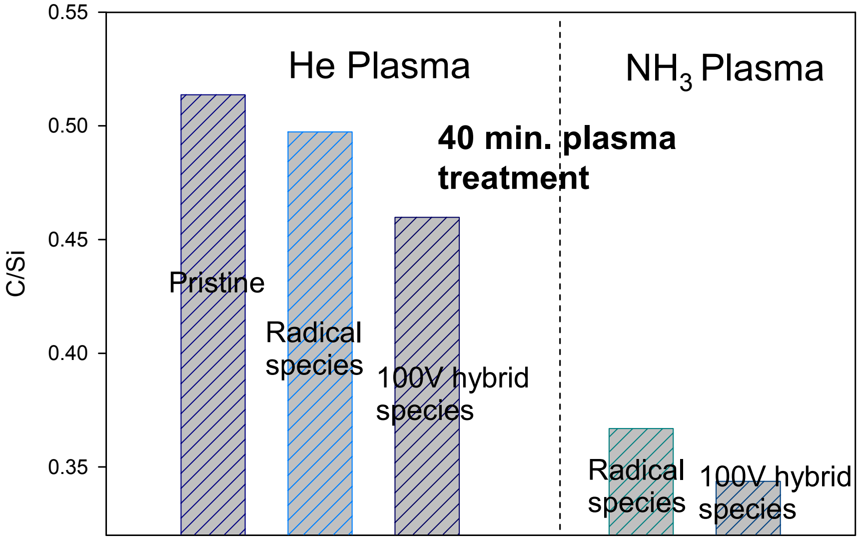

Fig. 4.12 **Ratios of C/Si within 5 nm at top of the low-κ film after He and NH_3 plasma treatment at 1 mtorr for 40 min.. Hybrid species include both ions and neutrals where the ion energy was 100eV and the radical species consist of neutrals only.**

The extent of plasma damage varied with not only the applied plasma species but also the category of low-κ materials. The composition and properties of κ=2.3 and κ=2.5 low-κ materials are compared in Table 4.3. The characterization of the downstream O_2 plasma damage to κ=2.3 and κ=2.5 low-κ materials is provided in Table 4.4. In general, the κ=2.3 ULK material incorporates higher carbon (C/Si ~ 0.47), more methyl groups, and more porosity (~30%) than κ=2.5 low-κ material. After downstream O_2 plasma damage, the change of C/Si, Si-CH_3/Si-O, Si-OH/Si-O, thickness, refractive index, and water contact angle on κ=2.3 ULK followed a trend similar to κ=2.5 low-κ material. As expected, the hybrid O_2 plasma treatment produced more damage than radical O_2 plasma. They all caused increase of Si-OH/Si-O, and refractive index and decrease of C/Si, Si-

CH_3/Si-O, thickness, and water contact angle. However, under the identical plasma treatment, either with hybrid O_2 or radical O_2, the ultra low-κ material with κ=2.3 exhibited more damage. That is to say, increase of Si-OH/Si-O and refractive index and decrease of C/Si, Si-CH_3/Si-O, thickness, and water contact angle were more significant after O_2 plasma treatment to κ=2.3 material, probably because the higher porosity in this material facilitated easier penetration of plasma species or enhanced the exposure of low-κ surfaces to plasma species. This enhancement exacerbated the plasma damage to porous low-κ materials.

Table 4.3 Characterization of κ=2.5 and κ=2.3 low-κ materials.

Low k film	C/Si	Si-CH_3/Si-O	Si-OH/Si-O	Thickness (Å)	Porosity	Refractive Index	Water contact angle (^{0})
κ=2.5	0.42	0.24	0	~950	25%	1.336	87.3
κ=2.3	0.47	0.27	0	~950	30%	1.319	90.7

Table 4.4 Comparison of hybrid and radical O_2 plasma damage to κ=2.5 and κ=2.3 low-κ materials.

	Plasma	Δ C/Si	Δ Si-CH_3/Si-O	Δ Si-OH/Si-O	Δ Thickness (Å)	Δ Refractive Index	Δ Water contact angle (^{0})
κ=2.5	Radical O_2	-0.037	-3.7e-3	0.022	-22.6	+0.11	-18.8
	Hybrid O_2	-0.110	-5.7e-3	0.023	-34.7	+0.11	-29.8
κ=2.3	Radical O_2	-0.051	-7.6e-3	0.022	-30.6	+0.11	-24.7
	Hybrid O_2	-0.152	-9.3e-3	0.024	-60.1	+0.10	-35.0

4.2 Mechanism of plasma damage

4.2.1 Impact of water absorption

Moisture uptake caused by plasma damage can result from two sources. First, plasma bombardment removes the weakly bonded methyl groups creating dangling bonds that can absorb water by forming Si-OH bonds. Second, the incorporated polar function groups such as $–NH_x$ can absorb moisture by forming hydrogen bonds [31]. Considering the high dielectric constant of water, around 78, a small amount of water incorporation may induce a large increase of the dielectric constant of the whole film.

To experimentally study the moisture effect on the dielectric constant, a heating stage was added to the Woollam Ellipsometer to monitor the refractive index during annealing. The dielectric constant can be directly related to the refractive index as $\varepsilon(\lambda)=n(\lambda)^2+\kappa(\lambda)^2$, where ε is the relative dielectric constant; n is the real part of the refractive index; κ is the imaginary part of the refractive index (extinction factor) and λ is the wavelength of the light source. The stage provided a clean and dry nitrogen environment to measure the refractive index during in-situ heating. Low-κ samples were separately treated with downstream plasmas of 600 eV hybrid He, 50 eV hybrid NH_3, and 400 eV hybrid Ar. After one hour of heating, their refractive indices at 633 nm were all reduced (Fig. 4.13). The reduction was most significant for the 50 eV hybrid NH_3 treated sample; from 1.44 to 1.36, close to that of the pristine sample. This suggested that κ was nearly fully recovered. The dielectric recovery for the higher energy He and Ar plasmas of 400 eV or 600 eV, respectively was less complete, particularly for the 600eV plasma.

As discussed already, energetic ions could alter Si-O-Si backbone bonds, making difficult the full recovery of the refractive index or the dielectric constant by pure heating.

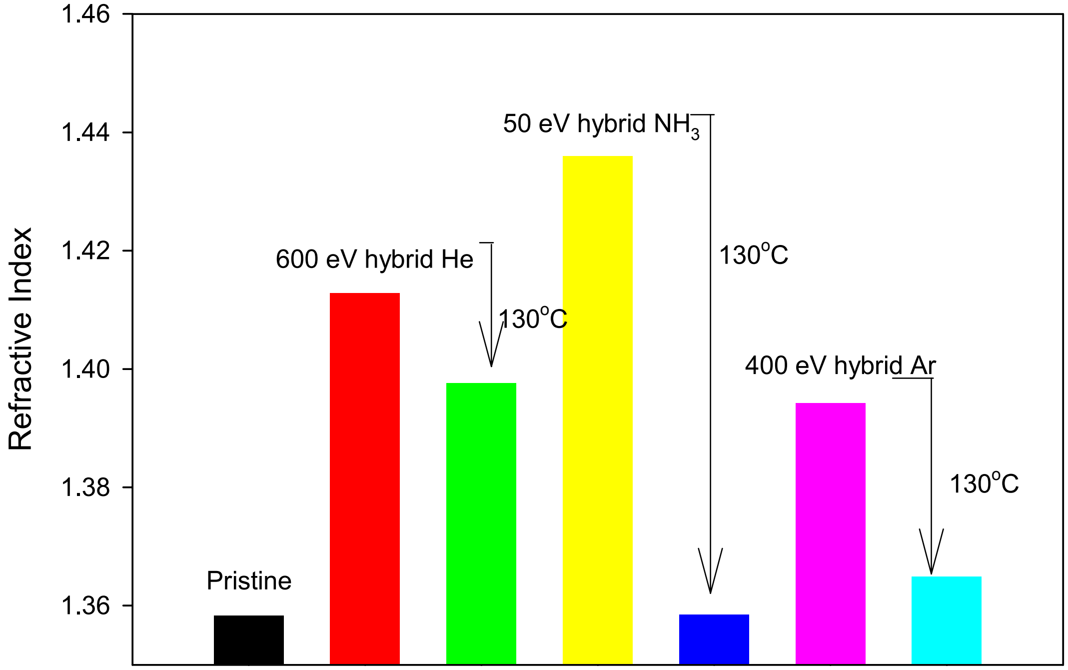

Fig. 4.13 **Recovery of the refractive index after plasma damage by annealing. Samples were treated by downstream hybrid plasmas of 600 eV He, 50 eV NH_3, and 400 eV Ar respectively at 1 mtorr for 40 min and then annealed at 130°C for 1 hour.**

Moisture removal was directly confirmed by monitoring the differential FTIR for low-κ samples after the N_2/H_2 plasma treatment (Fig. 4.14). With the temperature increasing from 100^0C to 140^0C or 250^0C, water and Si-OH between 3200 and 3600 cm^{-1} were found to decrease with corresponding increase in Si-O-Si between 950 and 1250 cm^{-1}. This indicated that moisture was gradually removed as adjacent Si-OH groups were condensed to form Si-O-Si bonds.

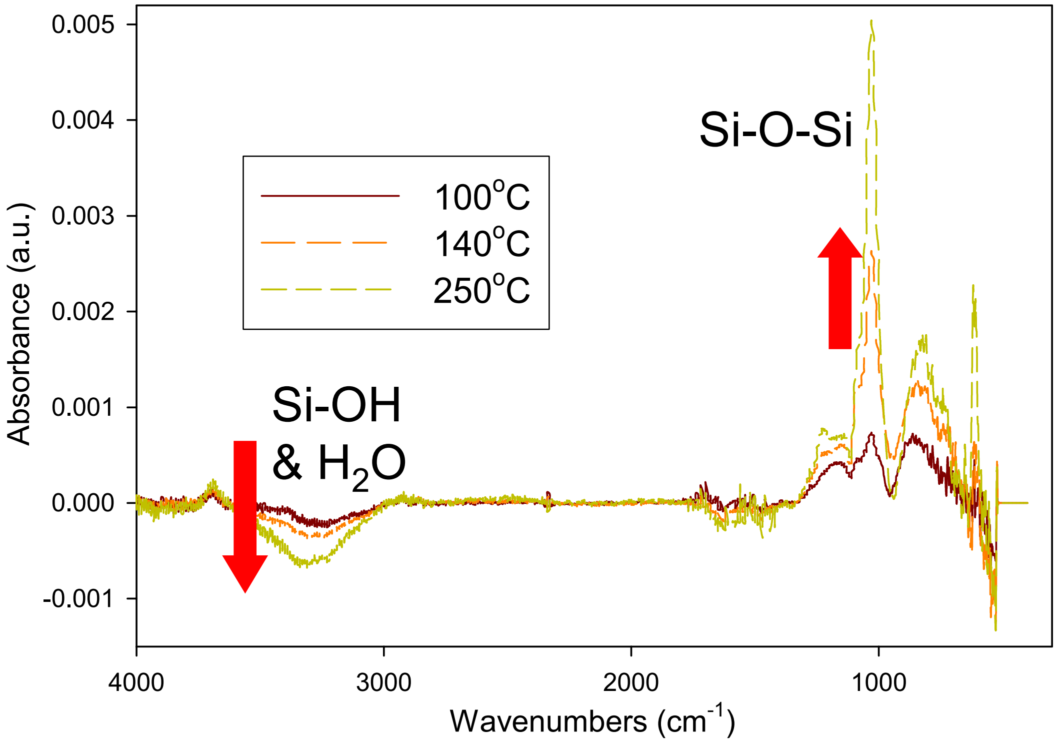

Fig. 4.14 **Differential FTIR spectra of low-κ films after annealing at 100°C, 140°C and 250°C for 1 hour respectively. Samples were damaged by N_2/H_2 plasma for 20 min. in an Oxford RIE chamber.**

4.2.2 Origin of dielectric loss

The dielectric constant (ε_r or κ), a frequency-dependent and intrinsic material property, consists of three components: electronic, ionic, and dipolar polarization [32]. A general expression is given as $\varepsilon_r = 1+\Delta\varepsilon_i+\Delta\varepsilon_e+\Delta\varepsilon_d$ comprising of ionic, electronic, and molecular dipole contributions, respectively. A more specific expression is given by the Debye equation $\frac{k-1}{k+2} = \frac{N}{3\varepsilon_0}(\alpha_e + \alpha_i + \frac{p^2}{3kT})$, where κ is the dielectric constant, ρ is the density, M is the molecular weight, α_e and α_i are the electronic and ionic polarizability repectively, and p is the dipole moment [33]. Therefore, dielectric loss after plasma damage is attributed to the combinative change of electronic, ionic and dipole components.

To take O_2 plasma damage as an example, the electronic polarizability of major elements involved in this damage process is given in Table 4.5 [34]. Low-κ material is usually full of elements Si, C, O, and H. With the incorporation of additional oxygen into low-κ materials, the electronic polarizability may rise a bit because the electronic polarizability of oxygen is only slightly higher than that of the lost hydrogen. Meanwhile, the decrease of electronic polarizability due to carbon loss may compromise the increase of electronic polarizability due to oxygen incorporation.

Table 4.5 Polarizability of major elements in low-κ materials. (From [30])

Atom	Polarizability/unit volume ($Å^{-3}$)
Si	5.38
O	0.802
C	1.76
H	0.667

The ionic characteristic of a certain molecule is determined by the difference of electronegativity of its composed atoms. The rank of electronegativity is F (4.0)>O (3.5)>C (2.5)>H (2.1)>Si (1.8) [35]. Physical properties of major bonds in low-κ materials are given in Table 4.6 [34] [35] [36] [37]. In pristine low-κ, difference of electronegativity of Si-CH_3 is 0.7 and that of Si-H is 0.3. After O_2 plasma treatment, part of Si-CH_3 or Si-H will be transformed into Si-O that has a much higher electronegativity difference of 1.7. Therefore, the ionic component of the dielectric constant may increase unless there may exist a number of Si-O-Si backbone bonds breaking due to energetic ion bombardment, which may reduce the ionic component significantly

Table 4.6 Physical properties of major bonds in low-κ materials. (From [34] [35] [36] [37])

Bond	Electronegativity difference	Polarizability/ unit volume (Å^{-3})	Bond energy (kJ/mol)	Bond length(Å)	P(e·Å)
Si-O	1.7	0.123	800	1.63	0.831
Si-C	0.7	0.076	451	1.87	0.224
Si-H	0.3	~0.07	<=299	1.48	0.037

The above discussion is based on the structure and composition changes due to plasma damage only. The effect of density change must also be considered because the measured dielectric constant reflects the collective behavior of all the atoms and bonds. But it is not simple to physically measure the density of certain atoms or bonds in a certain material. H. Shi et al have performed calculations to extract the electronic and ionic dielectric constant after plasma damage [38]. Since spectroscopic ellipsometer, FTIR, and MIS dielectric constant measurement reflect the response of dielectric constant at different frequency, it is theoretically possible to separate out the experimental data and extract the electronic, ionic and dipole contributions to the total dielectric constant. It was found that after typical O_2 plasma damage, the electronic component increased from 0.698 to 0.775 and the ionic component decreased from 0.347 to 0.323. The density factor was considered because the data were based on experimental spectroscopy. It was concluded that the electronic and ionic contributions to dielectric constant did not change much after plasma treatment especially if these two components were added up.

However, it was observed from the current experiments that the dielectric constant of low-κ CDO increased from 2.5 to 2.9, resulting in 16% increase after the plasma damage. Some other groups even reported 50% rise of dielectric constant after damage [39]. This 16%-50% rise can not be attributed to the internal changes of structures or components solely due to plasma damage. The third term, dipoles, must be seriously considered.

Quantum chemistry calculations based on the Gaussian '03 software were performed by H. Shi on a workstation to investigate how plasma modification of low-κ materials affected its dipole moments and increased its dielectric constant [40]. A detailed description of the Gaussian calculation is beyond the scope of this dissertation, so here only the final results are summarized briefly. The calculation was focused on the effect of moisture uptake compared with the effect of other surface bonding changes. Due to the local property of chemical reaction, $Si_8O_{12}H_{10}C_1$ was constructed as the basic cluster unit of a low-κ material. Structure geometry was optimized by HF/6-31G (d). Dipole moments were calculated with the basis set of HF/6-31G (d) [41]. Five cases were specifically considered:

1) Silanol effect: $-CH_3$ was replaced by $–OH$;
2) Water absorption effect: water formed hydrogen bonds with Si-OH;
3) Amino effect: $-CH_3$ was replaced by $–NH_2$;
4) Silicon dangling bond effect: $-CH_3$ was completed removed;
5) Oxygen dangling bond effect: $-CH_3$ was replaced by $–O$;

The calculated and normalized dipole moments of different bonding configurations were given in Table 4.7. Compared with other possible effects, the dipole moment induced by physisorbed water was at least one order of magnitude higher than all the other cases, implying the largest dielectric constant increase. The introduction of Si dangling bond had almost no effect on the dipole moment. The introduction of silanol groups, O dangling bond, or amino groups would cause a certain amount of dielectric loss, but still less than that by physisorbed water. In summary, the quantum chemistry calculation results showed that the dipole moment induced by physisorbed water was at least one order-of-magnitude higher than by any other effects on the molecular structures. Thus it should dominate the dielectric constant increase. This result is consistent with the experimental observation of significant moisture uptake after plasma damage in Section 4.2.1.

Table 4.7 Calculated and normalized dipole moments of different bonding configurations. (Courtesy of H. Shi)

Bonding configurations	Dipole Moment (c•m)	Normalized p^2
$\equiv$Si-CH_3	$2.924*10^{-30}$	1.000
$\equiv$Si-OH	$4.453*10^{-30}$	2.319
$\equiv$Si-OH-OH_2	$1.457*10^{-29}$	24.836
$\equiv$Si-	$5.905*10^{-31}$	0.041
$\equiv$Si-O-	$7.139*10^{-30}$	5.962
$\equiv$Si-CH=O	$8.867*10^{-30}$	9.198

In the 100 nm κ=2.5 CDO film, the damaged region of the top surface after plasma treatment was estimated to be about 20 nm by XPS depth profiling, XRR, and TEM. As illustrated in Fig. 4.15, the whole film could be regarded as two parallel plate capacitors (C_1 and C_2) connected in series. The total capacitance, C_{tot} can be expressed as:

$$\frac{1}{C_{tot}} = \frac{1}{C_1} + \frac{1}{C_2} \qquad (4.1)$$

Since $C = \frac{\varepsilon \times S}{4\pi\kappa \times d}$, if the metal contact area is assumed to be the same for the two capacitors, the total dielectric constant κ_{tot} can be expressed as:

$$\frac{d_{tot}}{k_{tot}} = \frac{d_{dam}}{k_{dam}} + \frac{d_{pristine}}{k_{pristine}} \qquad (4.2)$$

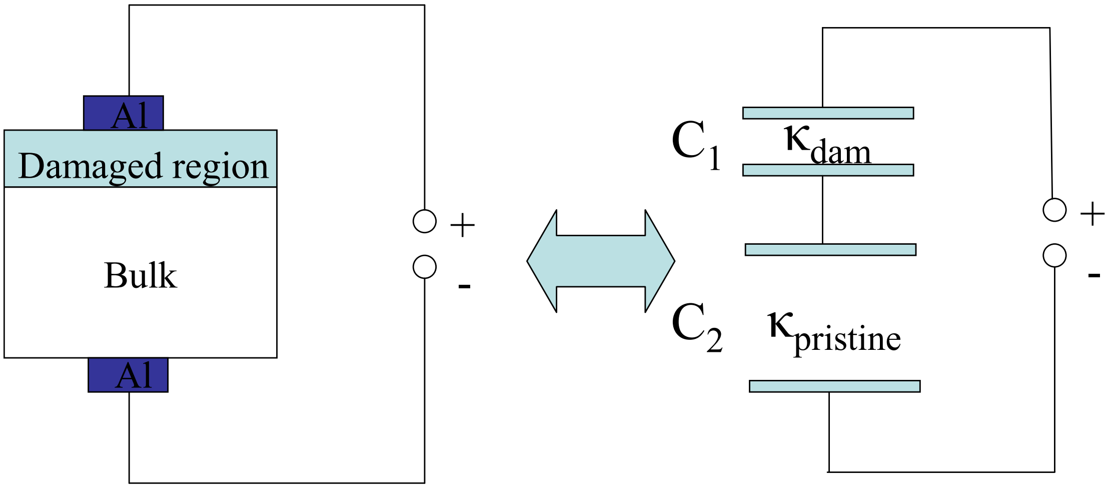

Fig. 4.15 Two equivalent circuits.

Since the top damaged region consists of damaged low-κ materials with a certain weight percentage of water, its effective dielectric constant κ_{dam} can be expressed as [42]:

$$k_{dam} = k_{dry} + \alpha C_w k_w \qquad (4.3)$$

Where κ_{dry} is the dielectric constant of pristine low-κ material, 2.5, α is the dielectric relaxation strength per unit moisture content that is typically around 0.3 for dielectric materials [43], C_w is weight percentage of moisture content and κ_w is the dielectric constant of liquid water, 78 at room temperature.

The dielectric constant of low-κ material after plasma damage was typically measured by experiments to be about 2.9. The effective dielectric constant of the damaged region κ_{dam} can be derived as:

$$k_{tot} = \frac{d_{tot}}{\frac{d_{dam}}{k_{dam}} + \frac{d_{pristine}}{k_{pristine}}} = \frac{100}{\frac{20}{k_{dam}} + \frac{80}{2.5}} = 2.9 \qquad (4.4)$$

Therefore, κ_{dam}= 8.1

Finally, $C_w = (k_{dam} - k_{dry}) / \alpha k_w = (8.1 - 2.5)/(0.3 \times 78) = 0.24$ (4.5)

The weight percentage of moisture content was derived to be 0.24%. Although it is small, the relative increase of dielectric constant is $\frac{2.9-2.5}{2.5} \times 100\% = 16\%$. If the moisture content were assumed to be 1%, the relative increase of dielectric constant would be $\frac{3.1-2.5}{2.5} \times 100\% = 24\%$. Clearly, moisture up, even of a small amount, can seriously affect the effective total dielectric constant of damaged low-κ materials.

4.3 Summary

Plasma damage of low-κ materials was found to be a complex phenomenon involving both chemical and physical effects. The physical effect was dominated by heavy molecular-weight plasmas at high energy/dose, which induced significant densification of the low-κ surface. The chemical effect was dominated by light molecular-weight plasmas at low energy/dose altering surface chemistry and composition. A study of the downstream plasma damage to blanket low-κ films indicated that ions played a more important role in causing plasma damage than the neutrals. Plasma damage induced changes in bonding configurations, decreasing the Si-CH_3, cage, and network structures while increasing the suboxide structure. The dielectric constant of CDO could increase up to 20% due to plasma damage and this could be attributed to the removal of the methyl group, converting the low-κ surface hydrophilic. Annealing was generally effective in mitigating moisture uptake to restore the κ value but the recovery was less complete for damage caused by higher energy plasmas. Quantum chemistry calculation confirmed that physisorbed water in low-κ materials induced the largest increase of dipole moments in comparison with changes of surface bonding configurations, and was primarily responsible for the dielectric constant increase.

Chapter 5 Oxygen Plasma Damage Mechanisms and Dielectric Recovery of Low-κ Materials

Oxygen plasma is widely used for stripping the photoresist due to its high reactivity with organic groups, which are major components of photoresist. However, the dielectric properties of low-κ materials will degrade under the exposure to plasma. This chapter focuses on exploring the mechanism of O_2 plasma damage and subsequent dielectric recovery. The CDO film studied had dielectric constant of 2.5 and refractive index of 1.33 at 633 nm. In the first part, the specific roles of ions and radicals during the damage process were studied. The capability of separating the ions and radicals in the remote ECR plasma source enabled such studies to be made. The possible reaction paths were proposed by analyzing the reaction byproducts with RGA. The damage of patterned low-κ materials by ions and radicals were examined to be quite different. Later, the interaction between the sidewall and the plasma was simulated by studying the plasma damage of blanket films at different incident angles. The kinetics of this process was established through a mathematical model. In the patterned low-κ material, the electron potential distribution determined the trajectory of ions and radicals that were major contributors to dielectric loss. Monte Carlo simulations revealed that the charging potential distribution and neutral and ion fluxes varied with the aspect ratio of trenches and had to be considered in order to account for damage formation. In the second part, various dielectric recovery techniques, e.g. CH_4 beam treatment and silylation, were briefly introduced. Their effects were examined and their limitations discussed.

5.1 Oxygen plasma damage to blanket and patterned low-κ films

5.1.1 Mechanistic study of O_2 plasma damage to blanket low-κ films

An oxygen discharge typically contains ground states O, O_2, O_3, O^+, O_2^+, O_4^+, O_3^-, O_2^-, O^-, electrons, and metastable states such as ^1D and ^1S of O, $^1\Delta_g$ and $^1\Sigma_g^+$ of O_2 [1]. As discussed before, the remote ECR plasma sources could be operated at hybrid (ion & neutral together) or atom (neutral or radical only) mode by switching the grid material at the open end of the plasma source from metal molybdenum (Mo) to dielectric boron nitride (BN). Positive voltage applied to the metal grid accelerated the ions in the hybrid beam into the chamber. Fig. 5.1 shows the XPS C1s specta after the treatment with 400 eV hybrid O_2 and radical O_2 for 15 min. Carbon in the pristine low-κ material bonded with hydrogen. The binding energy of C-H was around -285.2 eV. But after hybrid O_2 treatment, the carbon peak became broad and could be deconvoluted into four major components: C-H (-285.2 eV), C-O-H/C-O-C (-286.7 eV), C=O (-288.2 eV) and O-C=O (-289.2 eV) [2]. Their respective concentrations were 83.07%, 8.46%, 5.31%, and 3.16%. The concentration of C-H would decrease and that of C-O and C=O increase with the increase of ion energy. After radical O_2 treatment, carbon still bonded with hydrogen only as indicated by the unmodified peak at -285.2 eV in Fig. 5.1 (b).

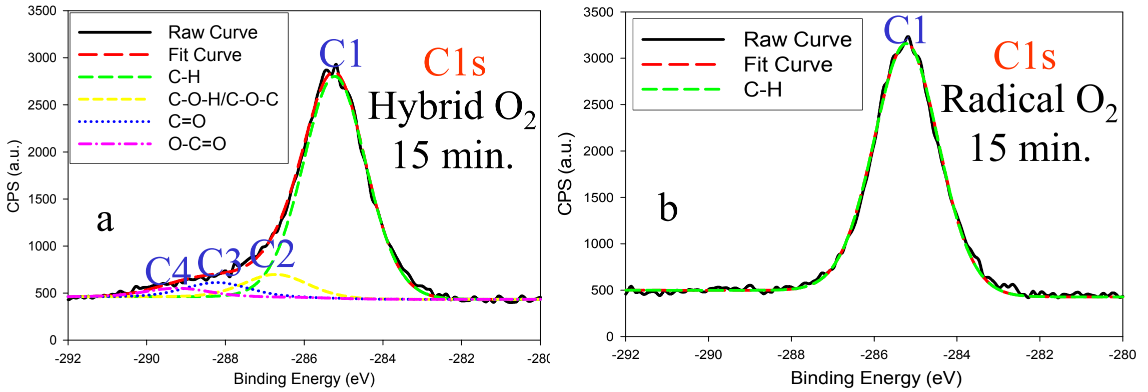

Fig. 5.1 XPS C1s sprectra after the treatment of (a) 400 eV hybrid O_2; (b) radical O_2 for 15 min.

Fig. 5.2 is the differential FTIR showing the modification of bonding configurations by the hybrid and radical O_2. After the hybrid treatment, Si-OH (3600~3200 cm^{-1}), C=O (1750~1625 cm^{-1}), and suboxide (~1023 cm^{-1}) increased but Si-H (2400~2200 cm^{-1}), Si-CH_3 (~1274 cm^{-1}), cage (~1135 cm^{-1}), and network (~1063 cm^{-1}) decreased [3]. The increase of CH_x after plasma treatment was suspected to be induced by contamination or polymer residues. The radical treatment induced a similar, but milder trend. Ellipsometry measurements indicated that the refractive index of the film at 633nm increased from 1.34 to 1.45 after hybrid O_2 treatment, while it increased to 1.41 after radical O_2 treatment. It appeared that damage to the film by the ions and neutrals was different.

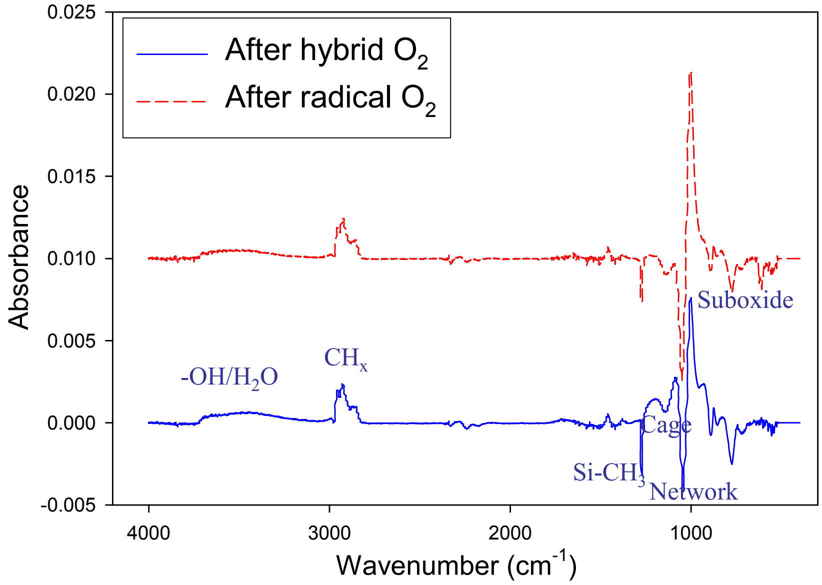

Fig. 5.2 **Differential FTIR spectra after the treatment of 400 eV hybrid O_2 and radical O_2 for 15 min..**

Fig. 5.3 compares the amount of carbon and Si-OH in the low-κ material after identical hybrid and radical O_2 treatments. The characteristic C-H peak at -285.2 eV after radical O_2 treatment was higher than that after hybrid O_2 treatment. Considering the capability of XPS surface scan of 5 nm at the 30^0 exit angle, this implied that hybrid O_2 caused more methyl depletion on the blanket film surface. It was confirmed by the comparison of Si-OH in the FTIR spectra. The peak area of Si-OH after hybrid O_2 treatment was larger than that after radical O_2 treatment as indicated by the more hydrophilic surface property after the methyl depletion by hybrid O_2 treatment.

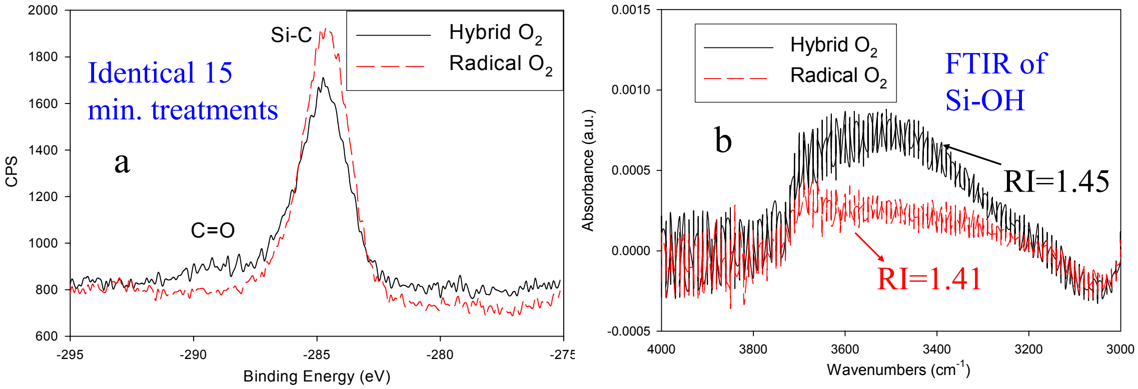

Fig. 5.3 (a) XPS C1s spectra and (b) FTIR Si-OH sprectra after identical 15 min. treatments by the hybrid O_2 and radical O_2.

The byproducts of the damage process were monitored by a residual gas analyzer, which was capable of measuring the partial pressure as low as 10^{-7} Torr. Species with different masses after hybrid O_2 treatment were measured and shown in Fig. 5.4. The vertical axis showed the partial pressure of individual species. The horizontal axis showed the scan that has an arbitrary unit. Usually, 10 scans lasted for 7 minutes. The increase of partial pressure during specific scan time of 15 minutes indicated the production of the correspondent products. Two significant byproducts were found to posses masses of 44 and 18. They were attributed to CO_2 and H_2O, respectively. After radical O_2 treatment, CO_2 and H_2O were also found. Fig. 5.5 compares the amount of CO_2 and H_2O produced by the identical hybrid O_2 and radical O_2 beams. The partial pressure corresponded to the amount of species according to the Clapeyron's equation $PV = nRT$. As indicated by the higher partial pressure, the amount of CO_2 and H_2O was higher after hybrid O_2 treatment probably due to the energetic ions in the hybrid beam.

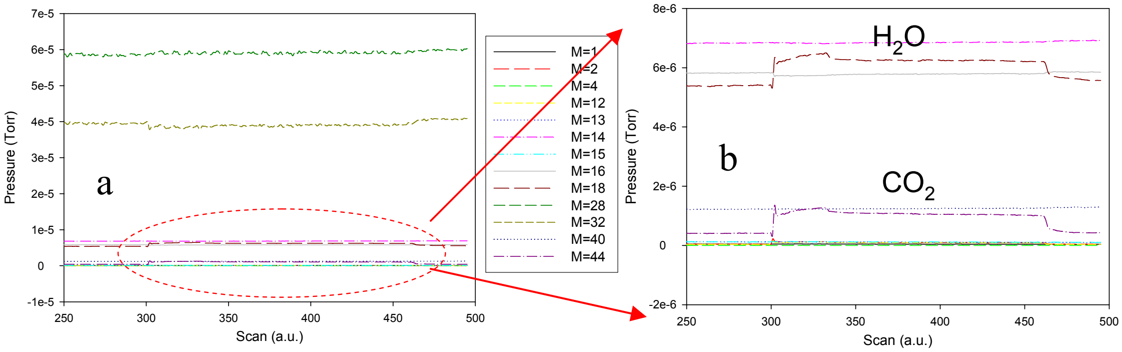

Fig. 5.4 (a) RGA scan of the reaction byproducts during the damage process by 200 eV hybrid O_2 for 15 min.; (b) Magnified RGA showing the production of CO_2 and H_2O.

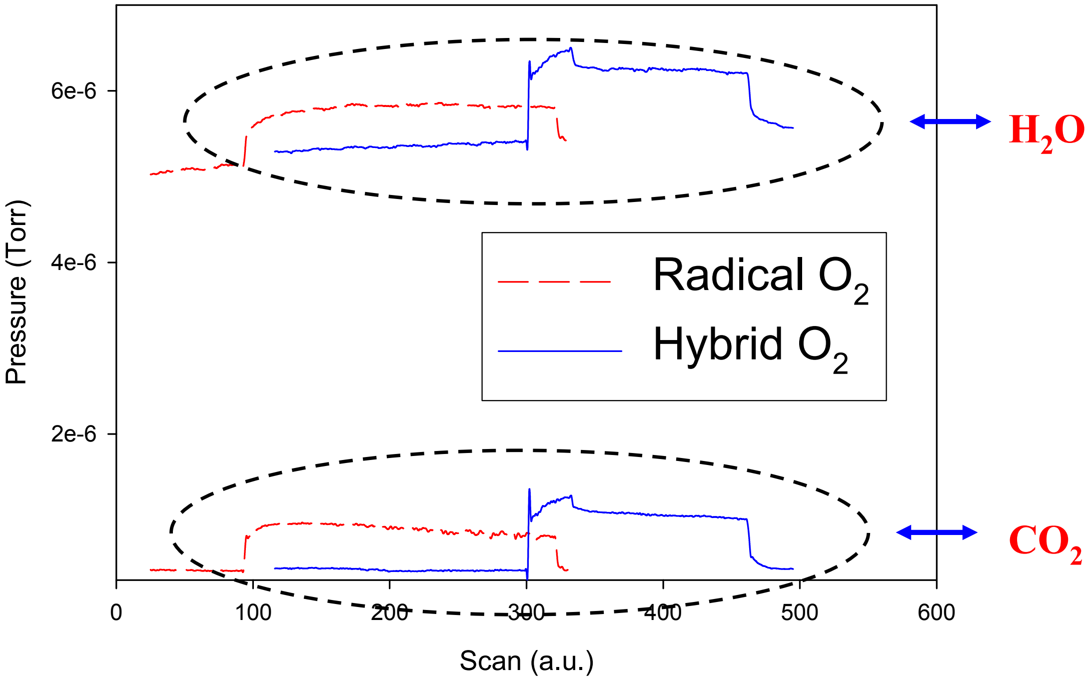

Fig. 5.5 RGA analysis of CO_2 and H_2O produced by identical hybrid and radical O_2 beam treatment.

To wrap up the results discussed above, the possible reaction paths involved in the surface interaction between oxygen plasma and low-κ dielectrics are:

$$Si-CH_3+O^- \rightarrow Si-CH=O+H_2O \tag{5.1}$$

$$Si-CH=O+2O^{-}[O]\rightarrow Si-OH+CO_2 \qquad (5.2)$$

$$Si-CH_3+4O^{-}[O]\rightarrow Si-OH+CO_2+H_2O \qquad (5.3)$$

The change of Gibbs free energy involved in the process of plasma O_2 damage to low-κ materials was calculated as follows. The Gibbs free energy of unit atom/molecule was obtained from Ref. [4].

$$\frac{1}{2}CH_3+O\rightarrow\frac{1}{2}CHO+\frac{1}{2}H_2O \qquad (5.4)$$

ΔG = -228.6×1/2+28×1/2-147.9×1/2-231.7 = -406.0 kJ/mol

$$\frac{2}{3}CHO+O\rightarrow\frac{2}{3}CO_2+\frac{1}{3}H_2O \qquad (5.5)$$

ΔG = -228.6×1/3-394.4×2/3-28×2/3-231.7 = -589.5 kJ/mol

$$\frac{2}{7}CH_3+O\rightarrow\frac{2}{7}CO_2+\frac{3}{7}H_2O \qquad (5.6)$$

ΔG = -228.6×3/7-394.4×2/7-147.9×2/7-231.7 = -484.6 kJ/mol

Judging from Eqs. (5.4) and (5.6), it seemed that CO_2 was easier to be produced than C=O in the process of plasma O_2 damage to low-κ materials due to the lower ΔG. But ions in the plasma could provide additional energy to help overcome the reaction barrier. Therefore, a large amount of C=O or C-O could still be formed. It is worth noting that ΔG of reaction (5.5) was -589.5 kJ/mol, which was the smallest among the three reactions. It indicated that formation of C=O could facilitate the subsequent production of CO_2 and H_2O. In short, ions in the plasma played a more important role in causing the carbon loss at the surface of blanket low-κ films.

5.1.2 Mathematical modeling of the damage process

Oxygen damage to low-κ dielectrics can be regarded as an ion energy-driven kinetic process for neutral oxygen atom etching of surface carbon [5] [6]. Fig. 5.6 is a schematic of the surface damage by O_2 plasma. Neutral oxygen adheres to the surface to form a metastable state C:O that may further interact with both neutral oxygen and ion oxygen to produce CO_2 [7].

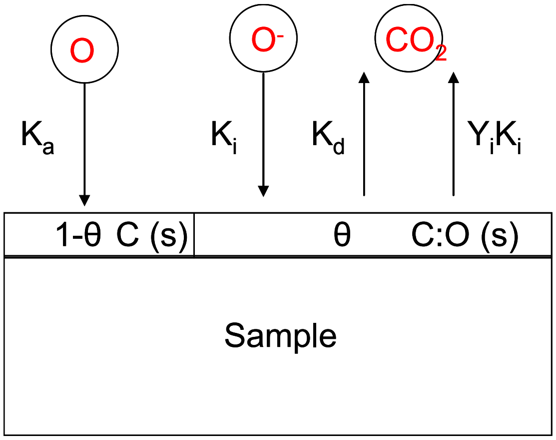

Fig. 5.6 **Schematic drawing of the kinetic damage process by oxygen ions and neutrals.**

The reactions can be expressed as:

$$O(g) + C(s) \xrightarrow{K_a} C:O \quad (5.7)$$

$$O(g) + C:O \xrightarrow{K_d} CO_2(g) \quad (5.8)$$

$$[O^-] + C:O \xrightarrow{Y_i K_i} CO_2(g) \quad (5.9)$$

where θ is the fraction of surface sites covered with C:O bonds; K_a is the oxygen atom adsorption rate; K_d is the rate coefficient for the production of CO_2; Y_i is the yield of CO_2 molecules desorbed per ion incident on a fully covered surface.

At the steady state, the processing time is long enough compared with the reaction and transport time of gases. All the gas-phase densities are constant. Desorption of CO_2 (g) is assumed to be the rate-limiting step. The steady state surface coverage is defined to be zero:

$$\frac{d\theta}{dt} = K_a n_{Os}(1-\theta) - K_d n_{Os}\theta - Y_i K_i n_{is}\theta = 0 \tag{5.10}$$

Where n_{Os} and n_{is} are the densities of neutrals and ions at the surface of low-κ films. θ at the steady state can be derived from the above equation:

$$\theta = \frac{K_a n_{Os}}{K_a n_{Os} + K_d n_{Os} + Y_i K_i n_{is}} \tag{5.11}$$

CO_2 molecules are produced through the reaction between O, [O^-] and C:O. The flux of CO_2 is found to be:

$$\Gamma_{CO_2} = (K_d n_{Os} + Y_i K_i n_{is})\theta n_0^{'} \tag{5.12}$$

Where $n_0^{'}$ is the area density of surface sites.

CO_2 comes from the damage region. The depth of the damage region is assumed to be linearly related to the production rate of CO_2.

$$D = \frac{\Gamma_{CO_2}}{n_c} t \tag{5.13}$$

Where n_c is the density of carbon atoms in the low-κ material; t is the process time. There are two extreme conditions. When the sample surface is vertical to the plasma beam, both ions and neutrals will strike the sample surface. This field damage is:

$$D_f = \frac{n_0^{'}}{n_c} \frac{1}{\frac{1}{K_d n_{Os} + Y_i K_i n_{is}} + \frac{1}{K_a n_{Os}}} \tag{5.14}$$

When the sample surface is parallel to the plasma beam, only neutrals will contribute to the carbon loss. The ions are so directional that they do touch the surface. The sidewall damage in the patterned low-κ materials is such an example. This sidewall damage can be derived as:

$$D_s = \frac{n_0^{'}}{n_c} \frac{1}{\frac{1}{K_d n_{Os}} + \frac{1}{K_a n_{Os}}} \tag{5.15}$$

Fig. 5.7 shows the normalized damage depth vs. K_a/K_d. In the ion energy dominant regime, $Y_iK_in_{is}>>K_dn_{Os}$ and $D_f>>D_s$, i.e. the field damage is much larger than the sidewall damage. In the neutral flux limited region, $K_an_{Os}<< K_dn_{Os}$ and $\theta_s <<1$. Here, the formation of C:O is rate limiting. Both D_f and D_s are determined by K_an_{Os}, the rate of arrival of oxygen atom. With the increase of K_an_{Os}, θ_s gets close to 1 and the normalized damage depth D_s saturates at 1 too. However, D_f still increases with K_an_{Os}. Only when $K_an_{Os}>>Y_iK_in_{is}$ in the ion flux limited region, θ_f gets close to 1. Then the normalized damage depth D_f saturates at $Y_iK_in_{is}/K_dn_{Os}$.

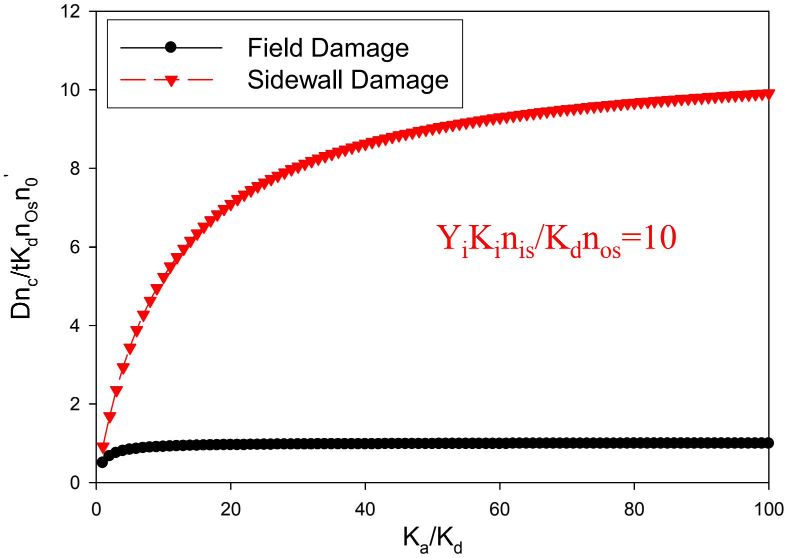

Fig. 5.7 **Relation between normalized field and sidewall damage and K_a/K_d. $Y_iK_in_{is}/K_dn_{Os}$ is assumed to be 10.**

Since desorption of CO_2 is assumed to be the rate-limiting step, $K_a n_{Os}$, $Y_i K_i n_{is} >> K_d n_{Os}$. The damage anisotropy is obtained as:

$$\beta = \frac{D_f}{D_s} = \frac{Y_i K_i n_{is}}{K_d n_{Os}} \frac{1}{1 + \frac{Y_i K_i n_{is}}{K_a n_{Os}}} \qquad (5.16)$$

In the ion flux limited region, $K_a n_{Os} >> Y_i K_i n_{is} >> K_d n_{Os}$, both θ_f and θ_s get close to 1. β has a maximum value at $Y_i K_i n_{is}/K_d n_{Os}$. In other words, the sidewall damage is almost negligible compared with the field damage in cases of high ion energy (high Y_i), high ion flux (high n_{is}), low substrate temperature (small K_d), and high atom flux (high n_{Os}).

In the neutral flux limited region, $K_d n_{Os} << K_a n_{Os} << Y_i K_i n_{is}$, θ_s gets close to 1 but θ_f does not. β gets close to K_a/K_d, which is independent of the flux of ions and neutrals.

5.1.3 Oxygen plasma damage to patterned low-κ material

The conclusions drawn from the studies of blanket films may be invalid in the patterned films because the latter contain numerous trenches and vias that may perturb the local plasma density close to the sample surface [8]. It is difficult to study the plasma damage to patterned low-κ films not only due to these unknown parameters but also due to the limitations of metrology [9]. Until now, angle resolved XPS [10], TEM/EELS [11], and electrostatic force microscopy (EFM) [12] were reported to be suitable metrology tools to observe the damage directly. Some other indirect ways include inferring the damage extent through measuring the capacitance [13] [14].

Fig. 5.8 shows the top-view of SEM images of patterned low-κ films after hybrid and radical O_2 beam damage. Although ion energy of the hybrid O_2 beam varied from 50 eV, 400 eV till 900 eV, damages, distortions or striations were not observed in Fig. 5.8 (a) (b) & (c). The patterns appeared unaltered. However, after radical O_2 treatment, striation of the line width was very clear almost everywhere on the sample. Some significant line distortions were circled in the SEM images. In order to inspect the trench profile, cross sectional SEM was tried but was not successful due to charging on the dielectric surfaces. Instead, TEM was employed because its image quality is unrelated to the charges on the samples. As indicated by Fig. 5.8 (e) and (f), line distortions occurred where there existed many trenches. Therefore, a small and thin piece was specifically selected from the area with many trenches for TEM study. Fig. 5.9 shows the cross sectional TEM images of the trenches after hybrid and radical O_2 treatment. The images were tilted due to improper mounting of samples on TEM sample holders. After 400 eV hybrid O_2 treatment, the trench sidewall in Fig. 5.9 (a) still looked vertical. However, after radical O_2 treatment for the same minutes, the sidewall profile in Fig. 5.9 (b) was severely distorted.

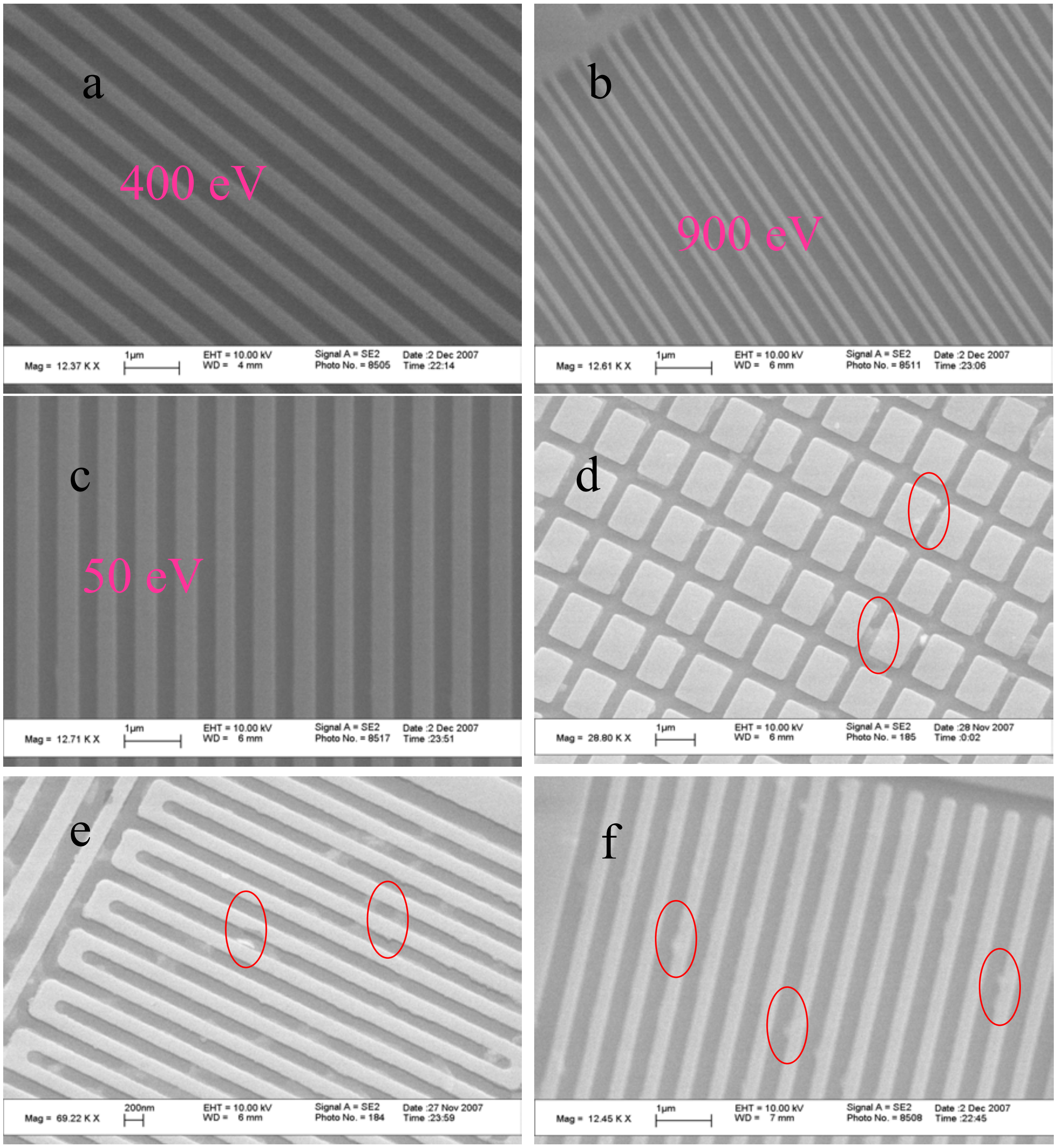

Fig. 5.8 **SEM images of patterned low-κ films after the treatment of (a) 50 eV hybrid O_2; (b) 400 eV hybrid O_2; (c) 900 eV hybrid O_2; (d) (e) (f) radical O_2. Significant damaged areas were circled out.**

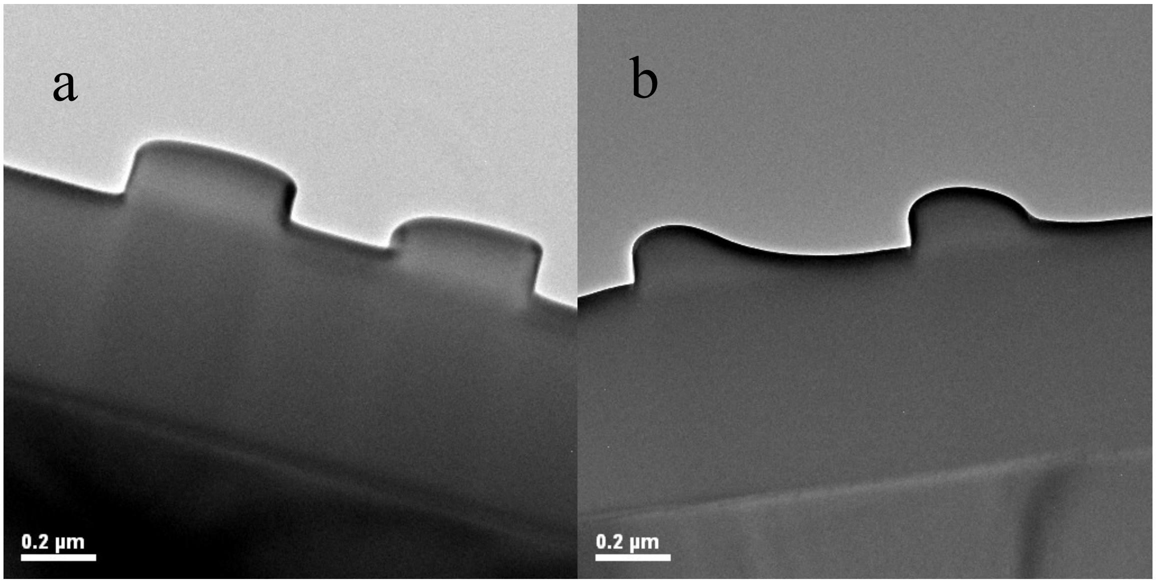

Fig. 5.9 **Cross section TEM images of patterned low k films after the treatment with (a) 400 eV hybrid O_2; (b) radical O_2.**

EELS is a powerful technique for element analysis. To protect the sample surface from contamination during TEM sample preparation by dicer and FIB, the damaged, patterned low-κ films were coated with ~30 nm Cr and ~20 nm Au by e-beam evaporation. Their deposition rates were controlled to be around 1 Å/s for Cr and 3 Å/s for Au so that the adhesion between metal and low-κ material could be strong and the interfaces between metal and low-κ material could remain unaltered. Given by Fig. 5.10, EELS line scan across the middle of the trench sidewall indicated the formation of a gradient region of carbon depletion after plasma treatment. Compared with hybrid beams, the radical beams are isotropic and therefore have more interactions with the carbon on the sidewall. The carbon depletion depth after radical O_2 was the largest: 140 nm. The carbon depletion depth decreased from 100 nm to 70 nm when the energy of the hybrid beam increased from 400 eV to 900 eV, implying that the intensified directional ions in higher energy hybrid beams penetrated shallower into the sidewall and produced less negative effects on the carbon loss on the sidewall.

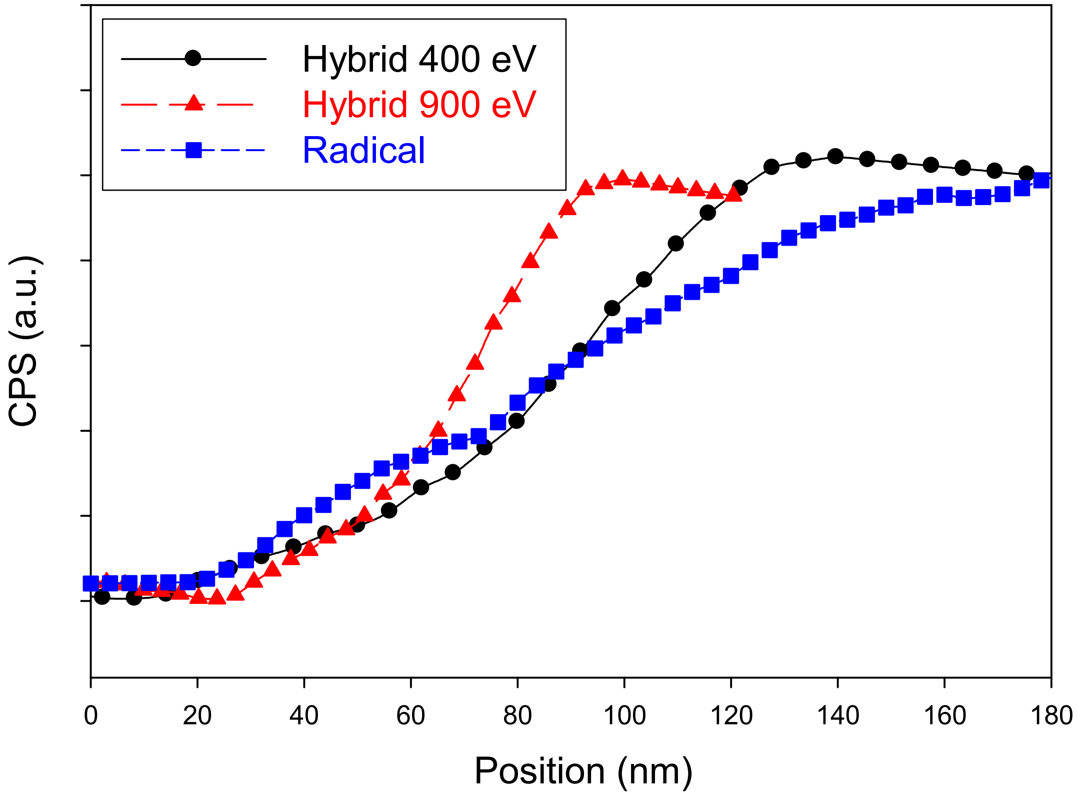

Fig. 5.10 **EELS line scan of the carbon concentration on the sidewall after the treatment with 400 eV hybrid O_2, 900 eV hybrid O_2 and radical O_2.**

Electrons can be focused to a very small local region through selecting proper apertures and adjusting condenser lens. Fig. 5.11 is the result of point EELS analysis. The beam point was focused to be as small as 0.7 nm. Three points, P1, P2, and P3, were probed. P1 was located closest to the metal/sidewall interface, P3 at the center of the trench, and P2 in the middle between P1 and P3. The height of the characteristic σ C peak at -285 eV was 6500 at P1, 8000 at P2, and 12500 at P3. The gradual increase of the C peak height from P1 to P3 confirmed the formation of a carbon depletion region at the sidewall after RIE O_2 plasma treatment.

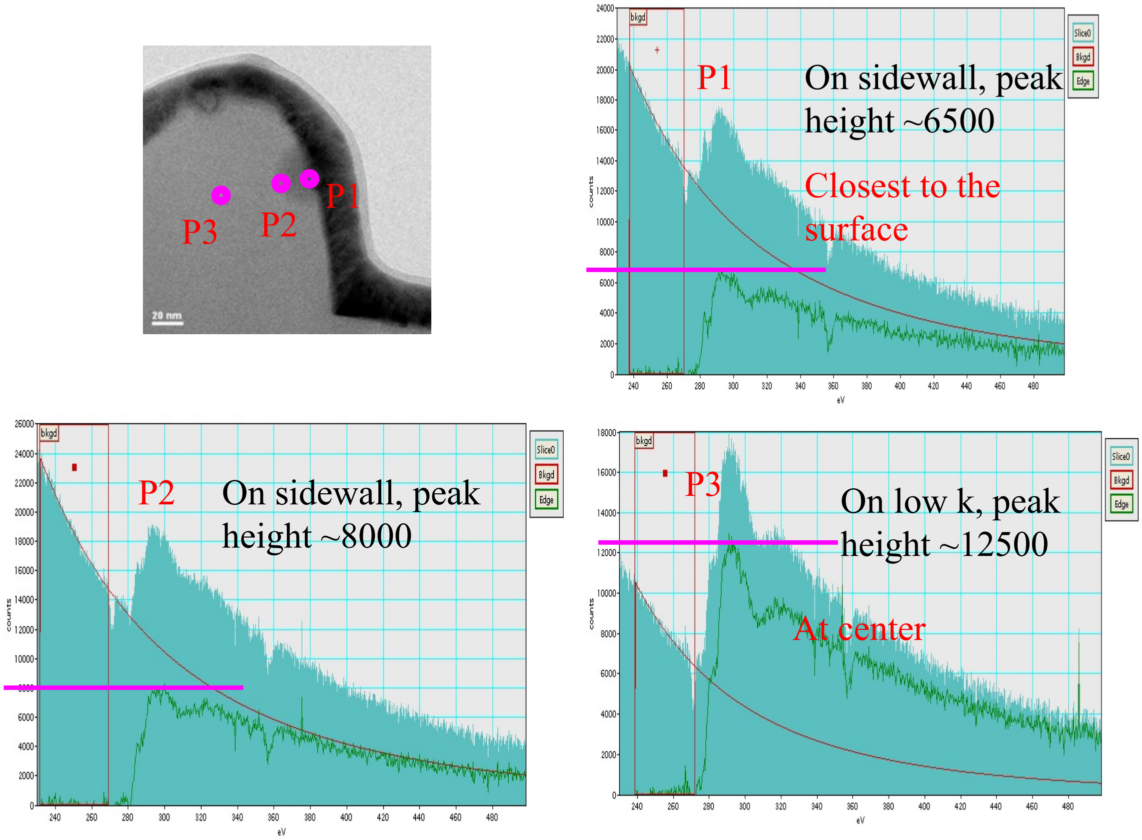

Fig. 5.11 **EELS point analysis of the carbon concentration on the sidewall after RIE O_2 plasma treatment.**

Nano beam EELS analyses were also performed to investigate the effect of the structure geometry on the extent of damage. If the aspect ratio of the structure was 1:1, i.e. the trench width equaled the trench depth, as indicated by Fig. 5.12, the carbon peak height on the sidewall was equal to that on the trench bottom. However, if the aspect ratio of the structure was 1/2, i.e. the trench width was twice the trench depth, as indicated by Fig. 5.13, the carbon peak height on the trench bottom was half that on the sidewall. With the reduction of trench aspect ratio, the ion flux probably became easier to reach the trench bottom and cause carbon depletion. This observation implied that the carbon damage distribution on patterned low-κ films after plasma treatment was not uniform. It was strongly correlated with the aspect ratio of the trenches.

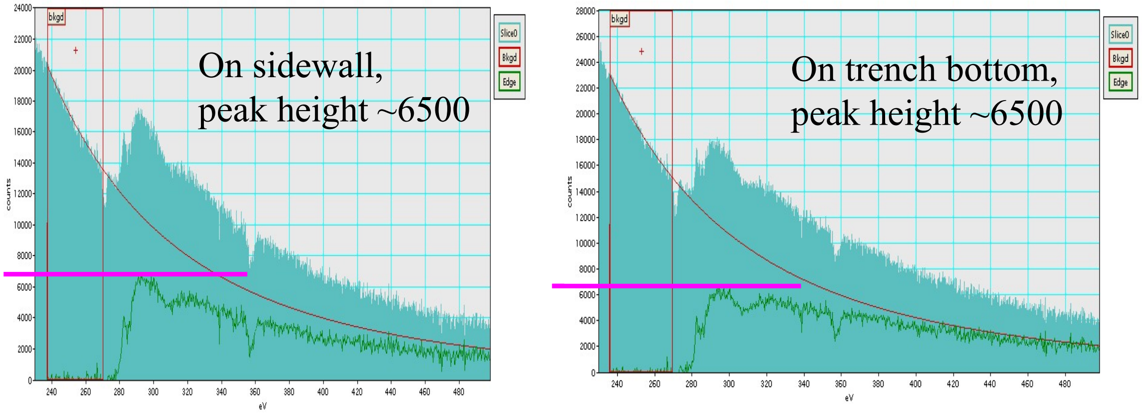

Fig. 5.12 **EELS point analysis of the carbon concentration on the sidewall and the trench bottom after RIE O_2 plasma treatment. The aspect ratio of the trench is 1:1.**

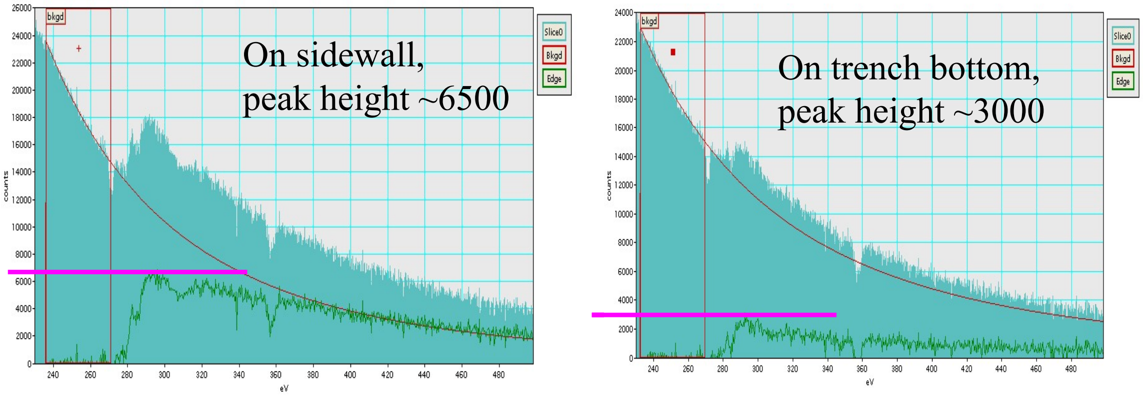

Fig. 5.13 **EELS point analysis of the carbon concentration on the sidewall and the trench bottom after RIE O_2 plasma treatment. The aspect ratio of the trench is 1:2.**

5.1.4 Angle dependence of oxygen plasma damage

In the patterned low-κ structures, the sidewall can be regarded as a surface that interacts with ions and neutrals in the plasma from different directions. Therefore, it is instructive to study how the beam incident angle affects the surface carbon concentration of low-κ films. By rotating the sample stage from 0^0 to 90^0, blanket low-κ films were treated by hybrid and radical oxygen beams at different incident angles for identical 15 mins. The beam was vertical to the sample surface at 0^0 while at the sidewall it was parallel at 90^0.

To examine the surface chemistry changes, analysis was focused on the loss of surface carbon concentration due to methyl depletion. For this purpose, the XPS carbon 1s peak after hybrid beam treatment was deconvoluted into three subpeaks of C-H (-285.2 eV), C-O (-286.7 eV), and C=O (-288.2 eV). Here the C-H bond represents the characteristic hydrophilic methyl groups. Fig. 5.14 showed that the C-H/Si ratio after hybrid O_2 treatment increased with the increasing incidence angle. In contrast, the C-H/Si ratio remained almost constant after radical O_2 treatment.

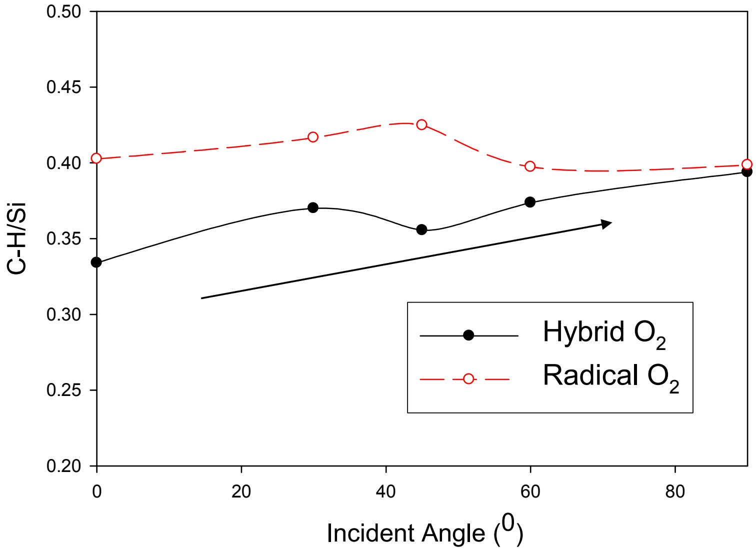

Fig. 5.14 Relation between C-H/Si and the beam incident angles after 400 eV hybrid O_2 and radical O_2.

The FTIR peak ratios of $Si\text{-}CH_3$ (1274 cm^{-1}) and Si-O (1250~950 cm^{-1}), Si-OH (3600~3200 cm^{-1}) and Si-O were shown in Fig. 5.15 (a) and 5.15 (b). After hybrid O_2 treatment, the $Si\text{-}CH_3$/Si-O ratio increased with increasing incidence angles while the Si-OH/Si-O ratio decreased. Interestingly, radical O_2 beam treatment did not seem to affect the $Si\text{-}CH_3$/Si-O and Si-OH/Si-O ratios in the low-κ film.

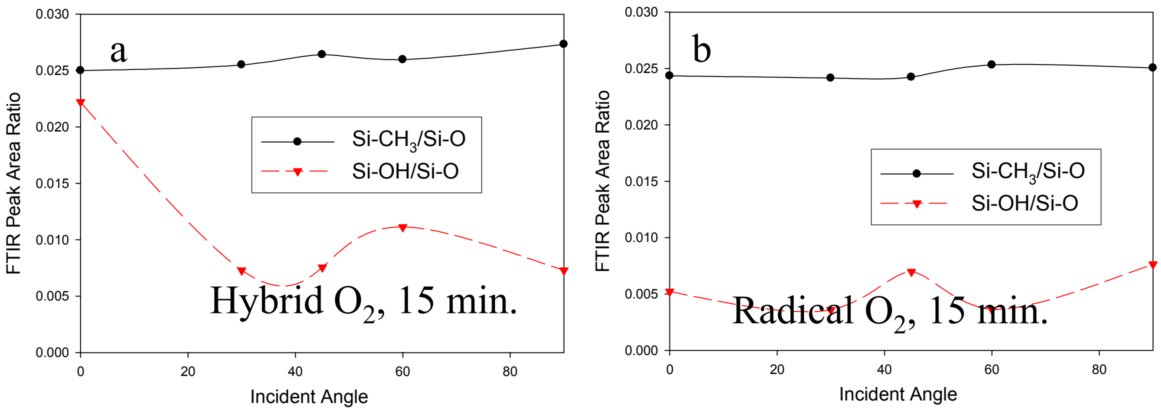

Fig. 5.15 **Relation between FTIR peak area ratio of $Si\text{-}CH_3$/Si-O and Si-OH/Si-O and the beam incident angles after (a) 400 eV hybrid O_2; (b) radical O_2.**

Measurement of water contact angles and refractive indices showed a similar trend. The water contact angle provides a measure of the intensity of the surface polar terms. In Fig. 5.16, the contact angle gradually increased from ~68^0 to ~90^0 as the O_2 hybrid beam changed from the vertical to the parallel direction. For the radical O_2 beam, the contact angles remained at around 85^0, independent of the beam incident angles. The small variation in the contact angle, $\pm 5^0$ was probably due to the process variations. To examine the extent of the dielectric loss, the refractive index, n which can be correlated with the dielectric constant was measured as a function of incidence angle. In Fig. 5.17, for hybrid O_2 beam, the refractive index at 633 nm was found to decrease with the increasing incidence angle. In contrast, there was almost no angular dependence of the refractive index for the radical beam.

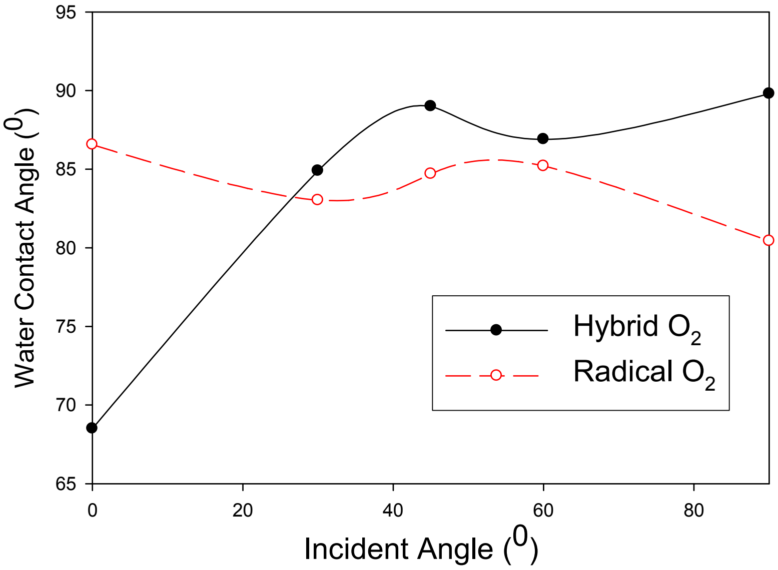

Fig. 5.16 **Relation between water contact angles and the beam incident angles after 400 eV hybrid O_2 and radical O_2.**

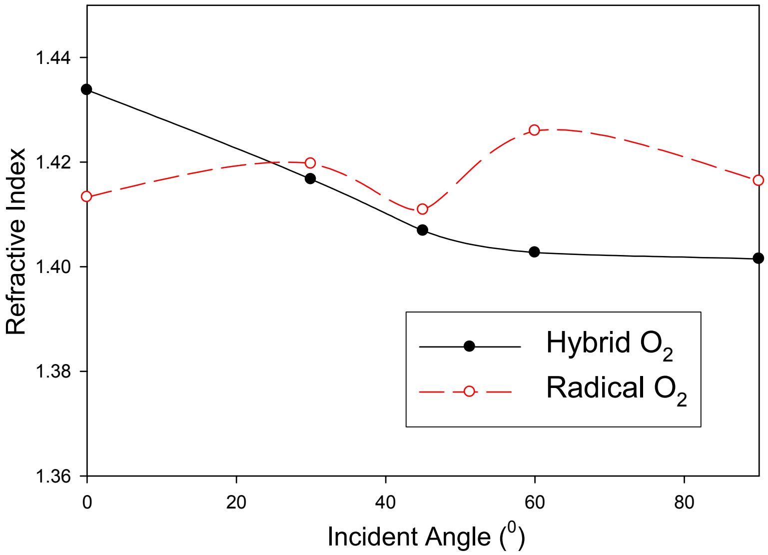

Fig. 5.17 **Relation between refractive indices at 633nm and the beam incident angles after 400 eV hybrid O_2 and radical O_2.**

The film density, thickness, and roughness were obtained by x-ray reflectivity measurements. The data was analyzed based on a double layer model, consisting of a damaged top layer and a bulk bottom layer. The results in Table 5.1 show a large difference in interface roughness between the top and the bottom layer, confirming the carbon density gradient observed by EELS. The highest density of the damaged layer after the hybrid beam treatment was found to be at 0^0 and was attributed to the directional ion bombardment of the hybrid beam. At 90^0, with the sample surface parallel to the beam direction, the hybrid O_2 beam caused only a limited surface densification while the bulk remained largely unchanged. Compared with the 0^0 vertical hybrid O_2 treatment, the thickness of the densification layer was also much reduced. The density distribution after radical O_2 treatment was similar at 0^0 and 90^0. Comparing with hybrid O_2, radical O_2 induced a thicker densification layer although its density was lower. The density of the bottom layer after radical O_2 treatment was higher than that after hybrid beam treatment. This indicated that the neutral oxygen diffused deep into the bulk of the low-κ film to cause methyl loss while the densified surface layer after hybrid O_2 treatment blocked penetration of ions and neutrals.

Table 5.1 Density, thickness, and roughness of the low-κ films after hybrid and radical O_2 treatment at 0^0 and 90^0.

Sample treatment	Density (g/cm^3)	Thickness (nm)	Roughness (nm)
Hybrid O_2, 0^0 (Vertical)	1.69 (top)	34.9	0.5
	1.34 (bottom)	57.1	~10
Hybrid O_2, 90^0 (Parallel)	1.67 (top)	13.6	0.6
	1.25 (bottom)	76.0	~20
Radical O_2, 0^0 & 90^0	1.52 (top)	47.3	0.6
	1.42 (bottom)	46.1	~15

Other reports on RIE vs. ICP plasma damage revealed a similar conclusion. Although ICP plasma source generated a plasma density at least 2 order of magnitude higher than RIE plasma source, the ion acceleration energy in an ICP plasma source was only 20-500V compared with 200-1000V in a typical RIE plasma source. As indicated by Table 5.1, the high energy ion bombardment induced a high density damage region that might have blocked the diffusion of plasma species. Therefore, the damage from RIE plasma could become saturated eventually. Shi et al. observed that under RIE plasma, the XPS C/Si and FTIR Si-OH/Si-O ratio became stable after a period of ashing time while under ICP plasma, the XPS C/Si ratio dropped to zero and the FTIR Si-OH/Si-O ratio increased continuously until all the carbon in the low-κ material was used up. The dielectric constant after RIE plasma was smaller than that after ICP plasma [15]. Tsai et al observed that RIE stripping by plasma sputtering was more significant than by chemical reaction. It reduced carbon depletion compared with ICP [16]. For this reason, the ashing process used in the industry has been shifting from the traditional high-temperature, oxygen-based isotropic ash plasma to either very directional RIE ash processes or hydrogen-based isotropic ash processes, depending on the integration scheme [17].

In summary, plasma interaction with low-κ surfaces is directionally dependent. Ions are energetic to remove methyl groups and cause surface densification but the effect is anisotropic. Radicals, with a certain kinetic energy, are not chemically active enough but the effect is isotropic. The depth of carbon depletion is determined by the diffusion of plasma species into the low-κ materials.

5.1.5 Monte Carlo simulations of charging and ion/neutral flux distribution

It is known that when patterned insulating structures are exposed to plasma, charges can accumulate on their surfaces due to the different directionality of ions and electrons that are anisotropic and isotropic, respectively. The local charging induces electric fields that may modify the trajectory, flux, and energy of incident ions and electrons. As a result, the insulating materials of the patterned structures may be altered non-uniformly. In the etching industry, the general objective is to obtain vertical sidewalls with a flat bottom, but irregular profiles such as undercutting, sidewall bowing, microtrenching, and reactive ion etching lag are frequently observed [18] [19] [20]. Especially as the device approaches nanometer scale geometry, the influence of an individual charge transferred to the patterned structures becomes larger, thus leading to larger variations of electron potentials on patterned structures. This gives rise to more difficult control of the etching profile as well as plasma damage profile.

Monte Carlo simulations were performed by E. Paek et al to determine the energies and fluxes of ions and neutrals arriving at the substrate. The modeling and simulation methods are described in detail elsewhere [21] [22]. Briefly, for charging simulations, ions and electrons emerged from a plane above the dielectric trench structure, with equal fluxes. Electrons were sampled from a Boltzmann distribution with the average temperature of 4 eV. Ion energies were a composite of a thermal component (Boltzmann, average temperature 0.1 eV) and a directed component, sampled from a unimodal energy distribution with a peak around 18 eV. Collisions with the structure transferred the appropriate charge to the surface, with the potentials within the entire simulation domain updated before consideration of the next particle. The potential was calculated using the Laplace equation, with Gauss's Law used to relate the surface charge. No surface conduction was considered, as the surface potential variation was insignificant. Once the potential distribution reached a steady state, kinetic energies, incident angles, and fluxes were recorded for ions and neutrals impinging on the substrate.

Fig. 5.18 shows the spatial variation in electrostatic potential within the simulation domain at steady state. When the trench aspect ratio was 1, with a trench width of 0.5 μm, the maximum potential of about 18 eV was obtained at the trench bottom. The high potential led to repelling of low energy ions while attracting electrons, making the electron and ion fluxes balanced at the trench bottom. In addition, high energy ions were decelerated by the electric field, thereby lowering the kinetic energy of ions impinging on the trench surfaces.

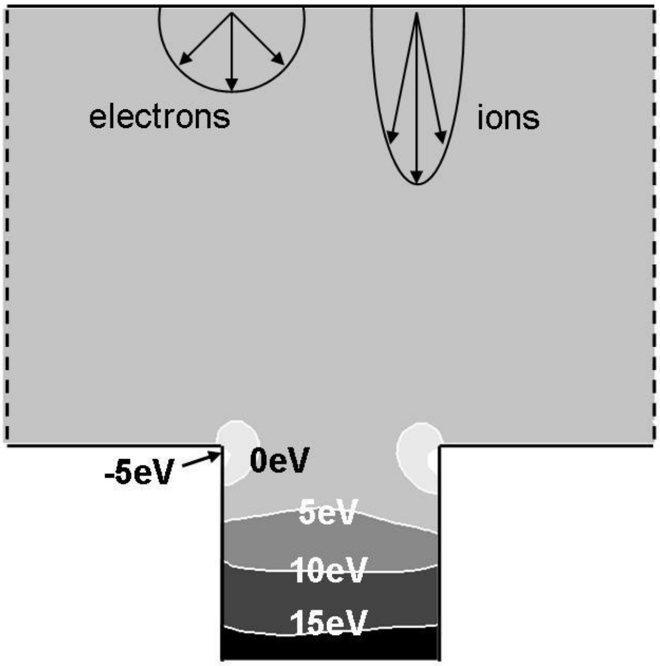

Fig. 5.18 **Potential contours within a 0.5 μm wide trench with AR=1. Electrons and ions are generated at the V=0 upper boundary. (Courtesy of E. Paek and Prof. G.S. Hwang)**

Fig. 5.19 and Fig. 5.20 show variations in the ion and neutral fluxes as well as the normalized ion kinetic energies along the trench surfaces. The isotropic spatial distributions of neutrals and anisotropic distributions of ions were consistent with the above experimental observations. The flux and energy information could be used to develop an improved kinetic model for the low-κ damage formation. Since the potential distribution varied with the trench geometry such as width and AR, the distribution of induced damage on different structures could also be different even if the kinetic parameters of ions and neutrals involved in the damage process were similar [23].

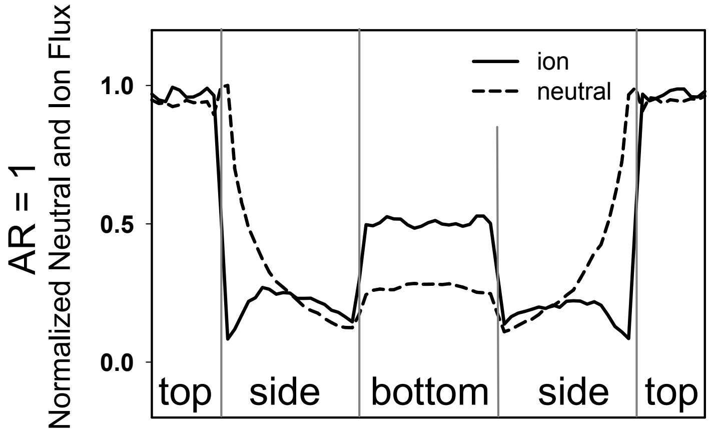

Fig. 5.19 Normalized neutral and ion flux at AR=1 trench. (Courtesy of E. Paek and Prof. G.S. Hwang)

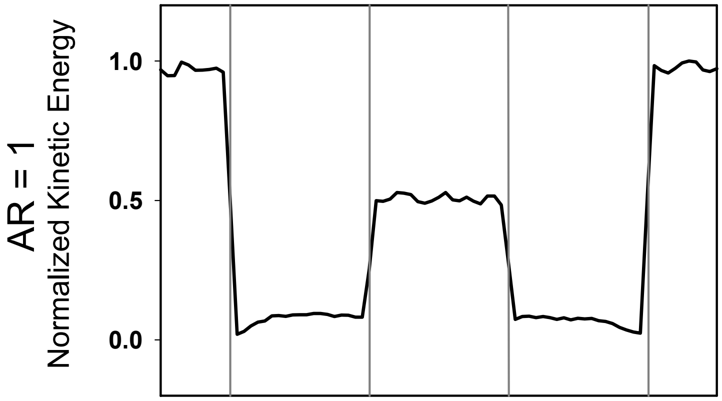

Fig. 5.20 Normalized incident kinetic energy of ions at AR=1 trench. (Courtesy of E. Paek and Prof. G.S. Hwang)

Previous publications showed that the electron potential distribution in patterned structures was strongly correlated with the geometry of structures. It was predicted that a potential oscillation in both magnitude and frequency would occur in high aspect ratio dielectric trenches, especially in very small structures. The flux and energy of ions passing through the trench would be affected accordingly. For example, low energy species were unable to pass through a 500 nm wide trench, but able to reach the trench exit if the width shrank to 100 nm or below [24]. These predictions were based on the charging simulations on a trench structure with an open bottom. In the present thesis, it should be more reasonable to perform simulations on a trench structure with a closed bottom. As indicated by Fig. 5.18, the bottom could also be accumulated with charges to contribute to shaping the electrical field inside the trench. The conclusions obtained in the open bottom model might be invalid in the closed bottom case.

Further simulation work is needed to investigate how the electron potential distribution, neutral and ion flux, and incident kinetic energy are affected by the geometry of the patterned structures. Once the potential distribution is understood, it may be coupled with the kinetic models proposed in Section 5.1.2 to delineate the plasma damage distribution on patterned low-κ structures. One critical element needed to merge the kinetic model with the Paek's simulations is to determine the kinetic parameters involved in the plasma damage process. They could not be obtained from experiments due to the limitation of the setup. An alternative is to borrow the parameters from the literature or even assume some reasonable values and apply them to the simulation work. On the other hand, it will be interesting to study how the kinetic parameters, which are strongly correlated with process conditions, affect the simulation results.

5.2 Dielectric recovery

Previous results showed that oxygen plasma used to strip photoresist would damage the low-κ surface by altering the surface chemistry and composition where the depletion of methyl function groups would cause increased moisture uptake and dielectric constant. There are two possible ways to break the Si-OH bonds and replace them with methyl groups. One is to use plasma beams such as CH_4; the other is to use silylation agents such as TMCS and DMDCS.

5.2.1 Recovery of CH_4 plasma

Some of the following CH_4 results and discussion were presented at MRS [25] and IITC [26] recently. To study the recovery effect by CH_4 plasma, it was applied to oxygen-ashed samples. Pristine CDO was ashed in a March asher for 5 seconds at 300 w, 50 sccm, then the damaged film was treated by CH_4 plasma for 1 min in the Oxford RIE chamber.

Table 5.2 shows the properties of the low-κ material after CH_4 treatment on oxygen-ashed CDO films. After the CH_4 plasma treatment, the surface hydrophobicity was restored as indicated by the recovery of the water contact angle from 13^0 to 72^0 and the refractive index from 1.40 to 1.29. Combined XRR and SE analyses indicated that a polymer layer was formed on the top surface. The thickness of this layer was estimated to be about 7 nm with its density gradually decreased from 1.9 g/cm^3 at the top to 1.7 g/cm^3 at the polymer low-κ interface. The average density was 1.85 g/cm^3. Further XPS depth profiling revealed that the top layer was very rich in carbon. Not much reduction of dielectric constant~~s~~ was observed at RT and 100^{0}C after CH_4 plasma treatment. The reason was that the O_2 ashing was so severe that almost all the carbon in the low-κ material was removed from the top to the bottom as indicated by the XPS depth profiling. The top polymer layer accounted for less than 10% of the total thickness of the CDO film. The modification was so surface limited that, with the current dielectric constant measurement instrument in the lab, it was unable to resolve their differences with enough confidence.

Table 5.2 Characterization of the low-κ material after plasma CH_4 treatment on oxygen ashed CDO films.

	Film after O_2 damage	Film after plasma CH_4 recovery
Thickness (nm)	85.65	7.08/80.67
Density (g/cm^3)	1.61	1.85/1.61
Refractive Index @ 633 nm	1.40	1.29
Water Contact Angle (°)	13°	72°
Dielectric Constant @ RT	5.77	6.40
Dielectric Constant @ 100°C	5.32	5.33

Whether the plasma CH_4 reacted with the damaged low-κ surfaces was examined by in-situ XPS analysis. Pristine and damaged low-κ surfaces were treated by remote hybrid and radical CH_4 beams and then transferred to an in-situ XPS analysis chamber. Fig. 5.21 (a) indicates that the pristine XPS C1s peak did not change after the treatment with hybrid or radical CH_4. The pristine low-κ surfaces, full of methyl groups, did not react with the plasma CH_4. However, in Fig. 5.21 (b), on damaged low-κ surfaces, the XPS C1s peak increased quite significantly after the treatment of hybrid or radical CH_4. The major carbon peak was located at -285.2 eV, implying that the plasma CH_4 transformed Si-OH on the surface into Si-CH_3. The similar XPS C1s peak of the damaged low-κ surface after the hybrid and radical CH_4 treatment indicated that radicals were mainly responsible for the formation of Si-CH_3 while ions were not.

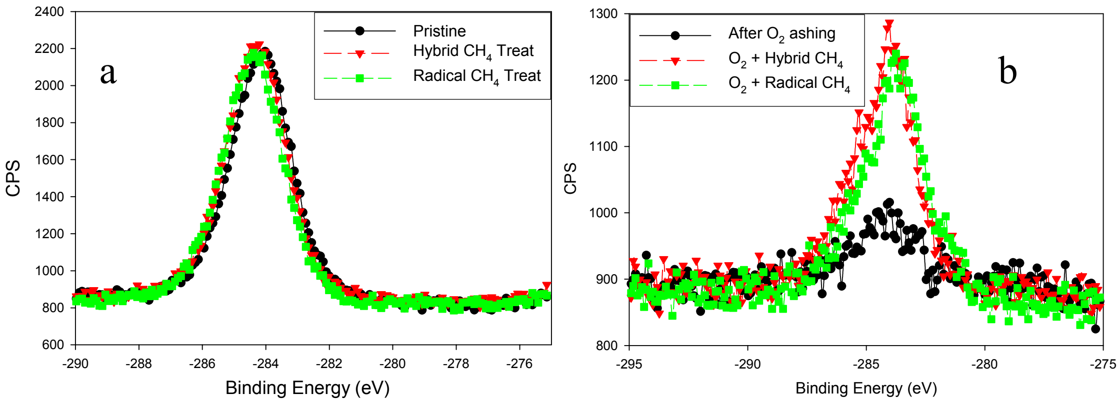

Fig. 5.21 Evolutions of XPS C1s peak after the treatment of hybrid and radical CH_4 on the surface of (a) pristine low k and (b) O_2 damaged low k.

Electrical performance of plasma CH_4 treated damage films was examined and compared with damaged films by C-V and I-V measurements. In Fig. 5.22 (a), the C-V hysteresis of O_2-ashed low-k film represented the electron charging and discharging with one cycle of applied voltages. It was much reduced after CH_4 treatment, indicating the partial removal of Si dangling bonds or polar silanol groups. In Fig. 5.22 (b), compared with the damaged films, when the electrical field was small, the large reduction of the leakage current was attributed to the removal of Si dangling bonds or polar silanol groups on the surface; when the electrical field was large, the small leakage current reduction in the high electrical field was attributed to charge buildup around the defects inside the bulk of the low-κ dielectrics caused by aggressive O_2 ashing recipe. Aimadeddine, et al. compared the plasma effects of He/H_2, NH_3, and CH_4, and drew a similar conclusion that plasma CH_4 treatment demonstrated the largest gain of dielectric reliability due to the passivation of porous low-κ sidewalls [27].

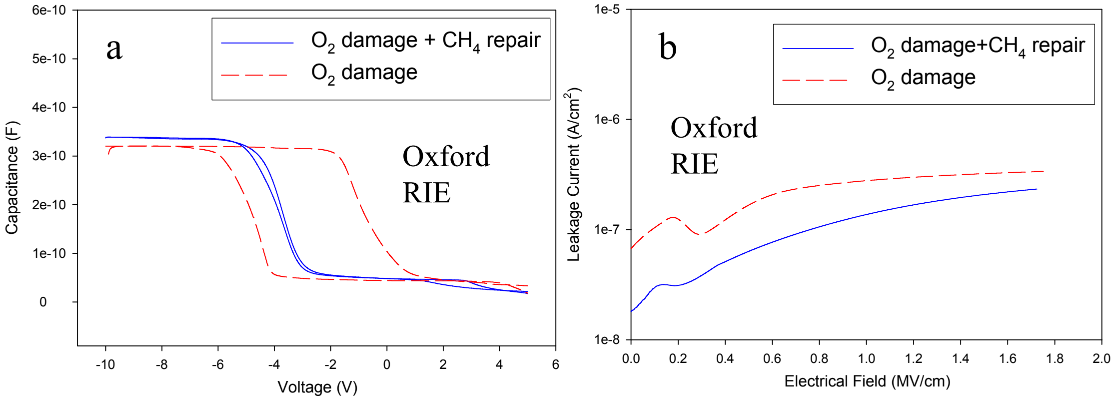

Fig. 5.22 **(a) C-V and (b) I-V characteristics of the oxygen ashed sample before and after plasma CH_4 repair.**

Although CH_4 plasma was useful for damage recovery, there were two factors that limited its effectiveness in recovery. First, Ramam spectra has indicated existence of a certain number of sp^2 C=C bonds in the top polymer layer. Due to the high polarizability of sp^2 C=C (1.643 $Å^{-3}$) than C-C (0.531 $Å^{-3}$) or C-H (0.652 $Å^{-3}$), the k value of the top layer could become higher than that of the ULK bulk. This was verified by the high average density (1.85 g/cm^3) of the polymer layer as compared with the density of 1.6 g/cm^3 for the bulk. Second, XPS depth profile indicated that carbon depletion in the oxygen-ashed sample was not limited to the film surface, but extended to the bulk. Aimadeddine, et al. conducted electromagnetic simulations to extract effective dielectric constant after ash chemistry on κ=2.5 porous SiOC. They reported an effective dielectric constant of 2.7 after plasma CH_4 stripping, as compared to 2.7 and 2.6 after plasma CH_4 and He/H_2 stripping, respectively [27]. Therefore, their results matched well with the current results, indicating that the CH_4 interaction with O_2-ashed low-κ materials was restricted to the surface due to the presence of the densified surface layer. Therefore, process optimization would be required to improve the quality of the polymer layer in order to achieve a full dielectric recovery.

To reduce sp^2 C=C bonds in the low-κ film after plasma CH_4, H_2 could be added into CH_4 in order to adjust the grain size, nanopore density, and amorphous carbon phase, which collectively determine the dielectric constant [28]. Raman measurement did not show C=C bonds after the treatment with CH_4/H_2 plasma, which suggested the formation of diamond-like C-C bonds on the low-κ surface through the reaction of $CH_n + H \rightarrow CH_{n-1} + H_2$. As seen in our measurements in Table 5.3, the additional H_2 did not show much effect on reducing the dielectric constant and refractive index of damaged low-κ films. FTIR measurement also did not show much improvement in the removal of Si-OH. Proper experiment windows are needed to optimize the effects of CH_4/H_2 on the dielectric recovery of damaged low-κ materials.

Table 5.3 Measurement of the refractive index @ 633 nm and dielectric constant of the pristine, ashed and subsequent CH_4/H_2 repaired low-κ films

	Pristine film	O_2 ashed film	50% H_2 +50% CH_4	100% H_2, no CH_4
Refractive Index @ 633 nm	1.338	1.399	1.407	1.389
Dielectric Constant	2.50	2.73	2.79	2.74

5.2.2 Silylation

Attempts to recover the dielectric properties of low-κ materials with silylation agents have gained a lot of popularity both in academia and industry. The publications generally fall into two categories. One is to choose silylation agents, characterize~~d~~ with different functional groups, and study their effects on recovering the dielectric loss. For example, Chang, et al. and Singh, et al. reported that TMCS could negate the OSG damage by plasma O_2 by converting hydrophilic Si-OH into hydrophobic Si-OSi$(CH_3)_3$ and replenishing the surface with C-H or Si-H [29] [30]; HMDS worked in a slightly different way through the initial reaction to form NH_3 and pendant –O-Si$(CH_3)_3$ groups at 150^0C – 540^0C and subsequent reaction of neighboring hydroxyl and -O-Si$(CH_3)_3$ groups to form CH_4 and bridging –O-Si$(CH_3)_2$-O groups at 300^0C or higher [31] [32]. The other category is to explore a better silylation medium. Vapor silylation is preferred due to an easier integration of vapor phase processes into the existing manufacturing tools. scCO_2 was reported to be a better medium because of the high dissolved concentration of silylation agents and favorable interfacial and transport properties of CO_2 [33] [34]. In the industry, it is expected that such silylation chemistry can restore the dielectric constant, provide pore sealing, and bring no harmful effects on subsequent film deposition simultaneously with a minimum amount of silylation agents. J. Liu, et al. designed phenyl containing agents to meet all these requirements [35]. Economically, while silylation techniques are promising in improving the reliability of BEOL integration, it requires additional chamber and process steps, and thus needs to be evaluated carefully.

Some of the vapor silylation results have been published in MRS Proceedings [36]. For example, Fig. 5.23 shows a schematic of the vapor silylation processes built by H. Shi, et al. Silylation chemicals were stored in the bubblers in the liquid phase at room temperature. They were carried into the silylation chamber by CO_2 gases. It was found that high CO_2 flow rate, hot bubbler, hot chamber wall, and hot substrate all helped the vapor interaction with low-κ films. However, the temperature should be kept below the decomposition temperature of silylation chemicals.

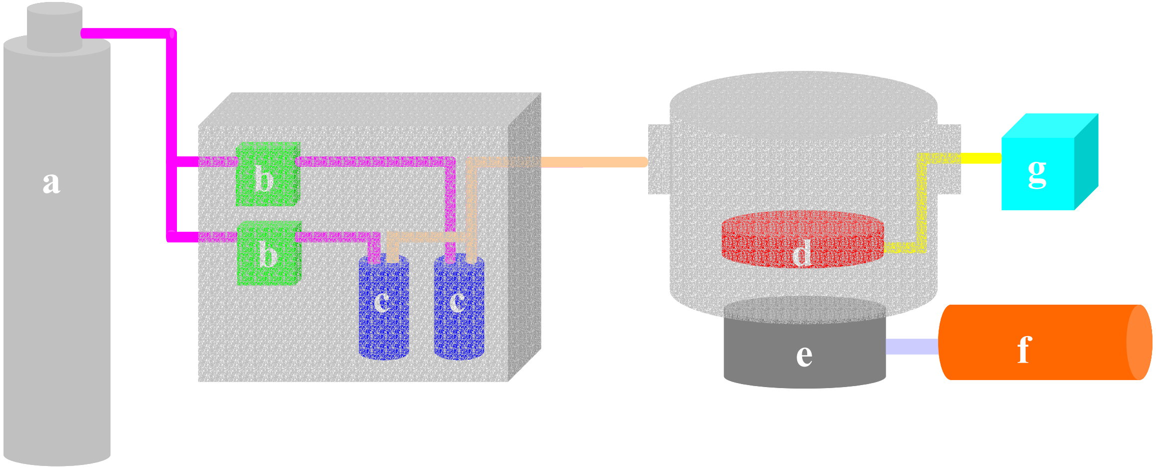

(a) Carrier gas bottle; (b) Mass flow controller; (c) Bubblers for silylation chemicals; (d) Heating stage; (e) Turbo pump; (f) Mechanical pump; (g) Temperature controller.

Fig. 5.23 Experimental setup of vapor silylation processes in Ho's lab. (Courtesy of H. Shi.)

Recovery effects of three silylation chemicals: trimethylcholorosilane (TMCS), dimethyldicholorosilane (DMDCS) and phenyl-trimethyloxysilane (PTMOS) were compared. PTMOS was mixed with TMCS in the treatment since the byproduct HCl from the reaction of TMCS and Si-OH was intended to be used as a catalyst to enhance the reaction of PTMOS and Si-OH [37]. The temperatures of the chamber wall, tube, and substrate were all maintained around 100^0C. The damaged samples were treated by the silylation agents for identical 60 minutes at 250 torr. Fig. 5.24 compares the XPS C1s spectra after various silylation treatments. Under similar conditions, the C1s peak of the sample after DMDCS treatment was the most comparable with that of the pristine sample. Thus, DMDCS was the most effective for replenishing the damaged surface with carbon, i.e. methyl groups. Water contact angles, reflecting the density of surface polar terms, are tabulated in Table 5.4. Among the three treatments, the best recovery came from the sample treated by DMDCS. Its water contact angle was recovered from 48.5^0 to 100.7^0, very close to the pristine sample's water contact angle of 97.8^0. DMDCS contains two methyl groups and two Cl leaving groups while TMCS contains three methyl groups and only one Cl leaving group. Although TMCS provides more methyl contents than DMDCS, it was suspected that the reaction between TMCS and surface silanols was incomplete because some silanols were too far to be captured by a single trifunctional silylation molecule, especially after the formation of siloxane bonds in the silylation process. The unreacted leaving groups may react to form a new silanol or initiate some oligomerization. In contrast, DMDCS, with fewer leaving groups, seemed to be more effective in using up its leaving groups. As a result, DMDCS exhibited better recovery effects than TMCS [38].

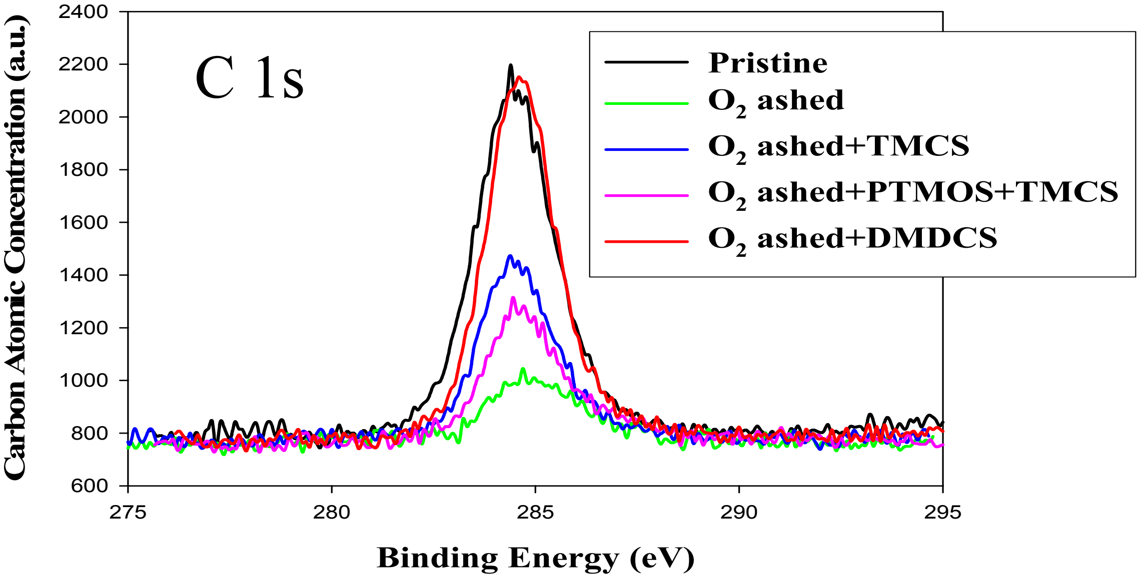

Fig. 5.24 XPS C1s spectra after the vapor silylation treatments of TMCS, DMDCS and PTMOS/TMCS (Courtesy of H. Shi).

Table 5.4 Measurement of water contact angles after the vapor silylation treatments of TMCS, DMDCS and PTMOS/TMCS (Courtesy of H. Shi)

Sample conditions	Contact Angle (^{0})
Pristine	97.8
O_2 ashed	48.5
O_2 ashed +TMCS	77.3
O_2 ashed +DMDCS	100.7
O_2 ashed +PTMOS+ TMCS	68.1

It was interesting that the FTIR spectra after O_2 ashing and after subsequent TMCS treatment were comparable. Given that FTIR reflects the property of the bulk film, the bonding configurations of the film remained largely unaltered after TMCS. It was therefore inferred that the effect of TMCS treatment was limited to the film surface. How to transport the silylation agents into the bulk of the damaged film will be critical in recovering the dielectric loss of low-κ films.

The silylation process is similar to the chemical vapor deposition. Therefore, it can be divided into two sequential steps: first the silylation agents are transferred to the wafer surface through a boundary layer; second the agents react with the functional groups on the surface. The fluxes of the mass transfer and the surface reaction are equal under steady state conditions. Fig. 5.25 illustrates these two processes near the wafer surface. The flux of mass transfer is expressed as $F_1 = h_G(C_G - C_S)$, where h_G is the mass transfer coefficient and $C_G - C_S$ is the concentration difference of silylation agents between the main flow and the wafer surface. The flux of surface reaction means the reactants consumed through surface reaction and is expressed as $F_2 = k_S C_S$. At steady state, mass transfer and the surface reaction reach dynamic equilibrium, therefore, $F_1 = F_2$. Simultaneously solving these equations, we obtain $C_S = \frac{h_G}{h_G + k_S} C_G$. The silylation reaction rate is $R = \frac{F}{N} = \frac{k_S h_G}{k_S + h_G} \frac{C_G}{N}$. Usually, h_G is a constant and $k_S = k_0 e^{-\frac{E_a}{kT}}$. The sylation rate is determined by the smaller one of h_G and k_S. i.e. If $h_G \ll k_S$, $R \approx h_G \frac{C_G}{N}$. This mass transfer controlled reaction may occur at a high temperature when the silylation agents react with the surface functional groups as soon as they arrive. If $k_S \ll h_G$, $R \approx k_S \frac{C_G}{N}$. This surface controlled reaction may occur at a low temperature or dominate in the situation of steric hindrance when the surface reaction rate is relatively low. In general situations, the above two reactions are competitive in figuring the total silylation reaction rate [39].

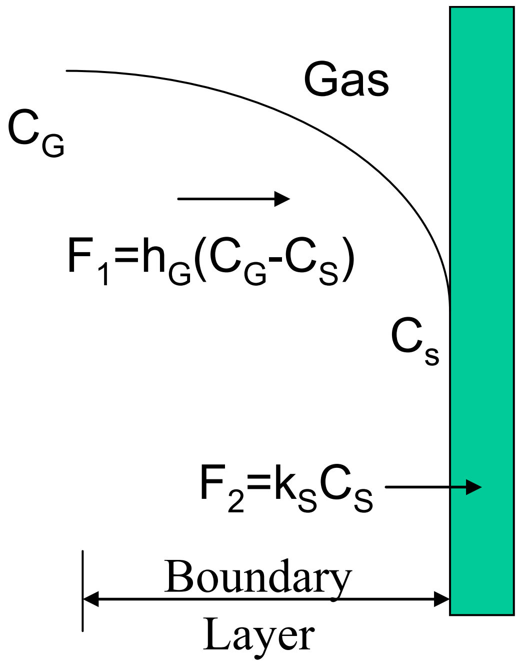

Fig. 5.25 Illustration of the mass transfer and surface reaction in the vapor silylation process.

The Laplace pressure, i.e., the capillary pressure, across a meniscus in a via or trench feature with a radius R of a dual damascene pattern, is given by $\Delta P = \frac{2\gamma\cos\theta}{R}$ where γ is the interfacial tension and θ is the contact angle. A positive capillary pressure for a wetting liquid, due to the higher external pressure compared with the pressure inside the material, tends to drag the solution into the material. However, the solutions tend to stay inside the material and will be difficult to be removed. On the other hand, a negative capillary pressure requires additional positive external forces to be applied on the liquid to force it into the material, and it will be easy to later remove the liquid through elimination of the external force. The surface tension γ of liquid CO_2 is only 1.5 mN/m at

25^0C and is almost zero at the critical point. Therefore, the capillary pressure is also close to zero for supercritical CO_2 [40] [41]. The very low capillary pressure enhances both the penetration and the removal of liquid, i.e. both mass transfer and surface reaction, during the silylation process.

Fig. 5.26 is the schematic view of a $scCO_2$ silylation system located at Prof. Johnston's lab. The process chamber with an outer diameter of 5", an inner diameter of 3", and an inside length of 3/16" was immersed in the water bath. The silylation chemicals like HMDS or TMCS were mixed with CO_2 in a small 300 ml stainless steel tube at room temperature. Pure CO_2 from an ISCO high pressure syringe pump, which was connected with the stainless tube, was used to pressurize the mixture. The mixture flowed into the process chamber through a stainless steel heat exchanger that had a length of 6 m and an inner diameter of 1.5 mm and was typically maintained at 45^0C and 10 MPa. After silylation, pure CO_2 flowed through the process chamber at a rate of 10 mL/min. for 1 or 2 minutes at the same temperature and pressure to rinse and dry the samples. Finally, the chamber was vented and samples were taken out.

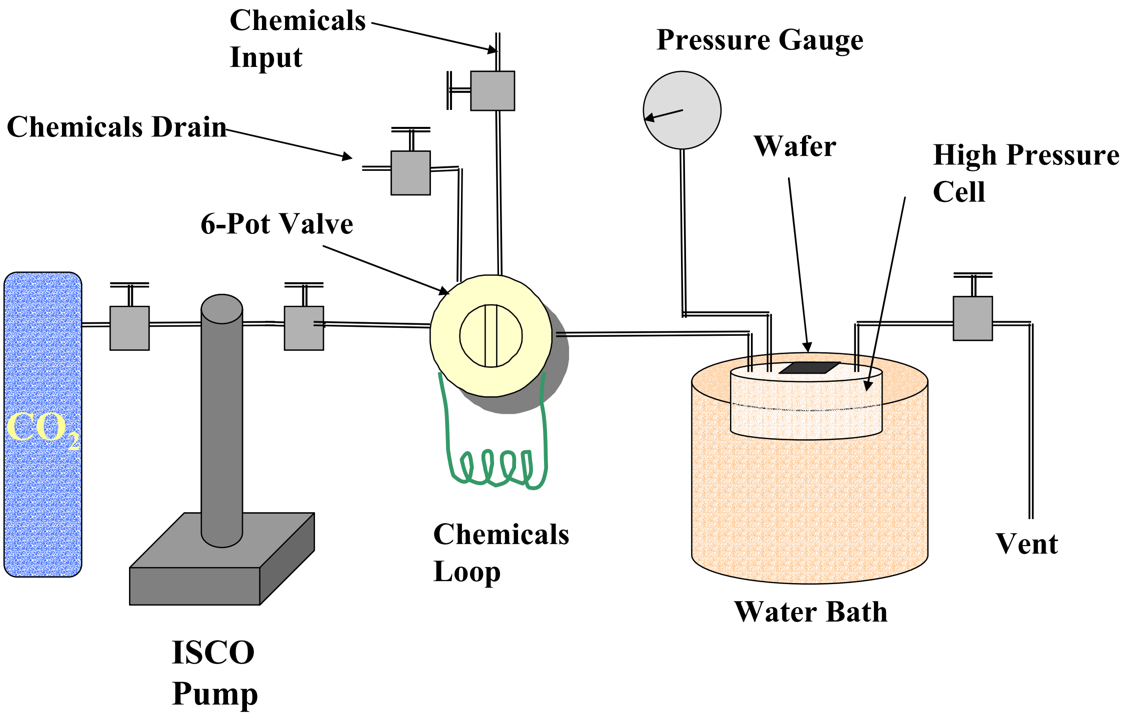

Fig. 5.26 Schematic diagram of a silylation process setup (Courtesy of Prof. K.P. Johnston & Lim)

FTIR spectra after $scCO_2$ TMCS silylation and subsequent annealing are presented in Fig. 5.27. Table 5.5 shows the calculated areas of major peaks in the FTIR spectra and the water contact angles of correspondent samples. The TMCS silylation was performed at 50^0C, 2000 psi with 0.5 ml TMCS for 2 min. TMCS reacted with sinanol groups in the O_2 damaged sample and replenished the sample with methyl groups, as indicated by the reduction of the Si-OH peak area from 1.22 to 0.78 and the increase of the $Si\text{-}CH_3$ peak area from 0.06 to 0.07. The water contact angle of the sample recovered from 48.5^0 to 86^0. The subsequent annealing at 300^0C for 1 hour improved the dielectric recovery by removing hydrogen bonded water and combining two adjacent silanols to form Si-O-Si. After annealing, the area of Si-OH peak was reduced from 0.78 to 0.34 and that of Si-O-Si peak rose from 5.70 to 5.83. The water contact angle of the sample further increased from 86.0^0 to 105.6^0, comparable to that of the pristine CDO.

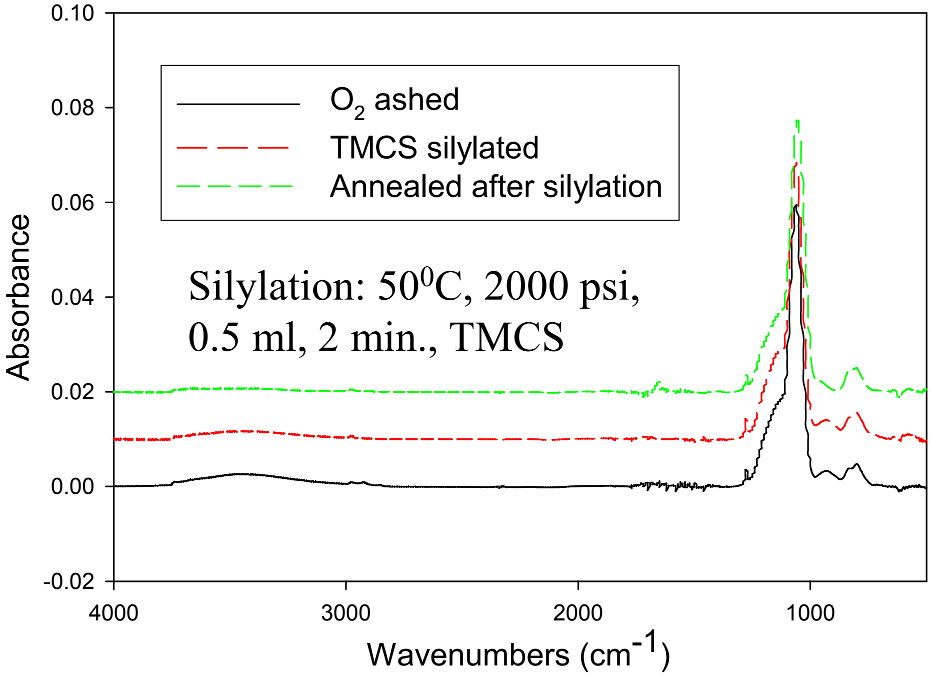

Fig. 5.27 **FTIR spectra of the sample after plasma O_2 ashing, $scCO_2$ TMCS silylation and subsequent annealing.**

Table 5.5 **Area of major FTIR peaks and the measurement of water contact angles.**

Sample \ Peak Area	Si-OH (3750~3050 cm^{-1})	$Si-CH_3$ (1290~1260 cm^{-1})	Si-O-Si (1240~980 cm^{-1})	Water Contact Angle(^{0})
Pristine CDO	0	0.12	5.92	97.8±7.8
O_2 ashed	1.22	0.06	5.61	48.5±0.7
TMCS silylated	0.78	0.07	5.70	86.0±1.0
Annealed after silylation	0.34	0.07	5.83	105.6±0.7

The effect of $scCO_2$ silylation could be enhanced through process optimizations. Fig. 5.28 shows the statistical distribution of water contact angles after adjustments of various process parameters. In principle, the water contact angles increased with the increasing amount of added silylation chemistry and applied pressure. And the pre or post silylation annealing further enhanced the recovery effect [42] [43].

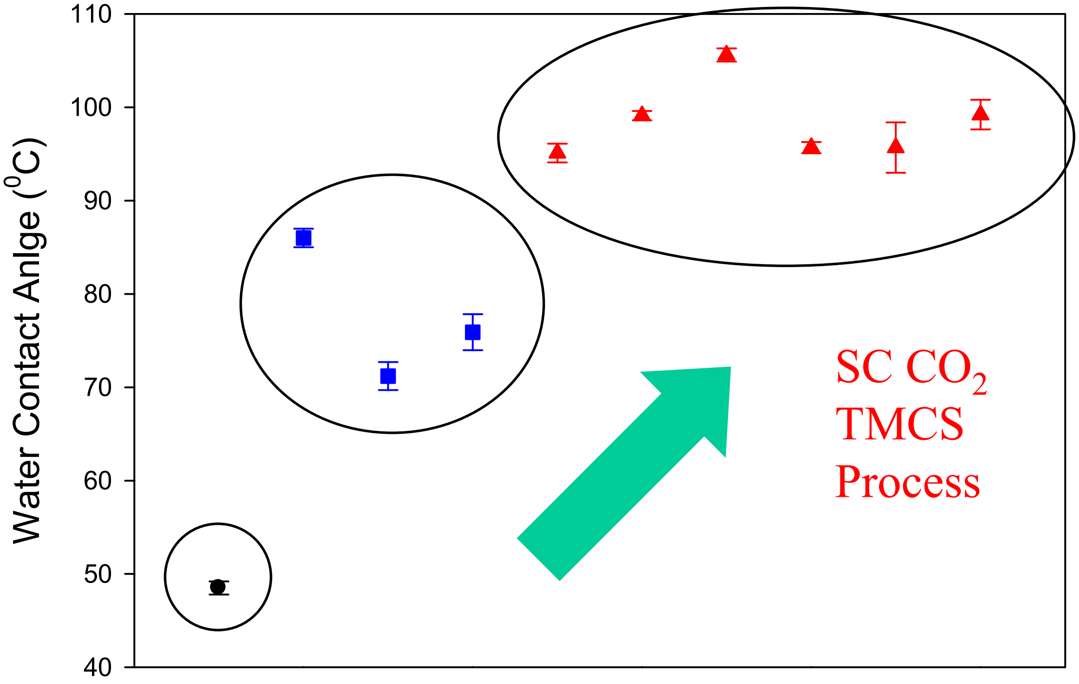

Fig. 5.28 **Distribution of water contact angles after various adjustments of silylation process parameters.**

5.3 Summary

Plasma damage to patterned low-κ dielectrics is a complicated phenomenon affected by the plasma species and the pattern structures. The energetic ions could remove methyl groups and cause surface densification to occur, but these ions were anisotropic and thus their effect depended on the impingement angle to the low-κ surface. Radicals, with less kinetic energy, were chemically active but isotropic and induced relatively uniform damage independent of the impingement angle. The depth of carbon depletion is determined by the diffusion of neutral species into low-κ materials. Therefore, the radicals caused deeper damage to the sidewall than ions, particularly for porous low-κ dielectrics. The distributions of charging potential, neutral, and ion fluxes in trenches were all affected by the aspect ratio of trenches.

The CH_4 plasma and silylation were found to be promising in repairing oxygen ashing damage~~s~~. They replaced the sinanols in the damaged low-κ dielectrics with methyl groups. But the recovery effect was only limited to a few nanometers on the surface of low-κ materials. CH_4 plasma induced the formation of a carbon-rich polymer layer, which seemed to limit the extent of the recovery of dielectric damage, while silylation chemicals were difficult to be transported deep into low-κ materials due to the limitations of surface reaction. To achieve full recovery of low-κ dielectric constant, process optimizations of CH_4 plasma or silylation are critical. Meanwhile, plasma damage to low-κ material should be minimized to the low-κ surface only.

Chapter 6 Conclusions and Future Work

6.1 Conclusions

Plasma-based technology is indispensable to the semiconductor industry. With the implementation of Cu/low-κ interconnects, it is increasingly important to understand the interaction between plasma and low-κ dielectric surfaces. This dissertation has been focused upon investigating how the plasma modifies the surface chemistry of low-κ dielectric materials. The surface engineering has led to two results: one was to facilitate the bonding and deposition of a thin, amorphous barrier material on low-κ surfaces; the other was to adversely induce the increase of dielectric constant of low-κ materials. The object of this dissertation work is to explore the mechanisms of the two phenomena.

Chapter 3 was devoted to the study of plasma enhancements of various surfaces with plasma beams. Transition metal carbides and nitrides such as TaN were selected to be the barrier films because they were pure, dense, conductive, conformal, thin, and provided good adhesion and low temperature processability ($<400^0$C). Atomic layer deposition technique was employed to achieve a thin and uniform barrier layer.

Analysis of the dielectric surfaces during ALD processes was performed in an ultra-high vacuum system capable of *in-situ* x-ray photoelectron spectroscopy analysis and equipped with an ECR hybrid plasma source. Ta_3N_5 was grown through the reaction $TaCl_5$ (g) + NH_3 (g) $\rightarrow$ Ta_3N_5 (s) + HCl (g). The hybrid source provided radical H or NH_x beams to enhance the process of atomic layer deposition.

Atomic layer deposition was a self-limiting surface chemistry process and therefore strongly depended on the functional groups of the substrate materials. ALD growth was performed on three different low-κ films: MSQ, OSG, and SiLK^{TM}. It was found that ALD nucleation on MSQ or OSG was slow due to the presence of a large number of methyl groups (Si-CH_3) and inadequate silanol (Si-OH) bonds on the surface, while Ta_3N_5 grew fast on SiLK^{TM} through the formation of charge transfer complexes between Ta and the benzene rings. It was concluded that Si-OH groups and benzene rings instead of Si-CH_3 groups in low-κ materials could provide good nucleation sites for Ta halide ALD processes.

Pretreatment of OSG low-κ dielectric surfaces with radical beams was found to enhance ALD growth through surface activation. Ta counts were observed to be much improved after the pretreatment of radical H_2 and NH_3. Quantification of the chemical composition of the low-κ surface after plasma treatment revealed that inactive methyl groups were replaced by active amino groups. And the radical H_2 helped to remove the surface contamination layer consisting of carbon and oxygen. Conformal Ta_3N_5 was also observed on patterned OSG films after radical H_2 and NH_3 pretreatments.

Monte Carlo simulations were carried out to illustrate the effects of the substrate surface chemistry and surface activation on ALD growth. One atom or molecule was represented by a grid point in a periodical 1D or 2D coordinate matrix. 1D Simulation results revealed that adequate substrate surface functional groups were very important for uniform and continuous layer by layer Frank-van der Merwe (FM) growth. After enough surface activation and sufficient nucleation, the film growth rate became faster due to the increase of the reaction probability. Further, 2D simulations were performed to compare the initial growth of ALD films on porous inactive surfaces with that on the activated surfaces. It indicated that it would take a long time for deposited molecules to form clusters to eventually bridge the inactive areas. But with enough surface activation, molecules could bridge and seal the pore openings in a very few initial cycles, finally resulting in continuous and uniform films.

Chapter 3 and Chapter 4 were devoted to the investigation of plasma damage to low-κ dielectric materials. The plasma damage is characteristic of carbon depletion, water incorporation, and surface densification. It was observed to occur at the open surfaces of low-κ films while the bulk remained largely unaffected. It was found that plasma damage was a complicated phenomenon involving both chemical and physical effects. The physical effect was dominated by heavy molecular-weight plasmas at high energy/dose, which induced significant densification of the low-κ surface. The chemical effect was dominated by light molecular-weight plasmas at low energy/dose, which altered surface chemistry and composition, such as carbon depletion from low-κ surfaces.

Downstream plasma damage to blanket low-κ films was characterized by various analytical techniques. It was discovered that ions induced more plasma damage to blanket low-κ films than neutrals due to energetics of ions helping to overcome the reaction barrier. Plasma damage also induced changes in bonding configurations, decreasing the Si-CH_3, cage, and network structures while increasing the suboxide structure. Up to 20% increase of the dielectric constant of low-κ materials was observed due to plasma damage and it was attributed to the removal of the methyl group, converting the low-κ surface to be predominantly hydrophilic. Among the three components of electronic, ionic, and dipolar polarization in dielectric constants, the dipolar polarization was changed mostly significantly due to incorporation of water molecules into low-κ molecular structures after plasma damage, as confirmed by Quantum chemistry calculations. Therefore, moisture uptake was primarily responsible for the dielectric constant increase. Annealing was generally effective in mitigating moisture uptake to restore the κ value but the recovery was less complete in the case of damage caused by higher energy plasmas.

Oxygen plasma damage to blanket and patterned low-κ materials was investigated. The results to blanket films indicated that the energetic ions could remove methyl groups and cause surface densification but they were anisotropic and thus their effect depended on the impingement angle to the low-κ surface. Radicals, with less kinetic energy, were chemically active but were isotropic so that they induced relatively uniform damage independent of the impingement angle. The depth of carbon depletion was determined by the diffusion of neutral species into low-κ materials. The possible reactions involved in the process of plasma damage to low-κ materials are summarized as follows:

$$Si-CH_3+O^- \rightarrow Si-CH=O+H_2O \qquad (6.1)$$

$$Si-CH=O+2O^-[O] \rightarrow Si-OH+CO_2 \qquad (6.2)$$

$$Si-CH_3+4O^-[O] \rightarrow Si-OH+CO_2+H_2O \qquad (6.3)$$

Monte Carlo simulations of plasma damage to low-κ materials were initiated. Less anisotropic electrons in plasma induced pattern-dependent differential charging. Flux and energy distribution of plasmas, particularly ions, in the trench was varied by the distribution of electron potential. It was therefore predictable that plasma damage to patterned structures was determined by both trench geometry and plasma conditions. EELS analysis of damaged patterned low-κ materials indicated that the radicals caused deeper carbon depletion to the sidewall than ions. And the damage to trench bottom and sidewall was observed to be not equal, depending on the trench geometry.

6.2 Suggestions for future work

With continued dimensional scaling of devices, more and more attention will be drawn to the interaction between plasma and dielectric. This dissertation has demonstrated the capabilities of many analytical techniques and enabled obtaining preliminary results of the fundamentals behind plasma low-κ interactions. This research work can be extended in both theoretical and experimental directions as follows:

Initial results of the electron potential distribution and ion/neutral flux distribution were already shown in Section 5.1.5 of Chapter 5 for patterned low-κ structure with AR=1. In order to describe the reactions involved in the O_2 plasma damage processes, a mathematical model was proposed in Section 5.1.2 of Chapter 5. The key parameters considered in such simulations were adsorption, desorption, and rate coefficients. These parameters were difficult to be determined individually by experiments, but in the simulations, they can be assumed from the literature references and by experience. Therefore, it is recommended that, by coupling the understanding of the physical and chemical processes into the Monte Carlo simulations, the distribution of carbon depletion, i.e. plasma damage to low-κ materials, be delineated. For example, it is possible to study various effects on plasma damage distribution; namely, the effects of process conditions such as pressure and temperature, the effects of plasma parameters such as ion/electron temperature, the effects of dielectric properties of low-κ materials, and the effects of low-κ structures such as line width, aspect ratio, and layered structures.

Experimentally, since the next generation of low-κ materials is typically characteristic of a large amount of carbon and porosity, it is therefore interesting to explore how the content of carbon and porosity influences the plasma damage. On the other hand, since plasma damage strongly depends on the process conditions, it is therefore necessary to investigate how the various parameters, such as plasma sources, species, energy, dose, and the process pressure and temperature, affect the plasma damage. In an effort to minimize the plasma damage, the tool companies are expected to work together with the material companies to figure out the optimal process windows for specific materials and plasmas.

Characterization of plasma damage to patterned low-κ materials is very challenging but urgently needed. As demonstrated in Chapter 2, ARXPS is a non-destructive technique to detect the element compositions on the field and trench sidewall separately. Once proper samples are obtained, ARXPS can be combined with EELS to investigate the plasma damage to patterned low-κ materials on different local areas of the structures. The effects of process conditions and trench geometries on the plasma damage to patterned low-κ materials can be fully studied. It is expected that experiments coupled with simulations can finally reveal the detailed mechanisms of this phenomenon.

Finally, the study of dielectric recovery should be on schedule. Although quite many techniques (plasma, vapor, scCO2, UV, annealing, etc) and agents (CH_4, HMDS, TMCS, DMDCS, phenyl containing agents, etc) seem promising, it will be interesting to combine and apply them together to damaged low-κ surfaces. Process parameters can be optimized and the effects can be evaluated and compared. To achieve the full integration of Cu/ULK interconnects, both minimization of plasma damage and recovery of dielectric materials should be optimized to seek the best process windows to meet the customer requirements.

Appendix: Modeling codes for the Monte Carlo simulation of atomic layer deposition

This is a typical 1D code to simulate 10 cycles of atomic layer deposition. It was debugged in Matlab software. Details of the simulation and results were presented in Chapter 2.

```
ALD=zeros(100);
PointerA=zeros(1,100,100);
i=1;
while i<=20
     j=ceil(100*rand)
     Sign=0
  if (i>1)
     for k=1:i-1
        if (PointerA(1,k,1)==j)
           Sign=1
        end
     end
  end
     if (Sign==1)
        i=i
     else
        PointerA(1,i,1)=j
        i=i+1
  end
  end;

for i=1:20
   j=PointerA(1,i,1)
   ALD(100,j)=1
   ALD(99,j)=2
end;

cycle=1
while cycle<=10
     q=100
     while q>=50
        for i=1:100
    if (i~=1 & i~=100 & ALD(q-1,i)==2)
      t=0
      if (ALD(q-1,i-1)==0)
         t=t+1
      end
      if (ALD(q-2,i-1)==0)
         t=t+1
```

```
    end
    if (ALD(q-2,i)==0)
       t=t+1
    end
    if (ALD(q-2,i+1)==0)
       t=t+1
    end
    if (ALD(q-1,i+1)==0)
       t=t+1
    end
    if (ALD(q,i+1)==0)
       t=t+1
    end
    if (ALD(q,i)==0)
       t=t+1
    end
    if (ALD(q,i-1)==0)
       t=t+1
    end

    k=rand
 if (k<=0.1 & t>=4)
    ALD(q-1,i)=3
    m=1
    if (ALD(q,i-1)==0 & m<=4)
       ALD(q,i-1)=4
       m=m+1
    end
    if (ALD(q-1,i-1)==0 & m<=4)
       ALD(q-1,i-1)=4
       m=m+1
    end
    if (ALD(q-2,i-1)==0 & m<=4)
       ALD(q-2,i-1)=4
       m=m+1
    end
    if (ALD(q-2,i)==0 & m<=4)
       ALD(q-2,i)=4
       m=m+1
    end
    if (ALD(q-2,i+1)==0 & m<=4)
       ALD(q-2,i+1)=4
       m=m+1
    end
    if (ALD(q-1,i+1)==0 & m<=4)
       ALD(q-1,i+1)=4
```

```
             m=m+1
         end
         if (ALD(q,i+1)==0 & m<=4)
             ALD(q,i+1)=4
             m=m+1
         end
         if (ALD(q,i)==0 & m<=4)
             ALD(q,i)=4
         end
     end
 end
end
 q=q-1
end

q=100
while q>=50
    for j=1:100
       if (j~=1 & j~=100 & ALD(q,j)==4 & ALD(q,j+1)==0 & ALD(q-1,j)==0)
        k=rand
        if (k<=0.1)
        ALD(q,j)=5
        ALD(q,j+1)=2
        ALD(q-1,j)=2
    end
end
end
           q=q-1
end
cycle=cycle+1
end


fid = fopen('C:\Bao\MC simulation\Ten cycles\ALD2.rtf','w');
for i=80:100
    for j=1:100
        fprintf(fid, '%f\n', ALD(i,j))
    end
    fprintf(fid, '%s\n', 'one layer finished')
end
fclose(fid)

Pointer=zeros(100)
for i=80:100
    for j=1:100
        if (ALD(i,j)~=0)
```

```
         Pointer(i,j)=101-i
      end
   end
end

fid = fopen('C:\Bao\MC simulation\Ten cycles\Pointer2.rtf','w');
for i=80:100
   for j=1:100
      fprintf(fid, '%f\n', Pointer(i,j))
   end
   fprintf(fid, '%s\n', 'one layer finished')
end
fclose(fid)

One=zeros(1,100)
for i=1:100
   One(1,i)=i
end
fid = fopen('C:\Bao\MC simulation\Ten cycles\One2.rtf','w');
for i=1:100
      fprintf(fid, '%f\n', One(1,i))
   end
fclose(fid)
```

Bibliography

Chapter 1

[1] G.E. Moore, *Electronics* **38** (8), April, (1965)

[2] S.-P. Jeng, M.-C. Chang, T. Kroger, P. McAnally, R. H. Havemann, *VLSI Tech. Symp. Tech. Dig.* 73 (1994)

[3] T.N. Theis, *IBM J. Res. Develop.* **44** (3), 379 (2000)

[4] M.T. Bohr, *Int. Elect. Dev. Meet. Tech. Dig.* 241 (1995)

[5] IBM web: http://www-03.ibm.com/press/us/en/pressrelease/21473.wss

[6] R.H. Havemann, J.A. Hutchby, *Proceedings of the IEEE* **89** (5), 586 (2001)

[7] S. Wolf, *Silicon Processing for the VLSI Era*, Vol. 4, Lattice Press, Sunset Beach, CA (2002)

[8] P.S. Ho, T. Kwok, *Rep. Prog. Phys.* **52**, 301 (1989)

[9] Stanford EE311 class notes: http://www.stanford.edu/class/ee311/NOTES/Interconnect_Al.pdf

[10] J.R. Lloyd, J. Clemens, R. Snede, *Microelectronics Reliability*, **39**, 1595 (1999)

[11] K.N. Tu, *J. Appl. Phys.* **94** (9), 5451 (2003)

[12] C. Christiansen, B. Li, J. Gill, R. Filippi, M. Angyal, *IIRW Final Report* 22 (2005)

[13] B. Li, T.D. Sullivan, T.C. Lee, *IEEE Trans. on Device and Materials Reliability* **4** (1), 80 (2004)

[14] J. Pyun, *PhD dissertation*, The University of Texas at Austin, (2007)

[15] E.T. Ogawa, K.-D. Lee, V.A. Blaschke, P.S. Ho, *IEEE Trans. Reliability* **51**, 403 (2002)

[16] K.-D. Lee, P.S. Ho, *IEEE Trans. on Device and Materials Reliability* **4** (2), 237 (2004)

[17] E.T. Ogawa, J. Kim, G.S. Haase, H.C. Mogul, J.W. McPherson, *IEEE 41st Annual International Reliability Physics Symp.* 166 (2003)

[18] F. Chen, O. Bravo, K. Chanda, P. McLaughlin, T. Sullivan, J. Gill, J. Lloyd, R. Kontra, J. Aitken, *IEEE 44th Annual International Reliability Physics Symp.* 46 (2006)

[19] C.D. Hartfield, E.T. Ogawa, Y.-J. Park, T.-C. Chiu, H. Guo, *IEEE Trans. on Device and Materials Reliability* **4** (2), 1 (2004)

[20] J.W. McPherson, C.F. Dunn, *J. Vac. Sci. Technol*. B, **5** (5), 1321 (1987)

[21] E. Ogawa, J. McPherson, J. Rosal, K. Dickerson, T. Chiu, L. Tsung, M. Jain, T. Bonifield, J. Ondrusek, W. McKee, *Proc. IRPS* (2002)

[22] Z. Suo, *Reliability of Interconnect Structures*, in Vol 8: Interfacial and Nanoscale Failure (W. Gerberich, W. Yang, Editors), Comprehensive Structural Integrity (I. Milne, R.O. Ritchie, B. Karihaloo, Editors-in-Chief), Elsevier, Amsterdam, 265 (2003)

[23] P.S. Ho, J. Leu, W.W. Lee, *Low Dielectric Constant Materials for IC Applications*, Springer, (2002)

[24] G. Wang, *PhD dissertation*, The University of Texas at Austin, (2004)

[25] C.-K. Hu, L. Gignac, R. Rosenberg, E. Liniger, J. Rubino, C. Sambucetti, A. Stamper, A. Domenicucci, X. Chen, *Microelectronic Engineering* **80**, 406 (2003)

[26] International Technology Roadmap for Semiconductors, Interconnect, http://www.itrs.net, (2007)

[27] L. Peters, *Semiconductor International* June (2006)

[28] R.P. Feynman, R.B. Leighton, M. Sands, *The Feynman Lectures on Physics*, Chap. 11, Adison Wesley, Reading, PA (1966)

[29] C. Kittel, *Introduction to Solid State Physics*, 6th ed., Wiley, NY (1986)

[30] S.M. Han, E.S. Aydil, *J. Appl. Phys.* **83** (4), 2172 (1998)

[31] D.R. Lide Editor, *Handbook of Chemistry and Physics*, 74th ed., CRC Press, (1993)

[32] L. Pauling, *General Chemistry*, Dover Publications, (1970)

[33] K. Maex, M.R. Baklanov, D. Shamiryan, F. Iacopi, S.H. Brongersma, Z.S. Yanovitskaya, *J. Appl. Phys.* **93** (11), 8793 (2003)

[34] A. Grill, D.A. Neumayer, *J. Appl. Phys.* **94** (10), 6697 (2003)

[35] M.V. Bavel, F. Iacopi, M. Baklanov, K. Maex, *Future Fab Intl.* **17,** (2004)

[36] M. Ritala, M. Leskelä, *Atomic Layer deposition* in Chapter 2, Vol. 1 Deposition and Processing of Thin Films, Handbook of Thin Film Materials (H.S. Nalwa Editor), Academic Press, (2002)

[37] J. Liu, J. Bao, M. Scharnberg, W.C. Kim, P.S. Ho, R. Laxman, *J. Vac. Sci. Technol.* A **23**, 1107 (2005)

[38] M.A. Worsley, S.F. Bent, N.C.M. Fuller, T. Dalton, *J. Appl. Phys.* **100**, 083301 (2006)

[39] P.M. Bellan, *Fundamentals of Plasma Physics*, Cambridge University Press, (2006)

[40] M.A. Lieberman, A.J. Lichtenberg, *Principles of Plasma Discharges and Materials Processing*, 2nd Ed., Wiley, NY (2005)

[41] J.D. Plummer, M.D. Deal, P.B. Griffin, *Silicon VLSI Technology: Fundamentals, Practice and Modeling*, Prentice Hall, Upper Saddle River, NJ (2000)

[42] S. Xu, C. Qin, L. Diao, D. Gilbert, L. Hou, A. Wiesnoski, E. Busch, R. McGowan, B. White, F. Weber, *J. Vac. Sci. Technol.* B 25 (1), 156 (2007)

[43] J. Bao, H. Shi, J. Liu, H. Huang, P.S. Ho, M.D. Goodner, M. Moinpour, G.M. Kloster, *J. Vac. Sci. Technol.* B 26 (1), (2008)

[44] Private discussions with A. Li at Applied Materials. Inc.

[45] T. Abell, J. Schuhmacher, Y. Travaly, K. Maex, *Mater. Res. Soc. Proc.* **812,** F 2.7 (2004)

[46] H. Cui, R.J. Carter, D.L. Moore, H.-G. Peng, D.W. Gidley, P.A. Burke, *J. Appl. Phys.* **97**, 113302 (2005)

[47] A. Grill, V. Patel, *J. Electrochemical Soc.* **153** (8), F169 (2006)

[48] T.J. Dalton, N. Fuller, C. Tweedie, D. Dunn, C. Labelle, S. Gates, M. Colburn, S.T. Chen, L. Tai, R. Dellaguardia, K. Petrarca, C. Dziobkowski, K. Kumar, S. Siddiqui, *Proceedings of IEEE IITC* 154 (2004)

[49] M.A. Worsley, S.F. Bent, N.C.M. Fuller, T.L. Tai, J. Doyle, M. Rothwell, T. Dalton, *J. Appl. Phys.* **101**, 013305 (2007)

[50] J. Bao, H. Shi, H. Huang, P.S. Ho, E. Paek, G.S. Hwang, M.L. McSwiney, M. Moinpour, G.M. Kloster, *Proceedings of IEEE IITC* (2008), submitted

[51] G.S. Hwang, K.P. Giapis, *Phys. Rev. Lett.* **79** (5), 845 (1997)

[52] T. Abell, J. Lee, M. Moinpour, *Mater. Res. Soc. Proc.* **914,** F 4.2 (2006)

[53] F. Iacopi, M. Stucchi, O. Richard, K. Maex, *Electrochemical and Solid-State Letters* **7** (4), G79 (2004)

[54] G. Mannaert, M.R. Baklanov, Q.T. Le, Y. Travaly, W. Boullart, S. Vanhaelemeersch, A.M. Jonas, *J. Vac. Sci. Technol.* B 23 (5), 2198 (2005)

[55] A. Matsushita, N. Ohashi, K. Inukai, H.J. Shin, S. Sone, K. Sudou, K. Misawa, I. matsumoto, N. Kobayashi, *Proceedings of IEEE IITC* 147 (2003)

[56] T.C. Chang, Y.S. Mor, P.T. Liu, T.M. Tsai, C.W. Chen, Y.J. Mei, S.M. Sze, *Thin Solid Films* **398-399**, 632 (2001)

[57] S.K. Singh, A.A. Kumbhar, R.O. Dusane, *Materials Letters* **60**, 1579 (2006)

[58] H. Shi, J. Bao, H. Huang, B. Chao, S. Smith, Y. Sun, P.S. Ho, A. Li, M. Armacost, D. Kyser, *Proceedings of IEEE IITC* (2008), submitted

[59] H. Shi, J. Bao, J. Liu, H. Huang, P.S. Ho, M.D. Goodner, M. Moinpour, G.M. Kloster, *Mater. Res. Soc. Proc.* **990, B** 3.12 (2007)

[60] J. Bao, H. Shi, J. Liu, H. Huang, P.S. Ho, M.D. Goodner, M. Moinpour, G.M. Kloster, *Proceedings of IEEE IITC* 147 (2007)

[61] Y.H. Wang, D. Gui, R. Kumar, P.D. Foo, *Electrochemical and Solid-State Letters* **6** (1), F1 (2003)

[62] C.Y. Wang, J.Z. Zheng, Z.X. Shen, Y. Lin, A.T.S. Wee, *Thin Solid Films* **397**, 90 (2001)

[63] Y.S. Mor, T.C. Chang, P.T. Liu, T.M. Tsai, C.W. Chen, S.T. Yan, C.J. Chu, W.F. Wu, F.M. Pan, W. Lur, S.M. Sze, *J. Vac. Sci. Technol.* B 20 (4), 1334 (2002)

[64] T.C. Chang, P.T. Liu, Y.S. Mor, T.M. Tsai, C.W. Chen, Y.J. Mei, F.M. Pan, W.F. Wu, S.M. Sze, *J. Vac. Sci. Technol.* B 20 (4), 1561 (2002)

[65] B. Xie, A.J. Muscat, *Mater. Res. Soc. Proc.* **812,** F 1.4.1 (2004)

[66] B.P. Gorman, R.A. Orozco-Teran, Z. Zhang, P.D. Matz, D.W. Mueller, R.F. Reidy, *J. Vac. Sci. Technol.* B 22 (3), 1210 (2004)

[67] B. Xie, A.J. Muscat, *Microelectronic Engineering* **82**, 434 (2005)

[68] B. Xie, L. Choate, A.J. Muscat, *Microelectronic Engineering* **80**, 349 (2005)

[69] S.V. Nitta, S. Purushothaman, N. Chakrapani, O. Rodriguez, N. Klymko, E.T. Ryan, G. Bonilla, S. Cohen, S. Molis, K. McCullough, *Proceedings of AMC* (2005)

[70] C. Smith, D. Mueller, P. Matz, R. Reidy, *Mater. Res. Soc. Proc.* **914,** F 04-04 (2006)

Chapter 2

[1] R. Geller, *Proc. 1st Int. Con. Ion Source* Salcay, 537 (1969)

[2] H. Postma, *Phys. Lett.* A **31**, 196 (1970)

[3] *OSMiPlas Mini Plasma Source Operating Manual*, Oxford Scientific, Oxford (2002)

[4] J. Liu, *PhD Dissertation*, The University of Texas at Austin, (2006)

[5] M.P. Marder, *Condensed Matter Physics*, Corrected Printing, John Wiley & Sons, NY (2000)

[6] D. Briggs, M.P. Seah, *Practical Surface Analysis: Auger and X-Ray Photoelectron Spectroscopy*, 2nd ed., John Wiley & Sons, NY (1996)

[7] B. Ulgut, S. Suzer, *J. Phys. Chem.* B **107** (13), 2939 (2003).

[8] M.A. Worsley, S.F. Bent, N.C.M. Fuller, T.L. Tai, J. Doyle, M. Rothwell, T. Dalton, *J. Appl. Phys.* **101**, 013305 (2007)

[9] E. Chason, *X-Ray Reflectivity for Studies of Surface and Interface Structure*, in *In Situ Real Time Characterization of Thin Films* (O. Auciello, A.R. Krauss, Editors), Wiley, NY, 167 (2001)

[10] P.F. Fewster, *Rep. Prog. Phys.* **59**, 1339 (1996)

[11] E. Chason, T.M. Mayer, A. Payne, D. Wu, *Appl. Phys. Lett.* **60** (19), 2353 (1992)

[12] M.F. Toney, S. Brennan, *J. Appl. Phys.* **66** (4), 1861 (1989)

[13] F. Huang, MINT Tutorial Seminar, MINT Center, AL (2005)

[14] *X'Pert Quick Start Guide*, 1st ed., PANalytical B.V., Almelo, Netherlands (2003)

[15] M. Schubert, *Annalen der Physik* **15** (7-8), 480 (2006)

[16] J.D. Jackson, *Classical Electrodynamics*, 3rd ed., Wiley, NY (1998)

[17] R. Synowicki, *Ellipsometer Workshop at UT-Austin*, Austin, TX (2006)

[18] C. J. Raymond, *Proc. SPIE* CR72, 147 (1999)

[19] Z. R. Hatab, J. R. McNeil, S. S. H. Naqvi, *J. Vac. Sci. Technol.* B **13** (2), 174 (1995)

[20] D.W. Gidley, W.E. Frieze, T.L. Dull, A.F. Yee, E.T. Ryan, H.-M. Ho, *Phys. Rev.* B **60** (8), R5157 (1999)

[21] H.-J. Lee, C.L. Soles, D.-W. Liu, B.J. Bauer, E.K. Lin, W.-L. Wu, A. Grill, *J. Appl. Phys.* **95** (5), 2355 (2004)

[22] M.R. Baklanov, K.P. Mogilnikov**,** *Proc. of 6th International Conference on Solid-State and Integrated-Circuit Technology* 352 (2001)

[23] W.A. Pliskin, *Semiconductor Silicon*, (H.R. Huff, R.R. Burgess, Editors), Electrochemical Society, NJ, 509 (1973)

[24] G.C. Schwartz, K.V. Srikrishnan, Editors, *Handbook of Semiconductor Interconnection Technology*, CRC Press, FL (2006)

[25] G. Socrates, *Infrared Characteristic Group Frequencies*, 2nd Edition, Wiley and Sons (1998)

[26] A. Grill, D.A. Neumayer, *J. Appl. Phys.* **94** (10), 6697 (2003)

[27] M. von Ardenne, *Zeitschrift fur Physik* (in German) **108**, 553 (1938)

[28] D.B. Williams, C.B. Carter, *Transmission Electron Microscopy: a Textbook for Materials Science*, Vol. I, Basics, Plenum Press, NY (1996)

[29] L. Rabenberg, *Course Packet for ME 387R: Electron Diffraction & Microscopy*, the University of Texas at Austin, Spring (2004).

[30] D.B. Williams, C.B. Carter, *Transmission Electron Microscopy: a Textbook for Materials Science*, Vol. IV, Spectrometry, Plenum Press, NY (1996)

[31] *e-Vision and e-Vision$^+$ User Manual*, MKS instruments, Inc. (2006)

[32] *Application Note*, MKS instruments, Inc. (2006)

[33] C.C. Tee, G. Sarkar, S.C.Y. Meng, D.L.H. Yu, L. Chan, *Proc. of Electron Device Meetings* 86 (1997)

[34] D.K. Schroder, *Semiconductor Material and Device Characterization*, 2nd Edition, Wiley-Interscience, (1998)

[35] M.L. Green, E.P. Gusev, R. Degraeve, E.L. Garfunkel, *J. Appl. Phys.* **90** (5), 2057 (2001)

[36] K. Maex, M.R. Baklanov, D. Shamiryan, F. Iacopi, S.H. Brongersma, Z.S. Yanovitskaya, *J. Appl. Phys.* **93** (11), 8793 (2003)

Chapter 3

[1] M. Leskelä, M. Ritala, *Thin Solid Films* **409,** 138 (2002)

[2] S.M. Rossnagel, H. Kim, *Proceedings of IEEE IITC* 3 (2001)

[3] H. Kim, *J. Vac. Sci. Technol.* B **21** (6), 2231 (2003)

[4] M. Ritala, M. Leskelä, *Atomic Layer Deposition*, in Vol. 1, in *Handbook of Thin Materials* (H.S. Nalwa editor), 1st edition, Academic Press, (2001)

[5] J. Kim, H. Hong, K. Oh, C. Lee, *Applied surface science* **210**, 231 (2003)

[6] J. Gelatos, L. Chen, H. Chung, R. Thakur, A. Sinha, *Solid State Technology* February, 44 (2003)

[7] ITRS Roadmap 2007, Interconnect, http://www.itrs.net

[8] D. Edelstein, C. Uzoh, C. Cabral, Jr., P. DeHaven, P. Buchwalter, A. Simon, E. Cooney, S. Malhotra, D. Klaus, H. Rathore, B. Aganvala, D. Nguyen, *Proceedings of IEEE IITC* 9 (2001)

[9] J. Liu, J. Bao, M. Scharnberg, W.C. Kim, P.S. Ho, R. Laxman, *J. Vac. Sci. Technol.* A **23**, 1107 (2005)

[10] The Dow Chemical Company, http://www.dow.com/silk/index.htm

[11] Y. Uchida, T. Fukuda, H. Yanazawa, *Suface and Interface Analysis* **36**, 677 (2004)

[12] D.D. Hawn, *Surface Science Spectra* **9**, 1 (2002)

[13] J. Liu, M. Scharnberg, J. Bao, J. Im, P.S. Ho, *J. Vac. Sci. Technol.* A **23** (4), 1422 (2005)

[14] M. Scharnberg, *Master thesis*, The University of Texas at Austin, (2003)

[15] R. Haight, R.C. White, B.D. Silverman, P.S. Ho, *J. Vac. Sci. Technol.* A **6** (4), 2188 (1988)

[16] D.R. Lide (Editor-in-Chief), *CRC Handbook of Chemistry and Physics*, 84th edition (2003-2004)

[17] http://chemviz.ncsa.uiuc.edu/content/doc-resources-bond.html

[18] J. Bao, J. Liu, H. Shi, P.S. Ho, SRC Deliverable for Project 1021.001 – LSI Custom Funding, Dec. (2005)

[19] J. Venables, *Introduction to Surface and Thin Film Processes*, Cambridge University Press, (2000)

[20] G.H. Gilmer, *Computational Materials Science* **12**, 354 (1998)

[21] C. Ratsch, UCLA Mathematics Colloquium, May, (2003)

[22] K.N. Tu, J.W. Mayer, L.C. Feldman, *Electronic Thin Film Science: For Electrical Engineering and Materials*, Pearson Education, (1996)

[23] D.V. Brunev et al, 4th Siberian Russian Workshop and Tutorials, **21** (2003)

[24] J.A. Venables, G.D.T. Spiller, M. Hanbucken, *Rep. Prog. Phys.* **47**, 399 (1984)

[25] M. Kalke, *PhD dissertation*, Indiana University, (2002)

[26] Z.S. Yanovitskaya, A.V. Zverev, D. Shamiryan, K. Maex, *Microelectronic Engineering* **70**, 363 (2003)

Chapter 4

[1] ITRS Roadmap 2007, Interconnect, http://www.itrs.net

[2] M. Morgen, E.T. Ryan, J.H. Zhao, C. Hu, T. Cho, P.S. Ho, *Annu. Rev. Mater. Sci.* **30**, 645 (2000)

[3] K. Maex, M.R. Baklanov, D. Shamiryan, F. Iacopi, S.H. Brongersma, Z.S. Yanovitskaya, *J. Appl. Phys.* **93**, 8793 (2003)

[4] D. Moore, R. Carter, H. Cui, P. Burke, P. McGrath, S.Q. Gu, D. Gidley, H. Peng, *J. Vac. Sci. Technol.* B **23**, 332 (2005)

[5] D. Shamiryan, M.R. Baklanov, S. Vanhaelemeersch, K. Maex, *J. Vac. Sci. Technol.* B **20**, 1923 (2002)

[6] F. Iacopi, M. Stucchi, O. Richard, K. Maex, *Electrochemical and Solid-State Letters* **7**, G79 (2004)

[7] M.A. Worsley, S.F. Bent, N.C.M. Fuller, T.L. Tai, J. Doyle, M. Rothwell, T. Dalton, *J. Appl. Phys.* **101**, 013305 (2007)

[8] J. Bao, H. Shi, J. Liu, H. Huang, P.S. Ho, M.D. Goodner, M. Moinpour, G.M. Kloster, *Proc. of IITC* 147 (2007)

[9] E. Kesters, Q. Le, W. Boullart, Q. Han, I. Berry, C. Waldfried, P. Mertens, M. Heyns, *Cleaning Technology in Semiconductor Devices Manufacturing IX. ECS* 319 (2005)

[10] H. Cui, R.J. Carter, D.L. Moore, H.G. Peng, D.W. Gidley, P.A. Burke, *J. Appl. Phys.* **97**, 113302 (2005)

[11] H. Shi, J. Bao, J. Liu, H. Huang, P.S. Ho, M.D. Goodner, M. Moinpour, G.M. Kloster, *Mater. Res. Soc. Symp. Proc*. **990**, B03-12 (2007)

[12] B.P. Gorman, R.A. Orozco-Teran, Z. Zhang, P.D. Matz, D.W. Mueller, R.F. Reidy, *J. Vac. Sci. Technol.* B **22**, 1210 (2004)

[13] Y.S. Mor, T.C. Chang, P.T. Liu, T.M. Tsai, C.W. Chen, S.T. Yan, C.J. Chu, W.F. Wu, F.M. Pan, Water Lur, S.M. Sze, *J. Vac. Sci. Technol.* B **20**, 1210 (2004)

[14] J. Liu, W. Kim, J. Bao, H. Shi, W. Baek, P.S. Ho, *J. Vac. Sci. Technol.* B **25**, 1071 (2007)

[15] D. Briggs, M.P. Seah, *Practical Surface Analysis*, Vol 1, Wiley & Sons, (1990)

[16] C.Y. Wang, J.Z. Zheng, Z.X. Shen, Y. Lin, A.T.S. Wee, *Thin Solid Films* **397**, 90 (2001)

[17] G. Socrates, *Infrared Characteristic Group Frequencies*, 2nd Edition, Wiley & Sons, (1998)

[18] P.F. Fewster, *Rep. Prog. Phys.* **59**, 1339 (1996)

[19] H.W. Kim, J.H. Myung, N.H. Kim, H.S. Lee, S.-G. Park, J.G. Lee, C.W. Chung, W. J. Park, C.-J. Kang, C.-G. Yoo, K.-H. Ko, J.-H. Woo, S.-D. Choi, D.-K. Choi, *Thin Solid Films* **506-507**, 222 (2006)

[20] J.-H. Shieh, Y.-N. Su, J.-S. Tsai, C.-N. Yeh, H.-J. Tao, US Patent 7029992

[21] Y.H. Wang, D. Gui, R. Kumar, P.D. Foo, *Electrochemical and Solid-State Letters* **6** (1), F1 (2003)

[22] G. Binnig, C.F. Quate, Ch. Gerber, *Phys. Rev. Lett.* **56**, 930 (1986)

[23] J. Malzbender, J.M.J. den Toonder, A.R. Balkenende, D. de With, *Materials Science and Engineering* R **36**, 47 (2002)

[24] K.-I. Yanai, T. Hasebe, K. Sumiya, S. Oguni, K. Koga, *Mater. Res. Soc. Symp. Proc.* **863**, B2.3.1 (2005)

[25] Q.T. Le, M. Patz, H. Struyf, M. Baklanov, W. Boullart, S. Vanhaelemeersch, K. Maex, Abs 140, 205th Meeting, *The Electrochemical Society*, Inc. (2004)

[26] S. Xu, C. Qin, L. Diao, D. Gilbert, L. Hou, A. Wiesnoski, E. Busch, R. McGowan, B. White, F. Weber, *J. Vac. Sci. Technol.* B **25**, 156 (2007)

[27] A. Grill, D.A. Neumayer, *J. Appl. Phys.* **94**, 6697 (2003)

[28] J.P. Chang, J.W. Coburn, *J. Vac. Sci. Technol.* A **21** (5), S145 (2003)

[29] G.S. Oehrlein, M.F. Doemling, B.E.E. Kastenmeier, P.J. Matsuo, N.R. Rueger, M. Schaepkens, T.E.F.M. Standaert, *IBM Journal of Research and Development* **43** (1-2), (1999)

[30] E.R. Fisher, *Plasma Sources Sci. Technol.* **11**, A105 (2002)

[31] B.A. Morrow, I.A. Cody, *J. Phys. Chem.* **80**, 1995 (1976)

[32] J.Y. Kim, M.S. Hwang, Y.H. Kim, H.J. Kim and Y. Lee, *J. Appl. Phys.* **90**, 2469 (2001)

[33] M.A. Omar, *Elementary Solid State Physics*, Addison-Wesley, New York, (1975)

[34] D.R. Lide (Editor-in-Chief), *CRC Handbook of Chemistry and Physics*, 84th edition (2003-2004)

[35] L. Pauling, *General Chemistry*, Dover Publications, (1970)

[36] S. Jain, V. Zubkov, T. Nowak, A. Demos, J.C. Rocha, *Solid State Technology* September, (2005)

[37] Ryan Scott Smith, *PhD dissertation*, The University of Texas at Austin, (2007)

[38] H. Shi, J. Bao, J. Liu, H. Huang, S. Smith, Q. Zhao, P.S. Ho, M.D. Goodner, M. Moinpour, G.M. Kloster, *Proc. of AMC* VB.3, (2007)

[39] Y.S. Mor, T.C. Chang, P.T. Liu, T.M. Tsai, C.W. Chen, S.T. Yan, C.J. Chu, W.F. Wu, F.M. Pan, W. Lur, S.M. Sze, *J. Vac. Sci. Technol.* B **20** (4), 1334 (2002)

[40] H. Shi, J. Bao, J. Liu, H. Huang, S. Smith, Q. Zhao, P.S. Ho, M.D. Goodner, M. Moinpour, G.M. Kloster, *To be submitted to Appl. Phys. Lett.*

[41] Gaussian online manual: http://www.gaussian.com/g_ur/g03mantop.htm

[42] P.D. Aldrich, S.K. Thurow, M.J. Mckennon, M.E. Lyssy, *Polymer* **28**, 2289 (1987)

[43] K.H. Lu, B. Chao, Z. Luo, L. Zhang, H. Shi, J. Im, P.S. Ho, L. Li, M. Ahmad, *Proc. 57th Electronic Components and Technology Conf.* 132 (1998)

Chapter 4

[1] S.M. Newman, A.J. Orr-Ewing, D.A. Newnham, J. Ballard, *J. Phys. Chem.* A **104**, 9467 (2000)

[2] M.S. Silverstein, M.Shach-Caplan, M. Khristosov, T. Harel, *Plasma Process. Polym.* **4**, 789 (2007)

[3] A. Grill, D.A. Neumayer, *J. Appl. Phys.* **94**, 6697 (2003)

[4] D.R. Lide (Editor-in-Chief), *CRC Handbook of Chemistry and Physics*, 84th edition (2003-2004)

[5] T.M. Mayer, R.A. Barker, *J. Vac. Sci. Technol.* **21** (3), 757 (1982)

[6] E. Zawaideh, N.S. Kim, *J. Appl. Phys.* **62** (6), 2498 (1987)

[7] M.A. Lieberman, A.J. Lichtenberg, *Principles of Plasma Discharges and Materials Processing*, 2nd Ed., Wiley & Sons, (2005)

[8] R.A. Gottscho, C.W. Jurgensen, D.J. Vitkavage, *J. Vac. Sci. Technol.* **10** (5), 2133 (1992)

[9] T. Abell, J. Lee, M. Moinpour, *Mater. Res. Soc. Symp. Proc.* **914**, 0914-F04-02 (2006)

[10] N.C.M. Fuller, M.A. Worsley, S. Nitta, T. Dalton, T.L. Tai, S. Bent, T. Magbitang, G. Dubois, R. Miller, W. Volksen, M. Sankar, S. Purushothaman, *Proc. of IITC* 24 (2006)

[11] O. Richard, F. Iacopi, H. Bender, G. Beyer, *Microelectronic Engineering* **84**, 517 (2007)

[12] T.S. Gross, S. Yao, S. Satyanarayana, *Mater. Res. Soc. Symp. Proc.* **863**, B.2.4.1 (2005)

[13] S. Chikaki, M. Shimoyama, R. Yagi, T. Yoshino, Y. Shishida, T. Ono, A. Ishikawa, N. Fujii, T. Nakayama, K. Kohmura, H. Tanaka, J. Kawahara, H. Matsuo, S. Takada, T.

Yamanishi, S. Hishiya, N. Hata, K. Kinoshita, T. Kikkawa, *IEEE International Symp. on Semiconductor Manufacturing* **422** (2005)

[14] F. Iacopi, M. Stucchi, O. Richard, K. Maex, *Electrochemical and Solid-State Letters* **7** (4), G79 (2004)

[15] H. Shi, J. Bao, H. Huang, B. Chao, S. Smith, Y. Sun, P. S. Ho A. Li, M. Armacost, D. Kyser, *submitted to IEEE IITC* (2008)

[16] J.S. Tsai, Y.N. Su, R.Y. Huang, J.M. Chiou, J.H. Shieh, H.Y. Chu, J.J. Lee, C.Y. Ting, S.M. Jang, M.S. Liang, *Proceedings of IEEE ISSM* 183 (2005)

[17] S. Satyanarayana, R. McGowan, B. White, S.D. Hosali, *Semiconductor International* June (2005)

[18] J.C. Arnold, H.H. Sawin, *J. Appl. Phys.* **70** (10), 5314 (1991)

[19] G.S. Hwang, K.P. Giapis, *J. Vac. Sci. Technol.* B, **15** (1), 2133 (1997)

[20] R.J. Shul, S.J. Pearton (Editors), *Handbook of Advanced Plasma Processing Techniques*, Springer, NY (2000)

[21] G.S. Hwang, K.P. Giapis, *Phys. Rev. Lett.* **79** (5), 845 (1997)

[22] J.A. Kenney, *PhD Dissertation*, The University of Texas at Austin, (2007)

[23] J. Bao, H. Shi, H. Huang, P.S. Ho, E. Paek, G.S. Hwang, M.L. McSwiney, M. Moinpour, G.M. Kloster, *submitted to IEEE IITC* (2008)

[24] J.A. Kenney, G.S. Hwang, *J. Appl. Phys.* **101**, 044307 (2007)

[25] H. Shi, J. Bao, J. Liu, H. Huang, P.S. Ho, M.D. Goodner, M. Moinpour, G.M. Kloster, *Mater. Res. Soc. Proc.* B, B03-12 (2007)

[26] J.J. Bao, H.L. Shi, J.J. Liu, H. Huang, P.S. Ho, M.D. Goodner, M. Moinpour, G.M. Kloster, *Proceedings of the IEEE IITC* 147 (2007)

[27] M. Aimadeddine, V. Arnal, D. Roy, A. Farcy, T. David, T. Chevolleau, N. Posséme, J. Vitiello, L.L. Chapelon, C. Guedj, Y. Brechet, F. Volpi, J. Torres, *Proceedings of the IEEE IITC* 81 (2006)

[28] Z.L. Wang, J.J. Li, Z.H. Sun, Y.L. Li, Q. Luo, C.Z. Gu, Z. Cui, *Appl. Phys. Lett.* **90**, 133118 (2007)

[29] T.C. Chang, P.T. Liu, Y.S. Mor, T.M. Tsai, C.W. Chen, Y.J. Mei, F.M. Pan, W.F. Wu, S.M. Sze, *J. Vac. Sci. Technol.* B 20 (4), 1561 (2002)

[30] S.K. Singh, A.A. Kumbhar, R.O. Dusane, *Materials Science and Engineering* B, **127**, 29 (2006)

[31] Y.S. Mor, T.C. Chang, P.T. Liu, T.M. Tsai, C.W. Chen, S.T. Yan, C.J. Chu, W.F. Wu, F.M. Pan, W. Lur, S.M. Sze, *J. Vac. Sci. Technol.* B **20** (4), 1334 (2002)

[32] S.V. Slavov, A.R. Sanger, K.T. Chuang, *J. Phys. Chem.* B, **104**, 983 (2000)

[33] B. Xie, A.J. Muscat, *Mater. Res. Soc. Proc.* **812,** F 1.4.1 (2004)

[34] B.P. Gorman, R.A. Orozco-Teran, Z. Zhang, P.D. Matz, D.W. Mueller, R.F. Reidy, *J. Vac. Sci. Technol.* B 22 (3), 1210 (2004)

[35] J. Liu, W. Kim, J. Bao, H. Shi, W. Baek, P.S. Ho, *J. Vac. Sci. Technol.* B **25** (3), 906 (2007)

[36] H. Shi, J. Bao, J. Liu, H. Huang, W. Kim, P.S. Ho, Y. Sun, M.D. Goodner, M. Moinpour, G.M. Kloster, *Mater. Res. Soc. Proc.* (2008), Accepted

[37] P.S. Ho, W.C. Kim, J. Liu**,** J. Bao, *Novel Surface Silylation Process for Porous Ultra Low k Integration*, US Patent, Pending

[38] S.V. Nitta, S. Purushothaman, N. Chakrapani, O. Rodriguez, N. Klymko, E.T. Ryan, G. Bonilla, S. Cohen, S. Molis, K. McCullough, *Proceedings of AMC* (2005)

[39] J.D. Plummer, M.D. Deal, P.B. Griffin, *Silicon VLSI Technology: Fundamentals, Practice and Modeling*, Prentice Hall, NJ (2000)

[40] J.A. Keagy, X. Zhang, K.P. Johnston, E. Busch, F. Weber, P.J. Wolf, T. Rhoad, *J. Supercrit. Fluids* **39** (2), 277 (2006)

[41] J.A. Keagy, Y. Li, P.F. Green, K.P. Johnston, F. Weber, J.T. Rhoad, E.L. Busch, P.J. Wolf, *J. Supercrit. Fluids* **42** (3), 398 (2007)

[42] T. Rajagopalan, B. Lahlouh, J.A. Lubguban, N. Biswas, S. Gangopadhyay, J. Sun, D.H. Huang, S.L. Simon, D. Toma, R. Butler, *Applied Surface Science* **252**, 6323 (2006)

[43] H. Shi, J. Bao, J. Liu, H. Huang, S. Smith, Q. Zhao, P.S. Ho, M.D. Goodner, M. Moinpour, G.M. Kloster, *Proceedings of AMC* VB.3, (2007)

Vita

Junjing (Jerry) Bao was born in Zongyang county, Anqing city, Anhui province of P.R. China on February 1, 1981, the second child to Shengchao Bao and Xiuling Shi. He received his Bachelor of Science in Physics from the University of Science and Technology of China in June, 2002.

He entered the Department of Physics of the University of Texas at Austin in September, 2002 and joined Prof. Ho's interconnect and packaging group as a graduate research assistant immediately. From June 2006 to September 2006 and June 2007 to August 2007, he was doing internships at Dr. Henry Nye's exploratory ULK BEOL integration group at IBM microelectronics, studying the back-end-of-line process integration and reliability issues of IBM 65nm technology and Qualcomm customized projects. He will return to the same group as an advisory engineer after PhD graduation**.** He has contributed to over 10 journal/conference papers, 5 technical reports, over 10 conference presentations and 1 US patent (Pending).

Permanent address: Rm. 305, Bldg. 39, Hui Xiang Xiao Qu
Anqing, Anhui, 246001
The People's Republic of China

This dissertation was typed by the author.